Surface Characterization and Functional Properties of Carbon-based Materials

A thesis submitted to the University of Oxford for
the degree of Doctor of Philosophy

Geoffrey Winston Nelson

Physical & Theoretical Chemistry
Department of Chemistry
University of Oxford
&
Hertford College

To my Parents and Grandparents,
whose love, and support for my education, never wavered

Surface Characterization and Functional Properties of Carbon-based Materials

Geoffrey W. Nelson, Hertford College, Trinity Term 2012

Abstract

Carbon-based materials are poised to be an important class of 21st century materials, for bio-medical, bio-electronic, and bio-sensing applications. Diamond and polymers are two examples of carbon-based materials of high interest to the bio-materials community. Diamond, in its conductive form, can be used as an electrochemical bio-sensor, whilst its nanoparticle form is considered a non-inflammatory platform to deliver drugs or to grow neuronal cells. Polymers, especially when chemically modified, have been used extensively in biological environments, from anti-microbial use to drug delivery. The large-scale use of either material for biological use is limited by two factors: ease of chemical modification and the paucity of knowledge of their surface chemistry in aqueous media. This thesis addresses aspects of both these issues.

The first study reported is an *in situ* study of the adsorption dynamics of an exemplar globular protein (bovine serum albumin, BSA) on nanodiamond using the relatively novel quartz crystal microbalance with dissipation (QCM-D) technique. For the first time, QCM-D enabled the detailed study of protein dynamics (i.e. kinetics, viscoelastic properties, overlayer structure, etc.) onto nanodiamond thin films having various surface chemistry and roughness. The dynamics of protein adsorption is found to be sensitive to surface chemistry at all stages of adsorption, but it is only sensitive to surface roughness during *initial* adsorption phases. Our understanding of the nanodiamond-biology interface is enhanced by this study, and it suggests that QCM-D is useful for the study of the surface chemistry of nanoparticle forms of inorganic materials.

A second study concerns a novel surface functionalization scheme, based on carbene and azo-coupling chemistry, which has been recently introduced as a practical, facile method for modifying the surfaces of polymers. Using modern surface characterization techniques, it is demonstrated that a chemical linker can be attached to polystyrene surfaces using carbene-based chemistry, and that further chemical functionality can be added to this chemical linker *via* an azo-coupling reaction. *In situ* studies of protein dynamics at these interfaces were conducted using QCM-D, thus enabling a link between specific protein behaviour and the polymer surface chemical termination chemistry to be made.

A third area of study of investigates the use of diamond electrodes as a bio-sensor for dopamine under physiological conditions. For these conditions, ascorbic acid interferes with the dopamine oxidation signal, in ways that render the two signals irresolvable. Various modifications are used in attempts to reduce this interference, including: small and large cathodic treatments, grafting of electro-active polymers, addition of carbon nanotubes, and hydrogen plasma treatment. Those modifications leading to the hydrogen-termination of diamond are shown to work the best. Notably, hydrogen plasma treatment effects the complete electrochemical separation of dopamine and ascorbic acid at a diamond electrode. This is the first time this has been accomplished without adding non-diamond materials to the diamond electrode surface.

Acknowledgements

I must first thank Professor John S. Foord, my supervisor, for taking me on as a D.Phil. student at Oxford. This D.Phil. thesis would never have come to fruition without his mentorship, scientific leadership, and his abundance of patience and good humour.

The resources and assistance of Dr Emily Parker, Professor Mark Moloney, Dr Chris Blanford, Dr Robert Jacobs, Dr Jingping Hu, Edward Lewis, Julia Doff and Kulveer Singh were instrumental to the development of this research. Professor Schofield and Dr Claire Vallance have been invaluable College-based mentors, and I thank them for providing me with the wonderful opportunity to tutor undergraduates within the 'Oxford tutorial' system, for two years. I am thankful to Professor Frank Marken, Professor Russ Egdell, and Dr David Payne, for their career guidance and advice. The Foord Group D.Phil students (Inga, Tony, Lu-Lu, Patrick, Montree, Dong Myung, Sirikarn) have helped me in my work and kept me sane, particularly whilst writing the thesis. The support and friendship of several Part II students over the years (Seb, Carl, Phil, Rachel, Ed, Rhys) is much appreciated. The Egdell Group, Softley Group, Vallance and Wallace Group have all contributed to a most enjoyable work environment in the CRL - they help make science fun!

Financial support was necessary for my doctoral studies and my education throughout life. The following institutions have my enduring gratitude for their investment in my university education: The June Opie Fellowship, The Alexander Graham Bell Association, The Governments of Canada and Ontario, Hertford College, Queen's University, Queen's University Residences, the Royal Military College Environmental Services Group, and the Royal Canadian Air Cadets. The financial support from my parents and grandparents was crucial to my early education, and for 'making-up' any difference in the cost of hearing aids, tuition fees, and living expenses. Without this financial support, my studies at Oxford would not have been possible.

I could not have come to Oxford without being fully prepared to conduct doctoral studies. My former supervisor, Professor Hugh Horton and other professors at Queen's University, gave me a superb undergraduate and post-graduate education. The opportunities at Queen's, from Queen's Bands to employment as a Don with Queen's Residence, ensured that I would flourish within a university environment. The teachers and educators at Mentor College and Lorne Park Secondary School are commended for teaching me the basics of learning, speech, and hearing.

The sociable company of the Hertford College Boat Club, the Hertford MCR, will always be remembered with fondness. Several College Staff, Fellows, and Rowing Coaches contributed to my sense of well-being in Oxford, particularly Claire Blake, Anna Baskerville, Simon Lloyd, Graham Topping, Chris Dalley, Principal John Landers, and the College Porters.

My morale was high for the vast majority of my university years – that would not have been possible without the steady support, hospitality, advice, and visits from my Canadian, Queen's Bands and Residences, Oxford, and Hertford Boat Club friends, particularly: Tina Lewis, Ruben Castellanos, Megan Elliott, Heather Yundt, Laura

Beaudin, Wayne Gow, Kyle and Laura Stephenson, Heather Mosher, Elizabeth Lance, Liz Winter, Katy Borbridge, Duncan Findlay, Andrew Naples, Kevin du Manoir, Mike Fergusson, Jenny Pigott, Rachel James, Matthew Powell, Kristian Klausen, Peter Morten, Alex Woolgar, James Hutton, Jon Beckett, Mark Valentine, Tom Anderson, Dan Parker, Joe de Hoop, Rob Carpenter, Kendall Paulson, Louise Ellis, Kat Bonsor, Rebecca Davies, Izzy Westbury, Brenda Slomka. Several families are counted, among these supportive friends - the Hart, Wintonyk, Kennedy, LeBlanc, and Keddie families.

I also thank Leanne's Family – 'clan' Murison – and their many relations, who have made me a part of their lives and support my studies - even if they preferred that I had studied in Scotland!

Finally, I must thank my own family, starting with my English relations, the Fishers, for welcoming me to this island with open arms.

The pets in my life – Wellington, Spike, Ted, Watson and Crick – all supported and comforted me throughout my university years and thesis writing.

I thank Mr. Nicholas and Merle Young, and the Rev. Neville and Noreen Bishop, for encouraging my curiosity and a life-long 'love of learning'. They are in many ways, part of our family.

My Aunts, Uncles and cousins - the Zarbs, the Hudgins, and the Goerees – have all kept in touch, and remind me that I will always have a home in Canada. I must mention Auntie Antoinette's old chemistry textbooks, which inspired an interest in the subject, when I was a young lad.

My brother, Jeremey Nelson, has been a constant presence in my life. He paved the way for my arrival in England by being the first to leave our native shores. On this island, he has been a never-ending source of joy, laughter, and familial presence. With him near, there was no chance I would be home-sick during my studies.

Leanne Murison's boundless faith in me, and her constant love, has supported me, from Oxford application to the completion of this D.Phil. thesis. I work best with her calming presence, her understanding, and her steady supply of tea. I love Leanne for this, and more.

My grandparents - Doris Gatt, and the late Paul Gatt, Geoffrey Nelson Sr., and Alice Nelson – by their example and love have supported me and my parents, in person and in spirit.

For as long as I can remember, my parents, Peter and Louise Nelson, told me that they hoped that I would go to university. It was never a sure thing, as my severe hearing impairment made the initial odds of getting into university quite slim, let alone earning two degrees from Queen's University, and now the near-completion of the Oxford D.Phil. degree. My journey to this point is testament to their devotion to my education, the hours they invested during my childhood to perfect my speech and hearing, and their unconditional love. Together, we beat the odds. Thank you, Mum and Dad, for everything.

Publications

1. K. Lawrence, J.D. Watkins, T.D. James, J.E. Taylor, S.D. Bull, **G.W. Nelson**, J.S. Foord, Y-T. Long, F. Marken. "Dioctylamine-sulfonamide modified carbon nanoparticles as high surface area substrates for co-enzyme Q10 lipid electrochemistry". Electroanalysis. **24** (2012) 1003-1010.

2. Vuorema, S. Shariki, M. Sillanpää, W. Thielemans, **G.W. Nelson**, J. S. Foord, S. E.C. Dale, S. Bending and F. Marken. "Enhanced TiO_2 surface electrochemistry with carbonised layer-by-layer cellulose-PDDA composite films". Phys. Chem. Chem. Phys., **13** (2011) 9857-9862.

3. J.D. Watkins, R. Lawrence, J.E. Taylor, S.D. Bull, **G.W. Nelson,** J.S. Foord, D. Wolverson, L. Rassaei, N.D.M. Evans, S. A. Gascon, F. Marken "Carbon nanoparticle surface functionalisation: converting negatively charged sulfonate to positively charged sulphonamide". Phys. Chem. Chem. Phys. **12** (2010) 4872-4878.

4. **G.W. Nelson**, E. Lewis, O.W. Williams, K. Singh, D. Staunton, C. Blanford and J.S. Foord. "Protein adsorption on nanodiamond thin films" *in preparation*

5. **G.W. Nelson**, E. Parker, R. Jacobs, C. Blanford, J.S. Foord, M. Moloney. "Protein adsorption on carbene modified polystyrene thin films" *in preparation.*

6. **G.W. Nelson** and J.S. Foord "Electrochemistry and surface chemistry of modified diamond electrodes for the improved detection of neurotransmitters" *in preparation*

.

Contents

1. Introduction

2. Experimental: Theory and Techniques

3. Protein Adsorption on Nanodiamond Thin Films

4. Characterization of Carbene Modified Polystyrene Thin Films

5. Protein Adsorption on Carbene Modified Polystyrene Thin Films

6. Neurotransmitter Detection with Diamond Electrodes

List of Figures

List of Figures

List of Figures

List of Tables

List of Tables

List of Abbreviations

AA	Ascorbic acid
ACBK	Acid chrome blue K
AFM	Atomic force microscopy (or microscope)
AIBN	Azobisisobutyronitrile
ATR	Attenuated total reflection spectroscopy
BASD	Bead-assisted sonication
BPO	Benzoyl peroxide
BSA	Bovine serum albumin
CRP	C- reactive protein
CVD	Chemical vapour deposition
DA	Dopamine
DCM	Dichloromethane
DEE	Diethyl ether
DLS	Dynamic light scattering
DMF	Dimethylformamide
DND	Detonation nanodiamond
DVB	Divinylbenzene
EB	Evans Blue
EPOG	Edge-plane pyrolytic graphite
FAT	Fixed analyzer transmission
FET	Field-effect transistor
FRR	Fixed retard ratio
FWHM	Full-width at half-maximum
HOMO	Highest occupied molecular orbital
HP	Hydrogen plasma
HSA	Human serum albumin
IMFP	Inelastic mean free path
LEED	Low energy electron diffraction
LUMO	Lowest unoccupied molecular orbital
MWCNT	Multi-walled carbon nanotubes
NIST	National Institute of Standards and Technology (U.S.A.)
PB	Phosphate buffer
PFTE	Poly(tetrafluoroethylene)
PMMA	Poly (methyl methacrylate)
PS	Polystyrene
QCM	Quartz crystal microbalance
QCM-D	Quartz crystal microbalance with dissipation monitoring
RAIRS	Reflection-adsorption infrared spectroscopy
RSA	Random sequential adsorption
SAC	Surface area corrected
SAD	Surface area difference

List of Abbreviations

SAM	Self-assembled monolayer
SIMS	Secondary ion mass spectroscopy
STM	Scanning tunnelling microscopy (or microscope)
UHV	Ultra-high vacuum
XPS	X-ray photoelectron spectroscopy

1. Introduction

1.1 Introduction to Solid-Liquid Interfaces

The study of interfaces is a major area of chemical research. In the past century, it has lead to industrial applications as diverse as semiconductor technology, heterogeneous catalysis, liquid crystals, and advanced protective coatings. The core of surface science research today concerns research in such areas as photovoltaic cells, surfaces for energy conversion or storage, nanoparticles, and bio-electronic interfaces. At the frontier of this field is the study of the solid-liquid interface. This area is of great importance in the 21st century, particularly in fields at the intersection of materials chemistry and biology.

The importance of surface science research was highlighted by Irving Langmuir's Nobel Prize in 1932. By the 1960's, the field had advanced dramatically, with the development of ultra-high vacuum (UHV) techniques to study surfaces using X-rays, electrons, photons and ions.[1, 2] Techniques such as X-ray photoelectron spectroscopy (XPS), low energy electron diffraction (LEED), secondary ion mass-spectroscopy (SIMS), among others, soon revolutionized our understanding of surface processes. In particular, the electronics industry and users of heterogeneous catalysis benefited from this understanding. For example, Gerhald Ertl's use of LEED helped elucidated the mechanism of ammonia synthesis at transition metal surfaces approximately 65 years after the process itself was discovered by Haber in 1909; this work earned him a Nobel Prize in 2007, thus honouring surface science, yet again, 75 years later.[3]

In the 21st century, surface science is poised to contribute to a deeper understanding of bio-surfaces and the material-biology interface. Self-assembled monolayers, artificial bone implants, medical treatments, and anti-microbial coatings are all fields which demand such understanding. These systems cannot be studied well using UHV techniques, since vacuum conditions are not representative of the ambient conditions in which most biological processes occur. To address this problem, surface scientists of the past three decades have been developing a range of techniques to probe these interfaces. Scanning probe techniques, such as atomic force microscopy (AFM) and scanning tunnelling microscopy (STM) are useful for measuring surface forces and topography.[4, 5] Innovative optical methods, such as attenuated total reflection spectroscopy (ATR), surface plasmon resonance (SPR), and reflection-adsorption infrared spectroscopy (RAIRS), among others, gather molecular information at such interfaces.[1, 2, 6] More recently, XPS has been adapted to perform in ambient conditions.[7] Advanced versions of acoustic-based mass sensors can probe the kinetics of bio-molecule deposition at surfaces.[8] Finally, synchrotron light sources and computational chemistry have each played a role in elucidating fundamental trends at the solid-liquid interface.[1, 2] The use of these and future techniques will be the foundation for research regarding the surface chemistry of materials in biological conditions.

Several key aspects of the solid-liquid interface in biology require further exploration. The surface chemistry of materials is known to govern their bio-compatibility .[1, 9] The safe use of advanced materials in biology requires knowledge of what surface chemistry leads to which material properties. The control of bio-compatibility is thus an important issue. The role of surface topography is thought to have an additional influence on a material’s bio-interface.[10] Topography is of particular importance to several fields, including tissue engineering, where surface topography is known to influence biological processes.[11] The third issue is that of interfacing materials directly to biological processes.[12] Successful bio-electronic devices require the development of materials capable of predictable, long-term performance, in biological environments. This field requires that new and existing materials be further developed to act as reliable bio-sensors. The study and control of surface chemistry, topography, and electronic performance at the solid-liquid interface is limited, and its further development will realize 21st century advances, such as neuronal interfacing[12], anti-microbial coatings[13], and nano-medicine[11].

1.2 Carbon-based Materials for Biological Studies

Devices and materials for use in biological systems are of increasing demand. The ideal material for this application would be robust, bio-compatible, easily modified for specific applications, and be conductive, thus enabling interfacing with electronic devices. A family of carbon-based materials has been identified as having many of these qualities, with their myriad of properties and applications being well reviewed.[14-18] Examples of these materials include: graphene, diamond, carbon nanotubes, graphite, fullerenes, edge-plane pyrolytic graphite (EPOG), glassy carbon, diamond-like carbon, and polymers. Pictorial representations of some of them are shown in Figure 1.1. Each has its advantages and disadvantages. For instance, conductivity is imparted to diamond by doping, but this is not required for graphene, as it is a semi-metal. These materials have found application in electrochemistry[14], platforms for cell growth[19], electronic devices[15], and nanoparticles for drug delivery[20], among many other applications.

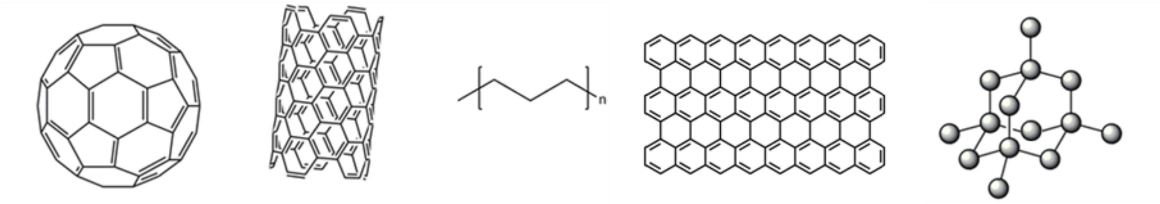

Figure 1.1: Structures of representative carbon-based materials. From left to right: fullerenes, carbon nanotubes, polymers, graphene and diamond.

1.2.1 Diamond

Diamond is valued both as a gemstone and as a material for 21st century applications. It has superior optical, mechanical, thermal, and electrical properties.[21] It is formed in nature by intense pressure and heat in the earth, and is found throughout the universe, even on extra-terrestrial meteorites and planets.[22] However, the natural world does not have a monopoly over the creation of diamond. Synthetic diamond can be made in laboratories worldwide using simple ingredients (e.g. methane and hydrogen gas), and controlled conditions. Chemical vapour deposition (CVD) of diamond films is possible by mixing these reagents in gaseous form in conditions of low pressure and high temperatures[15, 21, 23, 24]. Alternatively, detonating carbon-based explosives results in the formation of nano-diamond powders.[20] These methods of synthesizing diamond have revolutionized its use in various applications.[15, 25]

1.2.2 Bio-application of Diamond

Diamond is considered to be a bio-compatible material. Adverse bio-interactions are minimized by its sp^3 – based chemistry, which renders it reasonably un-reactive in biological conditions. This property of diamond has not been systematically studied until recently. Clinical and non-clinical studies have shown that diamond and nano-diamond are non-toxic at best, and minimally invasive at worst.[26, 27] For example, in vivo injections of nanodiamond into rabbits affect several biochemical properties of blood, but do not lead to the total destruction of blood cells.[26] Nanodiamond particles do accumulate in the circulatory and pulmonary systems of mice[28], but such accumulation has no adverse effects, with the particles easily ejected by the immune system .[29] Schrand and co-workers note that they generate low amounts of reactive oxygen species and do not affect the morphology of adsorbed cells.[30] The bio-compatible quality of diamond has led it to be considered a material of choice for use in biological, non-biological, and aqueous environments.

Biological applications of diamond are diverse. Unmodified nanodiamond particles have been considered to be a ‘universal adsorbent’ for the separation of proteins; they are capable of interacting with proteins in a multitude of ways (e.g. covalent, non-covalent, electrostatic, etc.), whilst still preserving protein structure.[26, 31] The same chemistry leads others to consider nanodiamond particles to be an ideal drug delivery vehicle.[32] The conductive and bio-compatible qualities of boron-doped diamond makes it a key material for the creation of electrochemical bio-sensors.[25, 33] The most ambitious research considers diamond to be an ideal platform for cell growth, neuronal interfacing, and retinal stimulation in human beings. [19, 20, 34] It is highly probable that diamond materials will be part of a myriad of bio-devices by the end of this century.

The surface modification of diamond is often required to impart biological or chemical functionality to its surface. The latest research in this area has been reviewed by Krueger and Lang.[35] Diamond can be hydrogen terminated after growth using hydrogen plasma[36, 37], annealing in hydrogen gas[38, 39], or electrochemical methods.[40, 41] Plasma or heat treatment in atmospheric conditions can add ketones, bridging oxygen groups, and carboxyl groups to a diamond surface.[42] Detonation nanodiamond has extensive oxygen functionality due to water or acid exposure during its manufacture.[35, 38] Oxygenated and hydrogenated diamond can be further modified by organic chemistry, including: chlorination[43], fluorination[44], carbene insertions[45], photochemical grafting[46], amination[47], attachment of polymers[48], among many others.[35] Two common reasons to functionalize diamond include the non-covalent and covalent attachment of bio-molecules, or the improvement of electrochemical devices.[25, 33, 41]

The surface chemistry of diamond is thought to govern its role and future potential has a bio-material. However, fundamental studies of the diamond-biology interface have been limited, to-date. Recent studies concerning this interface have been insightful. Wang *et al.*[49] showed that 80% of the α-helix structure of bovine serum albumin (BSA) is preserved on commercial nanodiamond particles. Rezek *et al.*[50] found that osteoblastic cells were selective for oxygenated, not hydrogenated diamond, in the presence of blood serum proteins. Electrochemical studies have shown that there is slight loss of α-helix protein structure, and function, on hydrogenated diamond *versus* oxygenated diamond.[51, 52] There is a limited consensus that oxygenated diamond facilitates stronger protein-protein interactions and consequently cell-surface interactions, compared to hydrogenated diamond.[53] Surface conductivity and AFM studies suggest that surface hydration has a different form on hydrogenated and oxygenated diamond; the former has initial ice-like layers of water with disordered layers above this, whilst the latter has nanoscopic and more disordered layers of water.[54] Surface hydration is important to surface-cell signalling and to protein adsorption studies, and thus these observations may have biological consequences.[54] More knowledge is needed to understand the nature of surface hydration at diamond, along with other gaps in present knownledge, including: the role of surface topography; the nature of the physical properties of protein layers at this interface; and the interface of diamond and non-globular proteins. Future bio-applications of diamond will rely on the fine control of diamond surface chemistry, which makes further study in this area necessary.

1.2.3 Polymer Surfaces

Polymers are ubiquitous in our world. Made in industrial quantities, they are now found in thousands of products ranging from the simple, such as chairs and tables, to the complex, such as targeted drug delivery in humans.[55 - 59] Polymers are created by linking chemical sub-units into long chains. For instance, styrene is the monomer for polystyrene – a polymer used for beverage containers and as a protective packaging material. Other polymers in wide chemical and medicinal use include, but are not limited to, the following: poly(ethylene terephthalate), polypropylene, poly(methyl methacrylate), and poly(dimethyl siloxane).[60] Common characteristics of value to all polymers include their ease of manufacture and ease of chemical modification. It is these qualities which make polymers a valuable set of materials in biological environments.

1.2.4 Bio-application of Polymers

Polymeric materials have found wide medical and biological application. The entire micro-fluidics industry is founded on the ease by which nano-scale channels can be imprinted into polymer-based labs-on-a-chip.[61] Some polymers are valued for their anti-microbial qualities, whilst still others can be made anti-microbial by an applied coating.[13] Food packaging requires the use of non-toxic polymers which retain the flavour of foods without imparting an undesirable taste to them.[62] More advanced research is focusing on the use of bio-compatible polymers for drug delivery and conductive polymers as part of bio-sensors.[60, 63, 64] The biological applications of polymers is limitless in terms of scope, and importance.

In most cases, modification of polymers is required to tailor their surface properties for a particular purpose. Polymers used in medicine must be safe and free of microbial contamination. The demand for such polymers has driven research in the field of anti-microbial coatings for polymeric materials. In general, these coatings change the surface properties of polymers in order to resist microbe adhesion. Strategies towards this end have been well-reviewed.[13, 65] Anti-microbial coatings either prevent a microbe from attaching to a surface directly, or a minimum, make the attachment of cells energetically unfavourable.

To accomplish this, specific molecules or chemical functionality is attached to the polymer surface by a variety of chemical means. Wet chemical, ionized gas, and poly-functional cross-linkers are a few of the methods used to achieve crucial anti-microbial properties on a polymer surface.

In the past decade, much research has focused on the surface properties required for anti-microbial properties to be imparted to polymer surfaces. Early insight was provided by research into self-assembled monolayers (SAMs) which resist protein adhesion.[66, 67] These studies identified chemical groups which attracted and resisted, protein and bacteria adsorption. The attachment of poly(ethylene glycol) to surfaces is now considered a standard approach to resist protein and microbe accumulation. Other surfaces which limit protein adhesion, include those having: tertiary amine oxides[68], phosphate derivatives[67, 69], no hydrogen donors[67], and electrical neutrality.[67] Also, hydrophilic surfaces are considered to attract fewer proteins than hydrophobic surfaces.[70] Information on other anti-microbial polymer surface treatments can be found elsewhere[13, 65], and many of them adopt the surface functionality first identified in these protein adsorption studies on SAMs.

Frontier chemistry in anti-microbial coatings aims to modify polymers on industrial scales, whilst ensuring manufacturing processes are ‘green’ and have low cost. Bio-mimetic chemistry, solvent-free chemistry, photochemistry, and ‘chemical linkers’ are being adapted for the application of anti-microbial coatings. Bio-mimetic chemistry uses nature as an inspiration to modify polymers. For example, mussel-mimetic catecholamine shown to be an ideal primer for the attachment of DNA to polystyrene and PMMA.[63] Solvent-free modification of polymers reduces the use of solvents known to be environmental hazards. Non-thermal plasma and organic vapour deposition methods are two techniques which accomplish solvent-free modification.[55, 72, 73] The use of light to modify surfaces is an alternative to the high energy requirements of thermal methods.[75] Lastly, the attachment of 'chemical linkers' to surfaces, followed by attachment anti-microbial groups to the linker, is a useful route to functionalization. This strategy is shown in Figure 1.2. Carbene-insertion chemistry[75, 76] '[77] and 'click'-chemistry[78, 79] are two methods which use 'chemical linkers' in two-step functionalization of polymers. These two methods are particularly promising, as they have low cost and material requirements, with an almost limitless ability to add functional groups to surfaces. Both methods can be scaled-up to functionalize polymers at an industrial scale, which has been a limitation of older functionalization methods. This 'chemical linker' approach has the most promise towards the application of the lessons of SAM-protein interactions to polymeric systems in an industrial setting.

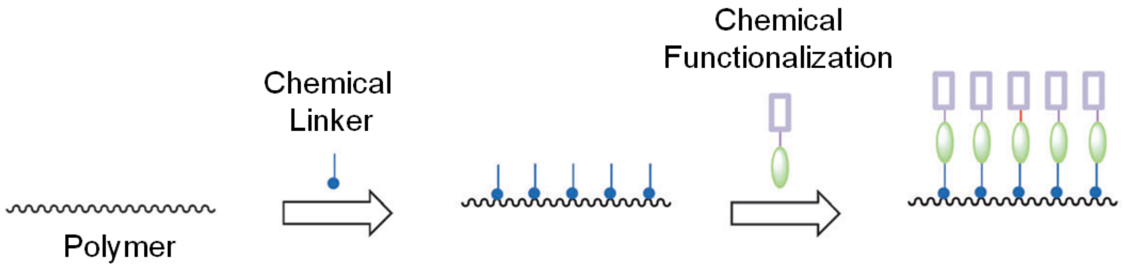

Figure 1.2: The 'chemical linker' strategy for functionalizing polymers. Figure is adapted from Choong *et al.*.[71]

1.3 Quartz Crystal Microbalance with Dissipation (QCM-D)

The quartz crystal microbalance with dissipation technique is a relatively new method of probing the solid-liquid interface. It is used extensively in this thesis to study protein adsorption onto diamond and modified-polymer materials.

The quartz crystal microbalance (QCM) is a well known technique for measuring the mass of gas molecules on surfaces in vacuum or air. King reported the first use of QCM in 1964.[80] QCM exploits a property of piezo-electric quartz crystals; under an applied voltage, these crystals can deform. When an alternating current is applied to the crystals, then crystal oscillations can be induced. The resonance frequency of these oscillations is monitored for changes, after mass is added to the crystal surfaces; the change in resonance frequency is proportional to added mass, as described by the Sauerbrey equation[81]; an added mass decreases the frequency of the quartz crystal. The QCM has found much use over the years as a vapour sensor, due to its simple operation and sensitivity to gas concentration (about 0.1 p.p.m.).

However, there are limitations to the QCM method. Conventional QCM underestimates added mass of non-rigid layers, particularly at the solid-liquid interface. In the late 1990s, a method to overcome this issue was found – dissipation monitoring.[8, 82] Hence the name of the most advanced version of the technique: quartz crystal microbalance with dissipation (QCM-D). Dissipation is the energy lost during free oscillations of the quartz crystal, with softer overlayers dissipating more energy than harder overlayers. This energy loss is measured when the applied current is periodically switched off, and is measured as an exponential decay in frequency as a function of time. The near-simultaneous measurement of frequency and dissipation can be later interpreted after modelling. Relevant modelling relates frequency and dissipation data to mass and visco-elastic data (i.e. viscosity and shear).[83] A simple case study is shown in Figure 1.3, where the deposition of a protein layer causes a decrease in frequency (i.e. added mass) and an increase in dissipation (i.e. loose, more visco-elastic layer). In this manner, QCM-D is able to measure added mass and adsorbed layer properties at the interfaces of solids with air, vacuum, and most importantly, liquids.

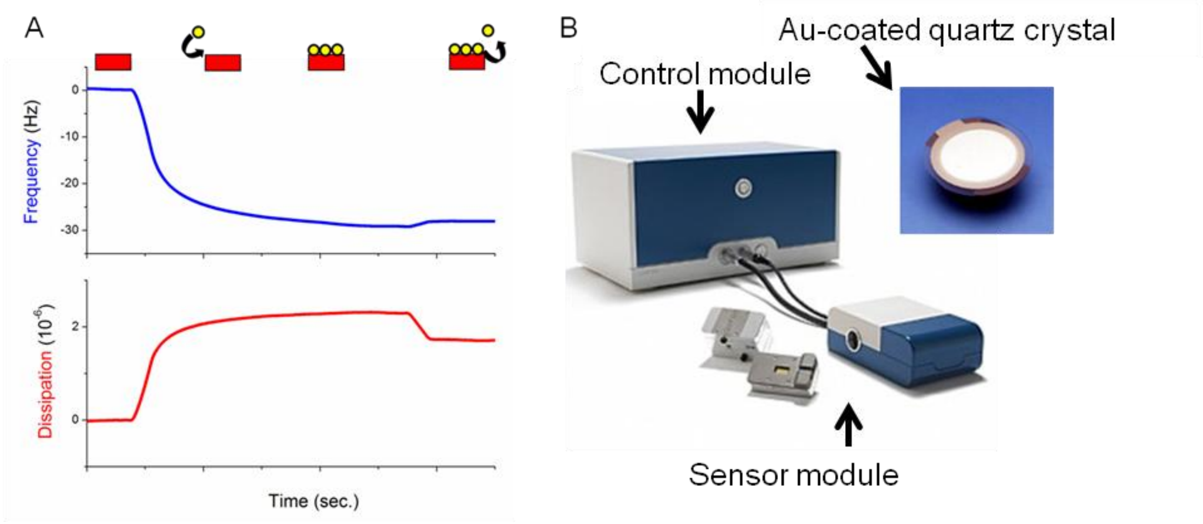

Figure 1.3: (A) Frequency and dissipation changes during the adsorption and desorption of a protein layer. (B) QSense E1 module for QCM-D data collection; inset shows a gold-terminated quartz crystal for QCM-D use.

QCM-D has revolutionized the study of adsorption at the solid-liquid interface. It has been used to study protein and biomolecule adsorption[84], anti-body interactions[85], and even natural phenomenon such as mussel protein cross-linking.[86] Its use offers considerable advantages. Biological phenomena are able to be probed *in situ*, rather than under UHV conditions. QCM-D is sensitive to 0.5 - 2 ng cm^{-2} of added mass. QCM-D measures the combined mass of bio-molecules at the surfaces and their surrounding fluids, whereas the most advanced optical methods can only measure the mass of the deposited bio-molecule.[85] The high data density of QCM-D – up to 200 points per second - enables kinetic data to be collected and analyzed, particularly at short time frames. Due to these features, QCM-D is now a well-developed technology, and an image of a QCM-D unit manufactured by the leading commercial developer, QSense (Sweden), is shown in Figure 1.3.

1.4 Scope of this Thesis

This thesis is concerned with the solid-liquid interface of two carbon-based materials that are used in biological environments and which have industrial importance: diamond and carbene-modified polystyrene. The QCM-D technique will be used for the first time to conduct protein adsorption studies on these two particular materials. These studies advance a fundamental understanding of the role that surface chemistry and topography have on protein adsorption on these materials. In addition, diamond's ability to act as an electrochemical sensor of neurotransmitters will be examined in this thesis. This will better enable diamond to be a material of choice for electronic interfacing with biology. An understanding of the chemistry at the solid-liquid interface of diamond and carbene-modified polymers will be crucial for their future development as useful biomaterials.

Discussion of the work in this thesis is organized as follows:

1. An *in situ* QCM-D study of the adsorption of proteins at the nanodiamond aqueous interface. An exploration of the influence of surface chemistry and topography on protein adsorption dynamics, will be a feature of this work. (Chapter 3)

2. The development of cross-linked polystyrene thin films, with imminent industrial importance, whose surfaces can be modified by novel, carbene-based chemistry. The chemistry of these surfaces is characterized throughout their synthesis. Their stability towards the harsh conditions of the carbene chemistry is demonstrated, and their future utility in QCM-D protein-adsorption studies is discussed. (Chapter 4)

3. An *in situ* QCM-D study of the adsorption of proteins at the carbene-modified polystyrene interface described in Chapter 4. The developed films are compatible with the QCM-D technique. This enables the first set of protein adsorption studies using QCM-D to be conducted on these materials. The wide-range of surface chemistry enables protein adsorption behaviour to be related to surface functionality.

These protein adsorption studies are conducted in conditions approaching the expected, and imminent, real-world application of these polymers. (Chapter 5)

4. Investigations towards improving the use of diamond interfaces towards the detection of neurotransmitters, in the presence of excess interferents. Those modifications which lead to the hydrogen-termination of diamond are better able to detect dopamine (DA) in the presence of ascorbic acid (AA). Of particular note, is the ability of hydrogen plasma to both separate the oxidation signals of these species, and to eliminate the catalytic cycle between ascorbic acid and an oxidation product of dopamine. Diamond has not accomplished this feat in the past, without the addition of non-diamond material to its surface. (Chapter 6)

References

[1] J.T. Yates, C.T. Campbell, Proceedings of the National Academy of Sciences, 108 (2011) 911-916.

[2] F. Zaera, Chem. Rev., 112 (2012) 2920-2986.

[3] H. Conrad, G. Ertl, E.E. Latta, Surf. Sci., 41 (1974) 435-446.

[4] G. Binnig, C.F. Quate, C. Gerber, Phys. Rev. Lett., 56 (1986) 930.

[5] G. Binnig, H. Rohrer, Sci. Am., 253 (1985) 50.

[6] A.R. Hind, S.K. Bhargava, A. McKinnon, Adv. Colloid Interface Sci., 93 (2001) 91-114.

[7] D. Zemlyanov, Nat Nano, 6 (2011) 612-613.

[8] F. Höök, "Development of a Novel QCM Technique for Protein Adsorption Studies", in: Ph.D Thesis, Chalmers University, (1997).

[9] M.D. Mager, V. LaPointe, M.M. Stevens, Nat Chem, 3 (2011) 582-589.

[10] K. Kulangara, K.W. Leong, Soft Matter, 5 (2009) 4072-4076.

[11] C. Minelli, S.B. Lowe, M.M. Stevens, Small, 6 (2010)

[12] T.W. Berger, M. Baudry, R.D. Brinton, *et al.*, Proceedings of the IEEE, 89 (2001) 993-1012.

[13] A. Muñoz-Bonilla, M. Fernández-García, Prog. Polym. Sci., 37 (2012) 281-339.

[14] Y. Shao, J. Wang, H. Wu, *et al.*, Electroanalysis, 22 (2010) 1027-1036.

[15] R.S. Sussman, CVD Diamond for Electronic Devices and Sensors, in: P.S.K. Dr. Peter Capper (Ed.) Wiley Series in Materials for Electronic and Optoelectronic Applications, John Wiley & Sons Ltd. (2009) p. 571.

[16] O.A. Williams, M. Nesladek, M. Daenen, *et al.*, Diamond Relat. Mater., 17 (2008) 1080-1088.

[17] O.C. Compton, S.T. Nguyen, Small, 6 (2010) 711-723.

[18] M.A.C. Stuart, W.T.S. Huck, J. Genzer, *et al.*, Nat Mater, 9 (2010) 101-113.

[19] A. Thalhammer, R.J. Edgington, L.A. Cingolani, *et al.*, Biomaterials, 31 2097-2104.

[20] A.M. Schrand, S.A.C. Hens, O.A. Shenderova, Crit. Rev. Solid State Mater. Sci., 34 (2009) 18-74.

[21] P.W. May, Philos. Trans. R. Soc. London, Ser. A, 358 (2000) 473-495.

[22] M. Bailes, S.D. Bates, V. Bhalerao, *et al.*, Science, 333 (2011) 1717-1720.

[23] B.V. Deryagin, D.V. Fedoseev, V.M. Lukyanovich, *et al.*, J. Cryst. Growth, 2 (1968) 380.

[24] W.G. Eversole, Synthesis of Diamond, in: US. Patents 3030187 and 3030188, (1962).

[25] C.E. Nebel, B. Rezek, D. Shin, *et al.*, J. Phys. D: Appl. Phys., 40 (2007) 6443.

[26] A.P. Puzyr, A.V. Baron, K.V. Purtov, *et al.*, Diamond Relat. Mater., 16 (2007) 2124-2128.

[27] A.M. Schrand, S.A.C. Hens, O. Shenderovab, Crit. Rev. Solid State Mater. Sci., 34 (2009) 18-74.

[28] Yuan Yuana, Yuanwei Chena, Jia-Hui Liua, *et al.*, Diamond Relat. Mater., 18 (2009) 95.

[29] Y. Yuan, X. Wang, G. Jia, *et al.*, Diamond Relat. Mater., 19 (2010) 291-299.

[30] A.M. Schrand, H. Huang, C. Carlson, *et al.*, J. Phys. Chem. B, 111 (2007) 2-7.

[31] V.S. Bondar, I.O. Pozdnyakova, A.P. Puzyr, Phys. Solid State, 46 (2004) 758-760.

[32] J. Li, Y. Zhu, W. Li, *et al.*, Biomaterials, 31 (2010) 8410-8418.

[33] Yuan Yu, Yanli Zhou, Liangzhuan Wu, *et al.*, International Journal of Electrochemistry, (2012), Article ID: 567171

[34] M. Peplow, “Artificial retina gets diamond coating”, Nature (2005) < http://www.nature.com/news/2005/050328/full/news050328-9.html>

[35] A. Krueger, D. Lang, Adv. Funct. Mater., 22 (2012) 890-906.

[36] B. Rezek, C.E. Nebel, Diamond Relat. Mater., 15 (2006) 1374-1377.

[37] H.A. Girard, T. Petit, S. Perruchas, *et al.*, PCCP, 13 (2011) 11517-11523.

[38] O.A. Williams, J. Hees, C. Dieker, *et al.*, ACS Nano, 4 (2010) 4824-4830.

[39] N. Simon, H. Girard, M. Manesse, *et al.*, Diamond Relat. Mater., 17 (2008) 1371-1375.

[40] C.H. Goeting, F. Marken, A. Gutiérrez-Sosa, *et al.*, Diamond Relat. Mater., 9 (2000) 390-396.

[41] R. Hoffmann, A. Kriele, H. Obloh, *et al.*, Appl. Phys. Lett., 97 (2010) 052103.

[42] H. Notsu, I. Yagi, T. Tatsuma, *et al.*, Electrochem. Solid-State Lett., 2 (1999) 522-524.

[43] B. Ohtani, Y.-h. Kim, T. Yano, *et al.*, Chem. Lett., 27 (1998) 953-954.

[44] M.A. Ray, T. Tyler, B. Hook, *et al.*, Diamond Relat. Mater., 16 (2007) 2087-2089.

[45] H. Wang, J.-P. Griffiths, R.G. Egdell, *et al.*, Langmuir, 24 (2008) 862-868.

[46] B.M. Nichols, J.E. Butler, J.N. Russell, *et al.*, J. Phys. Chem. B, 109 (2005) 20938-20947.

[47] K.-I. Sotowa, T. Amamoto, A. Sobana, *et al.*, Diamond Relat. Mater., 13 (2004) 145-150.

[48] X.Y. Zhao, J.B. Zang, Y.H. Wang, *et al.*, Electrochem. Commun., 11 (2009) 1297-1300.

[49] H.-D. Wang, C.H. Niu, Q. Yang, *et al.*, Nanotechnology, 22 (2011) 145703.

[50] B. Rezek, L. Michalíková, E. Ukraintsev, *et al.*, Sensors, 9 (2009) 3549-3562.

[51] L. Grieten, S.D. Janssens, A. Ethirajan, *et al.*, Phys. Status Solidi A, 208 (2011) 2093-2098.

[52] R. Hoffmann, A. Kriele, H. Obloh, *et al.*, Biomaterials, 32 (2011) 7325–7332.

[53] E. Ukraintsev, B. Rezek, A. Kromka, *et al.*, Phys. Status Solidi B, 246 (2009) 2832-2835; B. Rezek, E. Ukrainstsev, L. Michalikova, *et al.*, Diamond Relat. Mater., 18 (2009) 918-922.

[54] J. Ristein. Appl. Phys. A. 82 (2006) 377-384.; A.P. Somner, D. Zhu, K. Bruhne. Cyrstal Growth and Design, 7 (2007) 2298 – 2307.

[55] T. Desmet, R. Morent, N.D. Geyter, *et al.*, Biomacromolecules, 10 (2009) 2351-2378.

[56] D.I. Rożkiewicz, B.J. Ravoo, D.N. Reinhoudt, Immobilization and Patterning of Biomolecules on Surfaces, in: The Supramolecular Chemistry of Organic-Inorganic Hybrid Materials, John Wiley & Sons, Inc. (2010) pp. 433-466.

[57] R. Langer, D.A. Tirrell, Nature, 428 (2004) 487-492.

[58] N. Huebsch, D.J. Mooney, Nature, 462 (2009) 426-432.

[59] S. Kim, J.-H. Kim, O. Jeon, *et al.*, Eur. J. Pharm. Biopharm., 71 (2009) 420-430.

[60] J.M. Goddard, J.H. Hotchkiss, Prog. Polym. Sci., 32 (2007) 698-725.

[61] A.E. Guber, M. Heckele, D. Herrmann, *et al.*, Chem. Eng. J., 101 (2004) 447-453.

[62] P. Appendini, J.H. Hotchkiss, Innovative Food Science & Emerging Technologies, 3 (2002) 113-126.

[63] H.O. Ham, Z. Liu, K.H.A. Lau, *et al.*, Angew. Chem., 123 (2011) 758-762.

[64] M. Gerard, A. Chaubey, B.D. Malhotra, Biosens. Bioelectron., 17 (2002) 345-359.

[65] E.-R. Kenawy, S.D. Worley, R. Broughton, Biomacromolecules, 8 (2007) 1359-1384.

[66] R.G. Chapman, E. Ostuni, M.N. Liang, *et al.*, Langmuir, 17 (2001) 1225-1233.

[67] E. Ostuni, R.G. Chapman, R.E. Holmlin, *et al.*, Langmuir, 17 (2001) 5605-5620.

[68] S.J. Dilly, M.P. Beecham, S.P. Brown, *et al.*, Langmuir, 22 (2006) 8144-8150.

[69] Y. Inoue, K. Ishihara, Colloid Surface B, 81 (2010) 350-357.

[70] W. Norde, Colloid Surface B, 61 (2008) 1-9.

[71] C. Choong, J. Foord, J.-P. Griffiths, *et al.*, New J. Chem., 36 (2012) 1187-1200.

[72] A. Asatekin, M.C. Barr, S.H. Baxamusa, *et al.*, Mater. Today, 13 (2010) 26-33.

[73] M.E. Alf, A. Asatekin, M.C. Barr, *et al.*, Adv. Mater., 22 (2010) 1993-2027.

[74] F. Ercole, T.P. Davis, R.A. Evans, Polymer Chemistry, 1 (2010) 37-54.

[75] K.M. Awenat, P.J. Davis, M.G. Moloney, *et al.*, Chem. Commun., (2005) 990-992.

[76] M.G. Moloney, J. Phys. D: Appl. Phys., 41 (2008).

[77] E. Parker, Surface active polymers as anti-infective and antibiofouling materials, D.Phil. Thesis, Organic Chemistry, University of Oxford, U.K. (2012).

[78] H. Claudia, H. Stephanie, S.S. Ulrich, Nanotechnology, 19 (2008) 035703.

[79] C.E. Evans, P.A. Lovell, Chem. Commun., (2009) 2305-2307.

[80] W.H. King, Anal. Chem., 36 (1964) 1735-1739.

[81] G. Sauerbrey, Z. Physik, 155 (1959) 206-222.

[82] M. Rodahl, B. Kasemo, Rev. Sci. Instrum., 67 (1996) 3238-3241.

[83] M.V. Voinova, M. Rodahl, M. Jonson, *et al.*, Phys. Scr., 59 (1999) 391-396.

[84] A. Dolatshahi-Pirouz, K. Rechendorff, M.B. Hovgaard, *et al.*, Colloid Surface B, 66 (2008) 53-59.

[85] F. Höök, J. Vörös, M. Rodahl, *et al.*, Colloid Surface B, 24 (2002) 155-170.

[86] F. Höök, B. Kasemo, T. Nylander, *et al.*, Anal. Chem., 73 (2001) 5796-5804.

2 Experimental: Theories and Techniques

2.1 Surface Characterization Techniques

Surface characterization techniques are used widely throughout this thesis. The techniques used include: X-ray photoelectron spectroscopy (XPS), Atomic Force Microscopy (AFM), Dynamic Light Scattering (DLS), and Ellipsometry. Each of these techniques is surface sensitive to one or more of the following: chemical composition (XPS), topography (AFM), particle size (DLS), and film thickness (Ellipsometry, XPS). Complementary use of these techniques is key to detailed characterization of surfaces in this thesis.

2.1.1 X-ray photoelectron spectroscopy (XPS)

X-ray photoelectron spectroscopy - also known as Electron Spectroscopy Chemical Analysis (ESCA) – is sensitive to the chemical nature of surfaces. Kai Siegbahn (Uppsala, Sweden) was the first to develop the XPS technique[1], and later received the Nobel Prize for his efforts.[2] Today, use of XPS is widespread, with commercial XPS systems being manufactured for industrial and academic use by Thermo Fisher Scientific Ltd., Kratos Analytical, and Henniker Scientific Ltd., among others.

2.1.1.1 Introduction to XPS

The X-ray photoelectron process is a phenomenon in which electrons are ejected out of core atomic orbitals by X-ray radiation. Prior to Kai Siegbahn’s initial studies, this process was known to exist, as the related photoelectric effect was discovered by Heinrich Hertz in 1887[3], and then explained by Albert Einstein in 1905[4], which led to the latter earning a Nobel Prize in Physics in 1921. In the mid 20th century, this phenomenon was exploited to analyze the chemical character of materials. Two developments were particularly important to the development of a working XPS technique: first, the use of soft X-rays, such as Mg Kα

(1253.6 eV) and Al Kα (1486.7 eV), instead of hard X-rays (i.e. Mo Kα; 17.5 keV), minimized radiation damage to non-metallic surfaces; second, analyzer technologies with spectral resolutions of < 1.0 eV were developed.[5]

Today, XPS analysis occurs as follows: A surface is irradiated with monochromatic X-rays in UHV conditions. This energy excites core level electrons (*i.e.* 2s, 2p, 4f, etc.), which are then ejected as photoelectrons from the surface towards an energy analyzer. The photoelectrons are then separated based on their kinetic energy and their intensities are analyzed. Figure 2.1 shows this process. The kinetic energy of an ejected photoelectron is related to the binding energy of the core level using the following expression:

$$E_K = hv - E_B - \phi \qquad \text{(Equation 2.1)}$$

where hv is the irradiation energy, E_B is the binding energy of the core level from which the photoelectron was ejected, and ϕ is the spectrometer work function. Normally, only E_B is reported. As shown in Figure 2.1B, E_B is the energy required to eject the photoelectron from its core orbital to a position at the Fermi level. The work function is the energy required to eject the photoelectron from the Fermi level into vacuum. The flux of detectable photoelectrons is plotted against E_B to make a typical XPS spectrum. Core levels, and by extension their binding energies, are unique to each element, which enables this technique to identify elements and their relative abundance at surfaces.

Although electrons up to the X-ray penetration depth (≈ 10 μm) from the surface can be excited to generate photoelectrons, only those electrons within ≈ 5 nm of the surface are detected. This is due to the tendency of photoelectrons to undergo inelastic scattering and loss of kinetic energy, thus contributing to the substantial background seen in XPS spectra. The electron mean free paths for metals can be plotted as function of kinetic energy, as shown in Figure 2.2A, with those for other inorganic and organic compounds found elsewhere.[6] The maximum electron mean free path, for typical X-ray energies, is about 20

Ǻ, which confirms the surface sensitivity of the XPS method. Only those photoelectrons which undergo minimal or no inelastic scattering from the point of ejection to the detector lead to useful data.

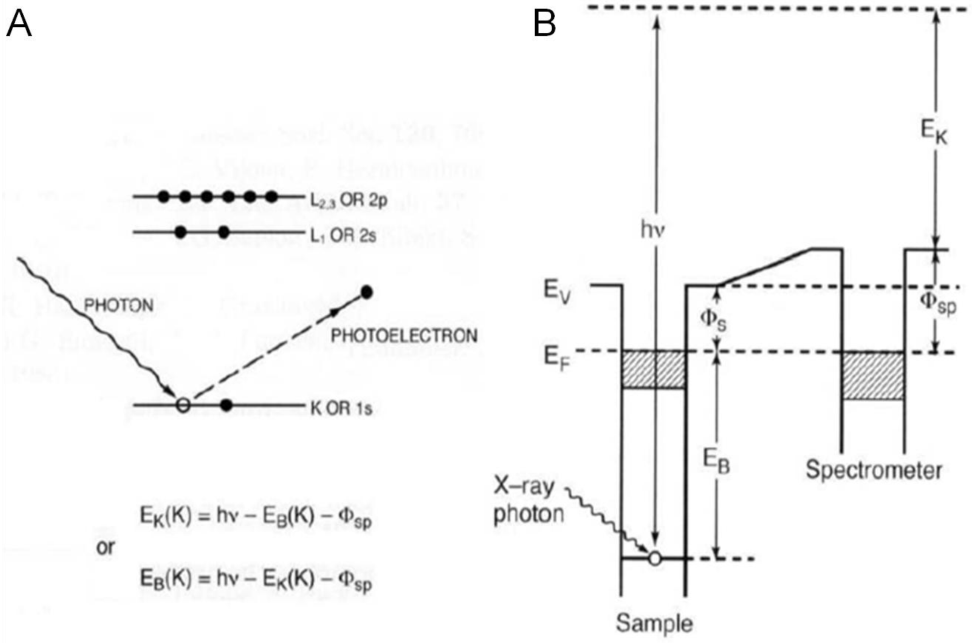

Figure 2.1: (A) X-ray photoelectron process; (B) Energy levels of core orbitals and spectrometer.[7]

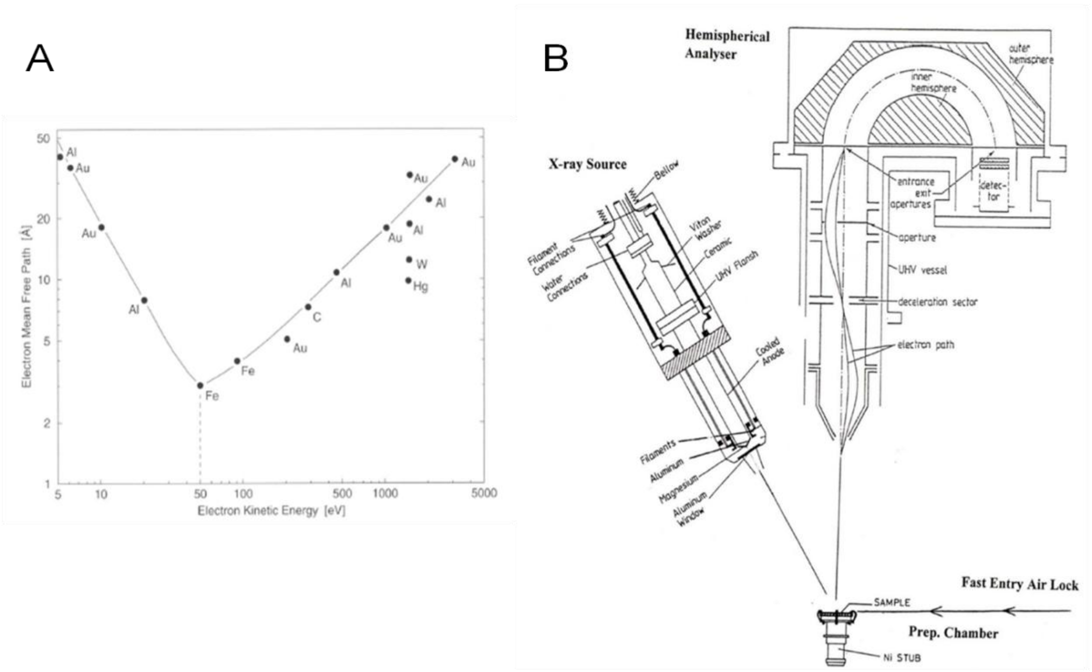

Figure 2.2: (A) Mean free path of electrons in metals as a function of their kinetic energy. This universal curve has a minimum at 2 – 5 Angstroms for E_K around 50 – 100 eV.[7]; (B) Experimental set-up of XPS apparatus.[8]

2.1.1.2 XPS Instrumentation

XPS experiments were conducted using an home-built X-ray photoelectron spectrometer which operates at 10^{-9} – 10^{-10} Torr. This spectrometer comprises X-ray source, an electron energy analyzer, and a detection system, all housed within UHV conditions. A scheme of the apparatus is seen in Figure 2.2B.

Samples enter and leave the UHV analysis chamber *via* a fast entry lock, which is separated from the UHV chamber by a preparation chamber. The preparation chamber is normally held at a pressure of 10^{-6} Torr, but is frequently raised to atmospheric pressure in order to load and extract samples from the apparatus. Samples are moved between chambers using magnetically controlled arms, and aligned to the detector by visual means. The angle between the X-ray beam, sample, and detector is approximately 45°. The UHV conditions under which XPS experiments take place are crucial. These conditions prevent gas molecules from adsorbing as a monolayer on surfaces during the time frame of an XPS experiment.[9] All XPS experiments in this thesis were conducted with pressures at or lower than 10^{-9} Torr.

Within the X-ray source, high energy electrons are ejected from one of two anodes and directed to one of two cathodes: aluminium or magnesium. Transitions from the 2p orbitals to the ionized 1s orbital in either material produce the Kα radiation.[9] XPS data in this thesis are the result of X-ray production from the aluminium cathode (1486.7 eV). This X-ray source is roughly mono-chromatic; whilst Al Kα X-rays dominate, X-rays from other processes do reach the surface of the sample.

Photoemission from the surface can cause surface charging to occur at the sample surface. This is particularly prevalent for those samples which are insulating or semi-conductive. Theoretically, the Fermi level of the spectrometer and the sample should be the same – with all reported energy values relative to the Fermi level of the spectrometer. Positive surface charging causes outgoing photoelectrons to lose kinetic energy, thus shifting photoelectron peaks to a higher binding energy. The correct peak position is obtained by calibrating spectra using an internal standard. In this thesis, that internal standard is the $Au4f_{7/2}$ or C1s photoelectron peaks at 84.0 eV and 285.0 eV, respectively.[9, 10]

Prior to detection, photoelectrons must be analyzed based on their kinetic energies, and the influence of background radiation must be minimized. This is done by passing the electrons through variable electron lenses and a hemispherical analyzer. Variable electron lenses retard the kinetic energy of incoming photoelectrons and focus those electrons towards the entrance of the hemispherical analyzer, thereby increasing the resolving power of the analyzer.[11]

In the analyzer, the electrons pass between two semi-circular plates which can be operated at a constant or variable potential. Thus, there are two methods to scan for photoelectron kinetic energy - one could vary the applied potential at the analyzer entrance and hold the potential between the analyzer plates constant, or *vice versa*. The former is called the fixed analyzer transmission mode (FAT), whilst the latter is the fixed retard ratio mode (FRR). Here the FAT mode is used, as its constant pass energy ensures consistent spectral resolution throughout all kinetic energies.[11] It should be noted that higher pass energies have lower resolution, but higher spectral intensity. Therefore, in this thesis high pass energies were used for ‘survey’ or ‘wide scan’ XPS spectra, and lower pass energies for higher resolution scans.

After energy analysis, the electrons of the correct pass energy are focussed on an electron detector, a multi-channel plate electron multiplier in this thesis.[11] Impacts with the walls of the detector ultimately produce an electron cascade for each initial electron entering the detector.[10, 11] The resultant current pulses are measured and recorded in counts per second by computer software, which also controls the analyzer.

2.1.1.3 XPS Spectral Features

In any XPS spectrum, there are a series of features which must be identified as unique to the sample, and then quantified. Often, this is not a trivial exercise, as the experimental set-up described earlier causes spectral features which do not relate to the sample under study. Spectral features associated with surface and instrumental sources are described in this section. A typical XPS spectrum is shown in Figure 2.3

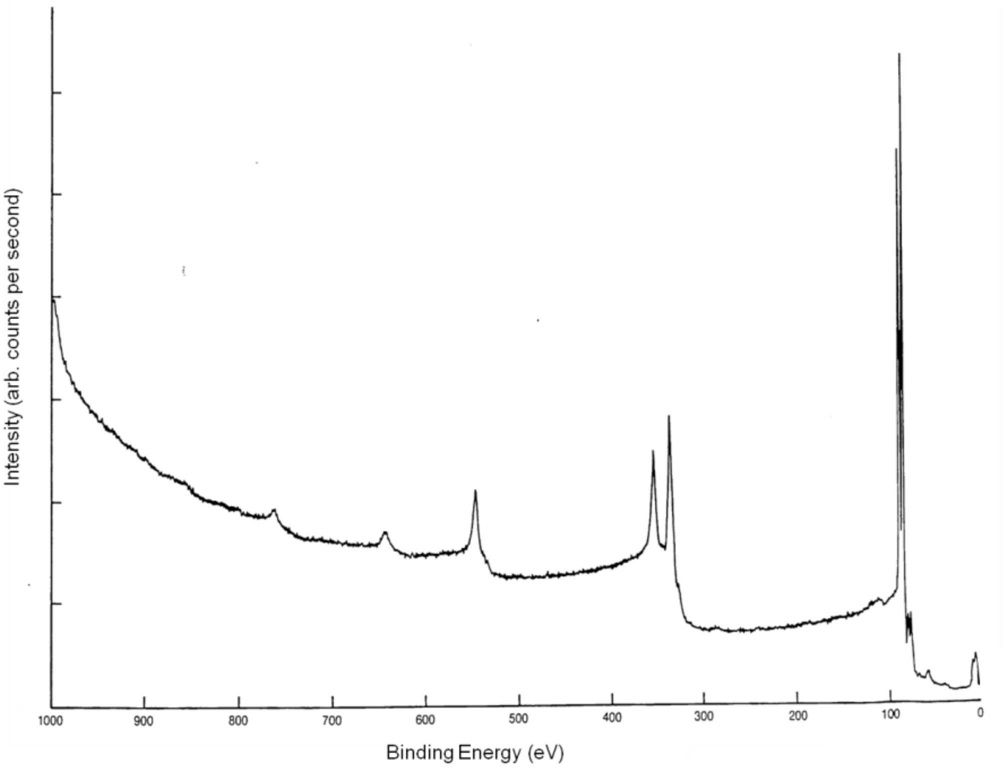

Figure 2.3: A typical XPS spectrum. This is the XPS spectrum of Au irradiated with Mg Kα radiation.[10]

(a) Main photoelectron line

Throughout a typical XPS spectrum, intense and narrow peaks can be seen. Most of these peaks are associated with a photoelectron ejected from a core orbital. The background originates from energy loss processes within the sample, electronic states of the material under study, the characteristics of the spectrometer, and Bremsstrahlung effects. Some asymmetry of photoelectron peaks is seen, which is due to a combination of effects: coupling to metal conduction band electrons, instrumental response, effects of non-monochromatic X-ray sources, energy loss processes, and the intrinsic lifetime of the positive holes formed after photoelectron ejection.[12] This gives each peak its characteristic shape with an associated full width at half maximum (FWHM). These peaks can be fitted by using a Gaussian function, a Lorentzian function, or both (Doniach Sunjic function).[12] Further discussion of peak asymmetry and spectral analysis is discussed in section 2.1.1.4(a).

The binding energy of each photoelectron peak is unique to the elemental core level from which the photoelectron originated. However, the chemical environment of the element or post-photoemission processes can cause chemical shifts from the expected binding energy. Higher oxidation states or an increased number of neighbouring atoms which are electronegative shift peaks to higher binding energies, and *vice versa*. An example of this phenomenon is shown in Figure 2.4A. This figure shows the direct correlation between binding energy of the C1s photoelectron and the oxidation state of the carbon atom from which it originates. Core hole screening, extra-atomic relaxation processes, and the influence of neighbouring atoms or ions can also cause chemical shifts. For example, compared to adventitious carbon, typical chemical shifts for carbon in an ether environment is about + 1.5 eV, whilst in a carboxyl environment it is about + 2.8 eV.[13] Tables of chemical shifts can be found in XPS manuals, handbooks and the National Institute of Standards databases (NIST).[10, 13, 14]

Another effect on XPS peaks is spin-orbit coupling, and an example of this is shown in Figure 2.4B. The energies of core levels can be split by this coupling, in which there is a singlet and triplet state (e.g. $2p_{1/2}$ and $2p_{3/2}$), in which the occupying electrons either have the opposite or same spin, respectively.[10] The former has a higher binding energy than the latter, whilst the latter has the higher peak intensity. If spin-orbit coupling is seen, then the signal is deconvoluted.

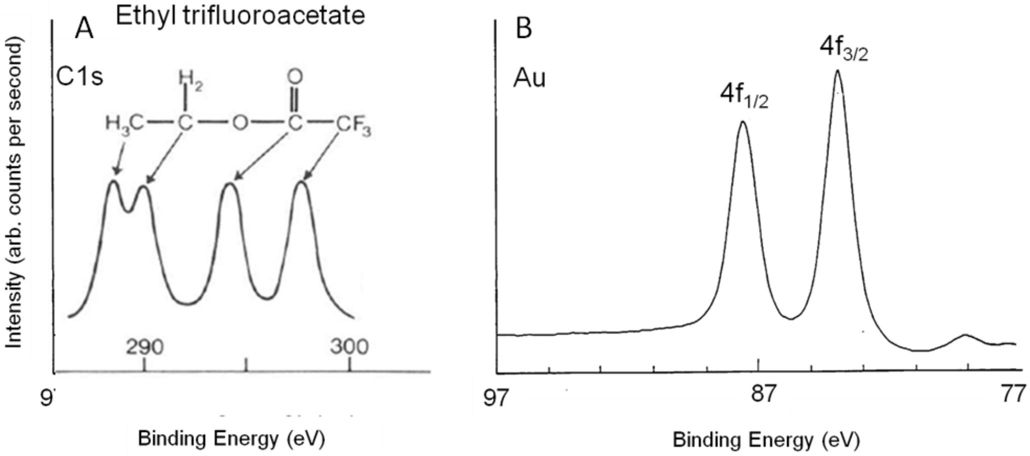

Figure 2.4: (A) Chemical shifts for C1s photoelectron signal for ethyl trifluoroacetate, with peaks at higher binding energy associated with photoelectrons originating from more electronegative chemical environments.[7]; (B) Spin-orbit coupling. Adapted from Moulder *et al.*.[10]

(b) Auger Peaks

Some peaks seen in XPS spectra are the result of non-fluorescent relaxation. Ejected photoelectrons leave behind positive holes, which can be filled by electrons at higher energy. The energy emitted by this transition can be absorbed by another electron, which is then emitted as an Auger electron. Auger electrons have kinetic energy, as follows[10]:

$$E_K = E_{B1} - E_{B2} - E_{B3} - \phi \qquad \text{(Equation 2.2)}$$

where E_{Bx} is the binding energy of: the ejected photoelectron (x = 1), the electron which subsequently occupies the resultant positive-hole (x = 2), and the binding energy of the Auger electron which is emitted (x = 3). Therefore, the initial vacancy created by the emitted photoelectron, leads to a final state having two vacancies. Auger peaks have a particular naming convention, with KLL, LMM, MNN, and NOO peaks being commonly seen; the first letter indicates the shell of the initial vacancy, whilst the two subsequent letters indicate the shells of the final vacancy.[10] Unlike photoelectrons, Auger electrons are emitted at a kinetic energy which is independent of the initial X-ray energy, providing a useful tool for their identification if the photon energy can be varied.

(c) Shake-up satellite

In XPS spectrum of polymers containing conjugated or aromatic systems, peaks of low intensity are often seen at binding energies higher than the main C1s photoelectron peak. These peaks are the result of ejected photoelectrons losing kinetic energy as they interact with the bonding to anti-bonding transitions (*e.g.* π - π^* transition) of those aromatic rings. These peaks have approximately 5 - 15% of the intensity of the main C1s photoelectron peak, with separations of up to 15 eV from this main line.[9] Shake-up satellite peaks are a common feature of polystyrene XPS spectra in the C1s region ($\approx$ 295 - 282 eV) and are also seen for inorganic materials.[15]

(d) Other spectral features

Plasmon loss, multiplet splitting, X-ray satellite lines, and X-ray ghost lines are all additional features of XPS spectra. Plasmon losses refer to the loss of kinetic energy by those photoelectrons which have induced plasmon oscillations of conduction band electrons.[9] Plasmon loss peaks are found at higher binding energies of the main photoelectron peak.

Multiplet splitting occurs when the angular momentum in the ionized core orbital couples to unpaired electrons in a core orbital, which can couple to unpaired electrons in an outer orbital. The spins of these electrons can be parallel or anti-parallel and each gives a different final energy state, with the former having the lower energy. An example of this is Mn^{2+} ($3s^2$ $3d^5$; ^6S) which photoemits an electron, leading to a new electronic configuration ($3s^1$ $3d^5$). The $3s^1$ electron could couple to the d^5 electrons with parallel (^7S ; S=2, L=0) or anti-parallel spin (^5S; S=3, L=0); the former has the lower energy of the two states. The result is a photoelectron peak which is split into two components, asymmetrically.

X-ray satellite peaks are caused by the use of non-monochromatic X-ray sources. In the case of Al cathodes, other transitions are possible after excitation, including the Al $K\alpha_{3,4}$ or Al Kβ; tables containing the energies for these transitions can be found in XPS handbooks.[10, 16, 17]

X-ray ghost peaks occur when photoelectrons are excited either *by* or *from* materials other than the cathode or sample, respectively. For instance, the samples are mounted on sample stubs made of molybdenum or stainless steel; thus, unwanted photoelectrons can originate from transitions within Mo or Cr, for example. Copper X-rays from exposed anodes can lead to unwanted photoelectron emission. Also, the aluminium film over the X-ray source window will generate X-rays if exposed to the anode. Photoelectron peaks which are unwanted have been clearly identified in this thesis.

2.1.1.4 Quantitative Analysis of XPS Spectra

(a) Peak Fitting

XPS peaks were deconvoluted using commonly used protocols. Background correction was applied first, using a Shirley background correction.[18] This requires that the background at lower binding energy is larger than that at higher binding energy, with a total background range of 10 eV or less.[12] If the assumptions of the Shirley method were not met, a linear background was used. This was often done in cases where an intense photoelectron peak is at slightly lower binding energy than the peak of interest [*e.g.* fitting of a weak S2p peak (162 eV) beside an intense Si1s peak (153 eV)]. The Shirley background algorithm assumes that the background at any given kinetic energy is proportional to the number of electrons at higher kinetic energy.

The use of the Gaussian and the Lorentzian functions allow the XPS user to account for lineshape broadening by homogenous and inhomogeneous processes, including: response of the analyzer, intrinsic lifetime broadening of the positive holes left by ejected photoelectrons, and surface charging, among other effects.[12] The photoelectron peaks were fitted using the product of the Gaussian and Lorentzian functions. The peak area of the fitted peak is simply the integral of the above peak fit. Constraints can be made to fitting parameters, but for the most part, constraints were avoided and the software was allowed to fit peaks automatically.

(b) Elemental Concentration Ratios

Before being used quantitatively, peak areas must be adjusted to reflect the different photo-ionization cross-sections of each core orbital. X-ray photoelectron intensity is proportional to several parameters[19]:

$$I \; \alpha \; [N]_i \sigma_i \lambda_i A_o [x] \qquad \text{(Equation 2.3)}$$

where I is photoelectron intensity, $[N]_i$ is the population of electrons in the core level, σ_i is the ionization cross-section for that core level, λ_i is the inelastic mean free path (IMFP) for the electron in the core level, A_0 is a constant which considers aspects of experimental set-up, and $[x]$ is the elemental concentration. This proportionality is different for each core level, and therefore is adjusted by use of ‘atomic sensitivity factors’ (ASF). The ASF values [20] normalize peak intensities to that of the F1s photoelectron peak.[20] The relative ratios of elements at the surface can thus be determined by the following expression:

$$\frac{[x]_A}{[x]_B} = \frac{\frac{R_A}{S_A}}{\frac{R_B}{S_B}} \qquad \text{(Equation 2.4)}$$

where R_i is the peak area for the photoelectron peak and S_i the appropriate ASF. Although frequently used, this method of estimating concentrations is strictly only applicable to samples with a homogeneous composition within the XPS analysis depth.

2.1.1.5 XPS Experimental Method

XPS experiments were conducted using an home-built X-ray photoelectron spectrometer at 10^{-9} – 10^{-10} Torr, using an Al K-α source (1486.6 eV) at 10 kV anode potential and 10 mA emission current. The Fixed Analyzer Transmission (FAT) mode was used to obtain spectra, using a pass energy of 50 eV or 25 eV, for 'wide' and 'narrow' XPS scans. XPS spectral intensities are the averages of 5 or 15 sweeps of the region of interest. All peak fitting was done using XPS Peak Fit (v. 4.1) software and is described in the previous sections. The reported binding energies have an error of ± 0.25 eV based on calibration to the $Au4f_{7/2}$ or C1s peaks. The reported, normalized, peak areas have an error of 10 - 15%.[21]

2.1.2 Atomic Force Microscopy (AFM)

Atomic Force Microscopy (AFM) was used in this thesis to image surfaces of nanodiamond thin films. Binning, Quante and Gerber invented the AFM technique in 1986 as a response to the need to image non-conductive surfaces, which could not be imaged by scanning tunnelling microscopy.[22] Instead of imaging surfaces by electron tunnelling between a conductive surface and tip, the AFM technique places tip, with nanometer-sized radius, close to the surface. This tip is part of a cantilever, with the entire unit made, typically, from silicon, silicon oxide, or silicon nitride. A laser beam is reflected off the back of the cantilever and its vertical and horizontal deflection can be related to the intermolecular forces between the tip and the sample. A diagram of the AFM system used in this thesis is shown in Figure 2.5.

The key components of the system are the cantilever tip, sample stage, laser, and photodiode detector. The cantilever tip has nanometer radius, pyramidal-shape, and is sharp. It is allowed to move across a sample. Typically, this tip has a spring-constant less than that between atoms, thus enabling it to respond to weak intermolecular forces (i.e. typical spring constants of 0.01 – 100 N m^{-1}).[23, 25] Since the cantilever responds based on Hooke's law this means that forces as low as nano-Newtons can be detected.[26] The laser beam is allowed to reflect off the back of the cantilever towards a detector, if necessary *via* a series of mirrors. The position of the reflection on the photodiode can be used in one of two ways: first, to determine the intermolecular and lateral forces between tip and the sample; second, as part of a feedback mechanism to control the distance between tip and sample.[22] This feedback mechanism controls a piezo-electric 'motor', which adjusts the vertical height and horizontal position of the tip above the sample.

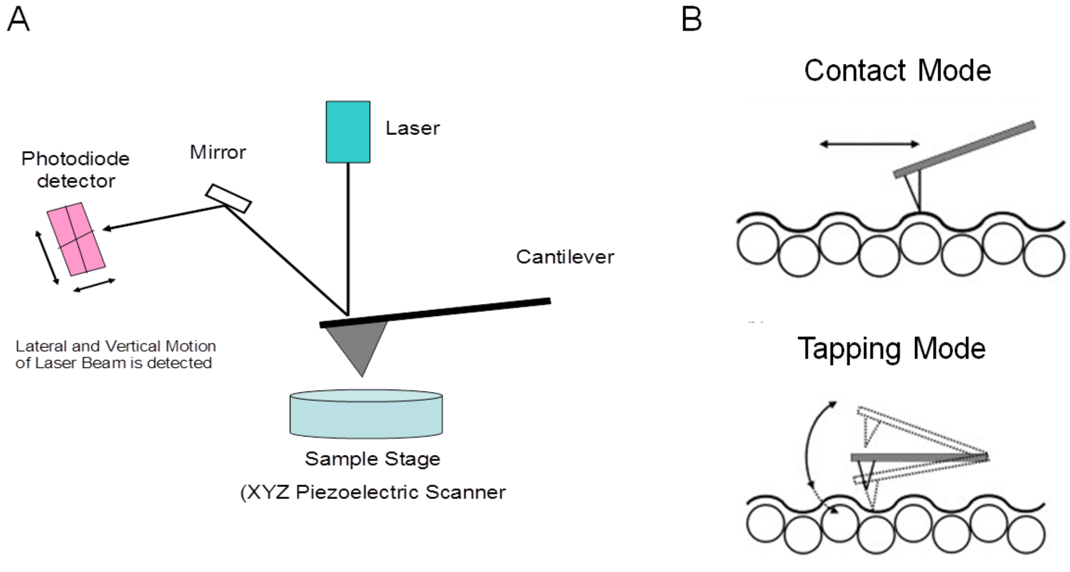

Figure 2.5: (A) AFM apparatus and operating principles.[23] (B) Operating modes of AFM.[24]

There are two modes of AFM operation. In the contact mode, the tip and sample are in contact throughout the raster scanning of a small area of the sample, with the forces between the tip and sample influencing the deflection of the cantilever. When studying soft-matter, a ‘tapping mode’ – also known as ‘non-contact’ mode - is used, thus avoiding damage to the surface or the removal of molecules from the surface during AFM operation. In tapping mode the cantilever is driven to oscillate at its resonance frequency by acoustic or magnetic means, whilst in intermittent contact with the surface. When the tip is in contact with the surface, the amplitude of the oscillation is reduced. The height above the surface is determined from the vertical displacement of the piezo-electric motor necessary to ensure constant oscillation amplitude.[23] It is also possible to monitor the phase-shifts of the oscillating cantilever, by oscillating the cantilever with constant height; this provides additional surface sensitive information.[27]

In this thesis, AFM images were recorded using a scanning probe microscopy unit (Digital instruments, Nanoscope IIIa controller), operated in constant-height tapping mode, using a raster scanner having a range of ≈ 100 µm in the x-y direction and ≈ 6 µm in the z-direction. Silicon probes (Nascatec, GmbH model NST NCHFR) with resonant frequencies of ≈ 320 kHz were used. The AFM was pre-calibrated by scanning a three dimensional reference grid from Digital Instruments. The roughness of samples was characterized by the root-mean-square roughness (R_{rms}), which is given by the following expression:

$$R_{rms} = \sqrt{\frac{\sum_{n=1}^{N}(z_n - \bar{z})^2}{N-1}} \qquad \text{(Equation 2.5)}$$

where z is the mean height in the z-direction. This expression represents the standard deviation of the height data. Large deviations from the average height are weighted more heavily when using R_{rms}, which is why this parameter is used rather than average height. Other measures of surface topography include the following:

- *Roughness average* (R_a): mean of the absolute values of surface height deviations from the mean horizontal plane.
- *Maximum Roughness* (R_{max}): maximum vertical distance between highest and lowest data points in an AFM image.

- *% Surface area difference*: Surface area of scanned AFM image is calculated and the percentage difference between this area and the area expected if the scan area was completely flat.

All experiments were conducted in the Department of Chemistry's Surface Analysis Facility.

2.1.3 Dynamic Light Scattering (DLS)

Dynamic light scattering was used to determine the particle size of detonation nano-diamond suspensions in aqueous conditions. It is a non-contact technique which determines the distribution of particle sizes in a suspension, by using the principle of light scattering by solid particles and Brownian motion. Brownian motion is the random movement of small particles in solution, as a result of interactions between particles and the surrounding fluid.[28, 29] Berne and Pecola have written a useful reference on this technique.[30]

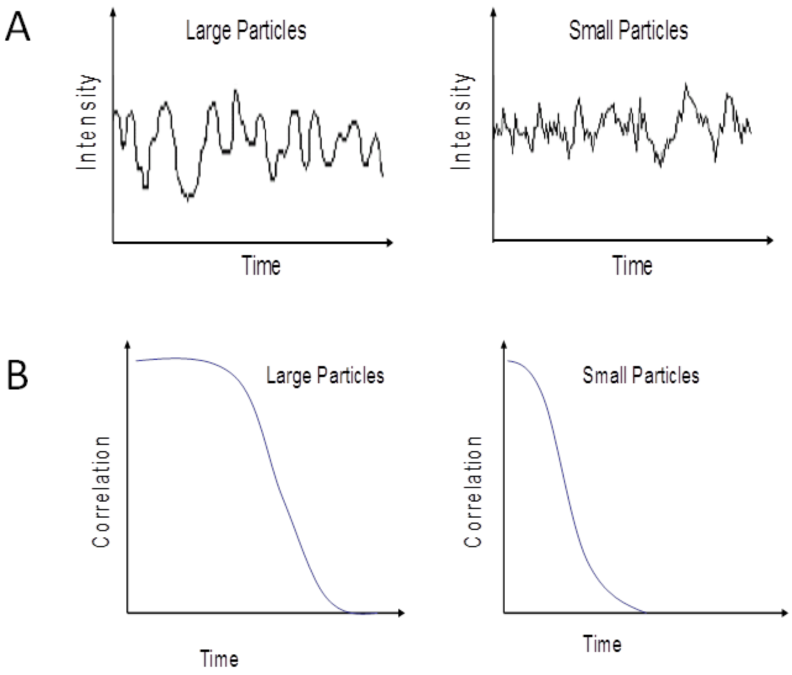

Figure 2.6: Typical DLS plots: (A) scattered light intensity fluctuations as a function of time for large and small particles in solution; (B) typical correlations functions for large and small particles in solution. Correlation functions. Figures are adapted from malvern.com[31]

The DLS apparatus consists of a cuvette containing the suspension of interest, with a mono-chromatic laser and detector perpendicular to each other. Particles undergoing Brownian motion will scatter some light perpendicular to the laser. This scattered light has constantly changing phase, with its consequential destructive and constructive interference pattern. The intensity and frequency of this constantly changing pattern of light (speckle pattern[30]) at the detector is unique to the particle sizes within the suspension. As shown in Figure 2.6A, smaller particles lead to a higher frequency of changes to the intensity of scattered light. The intensity changes are correlated over time, and the shape of typical correlation functions shown in Figure 2.6B, with smaller particles leading to sharper decreases in correlation over time. By understanding the relationship between particle size, diffusion and changes to the correlation functions, particle sizes can be determined. In this thesis, the Particle Size Detector (model 801, Protein Solutions) and OmniSIZE software was used to relate these correlation functions to a distribution of particle sizes in nanodiamond suspensions.

2.1.4 Ellipsometry

Ellipsometry is used in this thesis to measure thin film thickness. This technique measures the changes in the polarization of light upon reflection at a thin film, which can be related to film thickness and other physical properties. A basic schematic of the ellipsometry technique is shown in Figure 2.7, in which a light source is linearly polarized and directed towards the sample with incident angle (θ_i). The reflected light beam is elliptically polarized (i.e. the electric field vector of the light beam describes an ellipse on a stationary and intersecting plane which is normal to the direction of propagation) and the extent of this elliptical polarization varies as θ_i changes between 0^o and 90^o to the normal.

The classic explanation of the ellipsometric measurement of thin films was made by Winterbottom in 1946.[32] Typically, the extent of elliptical polarization is described by *p* and *s* co-ordinates in which *p* is parallel to the plane of incidence, whilst *s* is perpendicular to this plane. The amplitude of the light in each of these directions is described as r_s and r_p . Ellipsometry measures the complex reflectance ratio ρ, as follows :

$$\rho = \frac{r_p}{r_s} = \tan(\psi)\, e^{i\Delta} = \tan(\psi)\,(\cos\Delta + i\,\sin\Delta) = \mathrm{Re}(\rho) + \mathrm{Im}\,(\rho)\,i \qquad \text{(Equation 2.6)}$$

where Ψ is the amplitude component, Δ is the phase component, and the real (Re) and imaginary (Im) parts of the equation are indicated. The relative reduction in amplitude between the *s* and *p* components of the reflected light is described by Ψ, whilst the relative phase difference is described by Δ.[32]

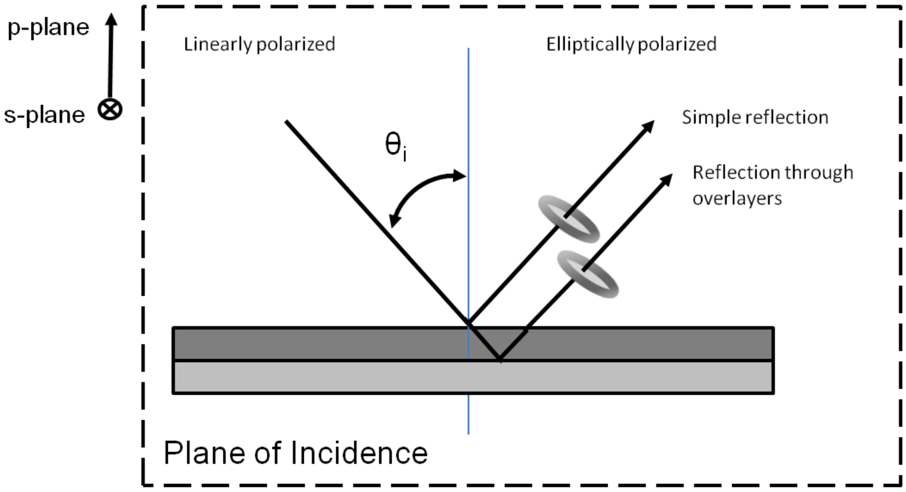

Figure 2.7: Schematic of the principles of an ellipsometry experiment.

Values of ρ lead to the derivation of complex optical constants for the simple system where reflection occurs at an interface[32]:

$$\frac{n_2}{n_1} = \frac{n_2(1+ik_2)}{n_1} = tan\phi_1[1 - 4\rho \times \frac{sin^2\phi_1}{(\rho+1)^2}]^{1/2} \qquad \text{(Equation 2.7)}$$

where n_x is the complex refractive index for each interface [i.e. $\overline{n_x} = n_x(1 + ik_1)$], k_x is the adsorption co-efficient of the interfaces. This equation assumes that the angles of propagation through the overlayer are related by $\overline{n_2} sin\phi_2 = \overline{n_1} sin\phi_1$ (Snell's Law). In this manner, Equation 2.7 directly convert Ψ and Δ into optical constants. When reflection occurs *through an overlayer,* there is superimposition of reflected light within the overlayer.[32] This complicates matters, and in this case, ellipsometry can only indirectly determine optical constants. This is done by establishing a series of layer models, in which the optical constants for the substrate, and overlayer, is fixed. Film thickness is allowed to vary by an iterative process until the calculated Ψ and Δ values match the experimental values.

In this thesis, variable-angle ellipsometry measurements of the bare gold and polystyrene overlayers were performed on a phase-modulated Picometer ellipsometry (Beaglehole Instruments, Wellingon, NZ) with a HeNe laser as the light source (632.8 nm). The real and imaginary parts of Equation 2.6 are related to *x* and *y* changes in reflectivity:

$$x = Re(r)\frac{2}{1+Re(r)^2+Im(r)^2} \qquad \text{(Equation 2.8)}$$

$$y = Im(r)\frac{2}{1+Re(r)^2+Im(r)^2} \qquad \text{(Equation 2.9)}$$

The optical constant of bare gold was 0.0003039 + [3.570i (n+ ik)] , with n being 1.45, the refractive index of polystyrene thin film (*n.b.* polystyrene thin films are assumed to be transparent, with k equal to zero).

2.2 Quartz Crystal Microbalance with Dissipation (QCM-D)

Two investigations on the dynamics of protein deposition on advanced materials are described in this thesis. The instrument used to study these protein dynamics was the quartz crystal microbalance with dissipation (QCM-D). In this section, the QCM-D technique will be described in detail, including its theory, modelling and standard experimental protocol. To conduct these protein studies, an exemplar globular protein was used throughout. A brief description of bovine serum albumin (BSA) and the dynamic behaviour of proteins at interfaces are described in an additional section.

2.2.1 History and Theory

Quartz-crystal microbalance with dissipation is used to measure the mass of deposited overlayers, as well as their viscoelastic properties.[33] This is accomplished by monitoring both frequency and dissipation changes of an oscillating quartz crystal. This technique is a variation on the well-known quartz crystal microbalance (QCM), which is a method of measuring the mass of rigid layers on surfaces. In both QCM and QCM-D, an electric field is applied to a piezo-electric quartz crystal by attached electrodes. This induces shear deformations within the crystal. This behaviour was first investigated by the Jacques and Pierre Curie in the late 1800s.[34] The cut of the crystal is key to its performance and the AT-cut is widely used in QCM or QCM-D applications, due to its stable oscillations.[35]

These shear deformations lead to vibrations or oscillations within the quartz crystal, which can be in-phase or out-of-phase with the applied electric field. However, if the quartz crystal has a thickness which is at odd integers of half wavelengths of these vibrations, then the quartz crystal can vibrate at its resonance frequency and harmonic overtones, without a change in the phase of the vibration. The resonance frequency depends on the physical parameters of the quartz crystal (*i.e.* thickness, density, shear modulus, and mass).

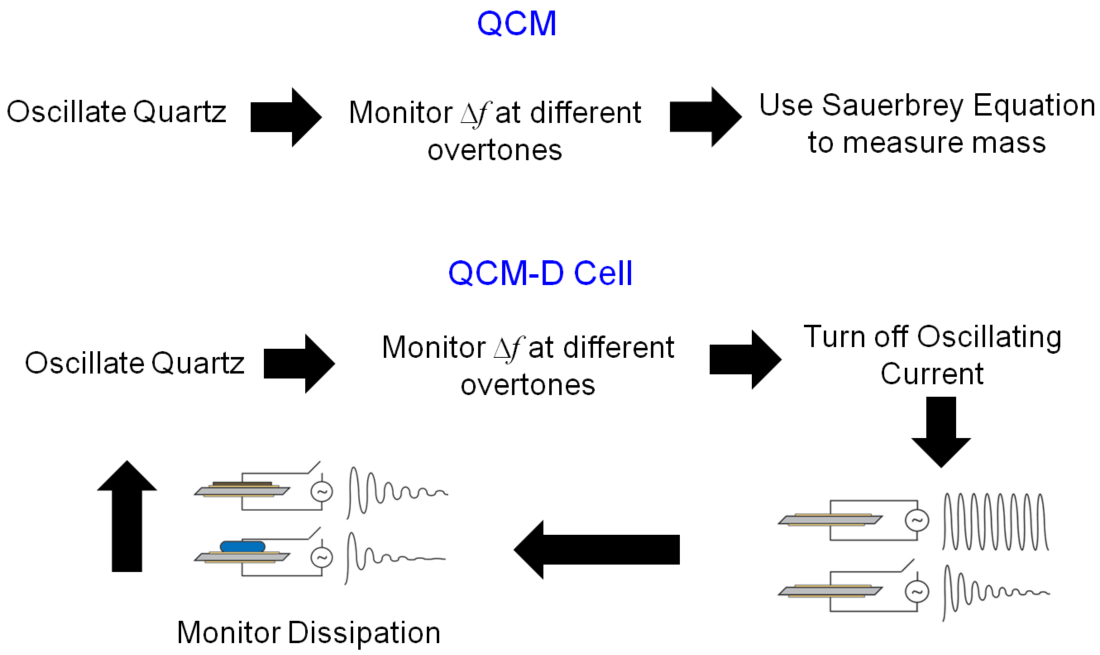

Figure 2.8: Summary of how QCM and QCM-D differ in their data collection. Note the exponential decay in the oscillation frequency when the applied current is switched off. The faster exponential decay seen for soft samples (blue, bottom) is compared to rigid samples (red, top). Figures adapted from Rodahl *et al.* and Voinova *et al.*.[37, 38]

The change of oscillation frequency is proportional to added mass, by the Sauerbrey equation[36]:

$$\Delta f = \frac{-2\Delta m f_0^2}{A\sqrt{\rho_q \mu_q}} \qquad \text{(Equation 2.10)}$$

where f is frequency (Hz), m is mass (g), f_0 is the resonance frequency of the oscillating crystal (≈ 4.95 Hz), ρ_q is the density of the quartz crystal (2.648 g cm^{-3}), μ_q is the shear modulus for an AT-cut crystal (2.95 x 10^{11} g cm^{-2}), and A is the active surface area of the crystal. Masses computed in this manner are referred to as Sauerbrey mass (m_s) and is reported with units of g cm^{-2} or ng cm^{-2}.

Typical QCM applications involve the measurement of *rigid* masses far less than that of the quartz crystal. The Sauerbrey equation is useful for determining the masses of such overlayers, for example the adsorption of gas monolayers on surfaces.[36] However, the QCM technique is limited by the use of the Sauerbrey equation. The Sauerbrey equation does not account for any energy loss processes at the surface, such as those caused by visco-elasticity or the coupling of a liquid overlayer to the surface. This equation *underestimates* the mass of 'soft' layers (*i.e.* proteins, bio-molecules, cells, *etc.*). QCM has other limitations, including: only for the study of solid-air or solid-vacuum interfaces; the change in frequency as a percentage of the fundamental frequency should be less than 2 %; and that part of the recorded Δf is affected by the mechanical load applied to the system.

The study of solid-liquid interfaces often involves the study of soft matter. The application of QCM to these systems was facilitated by two developments. The first was accomplished in 1980 by Nomura[39], who showed that stable oscillations are possible when a quartz crystal is placed in water. Later, the theory describing the solid-liquid interface at the quartz crystal in solution was developed by several groups. [37, 40, 41] Eventually, Fredrik Höök synthesized these developments into a working QCM-D technique. [33] This technique overcomes the limitations of the QCM technique for probing events at the solid-liquid interface, by simultaneously measuring frequency and energy dissipation losses; hence its abbreviated name, QCM-D.[33]

Dissipation is the rate of change of energy loss during a time interval in which a crystal's oscillations are not driven by an applied current. This is shown in Figure 2.8 for the QCM-D cell. During the brief interval, an exponentially decaying sine wave in the frequency trace is seen, whose shape is related to dissipation, with softer overlayers causing faster decays than rigid overlayers. The former has a higher dissipation.

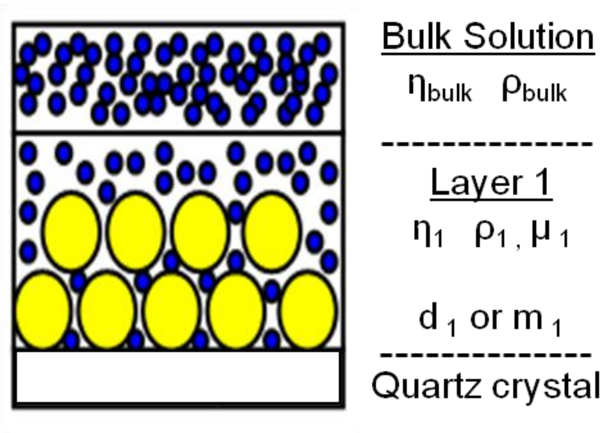

Figure 2.9: Schematic showing the one-layer model as described by Voinova *et al.*[37] The two layer model simply adds another overlayer to layer 1, between layer 1 and the bulk solution, with the relevant visco-elastic parameters (i.e. η_2, μ_2, etc.)

Voinova *et al.*[37] developed equations to describe the frequency and dissipation changes at one or two layer models at solid-liquid interfaces of QCM-D crystals. The one-layer model is shown in Figure 2.9. The propagation and loss of energy within a soft overlayer is assumed to be affected by the shear deformations induced by the oscillating quartz crystal. Energy losses in this overlayer are assumed to relate to the elasticity and viscosity at the interface. Thus, a Voight model can be used to describe the system, where energy losses are assumed to occur *via* an ideal viscous damper and ideal elastic spring.[37] The Voinova equations describe the changes in frequency and dissipation for one or two visco-elastic layers beneath a bulk liquid overlayer[37]:

$$\Delta f \approx -\frac{1}{2\pi\rho_0 h_0}\left[\frac{\eta_3}{\delta_3}+\sum_{j=1,2}\left(h_j\rho_j\omega-2h_j\left(\frac{\eta_3}{\delta_3}\right)^2\frac{\eta_j\omega^2}{\mu_j^2+\omega^2\eta_j^2}\right)\right] \qquad \text{(Equation 2.11)}$$

$$\Delta D \approx -\frac{1}{2\pi f\rho_0 h_0}\left[\frac{\eta_3}{\delta_3}+\sum_{j=1,2}\left(2h_j\left(\frac{\eta_3}{\delta_3}\right)^2\frac{\mu_j\omega^2}{\mu_j^2+\omega^2\eta_j^2}\right)\right] \qquad \text{(Equation 2.12)}$$

where η is viscosity, μ is shear modulus, ρ is density, h is layer thickness. Each layer is associated with an integer value j : quartz crystal (0); first viscoelastic layer (1); second viscoelastic layer (2); and bulk fluid (3). The first term in both equations relates to the visco-elastic contribution of the bulk liquid, whilst the second term relates to the mass and visco-elastic contributions of the overlayers. The angular frequency of a propagating acoustic shear wave is $\omega = 2\pi f$. The penetration depth (δ) of this propagating shear wave, through a viscoelastic medium, is described by:

$$\delta = \sqrt{\frac{2\eta}{\rho\omega}} \qquad \text{(Equation 2.13)}$$

where η is viscosity of the layer, ρ the density of the layer, and $\omega = 2\pi f$ is the angular frequency. By fixing certain variables, iterative fits to Equations 2.11 and 2.12 can be conducted to fit the theoretical model to the experimental data. There are several assumptions regarding the use of the Voight model to describe solid-liquid interfaces, including[37, 38]: bulk fluid is a Newtonian fluid; the overlayer is uniform, homogeneous, and covers the entire crystal surface; visco-elastic properties are uniform throughout the overlayers; and there is 'no-slip' between layers in the model, even during oscillations (*i.e.* layers are coupled to each other).[37, 38]

As a consequence of the QCM-D apparatus, and the use of Equations 2.11 and 2.12, several phenomena can be observed. First, the shear waves created by the oscillating crystal propagate from the surface. These shear waves are created within the liquid and are dampened by overlayers and the bulk liquid. For a crystal resonating at 5 MHz, this shear wave propagates ≈ 250 nm from the surface in water (see Equation 2.13).[33] All viscoelastic components within the shear wave region are detected by QCM-D, including all solvent or hydration shells. Therefore, any thin films added to the crystal surface (i.e. *via* spin-coating) should not be thicker than 100 nm, in order to maximize the chances of monitoring surface events by QCM-D. The surface sensitivity of QCM-D increases as the overtone number increases, thus allowing phenomena at short and long distances away from the crystal to be monitored. There is no means to directly de-couple the mass of the solvent from the mass observed by the QCM-D technique. Complementary techniques [e.g. ellipsometry, optical waveguide light spectroscopy (OWLS)] are needed to accomplish this task.[42] The mass sensitivity of QCM-D is approximately 0.5 ng cm^{-2}.[33] With the above in mind, QCM-D can be relied upon to measure the mass and visco-elastic properties with surface sensitivity.

2.2.2 Experimental Procedure

A typical QCM-D experimental apparatus is depicted in Figure 2.10, along with the QCM apparatus, for sake of comparison. Prior to use, gold-terminated quartz crystals were cleaned, in the following order: Piranha solution for 10 minutes using a 3:1 solution of concentrated H_2SO_4 (Fischer Scientific) and dilute H_2O_2 (30%, Alfa Aesar); copious rinsing with deionized, distilled water (dd-H_2O; MilliQ, Q-Guard-1 Filter); drying by N_2 gas; exposure to ozone plasma for 30 minutes. The addition of a thin overlayer to these crystals was added by spin-coating, if necessary. The cleaned crystal was mounted in the QCM-D module (E1, QSense, Sweden). This QCM-D module was housed in an aluminium box with a pre-heating element, which ensured a stable and consistent temperature (25°C) throughout all experiments.

Solutions containing phosphate buffer solutions with, and without, proteins were flowed through a cell containing the oscillating QCM-D crystal. Phosphate buffer (0.1M, pH 7.4) was made from K_2HPO_4●$3H_20$, KH_2PO_4 (both Sigma Aldrich), and Millipore water. The concentration of protein (BSA, Fraction V, Sigma Aldrich), in the relevant buffer solutions, was 0.08 g L^{-1}. A vacuum pump was used to de-gas solutions. The buffer solutions were flowed over the crystal surfaces until the frequency trace stabilised and all frequency drift induced by the experimental environment was minimized. This either took overnight for quartz crystals having a polystyrene overlayer, but only 20 minutes to 1 hour for crystals having a nanodiamond overlayer or for unmodified quartz crystals. The flow rate for all experiments was 0.1 mL min^{-1}, which was kept constant by a computer-controlled peristaltic pump.

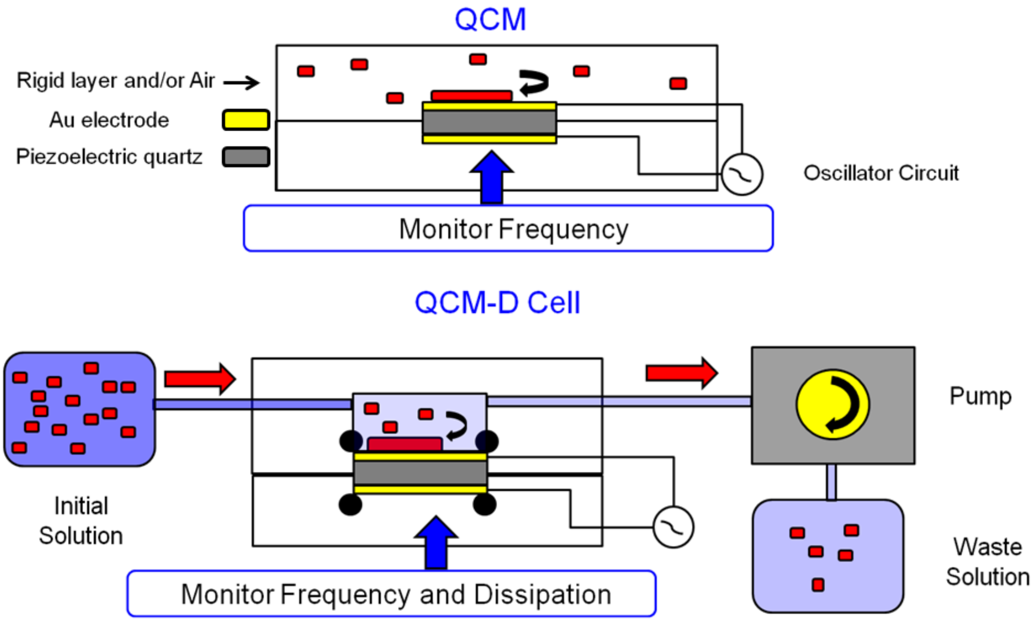

Figure 2.10: Schematic showing the QCM and QCM-D experimental set-up, with the latter representative of the apparatus used to conduct protein adsorption studies.

After system equilibrium was reached, the phosphate buffer solution was replaced by a phosphate buffered protein solution. As a consequence, a decrease in frequency and an increase in dissipation were seen, as protein deposits itself onto the surface. After the conclusion of a protein deposition experiment, the solution was replaced by the phosphate buffer, thus indicating the start of a rinse stage. BSA adsorption was studied on modified polystyrene, nanodiamond thin films, and for reference, on gold-terminated quartz crystals.

The dissipation and frequency data is recorded by QSoft and QTools software packages, which were provided with the instrument (QSense, Sweden). The frequency (*f*, Hz*)* and dissipation (D) data was collected for the 5th, 7th, 9th, and 11th overtones. Prior to modelling, data was zeroed (i.e. 0 Hz, no dissipation) based on the data of the 5th overtone's frequency and dissipation trace. Data was also normalized by its respective overtone value (i.e. *f*/*n* or D/*n* where $n = 5, 7, 9, 11$). The duration of the fit is clearly indicated throughout this thesis. The areal mass of BSA deposited on the surface was calculated using either the Sauerbrey, or the Voight model.

If the Voight model was used, then it is made clear whether the 1 or 2 layer model is used to fit the data. The quality of fit was evaluated by both visual and statistical means. In the case of the 1 layer Voight model, there are 6 physical parameters: η_3, p_3, μ_1, η_1, p_1 *and* h_1. Three of these variables need to be assigned fixed values; the remaining three variables are fitted by the software between flexible, maximum and minimum values deemed reasonable for a protein system and which optimized the fitting. Fluid density (p_3, 1000 kg m^{-3}), fluid viscosity (η_3, 0.001 kg m^{-1} s^{-1}) and layer one density (p_1, 1200 kg m^{-3}) were fixed. The other parameters were approximately fit as follows: layer 1 viscosity (η_1, $1\text{x}10^{-4}$ – $1\text{x}10^{-1}$ kg m^{-1} s^{-1}), layer 1 shear (μ_1, $1 \text{ x } 10^{3}$ – $1 \text{ x } 10^{14}$ Pa), and layer 1 thickness (h_1, $1 \text{ x } 10^{-10}$ – $1 \text{ x } 10^{-7}$ m). These are similar to values used by others.[43, 44] As well, the descending fit mode, 50 step initial grid fit, and logarithm fitting, as defined by the software, was used as required. In this thesis, 50 point, adjacent-average smoothing was used to smooth data for kinetic analysis. This smoothing represents about 14.5 seconds of experimental time.

2.2.3 Protein Adsorption Studies

2.2.3.1 Kinetics

The kinetics of protein adsorption can be determined using techniques which collect data at a fast rate. QCM-D is one such data-dense technique, with an ability to record data up to 200 times a second. In this thesis, frequency and dissipation data was obtained three times per second, which was sufficient to enable a detailed kinetic study of protein adsorption on advanced materials.

The kinetics of protein deposition and related dynamic properties are well-reviewed throughout the literature.[45 - 47] Whilst there exist several different kinetic interpretations of protein adsorption onto solid surfaces, two are most commonly used in the case of globular proteins to surfaces: the random sequential adsorption (RSA) model and the Langmuir isotherm.[48] Both of these models can be applied to the collected QCM-D data. Both models are described below and are summarized by Figure 2.11.

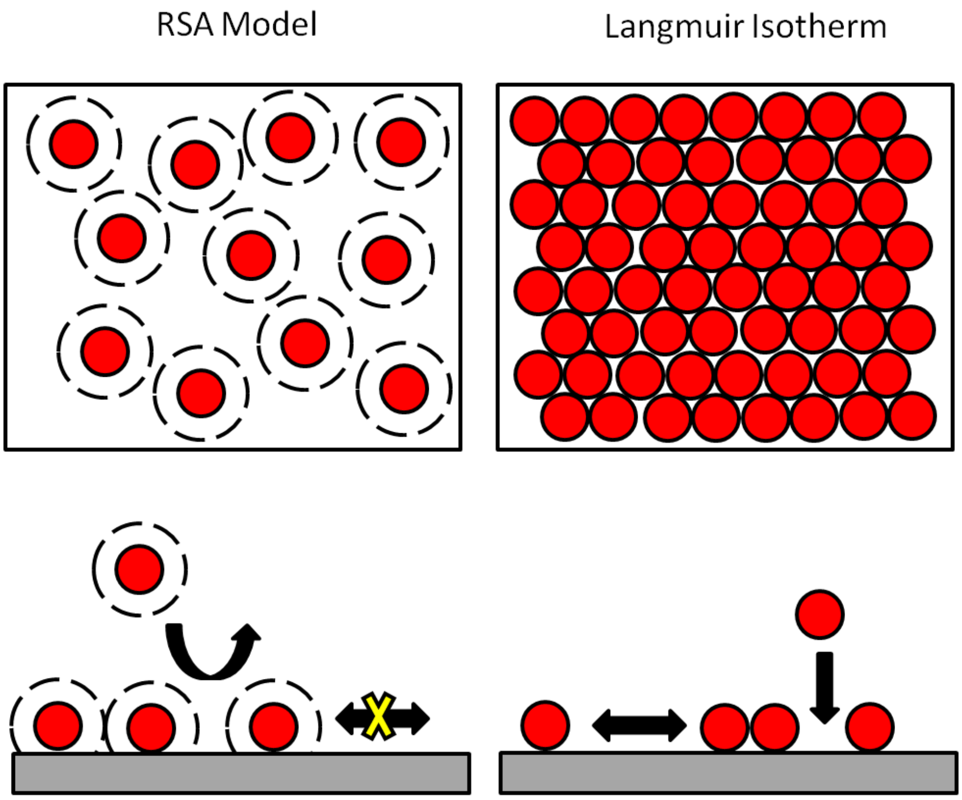

Figure 2.11: Scheme outlining the differences between the RSA and Langmuir isotherm for the ideal case The top and side views of a surface undergoing RSA or Langmuir adsorption are shown. Proteins (red) have excluded area in the former, which is depicted as dashed circles. The mobility and adsorption of proteins is depicted as block arrows.

The RSA model assumes protein adsorption is: irreversible, immobile, and that proteins can be approximated as hard spheres with excluded area, as shown in Figure 2.11. The adsorption behaviour is expected to follow this expression:

$$\frac{dm}{dt} = k_a c_v \Phi(m) \qquad \text{(Equation 2.14)}$$

where m is the adsorption mass, Φ(m) is the available area function, c_v is the surface concentration of the protein, and k_a is the adsorption rate constant.[46] The available area function can be approximated up to a fractional coverage of about 30% by using this equation:

$$\Phi(m) = 1 - 4\theta + A\theta^2 + B\theta^3 \qquad \text{(Equation 2.15)}$$

where θ is fractional coverage and the constants A and B related to the size of the excluded area. RSA kinetics do occur in the case of globular protein adsorption, and in the specific case of BSA adsorption at solid surfaces.[49-52]

In some cases, the available area function associated with protein deposition is found to have Langmuir-like dependence on surface coverage (i.e. $\Phi = 1 - \theta$). This behaviour implies that proteins can adsorb onto any unoccupied region of the surface and that adsorbed proteins can undergo surface diffusion, leading to clustering and aggregation.[51] Langmuir adsorption can be observed for the adsorption of blood serum albumins and other proteins, such as cytochrome p450, onto surfaces.[46, 50, 51]

In practice, the type of adsorption can be identified by comparing rate of change of mass adsorption as a function of added mass.[46] These are referred to throughout this thesis as ‘d*m*/dt’ plots. The shape of an individual plot is unique to the mechanism or mechanisms involved in the adsorption phenomenon.[46, 48] Linear plots suggest Langmuir adsorption, whilst exponential decay plots, convex to the mass axis, indicate RSA adsorption. This is shown in Figure 2.12. Of course, a range of behaviours is expected; those that are more linear have ‘Langmuir-like’ adsorption, whilst those which are more exponential have ‘RSA-like’ adsorption. Langmuir adsorption is capable of filling the substrate completely, whilst RSA adsorption is limited by the so-called ‘jamming’ limit, whereby surface coverage is limited to about 50%.[46, 48]

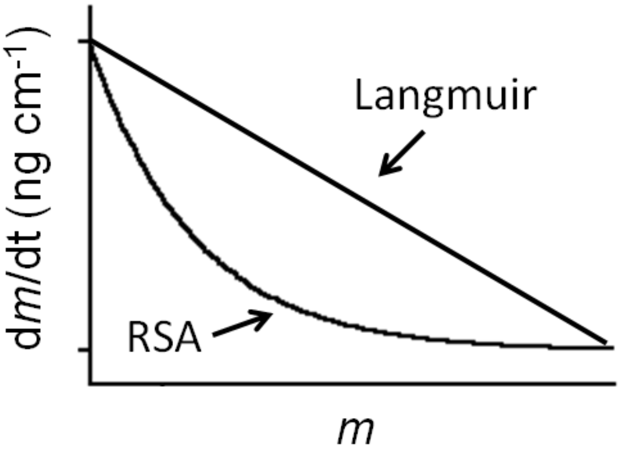

Figure 2.12: Scheme showing the rate of adsorption *versus* mass adsorption showing approximate behaviour expected for Langmuir and RSA adsorption.

Descriptive parameters of this type of kinetic behaviour can be extrapolated from the obtained data using methods developed by others.[46, 47, 53, 54] In reality, protein adsorption rarely has true RSA or Langmuir behaviour. However, these researchers note that RSA deposition is reasonably linear at small mass and short adsorption times. Thus, linear regions of the d*m*/dt plots can be fitted by use of a first-order expansion of Equation 2.14, as a simple and practical method of comparing protein deposition kinetics. The relevant expression is:

$$\frac{dm}{dt} = k_a c_b (1 + C_1 m) \qquad \text{(Equation 2.16)}$$

where C_1 is a constant related to steric factors of the adsorbed proteins and k_a is the rate constant. The parameter c_v from Equation 2.14 has been approximated by c_b, the concentration of protein in the bulk solution. From the intercept of the line to the y-axis, k_a is determined; C_1 calculated from the slope of the line. The rate constant and adsorption footprint have been previously associated with physical phenomena. Brusatori *et al.* [54] consider k_a to be related to the potential energy barrier that an incoming protein must overcome before adsorption, and that it can be used as a basic measure of protein-surface affinity.[46, 54] The steric factor is related to the adsorption footprint of proteins on a surface.[54, 55]

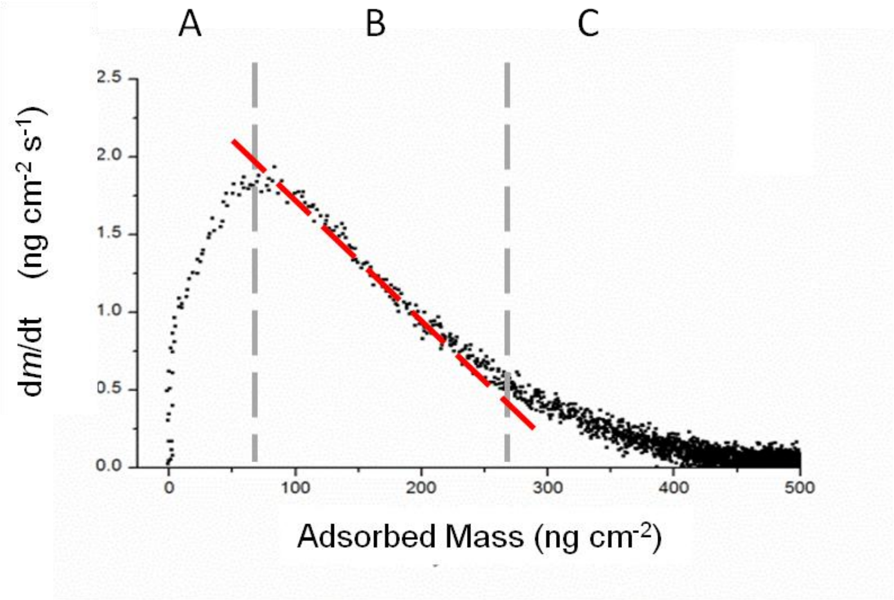

Figure 2.13: Example of a typical d*m*/dt plot with vertical dashed lines delineating the three regions of the plots: transport limited (A); reaction-limited (B); and asymptotic (C). The red line is the approximate fit to the reaction-limited region, which can be related to Equation 2.16 to solve for k_a and C_1, as described in this section.

Typical d*m*/dt plots can be divided into three regions corresponding to protein behaviour: transport-limited, reaction-limited, and asymptotic regions.[47] This is shown in Figure 2.13, and it is the linear fit to the reaction-limited region from which k_a and C_1 are determined.[47, 53, 54] This is the region in which protein adsorption is governed by non-equilibrium surface processes, and this region is important to the interpretation of results in this thesis. Adsorption before this period is limited by the flux of protein arriving at the surface due to the flow rate of protein to the surface region (transport-limited). Adsorption after this period is near equilibrium, and this asymptotic region is one where the conformation of proteins reaches a preferred state or orientation.[47]

In this thesis, these d*m*/dt plots are created by using the Sauerbrey mass data, with the aid of a 50 point (≈ 14 second) adjacent averaging of the d*m*/dt data. This enabled the resolution of the three kinetic regimes mentioned above. Even with unreasonable levels of adjacent point averaging (200 - 500 point), the Voight mass data did not produce resolvable d*m*/dt plots; this is due to the high level of scatter in the Voight mass data (see standard deviations for Voight masses in Table 3.7). Ideally, there would be no requirement to adjacent-average the d*m*/dt data, but this technique is required in order to reduce the scatter inherent to even the Sauerbrey mass data. This scatter is thought to be due to the increased number of small, but numerous events on the surface (i.e. hydration changes, conformational changes, etc.) which increase in number as adsorption mass increases.

2.2.3.2 BSA : A Model Protein

BSA has been chosen as a model protein for the adsorption studies in this thesis. It is a well-characterized protein, whose behaviour mimics that of its human-equivalent (HSA) and globular proteins, in general. This protein is a major constituent of blood serum in the cardiovascular systems of mammals.[56, 57] The human equivalent is HSA, which shares most of the structure of BSA, but only has one tryptophan residue, instead of two.[58] The behaviour of BSA at solid-liquid interfaces is well-studied and this behaviour is expected to be similar to that of other globular bio-macromolecules.[45,56] BSA is a globular, heart-shaped protein with a molecular weight of ≈ 66.4 kD, an equilateral triangular face of ≈ 8 nm and a thickness of ≈ 3 nm.[56, 59] It has a molecular volume of about 88.25 nm^3.[56, 59] BSA undergoes changes in conformation to minimize its energy upon adsorption.[56] An interplay of various forces in solution and at surfaces lead to conformational change, and they include the following: electrostatic forces, van der Waals forces, hydrophobic interactions, and hydrogen bonding; in addition, entropy of the system (i.e. hydration layers, protein conformation) is an important consideration.[60] The interplay of all these interactions are dependent on several factors, including: pH [56], protein concentration[61, 62], surface chemistry[63, 64], and surface roughness.[61, 65] BSA can deposit onto both hydrophobic and hydrophilic surfaces, but with greater protein-surface affinity and a loss of α-helix structure occurring on hydrophobic surfaces.[64] AFM studies of fetal bovine serum (FBS), of which BSA is a major constituent (≈ 15%), show that there is a time dependence on the adsorption of BSA onto diamond surfaces, which is dependent on surface chemistry.[57] The effect of roughness on BSA adsorption is not well-studied, and existing results are conflicting.[61, 65] For a more general description of the behaviour of soft, globular proteins like BSA, one may refer to the work of Norde. [60, 66]

2.3 Electrochemical Methods

The oxidation and reduction of organic compounds at conductive surfaces can be investigated using dynamic electrochemistry. There are several high quality reference books on the subject of electrochemistry[67-71], but the main aspects of this subject and related analytical methods will be summarized here.

2.3.1 Electrochemical Theory

(a) Equilibrium Electrochemistry

When there is a transfer of charge at the interface between an electrode and solution, an electrochemical reaction is said to have occurred. This can be described as follows:

$$\mathrm{Ox}_{(aq)} + ne^{-}_{(electrode)} \leftrightharpoons \mathrm{Red}_{(aq)} \qquad \text{(Reaction 2.1)}$$

such that $\mathrm{Ox}_{(aq)}$ represents an oxidized species in solution, which gains a certain number of electrons (n) from an electrode to generate reduced species, in the solution. At equilibrium, a potential difference between the electrode and solution will exist, since the above electrochemical reaction leads to charge separation between the solution and the electrode.

The potential difference can be expressed in terms of energy levels and the example of the reduction of a species at the surface, which is in its oxidized form.[68, 69] As shown in Figure 2.14, the valence band of an electrode prior to equilibrium is filled to the Fermi level (E_F), and the oxidized species has a LUMO (lowest unoccupied molecular orbital) available to be filled by an electron ($LUMO_{ox}$). For reduction of this species to occur, the energy level of E_F must be greater than the energy level of the LUMO. If this is the case, then a transfer of electrons from the electrode to the oxidized species will occur, with four consequences: first, the energy of $LUMO_{ox}$ will rise; second, a reduced species will form in solution having a distinct energy level for its highest occupied molecular orbital ($HOMO_{red}$) ; third, the energy of E_F will decrease; fourth, negative charge will build in the solution and positive charge on the electrode. It should be noted that the HOMO of the reduced species can transfer electrons back to the electrode if its energy level is equal to or higher than the electrode Fermi Level. At some point, the rate of electron transfer from the electrode to $LUMO_{ox}$ and the rate of electron transfer to the electrode from $HOMO_{red}$ will be equal. When this occurs, the system is said to have reached electrochemical equilibrium with its characteristic equilibrium potential difference between the electrode and solution.

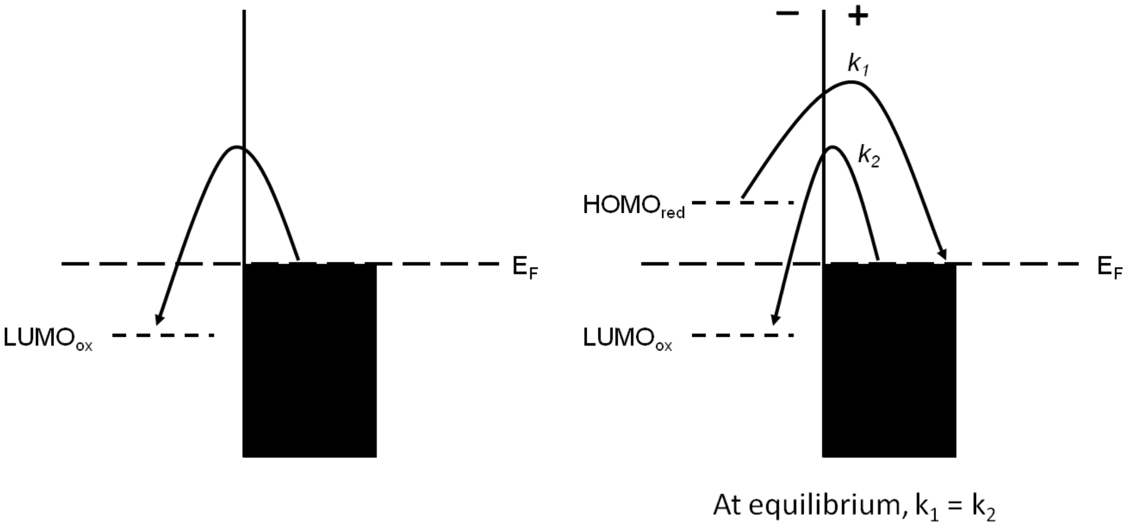

Figure 2.14: Energy level diagrams showing the process by which species in solution achieve electrochemical equilibrium with an electrode. There can be an oxidized species (ox) undergoing reduction, or a reduced species (red) undergoing oxidation. $LUMO_{ox}$ and $HOMO_{red}$ are defined in the text. k_i is the rate constant for the electron transfer associated with oxidation (1) or reduction (2) of species in solution. A potential difference between the solution and the electrode is formed at equilibrium. The Fermi energy is E_F. Adapted from Banks and Compton.[68]

The potential drop across the interface at equilibrium can be written as:

$$\Delta\Phi_{\mathrm{e/s}} = \Phi_{\mathrm{e}} - \Phi_{\mathrm{s}} \qquad \text{(Equation 2.17)}$$

where Φ_s is the solution potential and Φ_e is the electrode potential. This potential drop cannot be measured directly but it can be measured with regard to a second electrode which is used as a reference.[68] The potential drop at the electrode of interest (the working electrode) can then be expressed by the equation:

$$E = \Delta\Phi_{\mathrm{e/s}} + \text{ constant} \qquad \text{(Equation 2.18)}$$

The equilibrium potential difference (E_{eq}) can be predicted by using the Nernst equation, as follows:

$$E_{eq} = E^{o} - \frac{RT}{nF} ln\frac{a_{Red}}{A_{ox}} \qquad \text{(Equation 2.19)}$$

where E^o is the standard electrode potential of the electrochemical reaction, F is the Faraday constant (96 485 C mol^{-1}), n is the number of moles of electrons transferred, R is the universal gas constant (≈8.314 J K^{-1} mol^{-1}), T is temperature, and a_x is the activity of the species in solution (*i.e.* $a_x = \gamma[x]$, where γ is the activity coefficient). The standard electrode potential is the potential that a working electrode has when referenced to the standard hydrogen electrode, which is used as the reference note above at standard environmental conditions (*i.e.* 1 bar , 25^{o}C), and where species in solution have unit activity..

(b) Non-Equilibrium Electrochemistry

In many cases, in order to induce or change the direction of an electrochemical reaction, non-equilibrium potentials must be applied at the working electrode. The difference between E_{eq} and this applied potential is called the overpotential (η):

$$\eta = E - E_{eq} \qquad \text{(Equation 2.20)}$$

For solution oxidation to occur, the electrode potential E must be more positive than E_{eq}, and *vice versa* for reduction to occur. In the latter case, a cathodic current (i_c) is present where electrons flow from the more negative electrode to the more positive solution; the opposite is called the anodic current (i_a); both can be determined from the following expressions:

$$i_a = nAFk[Ox] \qquad \text{(Equation 2.21)}$$

$$i_c = nAFk[Red] \qquad \text{(Equation 2.22)}$$

where i is the current, n is the number of electrons transferred in the oxidation or reduction step, A is the electrode area, and k is the rate constant of the electron transfer, which is dependent on potential. The terms [*Ox*] and [*Red*] are the concentration of the oxidized and reduced species at the surface, with each associated with anodic or cathodic current, respectively. The rate constant can be related to thermodynamic parameters based on the principles of transition state theory[68], such that:

$$k_x = Ze^{\frac{-\Delta G^{\ddagger}}{RT}} \qquad \text{(Equation 2.23)}$$

where $G^{\ddagger}$ is the standard activation energy of the electrochemical process under investigation, and the term Z is a pre-exponential factor. The Butler Volmer model can be used to approximately describe the electrode kinetics. The free energy of the reactant is driven to the product by an applied overpotential (η), over an energy barrier related to the transition state. This process is shown in Figure 2.15, for a one electron reduction.

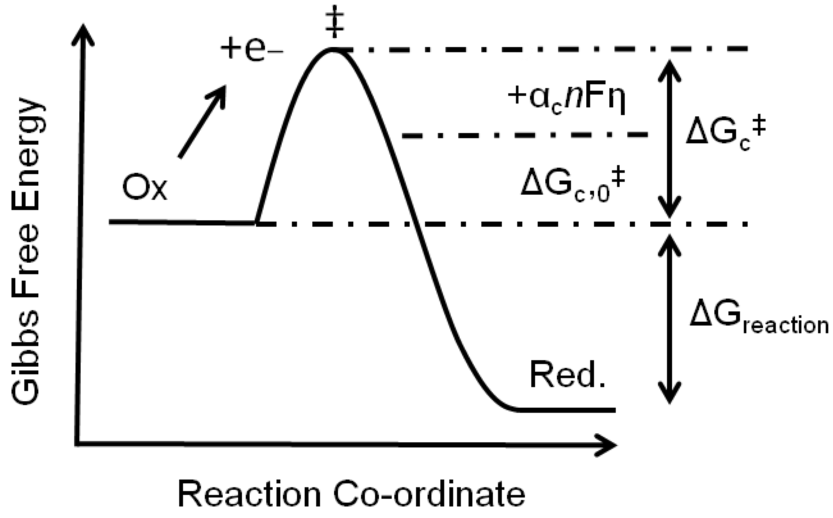

Figure 2.15: Free energy diagram for a one electron reduction. The relationship between activation energy and overpotential is shown in the diagram (see Equation 2.24). Adapted from Brett and Brett.[72]

The Gibbs free energy of the three points on the reaction co-ordinate (reactant, transition state, and product) is determined by the potential at the electrode interface, as described for the reduction and oxidation processes:

$$\Delta G_c^{\ddagger} = \Delta G_{c,0}^{\ddagger} + \alpha_c nFE \qquad \text{(Equation 2.24)}$$

$$\Delta G_a^{\ddagger} = \Delta G_{a,0}^{\ddagger} - \alpha_a nFE \qquad \text{(Equation 2.25)}$$

where α is measure of the asymmetry of the activation barrier and E is the potential applied to the electrode (i.e. η, the overpotential).[72] This value is about 0.5, and it is related to how the transition state responds to induced potential difference.[68] Equations 2.24 and 2.25 can be inserted into Equation 2.23, and rearranged to obtain a full expression for the relationship between current and η at the electrode, assuming that the reaction is first order at equilibrium and occurs directly at the electrode interface[72]:

$$k_c = k_0 e^{[-\frac{\alpha_c nF\eta}{RT}]} \qquad \text{(Equation 2.26)}$$

$$k_a = k_0 e^{[-\frac{\alpha_a nF\eta}{RT}]} \qquad \text{(Equation 2.27)}$$

where k_0 is the equilibrium electron transfer rate. These two formulas were first derived by Butler and Volmer.[73, 74] The observed current is proportional to the difference between the rate of oxidation and reduction reactions at the electrode surface[72]:

$$I = nFA\,(k_a[Red] - k_c[Ox]) \qquad \text{(Equation 2.28)}$$

Electrochemical reactions are not solely controlled by the rate constant, but on several other factors, such as mass transfer, chemical reactions prior to or after electron transfer, and other physical phenomenon.[67] Mass transfer is a general expression which encompasses all those processes, leading to redox species moving from the bulk solution to the electrode surface (e.g. diffusion, convection, migration, etc.). The chemical reactions in bulk solution would change the character of species about to undergo an electrochemical reaction, with protonation and decomposition being two common reactions. Other surface events such as adsorption and desorption, would change the character of the interface.

The diffusion of a species to a surface is driven by concentration differences, and it can be described by Fick's first and second law of diffusion. The first law is given by:

$$J = -D\frac{\delta\phi}{\delta x} \qquad \text{(Equation 2.29)}$$

where J is the molecular flux, D is the diffusion coefficient, $\phi$is the concentration of the species, and *x* is the position of the species. Diffusion can cause the concentration of species in solution to change, as described by the second law:

$$\frac{\delta\phi}{\delta t} = D\frac{\delta^2\phi}{\delta^2 x} \qquad \text{(Equation 2.30)}$$

However, to properly reflect electrochemical processes, one must also account for the influence of an electric field which changes in time:

$$E = -\nabla\phi - \frac{\delta A}{\delta t} \qquad \text{(Equation 2.31)}$$

where $-\nabla\phi$ is the potential gradient and A is the magnetic vector potential.[75] The above concepts can be combined to derive the Nernst-Planck equation.[67, 75] This equation describes the flux of ions within a concentration *and* potential gradient, with respect to time.

$$J_i(x) = -D_i\frac{\delta C_i(x)}{\delta x} - \frac{z_iF}{RT}D_iC_i\frac{\delta\nabla\phi(x)}{\delta x} + C_iv(x) \qquad \text{(Equation 2.32)}$$

where C_i is the concentration of the species of interest, z_i is its charge, D_i is the diffusion constant of the species in solution, $\nabla\phi$ is the potential gradient, and $v(x)$ is the velocity of diffusion. Each of the terms is related to a physical phenomenon, which are from left to right, diffusion, migration, and convection.

2.3.2 Cyclic Voltammetry

In cyclic voltammetry, the applied potential is changed at the working electrode linearly in two directions. This is shown in Figure 2.16A. The current is monitored throughout. At potentials where there is no electrochemical response, the current is non-Faradaic (*i.e.* capacitance), but at potentials near, and at, the overpotentials required to drive an oxidative or reductive process, the current becomes Faradaic.[68] As the potential is swept from lower to higher overpotentials, oxidation of solution-based species will occur, so an anodic current develops which reflects the changing rate constant for electron transfer, as well as mass transport to the electrode surface. Similarly, reduction of species in the electrode vicinity occurs on the reverse cathodic sweep, This leads to the characteristic redox curves seen in cyclic voltammograms, which are shown in Figure 2.16B.

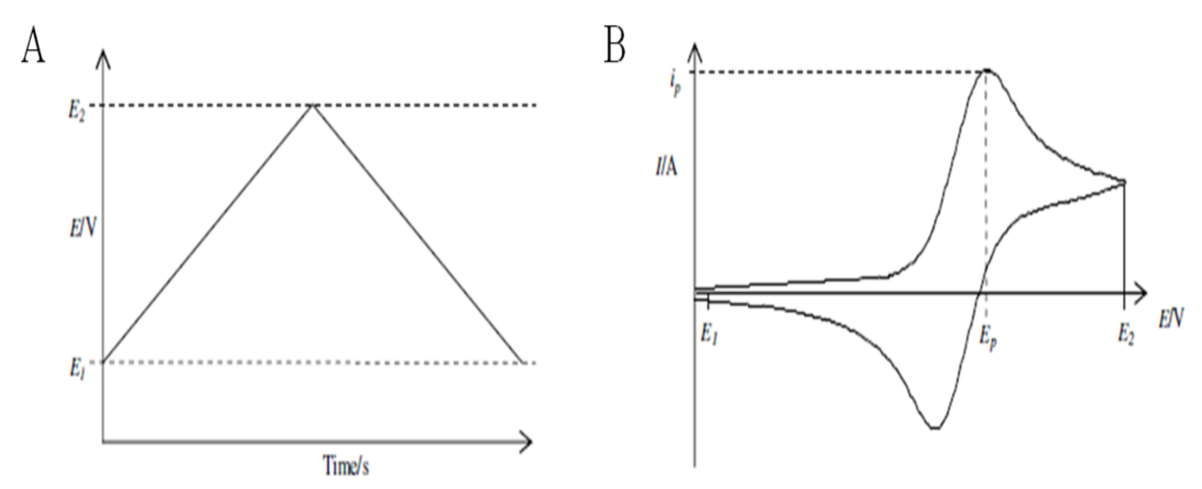

Figure 2.16: Linear potential sweep for cyclic voltammetry (A); Typical cyclic voltammogram for a reversible electrochemical reaction. Figures used are from *Understanding Voltammetry*.[68]

The peak current is a process dependent solely on diffusion kinetics, which can be described as follows for an oxidation or reduction process:

$$i_p = 0.4463\left(\frac{F^3}{RT}\right)^{\frac{1}{2}} n^{\frac{3}{2}} A D_i^{\frac{1}{2}} C_i v^{\frac{1}{2}} \qquad \text{(Equation 2.33)}$$

where v is the sweep rate, D_i is the diffusion coefficient, C_i is the reactant concentration, and all other terms are as described earlier.[68] A purely diffusion-controlled reaction would therefore have a peak current proportional to $v^{1/2}$. For a reversible process , that is a process displaying “fast” reaction kinetics, the peak-to-peak separation of the oxidation and the reduction peaks, independent of the scan rate, should follow this expression:

$$\Delta E_p = \left| E_p^{ox} - E_p^{red} \right| = 2.218\frac{RT}{nF} = 57\ mV \text{ (at 298 K)} \qquad \text{(Equation 2.34)}$$

In addition, for a reversible process, the ratio of peak currents of the oxidation and reduction peaks should be 1:1. Larger peak separations and deviations from these equations are all signs of irreversible processes displaying “slow” electron transfer. Cyclic voltammograms which show behaviour which is only semi-consistent with reversible processes are called ‘quasi-reversible’ reactions. In the common language of electrochemistry, irreversible processes represent slow reactions, reversible reactions are fast, and quasi-reversible reactions are intermediately fast / slow, as defined to a characteristic timescale, that depends on the scan rate used.[68]

2.3.3 Square Wave Voltammetry

Cyclic voltammetry suffers from high background currents, which limits the detection of small currents arising, for example, in sensitive electro-analytical chemistry. However, the non-Faradaic currents which typically contribute to the background, decay at a faster rate than the Faradaic current at short time frames; therefore, measuring the Faradaic current after this decay is a strategy for increasing the ratio of Faradaic to non-Faradaic current.[68, 71] In doing so, the background is reduced, and electrochemical sensitivity increased.

Square-wave voltammetry is a method which can increase the Faradaic to Non-Faradaic current ratio. Compton and Banks describe the basic concept of the technique, which is adapted here.[68] Central to this technique is the superimposition of a square-wave on a step-wise increase in the applied potential; this is shown in Figure 2.17A. Each pulse change of the potential is characterized by several parameters, including the pulse height (square-wave amplitude; ΔE_p), the height of the staircase (ΔE_s), the pulse time (t_p), and the pulse time (t_s). The pulse time is rarely used in practice, with users referring to a square-wave frequency (f=1/2t_p) instead.[68] The scan rate is equal to $f\Delta E_s$. Positions 1 and 2 in Figure 2.17A are the points at which the potentiostat records the current. The difference between these two currents is graphed, as a function of applied potential, to create a voltammogram with a single spectral trace. This difference is called the net current, and it represents a current with minimal contributions from non-Faradaic processes; this particular current remains constant over the small potential range between the two measurement points. Using this method, electrochemical sensitivity is increased, with concentrations of ≈ 10^{-8} M easily detectable.[68]

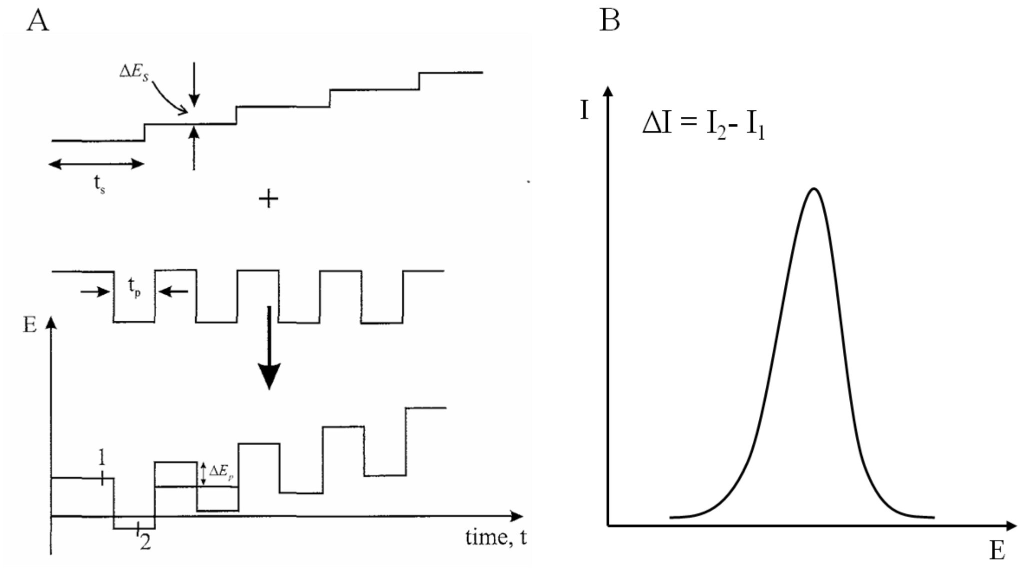

Figure 2.17: Square-wave voltammetry measurement with superimposed square-wave and potential step pulse[68] (A); Example of square wave output (B). Figures used are from *Understanding Voltammetry*.[68]

2.3.4 Experimental Technique

Throughout this thesis, experiments were conducted using a three-electrode electrochemical cell, which had a working electrode, a platinum counter-electrode and an Ag/AgCl reference electrode. These were all connected to a computer-controlled potentiostat (PGSTAT128N, Metrohm Autolab UK) with the General Purpose Electrochemical System software (v. 4.9); this experimental set-up is shown in Figure 2.18. The potentiostat system measures the current flowing between the working electrode at some programmed and measured potential at the working and reference electrodes. Importantly, this is measured under conditions where no current flows at the reference electrode, which can be achieved by using a feedback loop to adjust the potential of the counter electrode. In cyclic voltammetry, for example, the programmed potential is then selected to vary linearly with time as shown in Figure 2.16A; the current flowing in the cell is measured as a function of the potential. The reference electrode here has a potential of 0.209 V vs. the standard hydrogen electrode (SHE; Pt / H_2 / H^+ with all activities at unity). Measurements were performed at room temperature (20°C). Cyclic voltammetry was normally performed by using a scan rate of 0.05 V s^{-1}. The following parameters were used for square-wave voltammetry: 10 mV amplitude, 1 mV step potential, and a frequency of 10 Hz.

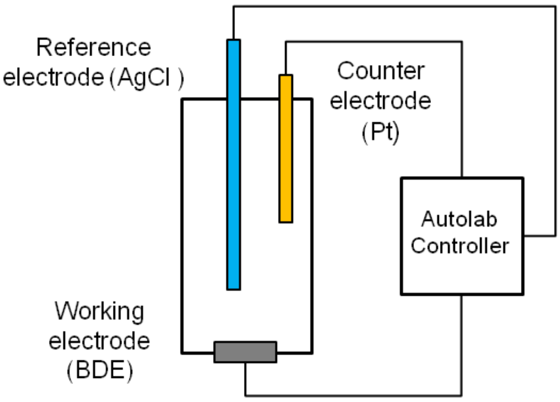

Figure 2.18: Electrochemical cell used in this thesis to conduct cyclic and square-wave voltammetry.

References

[1] K. Siegbahn, K. Edvarson, Nuclear Physics, 1 (1956) 137-159.

[2] K.M. Siegbahn, "Nobel Lecture: Electron Spectroscopy for Atoms, Molecules and Condensed Matter", Nobel Foundation (Ed.) (1981).

[3] H. Hertz, Annalen der Physik, 267 (1887) 983-1000.

[4] A. Einstein, Annalen der Physik, 322 (1905) 132-148.

[5] D. Briggs, J.T. Grant, "Perspectives on XPS and AES", in: D. Briggs, J.T. Grant (Eds.) Surface Analysis by Auger and X-ray Photoelectron Spectroscopy, IM Publications and Surface Spectra Ltd., Charlton and Manchester, UK, (2003) pp. 1-30.

[6] S. Tanuma, "Electron Attenuation Lengths", in: D. Briggs, J.T. Grant (Eds.) Surface Analysis by Auger and X-ray Photoelectron Spectroscopy, IM Publications and Surface Spectra Limited, London, (2003) p. 900.

[7] S. Huefner, Photoelectron Spectroscopy, 3rd ed., Springer, (2003).

[8] E. Fuchs, H. Oppholzer, H. Rehme, Particle Beam Microanalysis - Fundamentals, Methods and Applications, Wiley-VCH (1990).

[9] D. Briggs, “XPS: Basic Principles, Spectral Features, and Qualitative Analysis”, in: David Briggs, J.T. Grant (Eds.) Surface Analysis by Auger and X-ray Photoelectron Spectroscopy, IM Publications and Surface Spectra Ltd., Charlton, UK, (2003) pp. 31-56.

[10] F.F. Moulder, W.F. Stickle, P.E. Sobel, *et al.*, Handbook of Photoelectron Spectroscopy, Perkin-Elmer, Physical Electronics Division, (1993).

[11] I.W. Drummond, “XPS: Instrument and Performance”, in: D. Briggs, J.T. Grant (Eds.) Surface Analysis by Auger and Photoelectron Spectroscopy, IM Publications and Surface Science Spectra Ltd., Charlton, UK, (2003) pp. 117-145.

[12] N. Fairley, “XPS Lineshapes and Curve Fitting”, in: D. Briggs, J.T. Grant (Eds.) Surface Analysis by Auger and X-ray Photoelectron Spectroscopy, IM Publications and Surface Science Spectra Ltd., Charlton, UK, (2003).

[13] D. Briggs, J.T. Grant, “Polymer C1s Chemical Shifts”, in: Surface Analysis by Auger and X-ray Photoelectron Spectroscopy, IM Publications, Charlton, UK, 2003, p. 900.

[14] C.D. Wagner, A.V. Naumkin, A. Kraut-Vass, *et al.*, NIST X-ray Photoelectron Spectroscopy Database, in: N.I.o.S.a.T. (NIST) (Ed.), U.S. Secretary of Commerce, USA, Washington, USA, (2007).

[15] J. Larrieu, B. Held, H. Martinez, *et al.*, Surf. Coat. Technol., 200 (2005) 2310-2316.

[16] C.D. Wagner, W.M. Riggs, L.E. Davies, *et al.*, Handbook of X-ray Photoelectron Spectroscopy, Perkin-Elmer Corporation, U.S.A., (1979).

[17] D. Briggs, J.T. Grant (Eds.) Surface Analysis by Auger and X-ray Photoelectron Spectroscopy, IM Publications, Charlton, UK, (2003), p. 900.

[18] D.A. Shirley, Phys. Rev. B., 5 (1972) 4709.

[19] M.P. Seah, “Quantification in AES and XPS”, in: D. Briggs, J.T. Grant (Eds.) Surface Analysis: by Auger and X-ray Photoelectron Spectroscopy, IM Publications and Surface Spectra Ltd., Charlton, U.K. (2003) p. 345-376.

[20] “Database of Emperically Derivied Atomic Sensitivity Factors”, in: UK Surface Analysis Forum (1998) <http://www.uksaf.org/data/sfactors.html>

[22] G. Binnig, C.F. Quate, C. Gerber, Phys. Rev. Lett., 56 (1986) 930.

[23] S.N. Maganov, M.H. Whangbo, Surface Analysis with STM and AFM, VCH, Weinheim (1994).

[24] K.D. Jandt, Surf. Sci., 491 (2001) 303-332.

[25] D. Rugar, P. Hansma, Physics Today, 43 (1990) 23.

[26] E. Meyer, Prog. Surf. Sci., 41 (1992) 3.

[27] Q. Zhong, D. Inniss, K. Kjoller, *et al.*, Surface Science Letters, 290 (1993) L688-L692.

[28] R. Brown, Philosophical Magazine, 4 (1828) 161.

[29] A. Einstein, Ann. d. Phys., 17 (1905) 549.

[30] B.J. Berne, R. Pecora, Dynamic light scattering: with applications to chemistry, biology, and physics, Dover Publications, (2000).

[31] Dynamic Light Scattering: An Introduction in 30 Minutes, in, Malvern Instruments Ltd., (2011).

[32] A.B. Winterbottom, Transactions of the Faraday Society, 42 (1946) 487-495.

[33] F. Höök, Development of a Novel QCM Technique for Protein Adsorption Studies, Ph.D. Thesis, Chalmers University, (1997).

[34] J. Curie, P. Curie, Comptes rendus de l'Academie des sciences, 91 (1880) 294.

[35] C.K. O'Sullivan, G.C. Guilbault, Biosens. Bioelectron., 14 (1999) 663.

[36] G. Sauerbrey, Z. Physik, 155 (1959) 206-222.

[37] M.V. Voinova, M. Rodahl, M. Jonson, *et al.*, Phys. Scr., 59 (1999) 391-396.

[38] M. Rodahl, F. Höök, C. Fredriksson, *et al.*, Faraday Discuss., 107 (1997) 229-246.

[39] T. Nomura, A. Minemura, Nippon Kagaku Kaishi, (1980) 1621.

[40] K.K. Kanazawa, G. J.G., Anal. Chim. Acta, 175 (1985) 99.

[41] S. Bruckenstein, M. Shay, Electrochim. Acta, 30 (1985) 1295.

[42] F. Höök, J. Vörös, M. Rodahl, *et al.*, Colloid Surface B, 24 (2002) 155-170.

[43] K. Laos, R. Parker, J. Moffat, *et al.*, Carbohydr. Polym., 65 (2006) 235-242.

[44] J. Benesch, J.F. Mano, R.L. Reis, Acta Biomaterialia, 6 (2010) 3499-3505.

[45] M. Malmsten, Biopolymers at Interfaces, in: A.T. Hubbard (Ed.) Surfactant Science Series, Marcel Dekker, Inc., New York (2003), p. 908.

[46] J. Ramsden, Protein Adsorption Kinetics, in: M. Malmsten (Ed.) Biopolymers at Interfaces, Marcel Dekker, New York (2003) p. 199.

[47] C. Calonder, P.R. Van Tassel, Langmuir, 17 (2001) 4392-4395.

[48] M. Rabe, D. Verdes, S. Seeger, Adv. Colloid Interface Sci., 162 (2011) 87-106.

[49] R. Kurrat, J.E. Prenosil, J.J. Ramsden, J. Colloid Interface Sci., 185 (1997) 1-8.

[50] J.J. Ramsden, Phys. Rev. Lett., 71 (1993) 295.

[51] J.J. Ramsden, G.I. Bachmanova, A.I. Archakov, Phys. Rev. E, 50 (1994) 5072.

[52] R. Kurrat, J.J. Ramsden, J.E. Prenosil, J. Chem. Soc., Faraday Trans., 90 (1994) 587-590.

[53] G. Anand, S. Sharma, A.K. Dutta, *et al.*, Langmuir, 26 (2010) 10803-10811.

[54] M.A. Brusatori, Y. Tie, P.R. Van Tassel, Langmuir, 19 (2003) 5089-5097.

[55] P.R. Van Tassel, “Protein Adsorption Kinetics Under an Applied Electric Field”, in: Dekker Encyclopedia of Nanoscience and Nanotechnology, 2nd ed. , Taylor & Francis (2004) pp. 3031-3039.

[56] V.B.C. Figueira, J.P. Jones, J. Colloid Interface Sci., 325 (2008) 107-113.

[57] B. Rezek, E. Ukrainstsev, L. Michalikova, *et al.*, Diamond Relat. Mater., 18 (2009) 918-922.

[58] J. Steinhardt, J. Krijn, J.G. Leidy, Biochemistry, 10 (1971) 4005-4015.

[59] D.C. Carter, J.X. Ho, Advanced Protein Chemistry, 45 (1994) 153-203.

[60] W. Norde, “Driving Forces for Protein Adsorption”, in: M. Malmsten (Ed.) Biopolymers at Interfaces, Marcel Dekker Inc., New York (2003) pp. 21-43.

[61] A. Dolatshahi-Pirouz, K. Rechendorff, M.B. Hovgaard, *et al.*, Colloid Surface B, 66 (2008) 53-59.

[62] A.A. Feiler, A. Sahlholm, T. Sandberg, *et al.*, J. Colloid Interface Sci., 315 (2007) 475-481.

[63] J.I. Anzai, B. Guo, T. Osa, Bioelectrochem. Bioenerg., 40 (1996) 35-40.

[64] P. Roach, D. Farrar, C.C. Perry, J. Am. Chem. Soc., 127 (2005) 8168-8173.

[65] K. Rechendorff, M.B. Hovgaard, M. Foss, *et al.*, Langmuir, 22 (2006) 10885-10888.

[66] W. Norde, Colloid Surface B, 61 (2008) 1-9.

[67] A.J. Bard, L.R. Faulkner, Electrochemical Methods: Fundamentals and Applications, John Wiley and Sons (2001).

[68] C.E.B. Richard G. Compton, Understanding Voltammetry, 2nd ed., Imperial College Press (2011).

[69] R.G. Compton, G.H.W. Sanders, Electrode Potentials, Oxford University Press, Oxford (1996).

[70] A.C. Fisher, Electrode Dynamics, Oxford University Press, Oxford (1996).

[71] C.M.A. Brett, A.M.O. Brett, Electroanalysis, Oxford University Press, Oxford (1998).

[72] C.M.A. Brett, A.M.O. Brett, Electrochemistry; Principles, Methods and Applications, Oxford University Press, Oxford (1993).

[73] M. Volmer, Z. Physik. Chem., 150A (1930) 203.

[74] J.A.V. Butler, Trans. Faraday Soc., 19 (1924) pp. 29 and 734.

[75] Nernst-Planck Equation, in: Wikipedia, April 20, 2012.
<http://en.wikipedia.org/wiki/Nernst-Planck_equation>

3. Protein Adsorption on Nanodiamond Thin Films

3.1 Introduction

Detonation nanodiamond (DND) is a material which is of current interest due to its potential biomedical and electronic applications. There are many attractive features of DND, including a bio-compatible sp^3 core structure, optical transparency, and large surface area. All these properties have been exploited for use in: bio-medical implants, targeted drug delivery, fluorescent cell imaging, and as a platform for cell growth.[1-5] Whilst the use of DND in biological environments is ever increasing, there are few studies which address the fundamental chemistry at the nanodiamond-biological interface. The research described within this chapter aims to address this issue.

3.1.1 Background on Detonation Nanodiamond

Detonation nanodiamond is a carbon-based nanomaterial which is synthesised by the controlled combustion of explosives, followed by cleaning processes, such as acid treatment to remove metal impurities or deaggregation to reduce particle size.[4, 6, 7] The raw material has an inner, diamond core, which is 4 - 5 nm in diameter, and an outer, non-diamond shell.[8] This material tends to form aggregates in solution and has a high-oxygen content. Further processing and modification are required to purify DND, to prevent aggregation and ensure consistent surface chemistry.[4] Purified DND particles consist of perfect sp^3 diamond cores, surrounded by a shell of compressed diamond, which in turn is enveloped in a non-crystalline shell containing a mixture of sp^3 and sp^2 carbon.[9] Typically, the surface chemistry of a DND particle is a complex mixture of oxygen based functional groups, including carboxylic acids, esters and lactones.[4] A number of chemical modifications to this surface have been achieved: fluorination,[10] hydrogenation,[11] and surface termination with alkyl, amino, or amino acid functional groups.[10, 12] Modification of the nanodiamond surface chemistry can promote disaggregation of nano-diamond[11] and change the hydrophobicity of the diamond surface.[13]

The physical and chemical properties of DNDs depend strongly on the size of the nanoparticles.[11] Size control of DND is required to create stable colloidal suspensions of primary particles[8], or ensure specific photoluminescence and reactivity.[14],[15] Deagglomeration helps optimize the size of nanodiamond aggregates, by minimizing the electrostatic forces, covalent bonding and ‘soot structures’ which are known to promote aggregate formation.[8, 15, 16] Also, smaller particle size leads to a higher surface area of these particles (≈ 270 - 280 m^2 g^{-1}).[17] This high surface area has been exploited for the efficient separation and purification of proteins[17], as well as the detection of proteins at low concentrations, during mass spectrometry.

3.1.2 Aims and Overview

Most biological uses of diamond place the material in a solid-liquid interface with aqueous environments. However, the use of nanodiamond particles in biological environments is not supported by a strong understanding of the chemistry at the nanodiamond-aqueous interface. The interactions between DND and proteins are of particular interest, since DND will come into contact with proteins if used in the human body. A better understanding of these interactions is crucial to the safe and effective use of DND in the biological environments. Recently, progress has been made in understanding the nature of the interactions present between proteins and diamonds. Electrochemistry has been used to investigate both protein structure and functionality on diamond[18-23], as well as the bio-fouling properties of diamond.[24-27] Optical techniques, such as fluorescence, infrared, UV-visible, and circular dichroism spectroscopy, provide direct evidence for the preservation of protein structure on diamond.[5, 19, 28-30] Atomic force microscopy has been used to investigate protein layers on H and O terminated CVD diamond films.[31-33] Cytochrome c[18, 23], fetal-bovine serum (FBS)[32], bovine serum albumin (BSA)[5], fibrinogen[30], osteoblasts[33] and anti-CRP monoclonal antibodies[19] have all been recently studied with reference to the diamond-protein interface. There is some consensus within the above studies. First, protein structure (i.e. primary, secondary, etc.) is preserved on diamond compared to other substrates, like gold. Second, diamond surface chemistry seems to affect protein adsorption and behaviour. However, these limited conclusions have been made without direct evidence of either the real-time, *in-situ* adsorption of protein onto the nanodiamond-aqueous interface, or the viscoelastic properties of proteins at this particular diamond interface.

This chapter will advance the understanding of the nanodiamond-biological interface. This will be done by conducting the first real-time, *in situ* study of protein adsorption onto thin films made from nanodiamond particles, by use of the QCM-D technique. The protein used will be BSA, which is part of a family of blood proteins – the serum albumins - which are found in the cardiovascular systems of mammals (see section 2.2.3.2 for further details).[31, 34] BSA adsorption is well-characterized on various surfaces, thus making it an exemplar globular protein to study here. Studies of the BSA-diamond interface will further an understanding of the adsorption dynamics, viscoelastic properties, and protein-surface interactions of globular proteins at the nanodiamond-aqueous interface. Also, many of the conclusions reached in this study could apply to protein adsorption at this interface involving other types of proteins, or protein adsorption on nanodiamond aggregates.

An additional contribution of this work to the use of the QCM-D technique involves the spin-coating of diamond onto quartz crystals. The use of QCM-D requires that α-quartz crystals retain their piezoelectric property. Traditional CVD methods of creating diamond thin films require temperatures of 1000 K [35]; this temperature induces a phase change between α and β-quartz (846 K), which renders a loss of the piezoelectric properties of α – quartz.[36] Solutions to this problem have been proposed, including: low temperature CVD[37], re-flow soldering techniques[39], and the use of other piezoelectric materials which preserve their piezoelectric properties at high temperatures (e.g. Langasite[38] and Gallium Orthophosphate[36, 38]). However, none of these techniques have gained popularity. By spin-coating nanoparticles of diamond onto quartz crystals, a material which could not be studied by QCM-D is able to be studied by this technique. This method should have utility for other inorganic materials which have previously not been considered for QCM-D study.

3.2 Results

3.2.1 Disaggregation and Characterization of the DND Suspensions

The planned QCM-D experiments have several requirements, including the use of thin films (< 100 nm thick), which have controlled surface roughness and surface chemistry (hydrogenated and oxygenated). Commercially available DND (Molecular Biology Grade, ND2, Yorkshire Bioscience) contains large aggregates in aqueous suspension, and thin films made from this material are too rough for QCM-D – and AFM – analysis. Therefore, the disaggregation of DND aggregates became a crucial experimental step towards the formation of nanodiamond thin films. An explanation of the disaggregation of DND suspensions is made here. The explanation of how thin films were synthesized from these suspensions and the physical characterization of those thin films is found in following sections.

Several reported methods exist for disaggregating materials, including: hydrogen annealing[15], ball milling[40], thermal treatment in air[41], stirred media milling with micron-sized beads[42], dry media assisted milling with salt or sugar[40], and bead assisted sonication (BASD).[42] Whilst some of the above treatments were used in attempts to disaggregate DND, only those suspensions treated with BASD and hydrogen annealing were ultimately used to form the DND thin films. In this manner, particle size is controlled, and as a consequence, the surface roughness of DND thin films is controlled (see section 3.2.2).

The BASD technique involves the sonication of nanodiamond suspensions in the presence of micro-sized milling beads, followed by centrifugation to separate large aggregates from small aggregates. The schematic in Figure 3.1 shows the experimental set-up for the BASD technique used in this work. The milling beads which were added to the suspension were made of yttria-stabilized zirconia beads (ZrO_2 (95.0 %) and Y_2O_3 (5.0 %), diameter = 30 μm). Mechanical impact between the beads and the DND aggregates should result in smaller sized nanodiamond aggregates. The power ultrasound (Hielscher, Germany, UP200G, 24 kHz, 200W) had a 1.3 cm glass horn attached and was operated at 30 W cm^{-2} in nanodiamond suspensions with the Zirconia beads.[42, 43] The duration of sonication was varied to control particle size. After sonication, suspensions were centrifuged (3 x 5 minutes at 4000 rpm) in order to remove any remaining large aggregates. Dynamic light scattering (DLS) was used to determine the particle sizes within the deaggregated solutions.

DND particle size in suspension was controlled by varying the duration of sonication. The DLS histograms for this experiment can be found in Figure 3.2(i). DLS histograms from untreated DND suspensions were not able to be obtained, possibly due to the presence of large aggregates in solution. Partial disaggregation, for only 5 minutes, reduces particle size to < 58 nm, which produced thin films at about the maximum thickness allowable for subsequent QCM-D and AFM analysis – final films must be < 100 nm thick and have controlled roughness. Increased sonication time reduces particle size; after 12 hours of sonication, the majority of particles are approximately 4.2 to 26.2 nm in diameter. The use of this particular suspension produces films which are suitable for QCM-D and AFM analysis. Thus, the suspension represented by Figure 3.2i(c) is considered to be the ‘optimized’ DND suspension. These optimized suspensions were stable over a period of several months, as evidenced by the absence of separation, sedimentation, and colour change. A pair of partially disaggregated suspensions can be seen in Figure 3.2(ii). Longer disaggregation times lead to darker suspensions, due to increased light scattering. By contrast, untreated suspensions had sedimented within a few days, producing suspensions with a liquid and solid phase. Full disintegration to primary particles (< 4 nm) was not achieved here using BASD, unlike those suspensions prepared by Oliver Williams, by annealing aggregates of nanodiamond in hydrogen gas.[15]

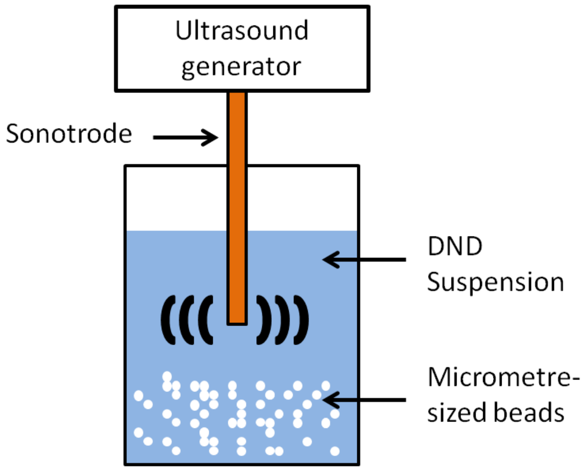

Figure 3.1: Apparatus for bead assisted sonication leading to disintegration of aggregates (BASD).

Some thin films were made from DND suspensions provided by Dr. Oliver Williams. These suspensions were made from DND which had been hydrogen annealed, thus ensuring the formation of mono-disperse colloids in aqueous solution, with primary particle size of 2 - 4 nm.[15] Nanodiamond disaggregated in this manner is hydrogenated, but can be oxygenated by use of oxygen-plasma.[44] Two suspensions were provided with one made by hydrogenated DND particles and the other by oxygenated DND particles. At pH 7.4, the former is shown to have high zeta potential (≈ + 40 mV), whilst the latter has negative zeta potential (≈ - 30 mV).[15] Since the DND particles in these suspensions have well-defined surface chemistry, they will be used to investigate the role of surface chemistry on protein deposition.

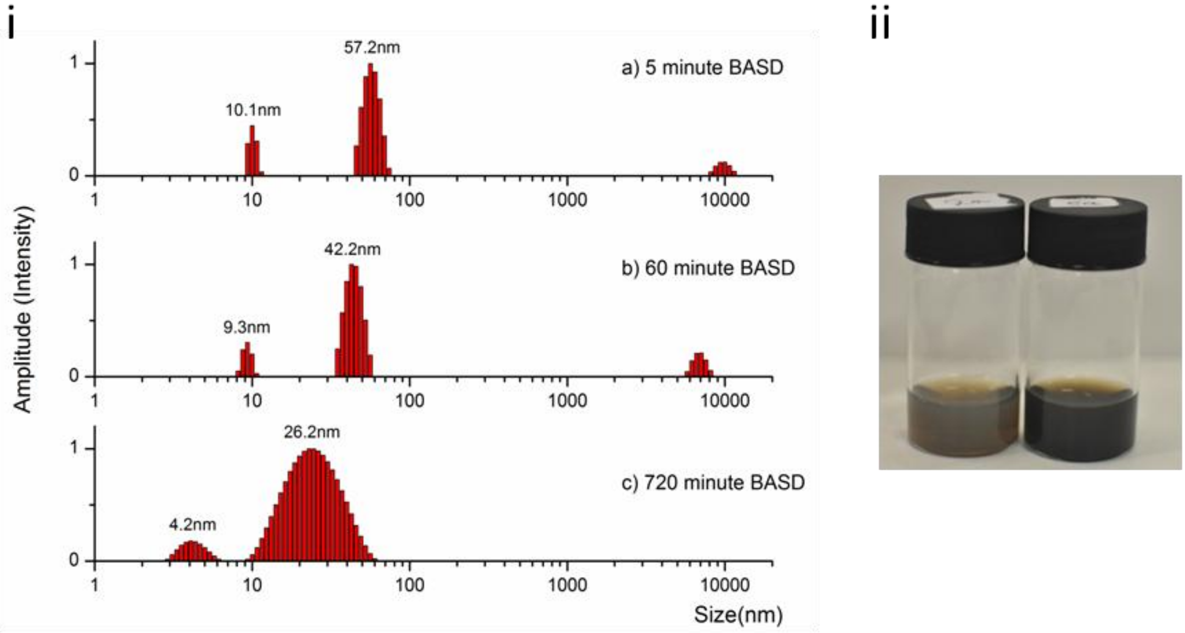

Figure 3.2: (i) Dynamic light scattering histograms showing particle distribution by size for DND suspensions prepared by BASD; (ii) Two partially disaggregated DND suspensions, after using BASD for 5 minutes (left) and 12 hours (right).

3.2.2 Synthesis and Physical Characterization of Nanodiamond Thin Films on Gold

QCM-D crystals are relatively expensive; therefore, complementary experiments not involving these crystals, were conducted on a substrate having a similar surface termination – gold evaporated onto silicon. The aim here is to develop the protocols necessary to ensure successful QCM-D studies using nanodiamond thin films. Surface uniformity, roughness, adhesion, and surface chemistry all need to be well-controlled and characterized. Spin-coating was the final method adopted to make the nanodiamond thin films. Topography was characterized by AFM, whilst surface chemistry was characterized by XPS.

3.2.2.1 Spin-coating

DND suspensions were spin-coated onto gold-terminated silicon wafers. They were prepared by using 1 cm^2 silicon wafers, which were coated with a 5 nm layer of chromium as an adhesion promoter for the subsequent deposition of 50 nm of gold using an Edwards Auto 406 evaporator. These gold-terminated substrates were cleaned in piranha solution (3:1 ratio of H_2SO_4 and H_2O_2 (35 %, aq.); Sigma Aldrich), followed by treatment in oxygen plasma. The resultant gold-terminated surface should be similar to that of a gold-terminated QCM-D crystal. A coating of nanodiamond was placed on the substrate by spin-coating (Laurell Technologies, WS-400-6NPP) droplets of aqueous suspensions of DND (see section 3.2.1) Each droplet (100µL) was spun at 3000 rpm for 1 minute, with 3 to 10 droplets required to make a uniform coating. For QCM-D experiments, the number of drops was optimized at 10 drops (ND_{ox} and ND_{red}) and 3 drops (ND_{crl}), in order to have approximately the same mass of DND on the crystal surface, as the [ND_{crl}] in solution was 1.5 g L^{-1} and the [ND_{red}] and [ND_{ox}] in solution was 0.5 g L^{-1} (n.b. 'ND' terms are defined on pg. 72). The same spin-coating method was later used to place DND thin films onto QCM-D crystals.

3.2.2.2 Protein Adsorption Studied by XPS

Nanodiamond thin films were exposed to BSA (0.08 g L^{-1}) in 100 mL of 0.1 M phosphate buffer (pH 7.4) for 30 minutes at room temperature (20^{o}C). They were then rinsed by exposing the thin film to 100 mL of protein-free buffer to remove any solution-phase protein from the interface. All samples were left to 'dry' in the XPS loading chamber for 1-2 hours. The aim of the above experimental set-up was to mimic QCM-D conditions, although here the thin films were exposed to non-flowing solutions of buffer, since the XPS apparatus is not suitable for flowing conditions.

3.2.2.3 Atomic Force Microscopy

The DND thin films were imaged using atomic force microscopy (AFM), along with a control comprising of a clean, unmodified gold surface. This was done to determine the relative topography of the as-prepared thin films. The AFM methods and apparatus used are described in section 2.1.2.

Thin films prepared by the BASD protocol were compared to those prepared directly from the commercially sourced nanodiamond. AFM images of the two surfaces are shown in Figure 3.3. These images show that BASD is capable of dramatically changing the topography of surfaces, due to its effectiveness at reducing the particle size in suspension. In contrast to commercial nanodiamond, thin films from BASD treated nanodiamond are smoother, have smaller features, lower peaks, and lower valleys than its commercial counterpart. These differences are quantified in Table 3.1, and R_{RMS} for the commercial films is greater than 100 nm. This value of R_{RMS} is higher than the upper limit of 100 nm recommended for thin films on QCM-D crystals.[45] The R_{RMS} for the BASD-treated film is less than 100 nm, and useful QCM-D results are possible if this film is used. It can be concluded that non-disaggregated nanodiamond cannot be used to prepare thin films for QCM-D study.

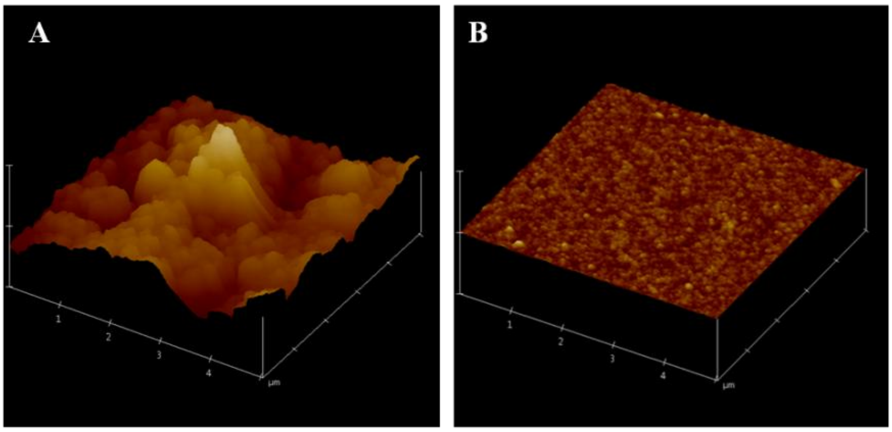

Figure 3.3: AFM images (size: 5 μm^2) of ND thin films spin-coated onto Au, prepared from the following DND suspensions: (A) untreated DND from commercial source (B) BASD treated suspension (12 hour sonication).

Therefore, it was decided that three types of films would be produced using disaggregated nanodiamond. Comparisons between films should highlight the roles of surface chemistry and surface roughness on protein deposition at diamond interfaces. These three thin films are:

- **ND$_{crl}$** : BASD-treated nanodiamond
- **ND$_{ox}$**: Oxygen-terminated thin film, from suspensions made by Oliver Williams
- **ND$_{red}$**: Hydrogen-terminated thin film, from suspensions made by Oliver Williams

An unmodified gold surface was also prepared as a reference sample. AFM images of these films are shown in Figure 3.4, with quantitative results in Table 3.1.

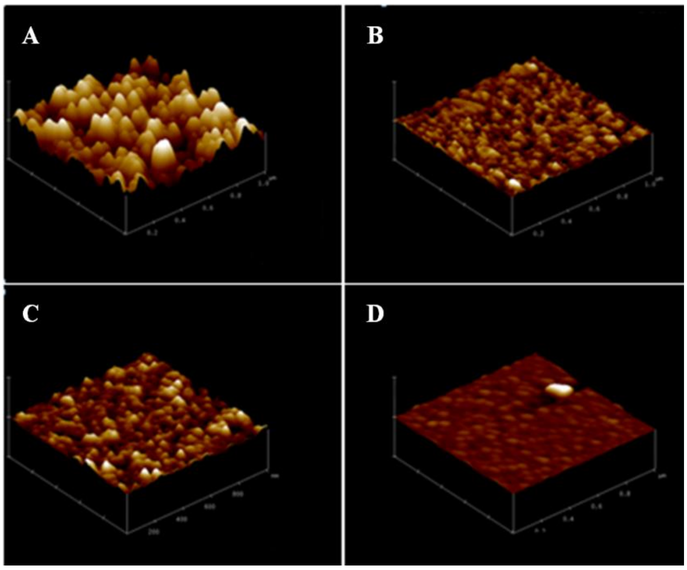

Figure 3.4: AFM images (size: 1μm^2) of the four surfaces to be used in QCM-D experiments: ND$_{crl}$ (A); ND$_{ox}$ (B); ND$_{red}$ (C); Au (D).

	Sample					
Method	**Untreated DND**	**ND$_{crl}$^{a}**	**ND$_{crl}$^{b}**	**ND$_{ox}$**	**ND$_{red}$**	**Au**
R_{RMS} (nm)	271.2	11.6	10.5	2.8	2.2	1.2
R_a (nm)	206.5	9.1	8.5	2.2	1.7	0.8
R_{max} (nm)	203.1	115.8	68.7	22.3	18.5	19.2
Surface Area Difference (%)	98.8	13.0	10.7	2.0	2.0	0.4

Table 3.1: Roughness and surface area measurements of the AFM images seen in Figures 3.3 and 3.4. Notes: ^{a} values associated with the 5 μm^2 image in Figure 3.3; ^{b} values associated with the 1 μm^2 image in Figure 3.4. Error is approximately ± 0.05 nm of reported roughness value. The surface area difference (SAD) is calculated by: $SAD = \frac{A_{rough}-A_{flat}}{A_{flat}} \times 100\%$

Relative to a clean gold surface, nanodiamond coatings increase the surface roughness and surface area. However, the surface roughness of ND_{crl}, ND_{ox}, and ND_{red} is less than 100 nm, thus each is suitable for QCM-D use. Thin films made from BASD-treated nanodiamond are about 5 times rougher than those made from DND provided by Oliver Williams. This indicates that hydrogen annealing remains a superior disaggregation technique to BASD treatment. The topographies of ND_{red} and the ND_{ox} are almost indistinguishable, suggesting that surface roughness is independent of chemical functionality. The size of the nano-rough features on ND_{ox} and ND_{red} are smaller than the size of a typical BSA molecule (8.5 nm x 3 nm x 3 nm)[34], whilst the nano-rough features on ND_{crl} are comparable or larger than these dimensions. The mechanical stability of spin-coated DND thin films was tested by washing the ND_{crl} sample with Millipore water, and then re-imaging the topography with AFM. Results indicate that the ND_{crl} coating was unaffected by such treatment (not shown). From the above, one concludes that, ND_{crl}, ND_{ox}, and ND_{red} are suitable for QCM-D applications, and provide a useful range of samples to enable the role of surface roughness on protein deposition to be determined.

3.2.2.4 X-ray Photoelectron Spectroscopy

X-ray photoelectron spectroscopy was used to characterize the surface chemistry of nanodiamond thin-films and adsorbed proteins, *ex situ*. Whilst providing useful insights, this technique is limited by two factors, both of which change the structure of adsorbed protein layers: first, proteins are studied in their dehydrated form; second, experiments are conducted under UHV conditions, which affects native protein structure. Regardless, XPS has been widely used to characterize BSA on surfaces.[46-48]

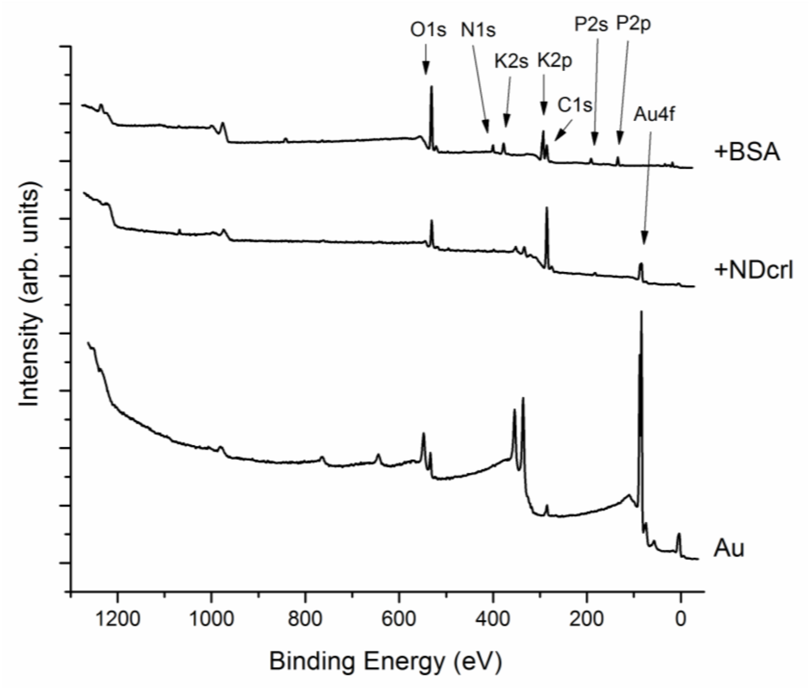

Figure 3.5: Wide scan XPS spectra of representative samples, showing the main photoelectron peaks and the results of sequential surface modification. S2p and S2s signal is present, but with low signal strength. Data is from the XPS of spin-coated ND overlayers (NDcrl) *via* a pre-exposure of the gold surface to phosphate buffer.

Wide-scan XPS spectra for representative samples are shown in Figure 3.5. The following photoelectron peaks were detected: Au $4f_{7/2}$, $Au4f_{5/2}$, C1s, N1s, O1s, S2p, S2s, P2p, P2s, $K2p_{3/2}$, $K2p_{1/2}$ and K2s.[49] The C, N, O, S and P photoelectron signals have organic origins, and the P, K and O-related photoelectron signals are likely to originate from phosphate buffer salts. The attenuation of the Au4f peaks can be observed after the creation of a nanodiamond thin film, and further attenuation is seen after this film is exposed to a phosphate buffer containing BSA. The addition of overlayers of nanodiamond and proteins onto an underlying Au substrate is expected to give such results, and confirms that BSA adsorbs on the interfaces in question.[50]

The C1s region is useful for characterizing the surface chemistry of carbon-based materials. The C1s profiles for ND and BSA films are shown in Figure 3.6, and related data obtained from peak fitting is recorded in Table 3.2 and Table 3.3. The C1s spectra of the ND films were deconvoluted into 5 chemical environments, as has been done for CVD thin films[51]: diamond and adventitious carbon (C-C, 285.0 eV), hydrocarbon (C-H, 285.5 eV), ether (C-O, 286.5 eV), carbonyl (C=O, 287.5 eV), and carboxyl (C(=O)OH, 288.5 eV). The sum of the resultant peak areas is also shown in Figure 3.6, immediately below the spectral data. The spectral lineshape associated with the hydrogenated diamond (see f, Figure 3.6) has reduced intensity at high binding energy. In contrast, for ND_{ox} and ND_{crl} the intensity in this region is higher. This is consistent with the higher oxygen-content expected for ND_{ox} and ND_{crl}, compared to hydrogenated diamond. The surface chemistry of ND_{ox} and ND_{crl} is thus probably similar. However, the ND_{crl} film does not have a carboxyl peak assignment. This suggests that ND_{crl} has more ether-like carbon on its surface. The two oxygenated nanodiamond films may have been treated using two different oxygenation methods, as suggested by known differences in the C1s spectra of wet and dry oxidized CVD diamond films.[52] Wet chemical oxidation leads to more ether character and less carboxyl character, compared to dry oxidation (i.e. O_2 plasma). This difference is subtle, so in this work both ND_{ox} and ND_{crl} are considered to have similar, highly oxygenated surface character. The above is confirmed by the strong O1s signal (not shown) associated with both ND_{crl} and ND_{ox}, along with the inability to resolve the individual O1s peaks into ether and carboxyl components, thus supporting the conclusion of similar surface chemistry for these two samples.

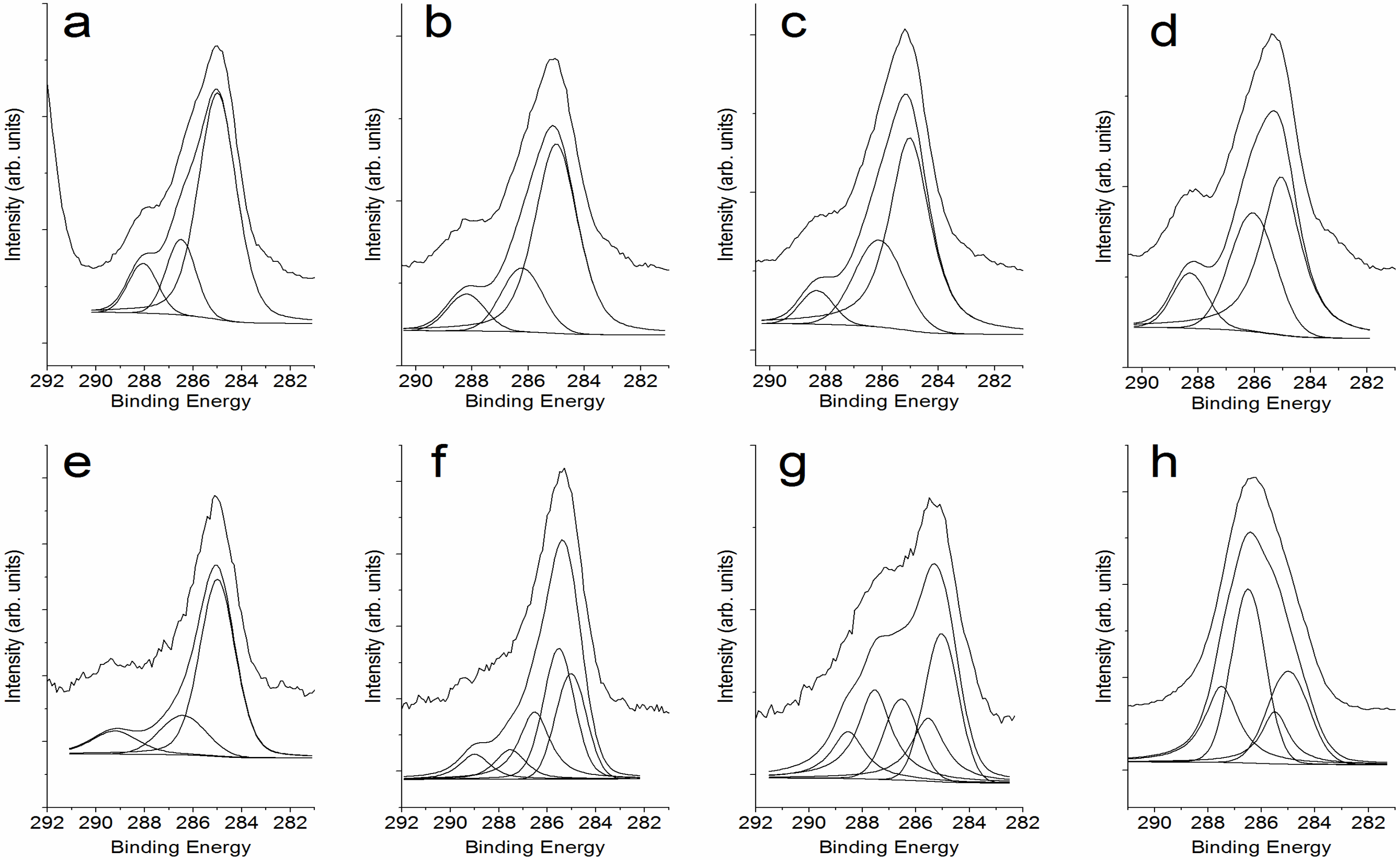

Figure 3.6: XPS data for the C1s regions for the four sample types studied, after exposure to either BSA or DND. The Au C1s spectrum is included as a reference. The labels refer to the following: **(a)** BSA on Au; **(b)** BSA on $\mathrm{ND}_{\mathrm{red}}$; **(c)** BSA on $\mathrm{ND}_{\mathrm{ox}}$; **(d)** BSA on $\mathrm{ND}_{\mathrm{crl}}$; **(e)** Au (Annealed); **(f)** $\mathrm{ND}_{\mathrm{red}}$; **(g)** $\mathrm{ND}_{\mathrm{ox}}$; **(h)** $\mathrm{ND}_{\mathrm{crl}}$. The underlying layers to the one shown were pre-exposed to phosphate buffer, with the exception of **e, f** and **g**. Details regarding peak fitting to spectral data can be found in the text.

	C1s Peak Assignment Composition (%)				
Sample	**adventitious**	**hydrocarbon**	**ether**	**carbonyl**	**carboxyl**
Au	69.3		18		12.7
ND_{red}	25.6	34.4	20.5	7.7	11.3
ND_{ox}	28.2	17.7	16.1	25.1	12.9
ND_{crl}	24.4	13.7	38.2	23.7	

Table 3.2 : Components of C1s fitting, corresponding to Figure 4, e- h. Percent composition of the C1s peak fit, based on five fitted peaks: C-C (285.0 eV); C-H (+ 0.5eV); C-N/C-O (+ 1.5 eV); C=O (+ 2.5 eV); COOH (+ 3.5 eV).

	C1s Peak Assignment Composition (%)		
Sample	**aliphatic**	**α**	**amide**
Au +BSA	72.8	16.4	10.8
ND_{red} +BSA	70.8	19.1	10.1
ND_{ox} +BSA	65.8	27	7.1
ND_{crl} +BSA	54.1	33.2	12.7

Table 3.3: Components of C1s fitting, corresponding to Figure 4 a-d. Percent Composition of the C1s peak fit, based on three fitted peaks: C-C (285.0 eV); C-H/C-N/C-O (+ 1.0 eV); carbonyl/carboxyl (+ 3.2 eV).

The C1s profile can be used to identify the presence of BSA. The C1s profiles for all BSA-containing samples (see a-d, Figure 3.6) are consistent with the literature.[46-48] A three-peak deconvolution scheme was used to resolve the BSA C1s spectra: aliphatic carbon [C-C/C-H, 285.0 eV], α–carbon [e.g. C(=O)-C*-NH_2, 286 - 287 eV], and amide carbon [C(=O)-N, ≈ 288 - 288.5 eV].[46-48] Most of the detected carbon signal is originating from the protein layers, since the C1s signal from underlying layers is mostly attenuated; protein layers are thicker than the escape depth of C1s (≈ 2.2 - 2.7 nm).[49] All C1s spectra for BSA-containing layers show a more resolvable peak at ≈ 288 eV than for spectra associated with the underlying DND substrate. This is indicative of the higher composition of carboxyl and amide functionality expected for a BSA overlayer.[46-48] Additional trends are seen in Table 3.3. For instance, the aliphatic carbon composition decreases and the α-carbon composition increases in the order: Au+BSA, ND_{red}+BSA, ND_{ox}+BSA, ND_{crl}+BSA. This trend may be consistent with a loss of secondary protein structure on hydrophobic surfaces.[53-55] As protein undergoes conformational change and/or unfolds, peptide bonds in the bulk of the protein would become less attenuated, thus increasing the α-carbon signal. Such an observation using XPS has not been made before, and it could relate simply to a change of structure by UHV conditions; however, it is consistent with other findings showing a loss of BSA α-helix structure upon binding to nanodiamond particles, with even greater structural loss on gold.[5] The above suggests that BSA is forming uniform layers at DND interfaces.

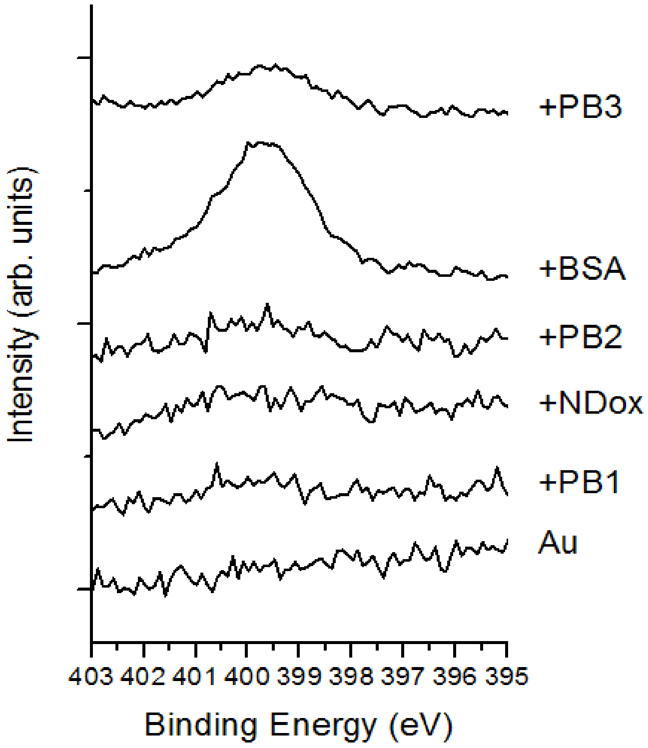

Figure 3.7: N1s spectra of various studied surfaces. This set of data is associated with the spin-coating of oxygenated ND suspension onto gold, with intermediate exposures of phosphate buffer (+PB1, +PB2), exposure to BSA-buffer solution, and finally a rinse with clean phosphate buffer (+PB3).

Nitrogen is a common element observed in XPS of protein layers, but it is rare to observe it by XPS on diamond surfaces. Therefore, the N1s photoelectron signal can be used to determine the presence of protein layers at diamond surfaces. As shown in Figure 3.7, N1s signal is only present on those samples which have been exposed to BSA-containing buffer.

After rinsing, substantial N1s signal remains. There is negligible N1s signal for all non-BSA containing samples. The binding energy of the N1s peaks for various samples is shown in Table 3.4, and these values are consistent with amide groups in the protein.[49] These observations are consistent with the formation of stable protein layers, with some protein irreversibly bound to the surface.

	N1s Binding Energies (eV)	
Sample	+BSA	+PB3
Au	400.1	401.5
$\mathrm{ND_{red}}$	400.4	400.4
$\mathrm{ND_{ox}}$	399.7	399.5
$\mathrm{ND_{crl}}$	400.3	399.5

Table 3.4: The N1s binding energies for Au and DND thin films having BSA overlayers before (+BSA), and after (+PB3), rinsing with phosphate buffer.

A convenient method to compare the XPS signals of adsorbed proteins is to evaluate the XPS elemental ratios, which are shown in Table 3.5. The ratios which are typically analyzed include the O1s/C1s, N1s/C1s, and S2p/C1s ratios, since all those elements are present within adsorbed protein layers. Here, the O1s/C1s ratio cannot be used with confidence, as it is higher than expected (i.e. >> 0.3, assuming typical protein composition: 65 % C, 15 % N and 20 % O). Most likely, this extra O1s signal originates from deposited phosphate salts from the buffer solution. From the nitrogen and sulphur signals, elemental ratios can be made in which the intensity of both is compared to the total C1s intensity (i.e. $C_{total} = C_1+C_2+C_3$, in which C1s photoelectron signal from aliphatic and adventitious carbon (1), α-carbon (2) and amide carbon (3) are considered). The N1s/(C_2+C_3) and S2p/(C_2+C_3) ratios do not take into account the adventitious carbon contamination. [47] These values can be compared to theoretical ratios calculated from the amino acid distribution in BSA.[47, 57] There is good agreement between the experimental and theoretical ratios for BSA on oxygenated diamond samples, regardless of surface roughness. This is not true for BSA layers on hydrogenated diamond or gold. This is not surprising, considering that hydrogenated diamond is known to affect the helical structure of BSA.[5] Differences in the intensity of the S2p signal may be affected by protein orientation, but orientation cannot be determined from this data, alone.[58] These observations indicate that protein is adsorbed onto all the nanodiamond surfaces, but that the nature of that adsorption differs on oxygenated and hydrogenated nanodiamond.

	Elemental Ratios			
Sample	**N1s/C1s**	**N1s/(C_2 +C_3)**	**S2p/C1s**	**S2p/(C_2 +C_3)**
Au +BSA	0.16	0.60	0.008	0.030
ND_{red} +BSA	0.17	0.59	0.004	0.015
ND_{ox} +BSA	0.16	0.48	0.008	0.024
ND_{crl} +BSA	0.22	0.48	0.014	0.031
Theoretical	0.26	0.49	0.013	0.025

Table 3.5 : Elemental Ratios for studied samples with BSA overlayers. The theoretical BSA values reported are from Ithurbide *et al.*[47] and Iucci *et al.*.[48]

The addition of diamond thin films to a gold substrate, followed by BSA adsorption should lead to a sequential increase in overlayer thickness. Attenuated Au peaks could be seen for the DND coated samples suggesting that some regions of the nanodiamond films were quite thin, which became more strongly attenuated after exposure to BSA. This enables a rough calculation of the quantity of BSA adsorbed in this region. Overlayer thickness can be determined using XPS, by employing the following expression[58-60]:

$$I_S = I_0 e^{-t/\lambda} \qquad \text{(Equation 3.1)}$$

where I_S is the peak intensity of the overlayer signal, I_0 is the peak intensity of the $Au4f_{7/2}$ signal of an unmodified gold film, t is the overlayer thickness, and λ is the attenuation length of a $Au4f_{7/2}$ photoelectron. For excitation by Al Kα radiation, the attenuation length of a gold $4f_{7/2}$ photoelectron through diamond is about 2.2 nm[61], whilst through organic overlayers is estimated to be 3.3 nm.[62] The thickness of both the Au and BSA layers was calculated using this method and data for BSA before and after rinsing BSA-free buffer shown in Table 3.6. The error in these XPS thicknesses is about ± 2 nm. For comparison, QCM-D thicknesses calculated using a 1-layer Voight model, as discussed later in section 3.2.3, is shown in the same table. The thickness of the as-prepared diamond thin films on gold substrates was found to be ≤ 20 nm (not shown). This is both consistent with AFM results (see Table 3.1) and less than the thickness recommended for QCM-D analysis.

The calculated experimental thickness of BSA on diamond surfaces are roughly on the same order of magnitude as the dimensions of BSA (8.5 nm x 3 nm x 3 nm, see section 2.2.3.2), suggesting that, approximately, a monolayer of protein adsorbs on the surfaces in question. The results indicate that BSA layers are thicker on oxygenated diamond, than hydrogenated diamond. In addition, BSA layers on hydrogenated diamond have similar thickness to that of BSA layers on gold surfaces. Also, BSA layers resist rinsing on nanodiamond surfaces, suggesting that some BSA is irreversibly bound to nanodiamond. These results suggest that the BSA layers on the as-prepared diamond thin films are both present and stable, particularly on oxygenated diamond. The results are not in very good quantitative agreement with the QCM-D data (see section 3.2.3), although the same qualitative trends are seen.

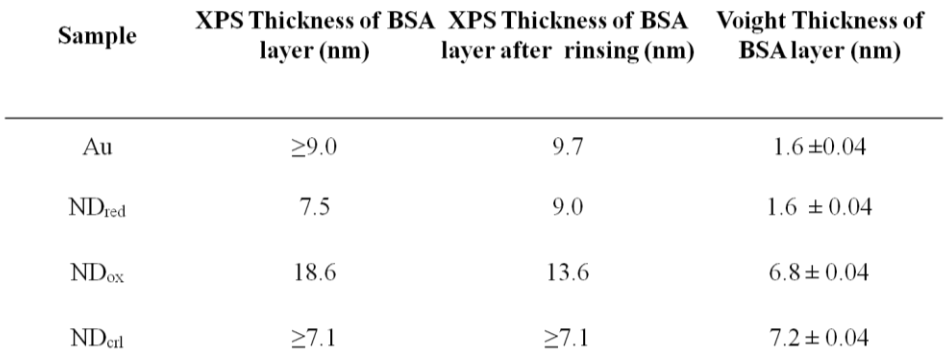

Sample	XPS Thickness of BSA layer (nm)	XPS Thickness of BSA layer after rinsing (nm)	Voight Thickness of BSA layer (nm)
Au	≥9.0	9.7	1.6 ±0.04
$\mathrm{ND_{red}}$	7.5	9.0	1.6 ± 0.04
$\mathrm{ND_{ox}}$	18.6	13.6	6.8 ± 0.04
$\mathrm{ND_{crl}}$	≥7.1	≥7.1	7.2 ± 0.04

Table 3.6: Thickness results obtained using XPS and QCM-D techniques. XPS thickness values are relative to the underlying ND surface, not the underlying Au substrate.

An estimate of the mass density of protein at the surface can be determined from the XPS and QCM-D thickness values, by assuming the following: uniform coverage of protein on a 1 cm^2 substrate, BSA molecular volume of 88.25 nm^3, and mass of BSA of 66.4 kD (see section 2.2.3.2). This generates a range of values from 200 - 2300 ng cm^{-2}. This is reasonably consistent with the theoretical range for hydrated BSA layers of 390 – 910 ng cm^{-2} [34], and mass densities determined directly from QCM-D experimentation (see Table 3.7).

3.2.3 QCM-D Characterization of BSA on Nanodiamond Thin Films

The work presented above characterizes the properties of the nanodiamond layers, and suggests that proteins from solution adsorb at these interfaces. QCM-D is an ideal method for probing the time-resolved kinetics of protein adsorption, in addition to determining the viscoelastic properties of deposited layers. It also has the advantage of being an *in situ* probe of protein dynamics. Here, it is used to probe the adsorption dynamics of BSA onto gold and the as-prepared DND thin films.

A typical QCM-D trace showing the deposition of BSA onto clean gold is shown in Figure 3.8. Before protein deposition, a reasonably stable dissipation (D) and frequency (f) trace is required in 0.1 M phosphate buffer at pH 7.4, and this is seen in the trace. Protein deposition begins when the crystal is exposed to 0.08 g L^{-1} BSA in this buffer solution, under controlled flow conditions. The QCM-D records the non-linear change in D and f after exposure to the buffer. The values of D and f stabilize at equilibrium. Upon rinsing, there is only a slight decrease in mass in all cases, which indicates that BSA binds irreversibly to gold and DND surfaces, under these conditions.

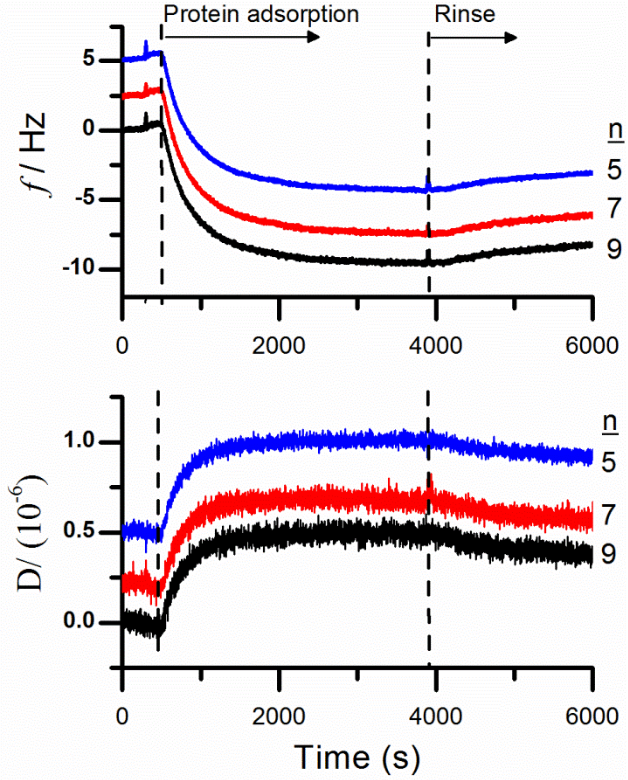

Figure 3.8: Representative QCM-D trace for experiments described in this chapter. These are frequency (top) and dissipation (bottom) *versus* time traces for BSA adsorption on Au-terminated crystals. The colours represent different overtones: blue is f_5 , red f_7 (middle) and black f_9 (bottom). The start of protein adsorption and the start of the rinse steps are shown as dotted lines.

The D and f traces for three different overtones (n = 5, 7, 9) are shown in Figure 3.8, and it is clear that these traces are nearly superimposed on one another. This is characteristic of deposited layers with low dissipation and low $\Delta D/\Delta f$ ratios. This suggests that the protein layers are rigid enough for the Sauerbrey equation (Equation 2.10) to be used as an approximation of mass density. Normally, the Sauerbrey equation is not used, since it underestimates the mass of soft, viscoelastic layers; use of the Voight model is necessary to obtain a more accurate mass density (see section 2.2.1). However, the fact that Sauerbrey mass could be a valid approximation of protein mass density is exploited throughout this section, but particularly when conducting the analysis of adsorption kinetics.

3.2.3.1 Sauerbrey and Voight Masses

The BSA adsorption mass densities at saturation were calculated from several overtones (n = 5, 7, 9) using either the Sauerbrey model or the Voight model. The Sauerbrey and Voight mass density ($m_{Sauerbrey}$ and m_{Voight}) at saturation is an average of the last 300 points in the adsorption run, and they are shown in Table 3.7. Equation 2.10 was used to calculate $m_{Sauerbrey}$, whilst the 1-layer Voight model was used to determine m_{Voight}. The methodology, including modelling parameters, is described in section 2.2.2. Technically, a 2-layer model should be used to determine m_{Voight}, since there are two layers above the crystal: a nanodiamond thin film and a layer of BSA. However, the 1-layer Voight model was used to analyse the QCM-D results, using the reasonable assumption that a nanodiamond thin film can be treated as a completely rigid layer. The duration of the Voight modelling is shown in Table 3.7, and this is the total time of the BSA adsorption which was modelled.

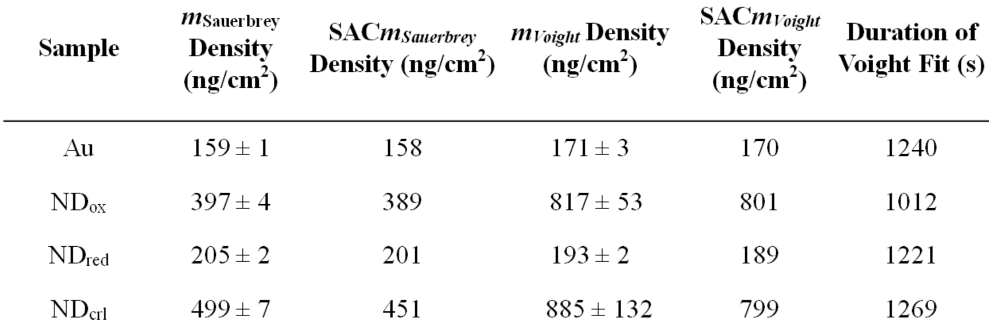

Sample	$m_{\text{Sauerbrey}}$ Density (ng/cm^2)	SAC$m_{Sauerbrey}$ Density (ng/cm^2)	m_{Voight} Density (ng/cm^2)	SACm_{Voight} Density (ng/cm^2)	Duration of Voight Fit (s)
Au	159 ± 1	158	171 ± 3	170	1240
ND_{ox}	397 ± 4	389	817 ± 53	801	1012
ND_{red}	205 ± 2	201	193 ± 2	189	1221
ND_{ctrl}	499 ± 7	451	885 ± 132	799	1269

Table 3.7: Mass densities calculated from QCM-D, using the average of the last 300 points of the adsorption run. The average of several overtones (n = 5, 7, 9) were used.

Mass densities can be corrected for differences in surface area across samples arising from roughness. This is done by normalizing mass densities by the surface area difference (SAD) reported in Table 3.1. This second type of mass density is referred to as ‘surface area corrected mass’ (SACm) and is calculated as follows:

$$SACm = \frac{m}{1+\frac{\text{SAD}}{100}} \qquad \text{(Equation 3.2)}$$

where m is either $m_{Sauerbrey}$ or m_{Voight}. Comparing SACm values, enables one to determine if surface roughness contributes to increased mass density, beyond the simple increase related to increased surface area.

With the above in mind, an analysis of the mass densities determined by QCM-D can be made. Immediately, one can see that m_{Voight} is significantly larger than $m_{Sauerbrey}$ for two of the samples, which may reflect the fact that m_{Voight} includes the mass of adsorbed protein and surrounding solvent. The inclusion of hydration within m_{Voight} does complicate its interpretation, as one does not know the individual contributions of protein or solvent mass to m_{Voight}. The mass densities for all the studied systems are consistent with the expected range of values for *hydrated* BSA on surfaces (390 – 910 ng cm^{-2}) or *dry* mass of BSA (80 - 200 ng cm^{-2}). [34, 63]

It is curious that the trends within the $m_{Sauerbrey},$ and m_{Voight} values do not conform to a simple interpretation of BSA-diamond interactions. First, consider the following factors: BSA has a net negative charge at pH 7.4[65]; ND_{red} and ND_{ox} particles are positively charged and negatively charged, respectively, at pH 7.4 (see section 3.2.1)[66]; hydrogenated and oxygenated diamond are considered to be hydrophobic and hydrophilic, respectively.[13] Second, consider that protein adsorption at a surface is most influenced by: hydrophobic interactions, hydrogen bonding, electrostatic interactions, and protein arrangements (i.e. conformation, orientation, etc.). Based on the above, one would expect that BSA has a higher affinity for hydrogenated diamond due to greater hydrophobic attraction and less electrostatic repulsion, compared to the BSA-oxygenated nanodiamond interface. Yet, the opposite trend is seen here, with substantial adsorption on oxygenated diamond, of equal surface roughness. Similar anomalous behaviour has been noted previously and various reasons can be put forward to explain these results.[55] One is that protein charge, as well as hydrophobic and hydrophilic functionality, is inhomogeneous on the outside of the protein.[53] This enables BSA to have interactions with a wide variety of interfaces *via* any orientational and conformational changes required to maximize favourable protein-surface interactions.[53] A second reason may be that much of the electrostatic, protein-surface interactions are screened by the high ionic content of the buffer. Thirdly, hydrogen bonding between BSA and oxygenated nanodiamond may exist. Yoon *et al.* [67] have shown that for surfaces containing a large number of carboxyl groups, such as carboxylated microspheres, hydrogen bonding is the main protein-surface interaction. An important conclusion is the fact that BSA adsorption does occurs on several different types of diamond surfaces.

The extent of protein adsorption may be determined by surface chemistry and/or surface roughness. Both properties are known to affect protein adsorption. Studies using self-assembled monolayers have shown the influence of surface chemistry on protein adsorption in detail.[68] The influence of surface roughness is less understood, but evidence does exist that it could increase protein adsorption by increasing the available surface area[69,70], or by affecting protein structure during adsorption.[69] The influence of surface chemistry or surface roughness on BSA deposition on nanodiamond, can be determined here.

Two surfaces with similar oxygen-based functionality, but different surface roughness, adsorb similar amounts of BSA. The results in Table 3.7 show near identical $\mathrm{SAC}m_{\mathrm{Voight}}$ for $\mathrm{ND}_{\mathrm{crl}}$ and $\mathrm{ND}_{\mathrm{ox}}$. This result suggests that surface roughness has no influence on saturation mass. However, there remains the possibility that surface roughness does have an influence. The $\mathrm{SAC}m_{\mathrm{Sauerbrey}}$ is 16 % higher for $\mathrm{ND}_{\mathrm{crl}}$, than $\mathrm{ND}_{\mathrm{ox}}$. This result cannot be dismissed, as it has been seen before when Sauerbrey mass is used to estimate the influence of roughness.[69] It be due to several factors[69]: (i) surface area may be underestimated due to the finite radius of the AFM tip; (ii) solvent trapped within a rough surface may be well-coupled to the QCM-D crystal, thus increasing mass density; (iii) a more dense protein layer may exist on $\mathrm{ND}_{\mathrm{crl}}$, induced by surface roughness; (iv) factors ii and iii can be combined, since conformational change induced by roughness could cause hydration changes at the surface. The first factor is not likely to cause the 16 % difference in $\mathrm{SAC}m_{\mathrm{Sauerbrey}}$.[69]

Further insight is required to identify the contributions of events ii, iii, and iv. It is interesting to note that Sauerbrey masses do not include the mass of non-coupled solvent. Therefore, it is possible that surface roughness has an effect within the immediate diamond-protein interface, where the protein and the surface would be well-coupled. Whereas, the similar SACm_{Voight} values seen for $\mathrm{ND_{crl}}$ and $\mathrm{ND_{ox}}$ suggest that surface roughness does not influence events within the non-coupled portion of the protein overlayer. This inability to isolate the role of surface roughness based on mass data is reflected in the literature, and contributes to the general controversy around this issue. The SACm_{Voight} comparison made here is consistent with studies showing that globular protein adsorption is unaffected by surface roughness on rough tantalum and titanium surfaces.[70,71] However, the SAC$m_{\mathrm{Sauerbrey}}$ comparison is consistent with a recent QCM-D study showing that surface roughness has an effect on BSA adsorption dynamics and structure at non-saturation conditions.[69] It is clear that the choice of model is important in initially identifying any influence of surface roughness on protein adsorption. More detailed QCM-D analysis is clearly necessary to isolate the role of roughness, if any (see next section).

Two surfaces of similar roughness, but different surface functionality ($\mathrm{ND_{red}}$ and $\mathrm{ND_{ox}}$) have vastly different saturation mass, regardless of the model used. These results suggest that surface chemistry influences saturation mass and protein layer structure. If m_{Voight} is assumed to be the *hydrated* mass density of the protein layers, then a flat monolayer of *hydrated* BSA should have m_{Voight} of 390 ng cm^{-2} and a vertical monolayer should have m_{Voight} between 800 - 910 ng cm^{-2}, depending on protein density.[34] From this, one could suggest that at hydrogenated surfaces BSA is in a flat orientation and has less-than-monolayer coverage; on oxygenated diamond BSA forms monolayers of vertically oriented BSA, or multilayers of BSA in a flat orientation. The exact nature of the protein layer will emerge in detailed analysis of the viscoelastic properties of the protein layers. At this point, it should be clear that the surface chemistry of diamond is likely influencing the adsorption mass and structure of the protein layer.

3.2.3.2 Dissipation versus Frequency Plots (ΔD vs. Δ*f* Plots)

QCM-D is a powerful technique for probing protein conformational changes at interfaces and for probing the physical nature of protein layers. The viscoelastic and kinetic data provided by this technique provide more insight into protein dynamics than the use of mass data, alone.

The viscoelastic properties of protein layers can be examined by plotting change of dissipation as a function of frequency change to create the so called, 'ΔD vs. Δ*f* plots'. These plots, shown in Figure 3.9, have several characteristic qualities which must be explained here. By eliminating time as an explicit variable, the *ΔD vs. Δf* plots directly probe the relationship between dissipation and added mass, and thus are a record of viscoelastic changes in the protein layers. The magnitude of dissipation may be affected by three factors: protein structure, surface hydration, and layer thickness. 'Loose' protein layers, high hydration, and thick layers contribute to higher dissipation and *vice versa*. The interplay of these three factors, during protein adsorption at a surface, leads to a series of linear regions in the *ΔD vs. Δf* plots, with each representing a protein configuration having different viscoelastic properties.[53,72] These different viscoelastic regimes can therefore be associated with the different phases of protein adsorption.[53,72] These adsorption phases are indicated by the changing gradients, and can also be linked to kinetic regimes, as indicated by the spacing of data points. Larger spacing is associated with faster kinetics (i.e. during initial binding) and smaller spacing is associated with slower kinetics (i.e. at saturation).

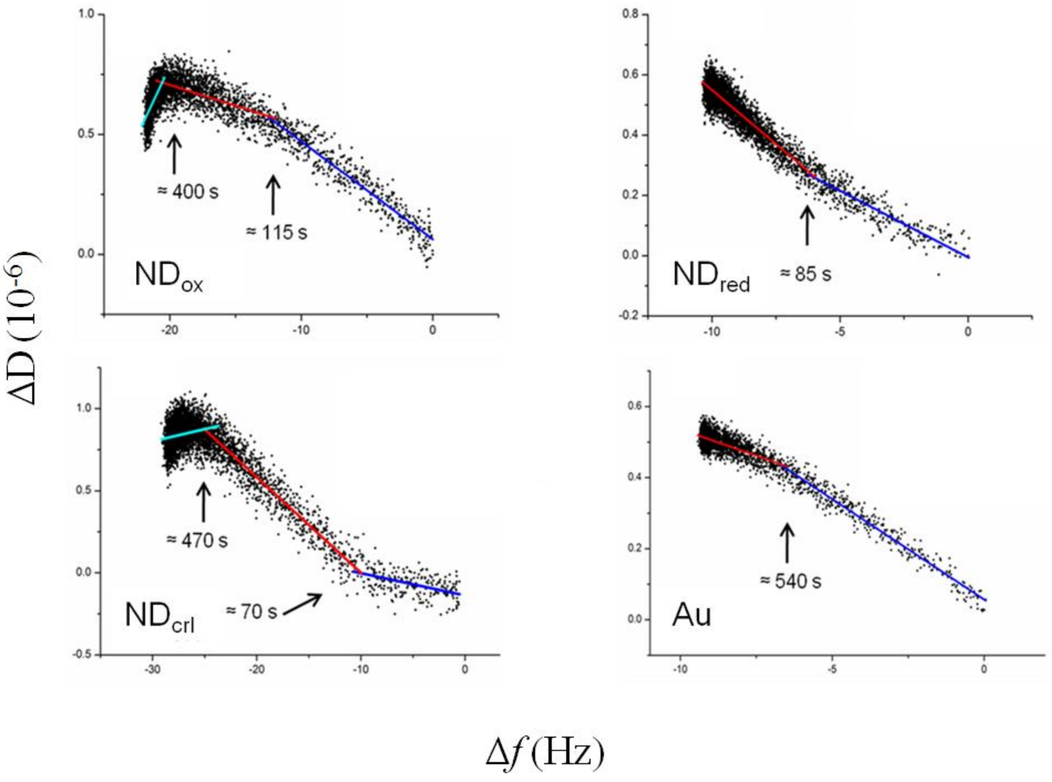

Figure 3.9: ΔD vs. Δ*f* plots for BSA deposition on ND and gold surfaces, using the data of the 9th overtone. Gradients for stage 1 (blue), stage 2 (red), and stage 3 (light blue) are shown.

Considering the previous paragraph, one can label the phases seen in Figure 3.9 as:

(1) *initial binding* – as shown by the initial linear segment

(2) *further adsorption to equilibrium* – as shown by the second linear segment (includes adsorption, rearrangement, conformational change)

(3) *saturation structural rearrangements* – as shown by the third segment (seen at ND_{crl} and ND_{ox} interfaces)

When discussing the viscoelastic properties, the sign of the gradient and the magnitude of the *ΔD/Δf* ratio are invoked. Positive and negative values indicate the presence of more rigid or looser protein layers, respectively.[69] In addition, similar values in two or more viscoelastic regimes indicate that overlayer structure is similar.[69] The gradients within the *ΔD vs. Δf* plots are quantified in Table 3.8, along with the ΔD/Δ*f* ratios at saturation. With the above in mind, the *ΔD vs. Δf* plots can be analyzed.

	Gradient			R^2			Endpoint $\Delta D/\Delta f$
Sample	**1**	**2**	**3**	**1**	**2**	**3**	
Au	-0.056	-0.031		0.95	0.55		-0.06
Ndred	-0.044	-0.072		0.99	0.8		-0.06
Ndox	-0.041	-0.017	0.117	0.91	0.38	0.32	-0.02
NDcrl	-0.018	-0.057	0.03	0.33	0.89	0.11	-0.03

Table 3.8: Gradient slopes of ΔD vs. Δf plots, along with R^2 values of the linear regression fit. The endpoint $\Delta D/\Delta f$ ratio is also shown. All linear regressions were done using the data presented in Figure 3.9. The stage numbers (1, 2, 3) refer to the gradients indicated in that figure.

BSA layers were adsorbed onto gold, in order to confirm the validity of the experimental protocol used here. The BSA-gold interface is well-characterized by QCM-D and other techniques, and the viscoelastic results shown here are consistent with those studies.[34, 73, 74] The behaviour of BSA on gold serves as a benchmark for evaluating the process of BSA adsorption onto the diamond thin films. Initial binding on gold is quite hydrated and loose, as indicated by a negative initial gradient. This initial phase is 5 - 6 times longer than on diamond, after which BSA layers transition to a second viscoelastic phase, leading to saturation. This second regime has a less negative slope, indicating that the protein layers are becoming more rigid during this phase. The magnitude of the final $\Delta D/\Delta f$ ratio is consistent with loose and hydrated BSA layers.

At hydrogenated diamond, BSA also adsorbs in a two phase process. The initial phase is quick, with a moderately negative slope. This indicates that initial binding is faster and BSA is in a more rigid conformation than at a gold interface. Subsequent adsorption is accompanied by increasingly negative gradient, indicating that protein layers are becoming thicker, looser, and/or more hydrated. At saturation, BSA layers on hydrogenated diamond have the same $\Delta D/\Delta f$ ratio as on gold. Therefore, the BSA layers on both of these substrates can be considered to form similar structures at saturation, comprising of looser formations of BSA than those BSA layers at oxygenated diamond interfaces, which have lower $\Delta D/\Delta f$

ratios. Despite the similar outcome, it is clear that the process by which BSA forms a final layer of protein on gold and hydrogenated diamond is different, as will be discussed later in this chapter.

The effect of surface chemistry on the viscoelastic behaviour can be determined by comparing two diamond surfaces of similar roughness, but different functionality (i.e. ND_{ox} and ND_{red}). The number of adsorption stages is different, with two and three stage adsorption associated with hydrogenated and oxygenated diamond respectively. This is likely the result of the formation of thicker protein layers on oxygenated diamond, during the time frame of the experiment.[31] Surface chemistry does not affect either the gradient associated with initial binding of BSA or the time taken for the transition from initial adsorption to subsequent adsorption. These results suggest that surface chemistry does not affect protein structure upon first contact with the surface. However, it does affect subsequent adsorption, as less negative and more negative gradients are seen for oxygenated and hydrogenated diamond, respectively. On oxygenated diamond, the less negative gradients are likely linked to the high mass density and more rigid packing of proteins.[72] By contrast, the mass density of BSA on hydrogenated diamond is lower; looser protein layers are probably formed, accompanied by viscosity and hydration changes associated with conformational change of BSA on a hydrophobic surface.[31, 32, 53] Spontaneous adsorption is driven by the release of free energy by increasing numbers of protein-surface interactions and by the entropy gain as surface, and protein, hydration is removed from the interfacial region. [31, 32, 53] Surface chemistry also affects the saturation structure of the BSA layers. The $\Delta D/\Delta f$ ratio associated with BSA layers on hydrogenated diamond is more negative than those on oxygenated diamond. In addition, BSA layers on oxygenated undergo an adsorption phase not seen at hydrogenated diamond – a move to positive gradient nearer to saturation, with little added mass. These two observations show that BSA is forming more rigid protein layers at saturation on oxygenated diamond. From this, one concludes that surface chemistry affects the dynamics of protein adsorption and the structure of the BSA layer at saturation.

The role of surface roughness can be ascertained by analyzing the ΔD vs. Δf plots associated with BSA adsorption on smooth and rough diamond, having same, or similar, surface chemistry (ND_{crl} and ND_{ox}). Surface roughness is independent of saturation layer structure, since both layers have the same $\Delta D/\Delta f$ ratio at saturation. However, the behaviour of BSA on rough diamond during initial binding is quite different. Initial binding on ND_{crl} has low gradient and low dissipation. This result is likely related to proteins entering the ‘valleys’ within the nano-rough surfaces. Low dissipation, as a result of this process, would be related to the lower surface hydration as buffer is dissipated, as well as the reduced ability for BSA to undergo conformational change by steric factors and/or an increased number of protein-surface interactions. Proteins arriving later would not ‘see’ a rough surface, but a surface of relatively intact proteins.[55] As a consequence, only initial adsorption is affected by surface roughness, with subsequent adsorption governed mainly by protein-protein interactions. This is not an unreasonable interpretation, as it has been shown in Table 3.1 that the topography of ND_{crl} can accommodate BSA molecules, whereas the topography of ND_{ox} cannot. Moreover, proteins have been shown to be trapped within nano-rough platinum surfaces and nano-textured diamond thin films by others.[23,69]

3.2.3.3 Additional Notes Regarding the ΔD *versus* Δ*f* plots

A note must be made about the affect of surface chemistry on protein orientation. Earlier, it was hypothesized that BSA forms vertical monolayers on oxygenated diamond and flat monolayers at hydrogenated diamond and gold. This can be further confirmed from the ΔD vs. Δf plots. The time points associated with the gradient changes in Figure 3.9 can be associated with Δf, and by extension a certain $m_{\text{Sauerbrey}}$. These mass densities can be compared to theoretical values for various types of monolayers, which are shown in Table

3.9. At the first gradient change, $m_{\mathrm{Sauerbrey}}$ for $\mathrm{ND_{red}}$ and gold is similar to those associated with flat monolayers of BSA, whilst for $\mathrm{ND_{ox}}$ and $\mathrm{ND_{crl}}$ the mass is lower and are thus associated with vertical monolayers of BSA. Therefore, one concludes that BSA is initially depositing with flat and vertical monolayers for each pair of substrates, respectively. At the second gradient change, seen only for oxygenated diamond, $m_{\mathrm{Sauerbrey}}$ has the mass associated with a triangular closed packed arrangement of 'heart-shaped' BSA. Similar trends can be observed if one conducts this comparison using value of m_{Voight}. This assignment is consistent with the mass density and viscoelastic behaviours described earlier.

	Theoretical Mass Density (ng cm^{-2})			
Orientation	**CP max.**	**RSA max.**	**Hydrated**	**Theoretical Thickness (nm)**
Flat	226	129	390	3
Vertical	155	84	800	6.9
Triangular Closed Packed	310		910	6.9

Table 3.9: Theoretical mass density and thickness values for different types of BSA layers. Values are obtained from Hook *et al.* and Figueira *et al.*. [34,63]

3.2.4 Adsorption Kinetics

The viscoelastic dynamics of BSA at diamond surfaces did suggest that the kinetics of protein adsorption were different at each of the diamond surfaces. However, a detailed analysis of kinetics is required to confirm conclusions from previous sections and to further probe the nature of the protein-surface interactions seen in this study. Information about the kinetics of adsorption can be determined from plots of protein adsorption rate as a function of mass density. Such plots are referred to as 'd*m*/dt plots', and have been used previously [75, 76, 77] ; the d*m*/dt plots associated with this study are shown in Figure 3.10.

The dm/dt plots confirm the existence of the transport-limited, reaction-limited and asymptotic regimes for BSA deposition onto gold and DND. The lineshapes are consistent with other results.[76, 78, 79] The demarcation of all three regimes is most clear in the case of BSA deposition on a hydrogenated diamond surface. All lineshapes are concave, thus justifying the assumption that RSA kinetics are occurring.[75,80] However, one must note that this concave lineshape is most prominent for BSA adsorption on hydrogenated diamond, but less so on oxygenated diamond or gold. BSA deposition on these latter substrates is likely more Langmuir-like, as adsorption rate is more proportional to mass during the reaction-regime.

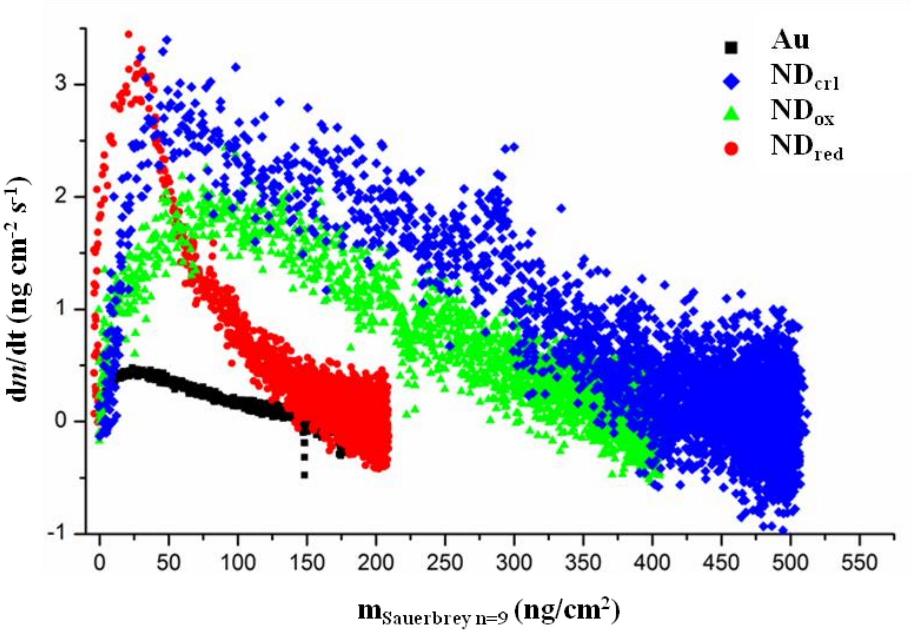

Figure 3.10: The dm/dt vs. m plots associated with BSA deposition. The Sauerbrey mass density data from the 9th overtone is shown. The y-axis data of these plots have been smoothed with the 50 point, adjacent-averaging.

3.2.4.1 Initial Adsorption Rates

The period of initial adsorption is said to be important for understanding protein dynamics.[75] A simple analysis of the kinetics of the early stages of BSA adsorption kinetics can be made by calculating the ‘initial’ adsorption rates from the QCM-D data. The initial rate is the average of the first 10 seconds of rate data seen in the transport-limited regime of Figure 3.10. The results of both calculations are shown in Table 3.10.

It is clear that surface chemistry affects the initial adsorption rate. Hydrogenated diamond has a higher rate of initial adsorption than oxygenated diamond. This may reflect the stronger protein-surface interactions at hydrophobic interfaces.[53] The initial adsorption rate on gold is low, compared to the nanodiamond interfaces. This observation may relate to the existence of stronger protein-surface interactions or the greater available area for adsorption at interfaces which are based on nanoparticles, which have higher surface area than a flat surface. A rough nanodiamond surface (ND_{crl}) has a higher initial rate than a smooth nanodiamond surface (ND_{ox}) with the same surface chemistry. This may be evidence that surface roughness affects initial adsorption of BSA to nanodiamond interfaces, due to increased surface area and/or increased surface-protein interactions.

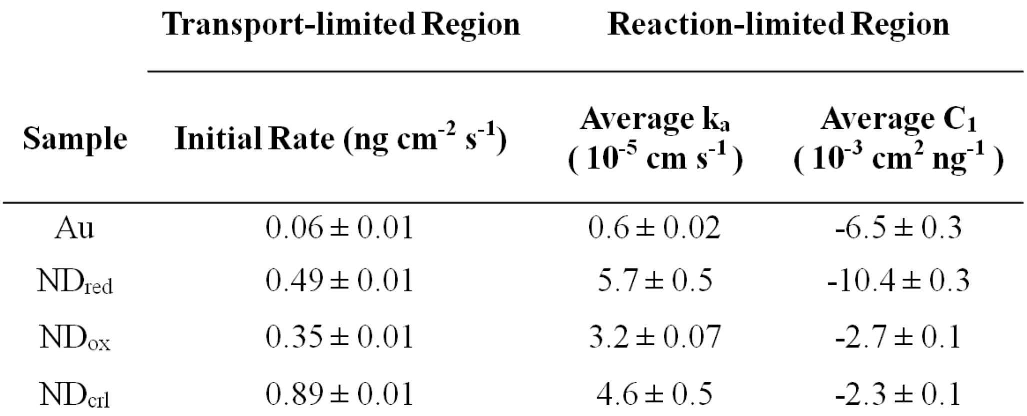

	Transport-limited Region	**Reaction-limited Region**	
Sample	**Initial Rate (ng cm^{-2} s^{-1})**	**Average k_a (10^{-5} cm s^{-1})**	**Average C_1 (10^{-3} cm^2 ng^{-1})**
Au	0.06 ± 0.01	0.6 ± 0.02	-6.5 ± 0.3
ND_{red}	0.49 ± 0.01	5.7 ± 0.5	-10.4 ± 0.3
ND_{ox}	0.35 ± 0.01	3.2 ± 0.07	-2.7 ± 0.1
ND_{crl}	0.89 ± 0.01	4.6 ± 0.5	-2.3 ± 0.1

Table 3.10: Kinetic parameters associated with traces in Figures 3.10 and 3.11. All data shown represent averages of relevant data using all overtones, n = 5, 7, 9, 11 and the Sauerbrey mass data.

3.2.4.2 Adsorption Rate *versus* Mass Density

Two kinetic parameters can be obtained by applying methods described in section 2.2.3 of this thesis to the data in Figure 3.10. These parameters are the rate constant (k_a) and the adsorption footprint (C_1). The C_1 value is a measure of the space needed for a protein to deposit onto the surface.[76,77] More negative values of C_1 indicate that a protein occupies more surface area. The results of this analysis are found in Table 3.10.

Surface chemistry has an effect on the rate constant and the adsorption footprint. The rate constant is higher on hydrogenated diamond, compared to oxygenated diamond. The rate constant associated with gold is lower than those associated with BSA adsorption on diamond. A higher rate constant is associated with a reduced energy barrier to adsorption. Factors which would reduce this energy barrier, include: surface wettability (i.e. hydrophobic vs. hydrophilic), larger available surface area for adsorption, stronger protein-surface interactions, and/or protein orientation upon initial adsorption.[53, 55, 80] The adsorption footprint is lower on oxygenated nanodiamond, than hydrogenated nanodiamond. Also, the adsorption footprint of BSA on gold is similar to that of BSA on hydrogenated nanodiamond. A higher footprint is associated with structural change and/or a flat orientation, whilst lower footprint is associated with preserved protein structure (i.e. near-native state), vertical ('end-on') orientation, and/or protein aggregation/clustering.[76, 77, 81] It is clear from these results that surface chemistry does affect the adsorption kinetics of BSA.

Surface roughness affects the rate constant, but not the adsorption footprint. The rate constant is higher for rough nanodiamond thin films (ND_{crl}), than smooth nanodiamond (ND_{ox}) thin films, having similar surface chemistry. This is consistent with the idea that surface roughness affects early protein adsorption. An increase in surface area would increase both the rate of adsorption and the number of protein-surface interactions. Stronger protein-surface affinity on rougher surfaces should be the net result, as noted elsewhere.[69] These effects would be further exacerbated if BSA is depositing into 'valleys' on the surface, with the potential for protein-surface interactions at multiple sides of the protein. The adsorption footprint of BSA on rough diamond is similar to that on smooth diamond. This suggests that the C_1 value is less dependent on surface roughness. Since C_1 is more dependent on adsorption mass during the reaction this result is not surprising (see Equations 2.14 and 2.16), and it is consistent with earlier results which showed the reduced influence of surface roughness at later stages of adsorption.

3.2.5 Adsorption Area

An estimate of adsorption size can be calculated from:

$$A_{ad} = \frac{M_w}{m\,N_A} \qquad \text{(Equation 3.3)}$$

where A_{ad} is the adsorption size, M_w is the molecular weight (≈ 66.4 kD for BSA), N_A is Avogadro's constant, and m is the mass density at saturation ($m_{\text{Sauerbrey}}$ or m_{Voight}). The values of A_{ad} are shown in Table 3.11, in both their unmodified and 'surface area corrected' forms. The footprint of BSA with molecular volume of 88.25 nm^3 is 2.4 x 10^{-13} cm^2 (see section 2.2.3.2). The results for A_{ad} obtained here are on the same order of magnitude as this theoretical size. It is interesting to note that there exist similar trends between the C_1 values and A_{ad}. This supports the use of C_1 as an estimate of BSA footprint size on diamond thin films. In addition, the A_{ad} values obtained for BSA on either oxygenated diamond sample is nearly the same, as the theoretical footprint. This suggests that BSA structure is preserved at oxygenated nanodiamond interfaces.

	$A_{ad: \text{Sauerbrey}}$ (10^{-13} cm^2 $molecule^{-1}$)		$A_{ad:\text{Voight}}$ (10^{-13} cm^2 $molecule^{-1}$)	
Sample	**Unmodified**	**Surface Area Corrected**	**Unmodified**	**Surface Area Corrected**
Au	6.9 ± 0.04	6.9	6.5 ± 0.1	6.5
ND_{ox}	2.8 ± 0.03	2.9	1.4 ± 0.1	1.4
ND_{red}	5.4 ± 0.05	5.5	5.8 ± 0.1	5.9
ND_{crl}	2.2 ± 0.03	2.5	1.3 ± 0.2	1.4

Table 3.11: Approximate surface areas of an adsorbed BSA molecule on various substrates.

3.3 Discussion

3.3.1 Nanodiamond Thin Films for QCM-D Applications

A detailed study of protein adsorption at the nanodiamond-aqueous interface has been accomplished using QCM-D. The method of spin-coating nanodiamond onto quartz crystals enabled this study to occur. To date, the study of the nanodiamond-aqueous interface has been limited and this study enables a further understanding of this interface, which is of increasing biological importance in the bio-materials and bio-sensing field. It also shows that QCM-D can be used to study inorganic interfaces of materials normally incompatible with the preservation of the piezoelectric properties of quartz, due to the elevated temperatures involved in their manufacture (e.g. CVD diamond). This study suggests that these inorganic materials can be studied by QCM-D, after spin-coating their nanoparticle forms onto quartz crystals.

There exist other essential features of the substrates prepared in this work. The preparation of smooth and stable nanodiamond thin films was made possible by the control of surface roughness. By disaggregating DND nanoparticles using BASD-treatment or hydrogen annealing, their size can be reduced to an extent that thin films made from them have surface roughness and thickness compatible with the requirements of the QCM-D technique. The BASD technique also enables particle size to be controlled by the duration of sonication. The chemical nature of DND particles was easily modified, and the surface chemistry of the spin-coated films was confirmed to be similar to that of CVD diamond films by XPS. The QCM-D results show that differing surface chemistry and roughness is maintained throughout this work.

3.3.2 *ex-situ* XPS

In this study, XPS was used to confirm the deposition of protein and its chemical character, *ex situ.* Caution was employed whilst interpreting data here, since the UHV conditions of XPS likely cause conformational changes to protein structure.[46] Moreover, there is large scatter in the XPS data and surface inhomogeneities do affect results. Despite these issues, XPS can be used to investigate protein adsorption phenomena, as done here and by others.[54, 58, 84] The protocol used to study adsorption of BSA by XPS was created to mimic the conditions of a typical QCM-D experiment (i.e. 30 min. deposition in phosphate buffer, followed by rinsing using protein-free buffer).

XPS analysis confirmed that BSA was adsorbing onto the nanodiamond thin films by noting that nitrogen photoelectron signal is only present on those films exposed to protein. Moreover, this signal persists after rinsing. Further XPS analysis showed that these protein layers have chemical composition associated with BSA adsorption, and that these layers are made of irreversibly bound proteins. Also, it was shown that BSA adsorption is more extensive on oxygenated nanodiamond than hydrogenated diamond, as evidenced by increased mass density and thickness on the former, compared to the latter. There is some XPS evidence for denaturation of BSA on hydrogenated diamond, compared to oxygenated diamond. Since the elemental ratios associated with BSA layers on oxygenated nanodiamond are close to the theoretical ratios for a pure BSA layer, it was determined that BSA structure was better preserved on oxygenated diamond, than hydrogenated diamond. After considering the XPS thickness, it was hypothesized that BSA is in a flat orientation on gold and hydrogenated diamond, but in a vertical orientation on oxygenated nanodiamond, regardless of surface roughness.

3.3.3 *in-situ* QCM-D

Unlike XPS, the QCM-D technique is an *in situ* technique and therefore has the advantage of mimicking real, biological conditions. Here, QCM-D was used to measure the mass and viscoelastic properties of BSA on the gold and as-prepared diamond thin films. The effect of surface chemistry and surface roughness on the dynamics of BSA adsorption was determined. By connecting various themes throughout the presentation of the QCM-D results, supported by the XPS results, a detailed description of BSA adsorption onto the four substrates studied here can be made. A schematic representation of this description is shown in Figure 3.11, and it will be justified in the following discussion.

3.3.3.1 Role of Surface Chemistry and Surface Roughness

The fact that surface chemistry affects both BSA structure and orientation is a theme which emerges throughout the results. Protein structure is preserved on oxygenated nanodiamond, but not on hydrogenated diamond or gold. QCM-D evidence suggests that BSA on gold and hydrogenated nanodiamond is undergoing significant structural change. As noted in section 3.2.3.2, BSA on gold and hydrogenated nanodiamond forms looser and more viscoelastic layers than on oxygenated diamond. Also, the adsorption footprint of BSA on these two surfaces is larger than on oxygenated diamond, which is consistent with structural change (see section 3.2.4.1). The adsorption footprint on oxygenated diamond is smaller, and more consistent with the preservation of native protein structure. This likely relates to the ability of hydrophilic surfaces to preserve protein structure.[55] As mentioned earlier, XPS results support the above assignment of protein structure at the studied interfaces.

Surface chemistry of nanodiamond also affects the orientation of BSA. In the literature, the determination of protein orientation can be a controversial subject.[64, 85] Thus, it is important to clearly identify the type of orientation occurring in the studied systems. In section 3.2.3.3, it was argued that initial monolayers of BSA are in a flat

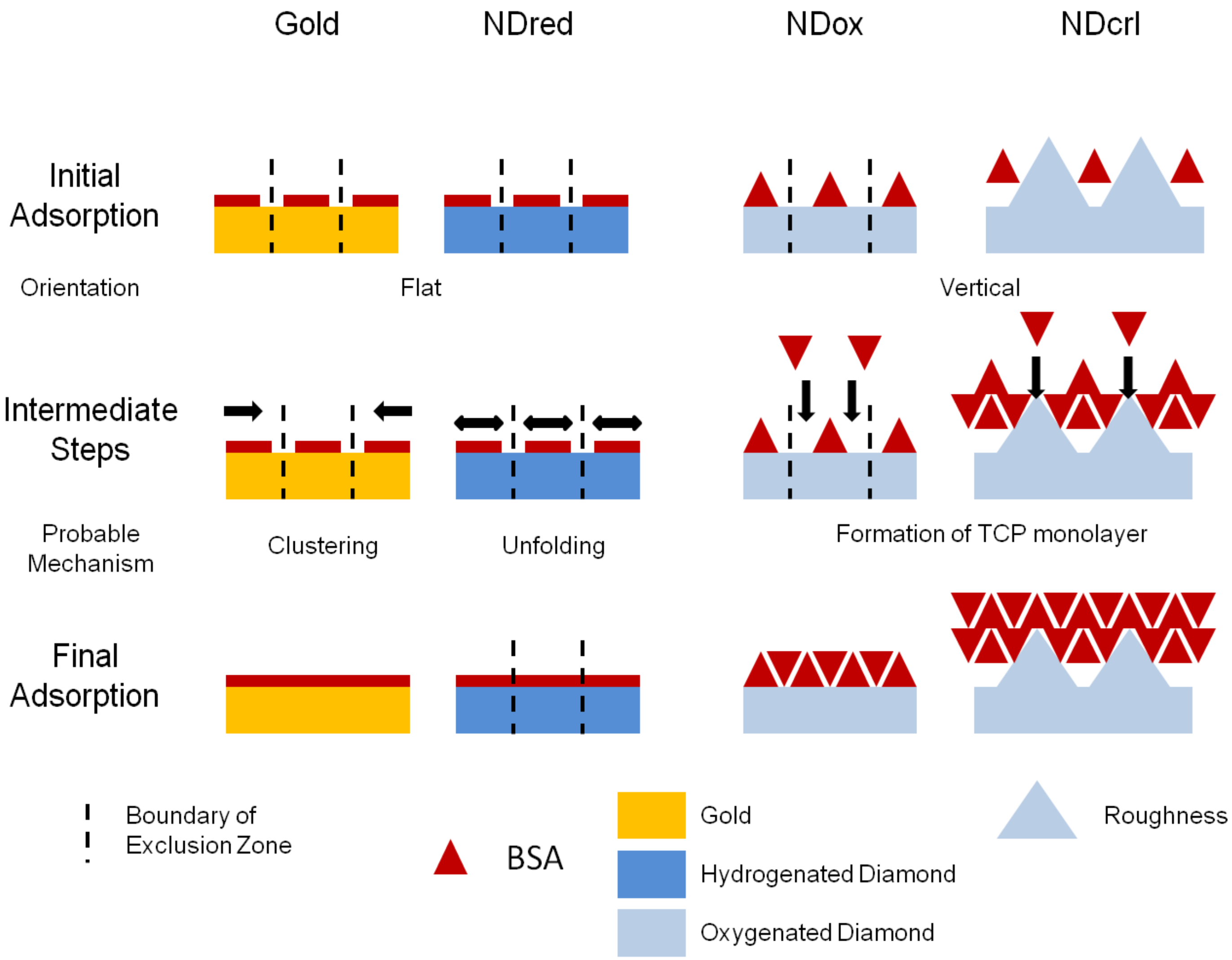

Figure 3.11: An overview of BSA interactions with the substrates studied here, with the most probable adsorption mechanisms and layer structures shown.

orientation on gold and hydrogenated diamond, after analyzing the mass densities associated with changes of gradient in the ΔD vs. Δ*f* plots (see also, Table 3.9). The same analysis determined that BSA deposits in a vertical (or end-on) orientation on oxygenated nanodiamond. At saturation, the orientation remains the same. A flat arrangement on hydrogenated diamond and gold is likely driven by the need for BSA to maximize the number of favourable protein-surface interactions on hydrophobic substrates.[53] On oxygenated diamond, other interactions are possible, which negate the need for BSA to adopt a flat orientation. Hydrogen bonding and covalent bonds (i.e. *via* aminolysis) are examples of the additional interactions possible between a well-oxygenated surface and BSA.[53]

Surface roughness also affects BSA adsorption, but only in the initial, not later stages of adsorption. In various sections, it was seen that surface roughness affects those parameters most sensitive to initial adsorption processes, such as initial rate, rate constant and the viscoelastic behaviour (i.e. very low dissipation) in the first ≈ 100 seconds of adsorption. Adsorption then proceeds as it would on a smooth surface having comparable chemistry in all regards. This second observation makes it unlikely that surface roughness is inducing major conformational change, orientation change, or a dramatic change of protein layer structure at later adsorption phases, or at saturation. The first observation could be explained in one of two ways: first, the high rate constant and initial rate seen could be due to the higher *initial* surface area of this rough nanodiamond film; second, it is possible that the low dissipation is related to the displacement of surface hydration by protein. In section 3.2.3.2, these two ideas were combined to argue for a scenario in which BSA displaces buffer within the ‘valleys’ of this nano-rough surface. After initial adsorption, incoming proteins would be unable to ‘see’ or interact with (i.e. *via* long range forces) the underlying, rough surface.[86] This is a plausible scenario, and there exists other experiments which show that protein can be confined within nano-valleys; for example, cytochrome c has been confined within nano-valleys on diamond surfaces for the purpose of electrochemical studies of its structure on differently terminated diamond surfaces.[23, 69] Also, as suggested by the high initial rate and rate constant data, the displacement of surface hydration by protein would be facilitated by an increase in favorable interactions between BSA and a surface with high surface area (i.e. increased probability of protein adsorption, and increased number of protein-surface interactions[69]).

3.3.3.2 Pathways towards BSA Adsorption

The analysis of the QCM-D data can be more innovative and detailed than presented thus far. BSA adsorption on gold and diamond is complex, but the actual arrangement of BSA within adsorbed layers, and the adsorption mechanisms, can be resolved by the results here. This will be justified in the following discussion, which is summarized by the schematic representation in Figure 3.11

Protein adsorption onto the studied surfaces is more complex than assumed by the RSA model. The basic model assumes that proteins are hard spheres, adsorb irreversibly in a single step, have excluded area, and have no mobility at the surface. On the other hand, the QCM-D results demonstrate that BSA adsorption on all studied surfaces is more complex, as best seen in Figures 3.9 and 3.10. Multiple gradient changes, in the former figure, indicate the presence of conformational change, surface hydration changes, and changes in protein Some lineshapes in Figure 3.10 are linear within the reaction-limited regime, which is indicative of adsorption behaviour more associated with Langmuir processes (i.e. mobile proteins, absence of excluded area), rather than the assumed RSA adsorption process. Careful consideration of this complexity leads to a more detailed picture of BSA adsorption on the studied surfaces.

The orientation and conformation of BSA during initial binding is straightforward. BSA monolayers have flat orientation on gold and hydrogenated nanodiamond, and vertical orientation on oxygenated nanodiamond, regardless of roughness (see section 3.2.3.3). BSA conformation is similar upon initial binding, with a preference for a looser conformation on gold compared to the nanodiamond substrates (see Table 3.8). In addition, at the rough oxygenated nanodiamond interface, BSA is filling the nano-valleys. After some period of time, BSA layers undergo a series of physical changes which mark the start of a second adsorption phase.

There are several, substrate dependent processes occurring during the second adsorption phase, as best seen in Figure 3.9. The case of the gold and hydrogenated diamond is considered first. At the gold interface, BSA slowly forms the initial monolayer, followed by a quick transition to a more rigid structure. On hydrogenated diamond, initial adsorption is quick, whilst the second phase is a slower process involving looser proteins. These observations parallel those seen in Figure 3.10, with adsorption on the former being more Langmuir-like, than the latter (based on linearity of reaction-limited regime). Finally, the initial rate, rate constant and adsorption footprint data suggests that BSA on hydrogenated diamond has a low barrier to adsorption (i.e. fast kinetics), which is likely due to the stronger protein-surface interactions related to having a flat orientation and a large adsorption footprint size. In the case of gold, BSA has a higher barrier to adsorption (i.e. slow kinetics), with a footprint size related to more moderate conformational change; this largely indicates that protein-surface interactions are weaker. The above supports the claim that saturation layers are formed *via* clustering and unfolding processes on gold and hydrogenated diamond, respectively. Clustering is known to occur for BSA at gold surfaces[81], and it is a process with Langmuir kinetics[75,80], involving mobile proteins which create overlayers more rigid than the initial monolayer.[81] Protein unfolding, after initial adsorption, is characterized by immobile proteins filling space at the surface by “spreading”[87] and “flattening”[88] – potentially filling some or all the available space within the excluded area around each protein. Such conformational change would be quick, involve looser protein structure, involve attractive protein-surface or protein-protein forces, and have RSA-like kinetics.[75, 80, 81] Either method leads to a protein layer at saturation with similar characteristics - a flat, close packed arrangement of BSA with conformational changes.

All that remains unresolved is the exact arrangement of BSA on oxygenated surfaces. Three arrangements of BSA in a vertical orientation are possible: (1) multi-layers; (2) a close-packed (CP) monolayer, where buffer is located between rows of BSA; or (3) a triangular close-packed (TCP) monolayer, where buffer between rows is displaced by heart-shaped BSA.[34] The *hydrated* saturation mass density associated with scenario 2 and 3 is 800 ng cm^{-2} and 910 ng cm^{-2}, respectively; in both cases the thickness would be 6.9 nm.[34] In this study, m_{Voight} values for these interfaces are between 800 ng cm^{-2} and 910 ng cm^{-2}, with layer thickness consistent with theory for vertical monolayers. This evidence suggests that scenario 1 is unlikely, and at minimum CP monolayers are being formed.

However, it is probable that some TCP structure is present, and possibly, extensive. The Langmuir-like kinetics observed in the reaction-limited regime of Figure 3.10, and the trend towards more positive ΔD vs. Δf gradients (see Figure 3.9) could be evidence for TCP formation. Space-filling at this interface could be occurring by incoming, heart-shaped proteins adsorbing adjacent to the pre-existing protein layer in an end-on arrangement (i.e. transition from scenario 2 to 3). A change to positive gradient occurring at about 80% of total mass may be related to incoming proteins adsorbing into a CP layer. Decreased protein-protein distance would remove hydration from the pre-existing CP monolayer and make it more rigid (i.e. less negative $\Delta D/\Delta f$ ratio, see Table 3.8). Favourable protein-protein interactions, such as hydrogen bonding, could be facilitating this phenomenon.[53]

3.4 Summary and Conclusions

In this chapter, an investigation regarding the dynamics of BSA adsorption onto diamond thin films has been presented. The as-prepared thin films were characterized for their surface chemistry and topography. The effect of both features on protein adsorption was investigated using the novel QCM-D technique. A number of conclusions have been made, with the most important being:

- Detonation nanodiamond suspensions which have been disaggregated to primary particle size can be used spin-coated onto gold-coated substrates to form thin films which are suitable for QCM-D application.
- The surface roughness of these surfaces can be controlled by adjusting the size of nanodiamond particles in suspension. This is done by adjusting the duration of the BASD method used to disaggregate the suspensions.
- The surface chemistry of the nanodiamond thin films prepared here is similar to that of CVD diamond thin films.
- BSA mass density is higher on oxygenated nanodiamond than hydrogenated nanodiamond (regardless of surface roughness).
- BSA structure is better preserved on oxygenated nanodiamond, than hydrogenated nanodiamond (regardless of surface roughness).
- BSA orientation is flat at hydrogenated nanodiamond interfaces, and vertical at oxygenated nanodiamond interfaces (regardless of surface roughness).
- BSA adsorption is fast on hydrogenated diamond and slow on oxygenated nanodiamond (regardless of surface roughness).
- BSA has an adsorption footprint consistent with a near-native state on oxygenated nanodiamond (regardless of surface roughness)
- Surface roughness affects the early stages of BSA adsorption, but has little effect on the dynamics of later adsorption processes.

- A detailed summary of BSA adsorption on hydrogenated and oxygenated nanodiamond thin films was presented. On oxygenated diamond films, BSA structure is preserved, with the slow formation of densely packed layers of BSA in a vertical orientation. On hydrogenated diamond films, BSA structure is not as well preserved, with the faster formation of looser arrangements of BSA in a flat orientation.

This study was the first real-time, *in situ* viscoelastic study of BSA adsorption on nanodiamond thin films. This is an important study, as the more extensive use of nanodiamond particles in biological systems is imminent. As an added benefit, it has been demonstrated that QCM-D can be used to study the biological interactions of inorganic materials normally made using high temperature manufacturing techniques. The direct growth of such materials on quartz crystals would remove the piezo-electric properties which are crucial to its use in QCM-D. This investigation represents an important contribution to the study of the inorganic material-biology interface using the QCM-D technique.

References

[1] C.C. Fu, H.Y. Lee, K. Chen, *et al.*, Proc. Natl. Acad. Sci. USA, 104 (2007) 727-732.

[2] R. Lam, M. Chen, E. Pierstorff, *et al.*, ACS Nano, 2 (2008) 2095-2102.

[3] A. Thalhammer, R.J. Edgington, L.A. Cingolani, *et al.*, Biomaterials, 31 (2010) 2097-2104.

[4] A.M. Schrand, S.A.C. Hens, O.A. Shenderova, Crit. Rev. Solid State Mater. Sci., 34 (2009) 18-74.

[5] H.-D. Wang, C.H. Niu, Q. Yang, *et al.*, Nanotechnology, 22 (2011) 145703.

[6] V. Danilenko, Phys. Solid State, 46 (2004) 711-715.

[7] V.Y. Dolmatov, M.V. Veretennikova, V.A. Marchukov, *et al.*, Phys. Solid State, 46 (2004) 611-615.

[8] A. Krueger, M. Ozawa, G. Jarre, *et al.*, Phys. Status Solidi A, 204 (2007) 2881-2887.

[9] B. Palosz, C. Pantea, E. Grzanka, *et al.*, Diamond Relat. Mater., 15 (2006) 1813-1817.

[10] Y. Liu, Z.N. Gu, J.L. Margrave, *et al.*, Chem. Mater., 16 (2004) 3924-3930.

[11] I. Kulakova, Phys. Solid State, 46 (2004) 636-643.

[12] A. Hartl, E. Schmich, J.A. Garrido, *et al.*, Nat Mater, 3 (2004) 736-742.

[13] R. Hoffmann, A. Kriele, H. Obloh, *et al.*, Appl. Phys. Lett., 97 (2010) 052103.

[14] P.H. Chung, E. Perevedentseva, C.L. Cheng, Surf. Sci., 601 (2007) 3866-3870.

[15] O.A. Williams, J. Hees, C. Dieker, *et al.*, ACS Nano, 4 (2010) 4824-4830.

[16] A. Kruger, F. Kataoka, M. Ozawa, *et al.*, Carbon, 43 (2005) 1722-1730.

[17] V.S. Bondar, I.O. Pozdnyakova, A.P. Puzyr, Phys. Solid State, 46 (2004) 758-760.

[18] R. Hoffmann, A. Kriele, H. Obloh, *et al.*, Biomaterials, 32 (2011) 7325–7332.

[19] L. Grieten, S.D. Janssens, A. Ethirajan, *et al.*, phys. status solidi A, 208 (2011) 2093-2098.

[20] S. Haymond, G.T. Babcock, G.M. Swain, J. Am. Chem. Soc., 124 (2002) 10634-10635.

[21] F. Marken, C.A. Paddon, D. Asogan, Electrochem. Commun., 4 (2002) 62-66.

[22] M. Chiku, T.A. Ivandini, A. Kamiya, *et al.*, J. Electroanal. Chem., 612 (2008) 201-207.

[23] N. Yang, R. Hoffmann, W. Smirnov, *et al.*, Diamond Relat. Mater., 20 (2011) 269-273.

[24] R. Trouillon, D. O'Hare, Electrochim. Acta, 55 (2010) 6586-6595.

[25] D. Shin, D.A. Tryk, A. Fujishima, *et al.*, Electroanalysis, 17 (2005) 305-311.

[26] R. Trouillon, D. O'Hare, Y. Einaga, PCCP, 13 (2011) 5422-5429.

[27] T. Goto, T. Yasukawa, K. Kanda, *et al.*, Anal. Sci., 27 (2011) 91-94.

[28] J.J. Sakon, G.J. Ribeill, J.M. Garguilo, *et al.*, Diamond Relat. Mater., 18 (2009) 82-87.

[29] L.C. Lora Huang, H.C. Chang, Langmuir, 20 (2004) 5879-5884.

[30] R.J. Hamers, C. Stavis, A. Pokhrel, *et al.*, Diamond Relat. Mater., 20 (2011) 733-742.

[31] B. Rezek, E. Ukrainstsev, L. Michalikova, *et al.*, Diamond Relat. Mater., 18 (2009) 918-922.

[32] E. Ukraintsev, B. Rezek, A. Kromka, *et al.*, Phys. Status Solidi B, 246 (2009) 2832-2835.

[33] B. Rezek, L. Michalíková, E. Ukraintsev, *et al.*, Sensors, 9 (2009) 3549-3562.

[34] V.B.C. Figueira, J.P. Jones, J. Colloid Interface Sci., 325 (2008) 107-113.

[35] F.G. Celii, J.E. Butler, Annu. Rev. Phys. Chem., 42 (1991) 643-684.

[36] J. Haines, O. Cambon, N. Prudhomme, *et al.*, Phys. Rev. B, 73 (2006) 014103.

[37] F. Fendrych, A. Taylor, L. Peksa, *et al.*, J. Phys. D: Appl. Phys., 43 (2010) 374018.

[38] O.A. Williams, V. Mortet, M. Daenen, *et al.*, J. Nanosci. Nanotechnol., (2009) 3483-3486.

[39] Y. Zhang, S. Asahina, S. Yoshihara, *et al.*, J. Electrochem. Soc., 149 (2002) H179-H182.

[40] A. Pentecost, S. Gour, V. Mochalin, *et al.*, ACS Appl. Mater. Interfaces, 2 (2010) 3289-3294.

[41] K. Xu, Q.J. Xue, Phys. Solid State, 46 (2004).

[42] Y. Liang, M. Ozawa, A. Krueger, ACS Nano, 3 (2009) 2288-2296.; F. Neugart, A. Zappe, F. Jelezko, *et al.*, Nano Lett., 7 (2007) 3588-3591.

[43] C.H. Goeting, F. Marken, A.R. Osborn, *et al.*, Electrochem. Solid-State Lett., 4 (2001) E29-E31.

[44] H. Notsu, I. Yagi, T. Tatsuma, *et al.*, Electrochem. Solid-State Lett., 2 (1999) 522-524.

[45] L. Daikhin, a. Michael Urbakh, Faraday Discuss., 107 (1997) 27-38.

[46] C.D. Tidwell, D.G. Castner, S.L. Golledge, *et al.*, Surf. Interface Anal., 31 (2001) 724-733.

[47] A. Ithurbide, I. Frateur, A. Galtayries, *et al.*, Electrochim. Acta, 53 (2007) 1336-1345.

[48] G. Iucci, L. Rossi, N. Rosato, *et al.*, J. Mater. Sci. Mater. Med., 17 (2006) 779-787.

[49] C.D. Wagner, A.V. Naumkin, A. Kraut-Vass, *et al.*, “NIST X-ray Photoelectron Spectroscopy Database”, in: N.I.o.S.a.T. (NIST) (Ed.), U.S. Secretary of Commerce, USA, Washington, USA (2007).

[50] Dissociation Constants for Acids and Bases, Zirchrom Separations Inc, April 21, 2012. <www.zirchrom.com/organic.htm>

[51] S. Ferro, M. Dal Colle, A. De Battisti, Carbon, 43 (2005) 1191-1203.

[52] J.I.B. Wilson, J.S. Walton, G. Beamson, J. Electron. Spectrosc. Relat. Phenom., 121 (2001) 183-201.

[53] W. Norde, Colloid Surface B, 61 (2008) 1-9.

[54] G.M.L. Messina, C. Satriano, G. Marletta, Colloid Surface B, 70 (2009) 76-83.

[55] P. Roach, D. Farrar, C.C. Perry, J. Am. Chem. Soc., 127 (2005) 8168-8173.

[56] D. Briggs, J.T. Grant, Surface Analysis by Auger and X-ray Photoelectron Spectroscopy, IM Publications, Charlton, U.K. (2003), p. 900.

[57] J.B. Lhoest, M.S. Wagner, C.D. Tidwell, *et al.*, Journal of Biomedical Materials Research, 57 (2001) 432-440.

[58] G.W. Nelson, M. Perry, S.-M. He, *et al.*, Colloid Surface B, 78 (2010) 61-68.

[59] R. Flitsch, S.I. Raider, Journal of Vacuum Science and Technology, 12 (1975) 305-308.

[60] D.Y. Petrovykh, H. Kimura-Suda, M.J. Tarlov, *et al.*, Langmuir, 20 (2003) 429-440.

[61] J. Zemek, J. Potmesil, M. Vanecek, *et al.*, Appl. Phys. Lett., 87 (2005) 262114.

[62] M.P. Seah, W.A. Dench, Surf. Interface Anal., 1 (1979) 2-11.; M. Textor, L. Ruiz, R. Hofer, *et al.*, Langmuir, 16 (2000) 3257-3271. ; D.H. Tsai, F.W. DelRio, A.M. Keene, *et al.*, Langmuir, 27 (2011) 2464-2477.

[63] F. Höök, J. Vörös, M. Rodahl, *et al.*, Colloid Surface B, 24 (2002) 155-170.

[64] H. Fitzpatrick, P.F. Luckham, S. Eriksen, *et al.*, Colloids and Surfaces, 65 (1992) 43-49.

[65] M.K. Menon, A.L. Zydney, Anal. Chem., 70 (1998) 1581-1584.

[66] O.A. Williams, J. Hees, C. Dieker, *et al.*, ACS Nano, 4 4824-4830.

[67] J.Y. Yoon, H.Y. Park, J.H. Kim, *et al.*, J. Colloid Interface Sci., 177 (1996) 613-620.

[68] E. Ostuni, R.G. Chapman, R.E. Holmlin, *et al.*, Langmuir, 17 (2001) 5605-5620.

[69] A. Dolatshahi-Pirouz, K. Rechendorff, M.B. Hovgaard, *et al.*, Colloid Surface B, 66 (2008) 53-59.

[70] D.D. Deligianni, N. Katsala, S. Ladas, *et al.*, Biomaterials, 22 (2001) 1241-1251.

[71] K. Rechendorff, M.B. Hovgaard, M. Foss, *et al.*, Langmuir, 22 (2006) 10885-10888.

[72] F. Höök, B. Kasemo, T. Nylander, *et al.*, Anal. Chem., 73 (2001) 5796-5804.

[73] K. Reimhult, K. Petersson, A. Krozer, Langmuir, 24 (2008) 8695-8700.

[74] V. Silin, H. Weetall, D.J. Vanderah, J. Colloid Interface Sci., 185 (1997) 94-103.

[75] M. Rabe, D. Verdes, S. Seeger, Adv. Colloid Interface Sci., 162 (2011) 87-106.

[76] M.A. Brusatori, Y. Tie, P.R. Van Tassel, Langmuir, 19 (2003) 5089-5097.

[77] G. Anand, S. Sharma, A.K. Dutta, *et al.*, Langmuir, 26 (2010) 10803-10811.

[78] C. Calonder, P.R. Van Tassel, Langmuir, 17 (2001) 4392-4395.

[79] P.R. Van Tassel, “Protein Adsorption Kinetics Under an Applied Electric Field”, in: Cristian I . Contescu, K. Putyera (Eds.) Dekker Encyclopedia of Nanoscience and Nanotechnology, CRC Press (2008) pp. 3569–3577.

[80] J. Ramsden, “Protein Adsorption Kinetics”, in: M. Malmsten (Ed.) Biopolymers at Interfaces, Marcel Dekker, New York (2003) p. 199.

[81] A.M. Moulin, S.J. O'Shea, R.A. Badley, *et al.*, Langmuir, 15 (1999) 8776-8779.

[82] G. Belfort, A.L. Zydney, “Interaction of Proteins with Polymeric Synthetic Membranes”, in: M. Malmsten (Ed.) Biopolymers at Interfaces, Marcel Dekker Inc., New York (2003).

[83] T. Wei, S. Kawewtathip, K. Shing, J. Phys. Chem. C, 113 (2009) 2053-2062.

[84] S.L. McArthur, G.J.S. Fowler, G. Mishra, J. Surf. Anal., 14 (2008) 370-375.

[85] J.-P. Gallinet, B. Gauthier-Manuel, Colloids and Surfaces, 68 (1992) 189-193.

[86] P. Roach, D. Farrar, C.C. Perry, J. Am. Chem. Soc., 128 (2006) 3939-3945.

[87] F. Caruso, D.N. Furlong, P. Kingshott, J. Colloid Interface Sci., 186 (1997) 129-140.

[88] Q. Luo, J.D. Andrade, J. Colloid Interface Sci., 200 (1998) 104-113.

4. Characterization of Carbene Modified Polystyrene Thin Films

4.1 Introduction

4.1.1 Background

Attachment of life-endangering microbes to surfaces is of great concern in hospitals, sterile research facilities, food processing plants, water purification plants and schools.[1-3] Inside the human body, microbial attachment to polymeric catheters or implants can have other serious consequences, such as polymer degradation or polymer-centred infection.[4-6] There is a clear need to develop methods by which anti-microbial properties can be imparted to polymeric surfaces, in a manner which preserves their utility and low manufacturing cost.

Several broad methods for imparting anti-biological properties to polymers exist, including: polymer-nanoparticle hybrids, polymer brushes, positively-charged surfaces and chemical modification.[4, 5, 7-11] It is this last type of modification which is the focus of this chapter, and extensive reviews are found throughout the recent literature.[5, 11-13] Chemical modification of polymers is seen to be a facile and long-lasting method to impart anti-microbial properties, due to ease of synthesis and covalent attachment of modifiers to the polymer substrate. The attachment of small, antimicrobial molecules or peptides is a common means to confer such properties to a polymer.[12] Extensive research has been done to identify functional groups and molecules which impart anti-fouling and anti-microbial activity to surfaces using self-assembled monolayers (SAMs) or pharmaceutical-related research.[12, 14] They have proved to be good models for various surface chemistries, but SAMs, and related films, suffer from two main disadvantages: first, they are not robust films; second, they are used primarily to functionalize inorganic, not organic substrates.[15] Thus, there is a key need to develop practical approaches to the controlled functionalization of a wide range of organic materials.

Recently, to address this issue, a powerful synthetic approach towards the modification of polymeric materials has been developed by Moloney and co-workers.[16-20] This group has demonstrated that a wide range of polymeric materials can be modified using carbene-based chemistry.[16-20] In their work, a ring substituted diaryl-diazo compound is activated, by gentle heating, in the presence of a surface. This generates a carbene species *in situ*, which then reacts with the surface and covalently binds the diaryl species to it. Ring substituents can be exploited to bind a wide range of surface functional groups, thereby achieving "surface functionalization". This chemistry can be used on polystyrene, polythene, nylon, and silica, with the promise of effective modification of other materials.[16] In this manner, a single chemical linker can modify many different materials with differing surface chemistry.

4.1.2 Aims and Overview

Whilst the carbene-based chemistry for the modification of polymers has been demonstrated[16-18, 20], there is little work done regarding its application to the creation of anti-fouling or anti-microbial materials. Also, there is a need to investigate the physical consequences of using this attachment chemistry on polymeric materials; some results indicate that this chemistry can be quite harsh to polymeric surfaces. such as polystyrene beads.[16, 17] Therefore, the purpose of the present project is to investigate this route to surface functionalization, using polystyrene thin films as an exemplar material. The biofouling properties, controlled by the differing surface functionalization, will be studied using dissipative quartz crystal microbalance techniques, which are described in the following chapter.

A variety of unmodified, cross-linked, and chemically modified polystyrene surfaces were synthesized, and their surfaces characterized by surface science techniques. The investigation had several aims:

- To find a polystyrene thin film which could be stable to the conditions of the carbene and azo-coupling chemistry
- To create polystyrene thin films which are suitable for QCM-D analysis
- To confirm the successful modification of polystyrene thin films by the carbene and azo-coupling chemistry
- To obtain information about the physical properties and surface chemistry of these modified surfaces
- To learn about the nature of the carbene insertion step in the thin film synthesis.

The accomplishment of these aims will increase our understanding of carbene chemistry at polymeric surfaces, and lay the foundations for the later analysis of their anti-fouling properties using QCM-D in the following chapter.

4.2 Experimental Details

4.2.1 Chemicals

MilliQ water was used throughout this work. Piranha solution was used to clean gold surfaces, and it was prepared as a 3:1 ratio of concentrated sulphuric acid (Fischer Scientific) and dilute H_2O_2 (30 % v/v, Alfa Aesar). Toluene (Sigma Aldrich) was used as a solvent for polystyrene powders, and it was filtered before use by PFTE filters (Rathburn Chemicals Ltd.; glass distilled grade). The polystyrene powder (Sigma Aldrich, M_w = 211, 600) was made into a suspension by dissolving it in toluene in order to facilitate spin-coating of thin films of polystyrene on various substrates, as described in this chapter. These thin films were compared to polystyrene XAD beads (Sigma Aldrich, Amberlite XAD-4, 20-40 mesh) for the described chemistry. Cross-linking of polystyrene thin films was carried out using divinylbenzene (DVB, Sigma Aldrich) and a common thermal radical initiator, benzoyl peroxide (BPO, 40 wt. % blend in dibuytl phthalate, Aldrich). Other solvents used during the course of these experiments, include dichloromethane (DCM , 1w/v%, Sigma Aldrich) and diethyl ether (DEE, Sigma Aldrich). The chemicals for the carbene modification chemistry described in this chapter are found in section 4.2.3.

4.2.2 Supporting Substrates

Polystyrene thin films were spin-coated onto a supporting substrate prior to subsequent modification and characterization. The supporting substrates used were glass microscope slides, molybdenum metal, Au-coated silicon squares, and QCM-D crystals. Glass slides were used as an inexpensive means to support the thin films during initial studies. Gold-coated squares were used to better mimic the conditions of a gold-coated QCM-D crystal, since the crystals themselves are expensive. Also, the $Au4f_{7/2}$ peak is a known internal standard for XPS binding energies, and an analysis of its attenuation can lead to a determination of overlayer thickness. Molybdenum substrates were used in experiments which required X-ray photoelectron signals from silicon to be minimized. Lastly, gold-coated QCM-D crystals (QSense, Sweden) were used, mostly, in the QCM-D experiments described in Chapter 5, but some reference to these substrates are in this chapter.

The glass slides and Mo substrates were used after cleansing with water and acetone. The Au layers on silicon were deposited using the methods of Hyde *et al.*.[21] Prior to Au deposition, the squares were exposed to an oxygen discharge for 10 minutes at a pressure of 0.1 mBar. This was followed by the deposition of 5nm of chromium, which was evaporated from chrome-plated, tungsten rod (R.D. Mathis, Long Beach, C.A), using a power supply of

10V and 90A. Gold (99.99 %, Alfa), from an alumina-coated molybdenum boat (R.D. Mathis, Long Beach, C.A.), was then deposited to a thickness of 50nm on top of this Cr-Si substrate. Prior to use the Au-coated silicon squares and the Au-coated QCM-D crystals were placed in piranha solution for 10 minutes, cleaned with copious amounts of water and acetone, and then placed in a broad-band UV source for ozone cleaning for 30 minutes.

4.2.3 Carbene Modification Chemistry

Carbene chemistry is a new and powerful approach to modifying materials.[18] This chemistry enables polymer films to be easily modified by a chemical linker, which can itself be modified to terminate the surface with a range of chemical functionality. This general strategy was briefly mentioned in section 1.2.3 and Figure 1.2. Here, the chemistry is described in more detail.

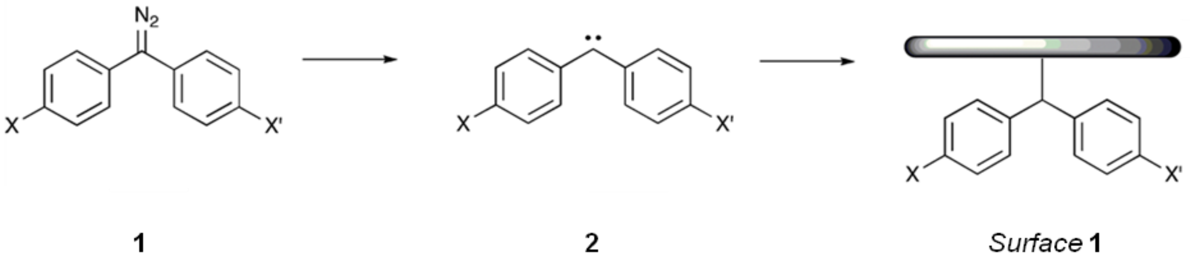

Figure 4.1: A schematic showing the general method for modifying materials. Adapted from Wang *et al.*.[20]

The approach is based on the reactivity of carbenes generated from the thermal-activation of diazo-compounds.[20] These carbenes are able to bond with a wide range of materials, including polymers, silica, and diamond.[16, 18] [20] If the diazo-compound is functionalized appropriately, then it can act as a chemical linker. Subsequent chemistry can add a diverse range of surface functionalization, such as alkyl , amino, carboxyl, and phosphate groups.[17] These carbene compounds are the foundation of an industrially relevant coating process, capable of easily transforming the macroscopic properties of the material it modifies.[17] The general chemistry for this process is shown in Figure 4.1.

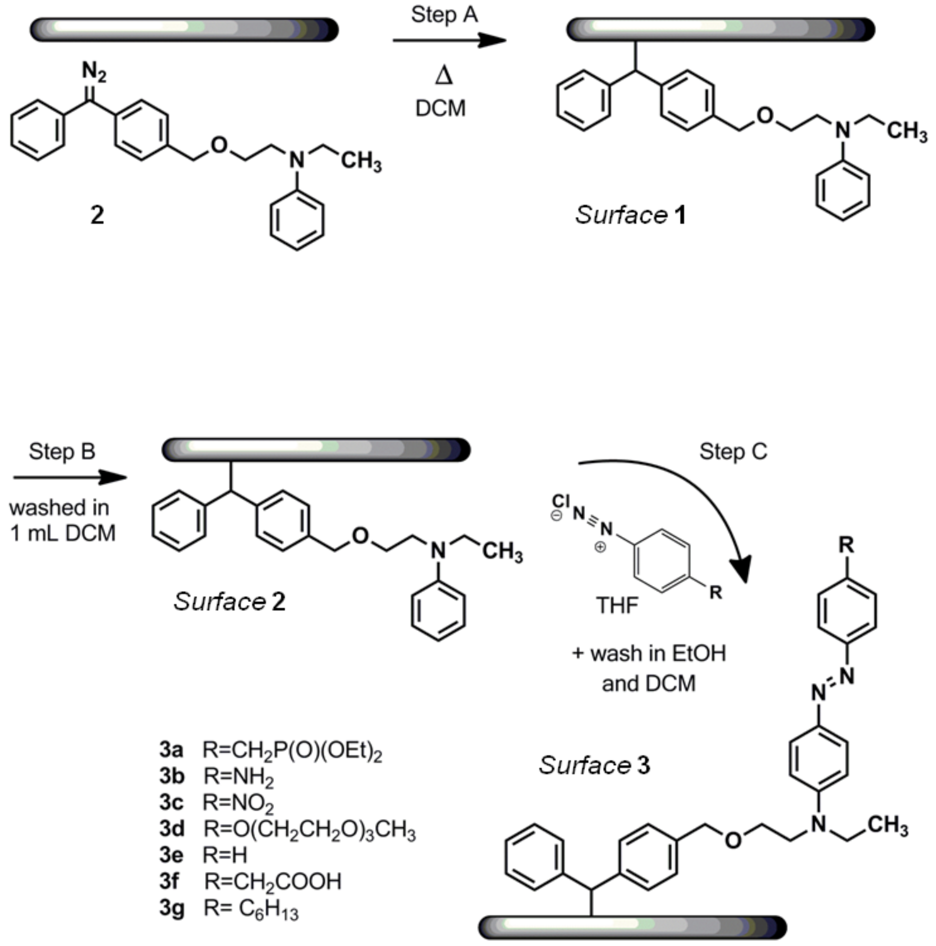

Figure 4.2: A schematic showing the general method for modifying polystyrene surfaces.

In this chapter, most 'carbene chemistry' involved the addition of a diazo-compound - terminated with an aniline group - onto polystyrene thin films, and the subsequent functionalization of these films by diazonium chemistry. In this way, a range of surface terminations were grafted onto polystyrene thin films. This chemistry is summarized in Figure 4.2, with the chemicals having been prepared by Emily Parker.[19] Specifically, the diazo-compound [(4-((2'-(ethyl(phenyl)amino)ethoxy)methyl)phenyl(phenyl)diazo] (Compound **2**) was used as the chemical linker. Compound **2** was dissolved in dichloromethane (DCM; 1 w/v %; approx. 0.2 mL per 1 cm^2), and the entire film was covered with a droplet of this pink suspension. After this point, the surface was pink in colour. This system was then heated to 180^oC for four minutes, during which time the pink colour disappeared. The resultant surface is terminated with a tertiary aniline, and is labelled *surface* **1** in Figure 4.2. This surface was washed with 1 mL of DCM (to remove any unreacted diazo compounds) and dried with N_2 gas, thus creating *surface* **2**. After the azo-coupling of diazonium salts having various functional groups (**R**), the surface termination of *surface* **2** was converted to that of *surface* **3**. The functional groups added to the polystyrene films in this manner are labelled, **3a** – **3g**; they include: phosophate diester, amine, nitro, glycol, carboxyl, phenyl and alkyl groups. The unmodified polystyrene substrate, *surface* **2** (i.e. aniline-terminated), and *surface* **3e** (i.e. phenyl terminated), all serve as experimental controls.

The success of this carbene chemistry on the prepared polystyrene, and the grafting density of the coating, needed to be chemically confirmed using XPS. This is best done by introducing an element to the surface, which is not common to any of the chemicals or thin films prepared here. Iodine was chosen as this element, since many I core levels have high photo-emission cross-section, which enables a surface bound compound to be detected by XPS.[20] This was recently exploited by Wang *et al.*[20] to confirm the insertion of diarylcarbenes into diamond surfaces. A special version of compound **1**, called bis(4-iodophenyl)diazomethane was prepared by Dr. John-Paul Griffiths (Oxford Advanced Surfaces) to exploit this $I3d_{5/2}$ photoelectron signal, and whose method of synthesis is found elsewhere.[20] This special modification to polystyrene is shown in Figure 4.3. A droplet of bis(4-iodophenyl)diazomethane was added to the surface and heated until the removal of the initial pink colour disappeared. The temperature and time of insertion varied, as indicated in the text. After modification with bis(4-iodophenyl)diazomethane, the surfaces were cooled, washed with DCM, dried with N_2 gas, and then analyzed using XPS.

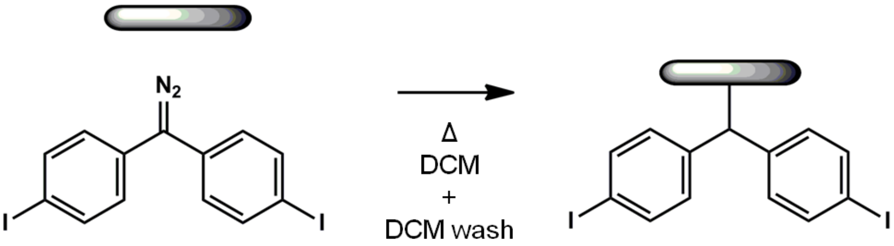

Figure 4.3: A general scheme for the modification of polystyrene with bis(4-iodophenyl)diazomethane.[20]

4.3 Results and Discussion

4.3.1 Preparation of Polystyrene Thin Films

Various polystyrene thin films were prepared here by spin-coating (see below), in order to evaluate their stability when exposed to carbene chemistry and their suitability for QCM-D applications. Initially, non-cross-linked polystyrene thin films were made and studied. Such films have been used successfully in other protein adsorption studies involving the use of QCM-D.[22, 23] However, non cross-linked polystyrene is known to dissolve in the presence of organic solvents or vapours.[24] By contrast, cross-linked polystyrene has resistance against dissolution in such condition. This type of polystyrene thin film was also studied, in case its non cross-linked counterpart proved unsuitable or unstable. There are a variety of ways to cross-link polystyrene, but surface cross-linking using UV radiation[25, 26] and the use of divinylbenzene and a thermally activated chemical initiator, benzoyl peroxide (BPO), are popular methods for cross-linking polystyrene.[27] Non cross-linked, UV cross-linked, and DVB cross-linked surfaces were all evaluated in this study for their suitability as substrates for carbene modification and for protein adsorption studies using QCM-D.

The most suitable polystyrene film must be stable to all aspects of the surface modification protocol (solvents, carbene insertion, azo-coupling) and be able to demonstrate different surface chemistry after modification. This thin film must also be less than 100 nm thick, which is the recommended limit for a thin film being used on a QCM-D crystal. A thicker surface could exceed the propagation limit of the shear wave emanating from the surface of an oscillating QCM-D crystal – a distance of approximately 250 nm for a 5 MHz crystal (see Equation 2.13). [28]

A popular method to create polymeric thin films is spin-coating. This method is used in the manufacture of solar cell, nanomaterials, and coatings.[29, 30] Existing protocols were modified to create the polystyrene thin films prepared here.[22, 27, 31, 32] All polystyrene thin films were made from a prepared solution of polystyrene dissolved in toluene (20 mg mL^{-1}) which was then sonicated, for 15 minutes, to ensure a homogeneous solution. From this solution, polystyrene films were spin-coated onto a substrate using five 200μL droplets of solution, with each droplet being spin-coated for 1 min at 2000 rpm (*Apparatus*: Laurell Technologies Corp., Model WS-400B-6NPP/LINE). Afterwards, the thin films were baked at 170^{o}C for 2 hours. This temperature is above their estimated glass transition temperature (T_g of 110^{o}C)[33], thus ensuring film homogeneity and the evaporation of trapped solvent. Unmodified versions of these prepared films were not cross-linked and are labelled β-PS throughout this thesis, and in the figures.

Some of these unmodified films were cross-linked using UV radiation or wet chemistry.[25, 27] It is known that UV radiation causes cross-linking *via* carbon-carbon scissions and reactions involving the aromatic rings of the styrene monomers; it is also known that photo-induced cross-linking is limited to the surface, as penetration of the UV light into the bulk is limited.[25] Ultra-violet radiation has been used before to control the integrity of polystyrene beads during exposure to toluene.[26] Here, the unmodified thin films were exposed to a broad band UV radiation source for 30 minutes, with the aim of inducing greater thin film stability through surface cross-links in the polystyrene structure. These UV cross-linked films are labelled γ-PS throughout this thesis.

Cross-linking polystyrene using wet chemistry should impart even greater stability to the thin film. Here, this cross-linking was done using divinylbenzene (DVB) and a thermally activated chemical initiator, benzoyl peroxide (BPO) due to its simplicity and its proven utility. Crucially, BPO does not contain nitrogen, unlike a common alternative photo-initiator azobisisobutyronitrile (AIBN). This enables nitrogen, throughout the surface modification depicted in Figure 4.2, to be used as an indicator of chemical change at the surface from analysis of the N1s photoelectron signal, obtains using XPS.

The DVB cross-linked polystyrene films were made by adding DVB to a 20 mg mL^{-1} suspension of polystyrene in toluene. The amount of DVB used was controlled to obtain approximately 2% cross-linking of the polystyrene monomers; this required 0.55 µL mL^{-1} of DVB in the suspension. The resultant solution was sonicated for 5 minutes. BPO was then added to this solution such that the ratio of BPO and the styrene monomers of the polystyrene in solution were in a 1:1 ratio.[27] This solution was immediately shaken for 1 minute and then spin-coated onto the supporting substrate. Once spin-coated, the thin films were quickly isolated from atmospheric conditions by placing the substrates into a flask, which was covered by a rubber septum. The environment inside this apparatus was made oxygen-free by flowing N_2 gas into the flask. To complete the cross-linking of the polystyrene, the flask was kept at a constant temperature of 90^{o}C, for 8 hours to enable the BPO to become thermally activated and initiate the cross-linking of polystyrene. The cooled films were then used and they are labelled δ-PS throughout this work.

4.3.2 Study of Polystyrene Thin Films by Optical Microscopy

Optical microscopy is a quick and inexpensive means to evaluate the physical structure of polymer thin films; it has been used to characterize polymer films undergoing dewetting and degradation by others.[24, 34] Here, optical microscopy is used to monitor thin film stability in organic solvents and after modification with carbene chemistry. Optical microscopy images of various polystyrene thin films are shown in Figure 4.4.

In order to mimic the conditions of the QCM-D experiments, polystyrene thin films were spin-coated onto a silicon-supported, gold-coated surface (and in the case of image B, an actual QCM-D crystal). A cleaned gold surface is shown in image A and it is relatively featureless. After preparing a polystyrene thin film on top of these gold surfaces, polystyrene could be observed on these surfaces. The thin film shown in image B shows all the features of these surfaces. Mostly, the polystyrene thin films are characterized by surface inhomogeneity in the form of discoloured spots, otherwise known as mottling; mottling is a known feature of these films.[24] When the film is prepared over a QCM-D crystal, there are several underlying surfaces, including smooth gold (sensor), matted gold, chromium, and the quartz crystal itself; these interfaces meet around the inner and outer edges of the matted gold ring seen in the inset to image B. Thin films covering these regions were found to be particularly prone to cracking, when not cross-linked. This has been seen before in other polystyrene films, and is considered to be a feature of the drying process, solvent-polymer interactions, and the inherent constraints imposed to the overlayer by the underlying, and rigid, substrates.[36] The above phenomena was seen to some extent for UV cross-linked polystyrene, but to a reduced extent. On the other hand, this phenomena was rarely seen for the DVB cross-linked polystyrene, possibly due to its greater physical strength and reduced organic solvent content, both of which mitigate cracking.[26]

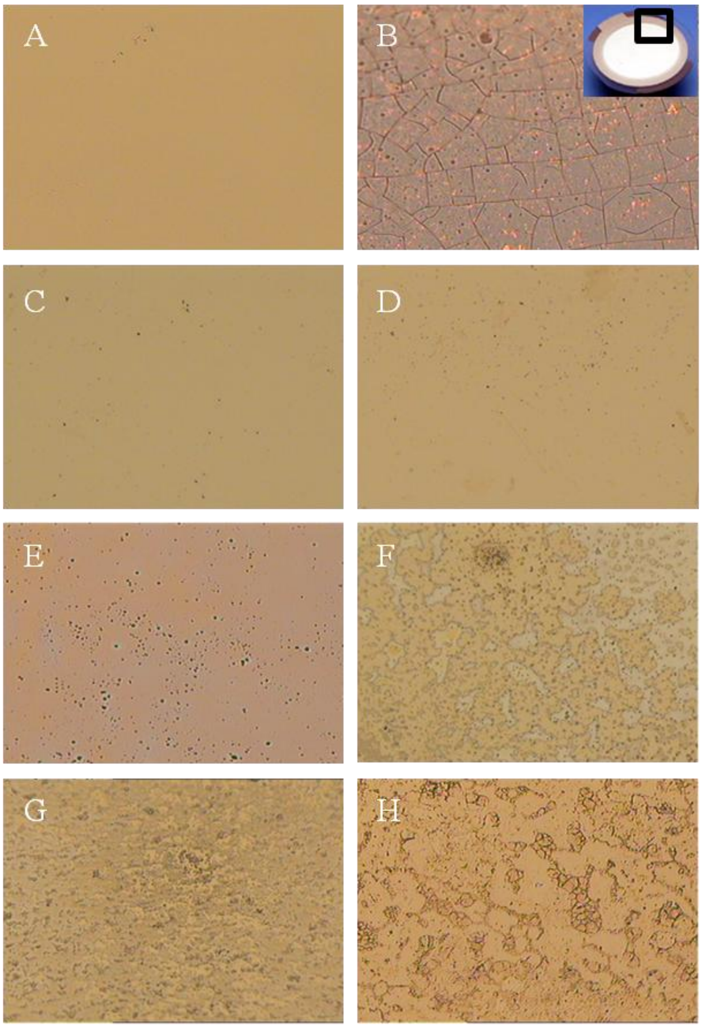

Figure 4.4: Images of various polystyrene (PS) thin films taken using an optical microscope at 1x magnification: Gold (A); Non cross-linked PS over Gold/matted gold/Cr interface on QCM crystals (B), inset shows QCM-D crystal with this interface highlighted[35]; Non cross-linked PS after 48 hour exposure to toluene (C); Non cross-linked PS after carbene-insertion (D); 2 % DVB cross-linked PS (E); 2 % DVB cross-linked PS after 48 hour exposure to Toluene (F); 2 % DVB cross-linked PS after carbene-insertion (G); modified 2 % DVB cross-linked PS thin film after 30 minutes of phosphate buffer containing 0.08 g L^{-1} of BSA (H).

The carbene chemistry used to modify the thin films usually, but not exclusively, requires the use of toluene as the solvent.[17-19] Toluene is known to dissolve polystyrene and this solvent property was exploited in the spin-coating of the polystyrene films. Thus, it is not unreasonable to expect that toluene may degrade the prepared thin films, as suggested by others.[24, 26, 34] Therefore, a simple test was prepared for the three polystyrene thin films; they were all exposed to toluene for 48 hours. The image of a non cross-linked polystyrene film after it had been exposed to toluene for this time frame is shown in Figure

4.4C. This image is featureless and not unlike that of the clean gold surface in image A. This suggests that the non cross-linked polystyrene film is no longer present on the surface. On the other hand, DVB cross-linking seems to lead to minimal evidence of dewetting or degradation, under the same conditions (see Image F, Figure 4.4). The UV cross-linked polystyrene film had behaviour intermediate to these two extremes (not shown). The presence of a polystyrene film is further confirmed by the mottling and slight shadow seen in image F. These results are consistent with the higher stability expected for bulk cross-linked polystyrene films.[26] Whilst DVB cross-linked polystyrene is most suitable to the chemical conditions found here, the use of a solvent which does not dissolve polystyrene to the same extent may be beneficial, and this is explored later.

A prepared thin film must be stable to the carbene chemistry involved in the modification scheme (step A, Figure 4.2). The carbene insertion step involves harsh chemistry and conditions: it requires heat (up to 180^{o}C), it forms C-C bonds between the diaryl compound and the polymer, and it exposes the films to organic solvents.[17, 18, 20] Non cross-linked polystyrene and DVB cross-linked polystyrene were both exposed to this chemistry and the resultant images are D and G in Figure 4.4, respectively. In case of a non cross-linked polystyrene film, its image shows no difference to that of the gold control and no evidence of those features characteristic of polystyrene thin films, such as mottling, obvious dewetting or cracking (see image D). However, we do see evidence for the presence of a DVB cross-linked polystyrene film after this chemistry (see image G), albeit in a degraded state. After exposure to the same conditions, UV cross-linked polystyrene is still present, but in a more degraded form, and is considered to be intermediately dewetted (not shown). These results are consistent with the higher stability expected for bulk cross-linked polystyrene films.[26] This evidence shows that the DVB cross-linked surfaces are the most stable thin film for the carbene chemistry used here.

The stability of an ideal DVB cross-linked film towards the conditions of a typical protein adsorption experiment was mimicked by exposing this surface, for 30 minutes, in a BSA-containing phosphate buffer at pH 7.4. The result of this exposure is shown as image H in Figure 4.4. This image has various unknown topographical features, which seem to be on top of a polystyrene thin film. If one assumes that polystyrene is not soluble in water[37] and that the thin film has not dissolved, then features in the image could be a combination of protein aggregates, salt aggregates, and the underlying polystyrene thin film. It is notable that in this *ex situ* experiment, the aggregates on top of this film seem to be inhomogeneous. This experiment suggests that the DVB cross-linked polystyrene films are stable to exposure to the phosphate buffer and BSA adsorption, which is one of the general requirements of an ideal polystyrene thin film for use in physiological conditions.

The optical microscopy experiments showed that the DVB cross-linked polystyrene films were stable to 48-hour exposure to toluene and to carbene chemistry. The DVB cross-linked polystyrene thin films are the most suitable for the chemical conditions inherent to this study. There is scope to adjust various chemical conditions (e.g. choice of solvent, carbene insertion conditions), and this is the topic of the next section.

4.3.3 Various Effects of Organic Solvents and Carbene Chemistry

The polymer thin films must remain stable to the organic solvents used and the carbene chemistry, as they need to be stable for their subsequent QCM-D use. In this section, various aspects of the thin film synthesis were explored and the results suggest an optimized protocol, which would lead to the development of polystyrene thin films stable to both the chemistry involved and for future QCM-D usage.

4.3.3.1 Choice of Solvent

The solvents typically used in the carbene insertion chemistry are diethyl ether (DEE), dichloromethane (DCM), or toluene.[19] There may be some advantage in using a solvent with a higher dipole moment than toluene, thus reducing polystyrene dissolution.[38]

The effect of DEE or DCM on the stability of polystyrene was probed using XPS. Table 4.1 shows the XPS elemental ratios belonging to various cross-linked polystyrene thin films on glass substrates, after exposure to differing solvents. These elemental ratios are considered to have an error of 10 - 15%.[39] Any polymeric degradation, dewetting, or swelling induced by solvent adsorption, should manifest itself as a higher O1s/C1s or Si2p/C1s ratio, due to photoelectron signal from the underlying SiO_2 structure being less attenuated by an overlayer. Conversely, polystyrene thin films which maintain their structure have a more constant O1s/C1s or Si2p/C1s ratio, when exposed to solvent. Solvent was exposed to the thin films in one of two ways: a series of 0.5 mL droplets or in a beaker containing 20 mL of solvent, for the noted duration. Substrates were then dried under N_2 gas and analyzed by XPS.

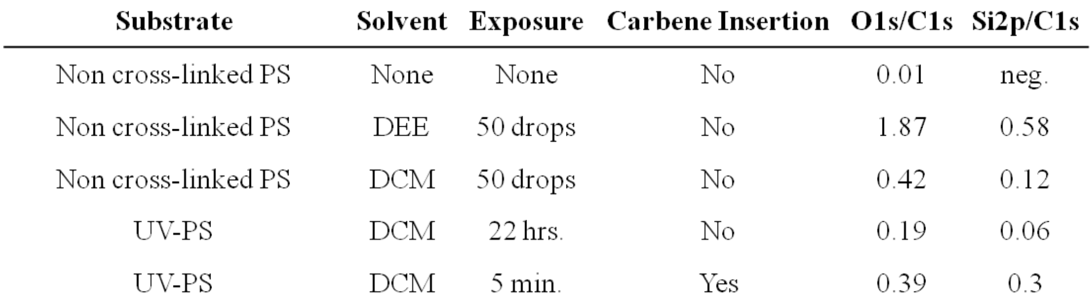

Substrate	Solvent	Exposure	Carbene Insertion	O1s/C1s	Si2p/C1s
Non cross-linked PS	None	None	No	0.01	neg.
Non cross-linked PS	DEE	50 drops	No	1.87	0.58
Non cross-linked PS	DCM	50 drops	No	0.42	0.12
UV-PS	DCM	22 hrs.	No	0.19	0.06
UV-PS	DCM	5 min.	Yes	0.39	0.3

Table 4.1: Elemental ratios for Non cross-linked PS and UV-PS thin films, spin coated onto glass slides, after exposure to various experimental conditions. See Table 4.2 for elemental ratios of control samples (i.e. NCL PS, UV PS, and 2% DVB PS).

First, non cross-linked polystyrene films were exposed to DEE and DCM. In both cases, the elemental ratios increased, compared to the control surface. This observation suggests that a degree of dewetting or degradation is occurring. However, the surface exposed to DCM has lower values for its elemental ratios, which indicate that polystyrene is more stable in this particular solvent. This is consistent with known trends in dipole moment and solubility tables.[37, 38, 40] Non-polar solvents with low dipole moments are known to better dissolve polystyrene[38]; the polar aprotic character of dichloromethane makes it a less potent solvent for polystyrene.[41] Based on these results, DCM became the solvent of choice during the carbene insertion, with tetrahydrofuran (THF) - another polar aprotic solvent having a similar dipole moment – was chosen for the azo-coupling reaction.

4.3.3.2 Degree of Cross-linking

The degree of cross-linking is known to offer stability to polymer thin films. UV exposure for longer durations is thought to increase the stability of polystyrene towards organic solvents.[25, 26] Here, a polystyrene sample was exposed to UV-radiation for 30 minutes and then analyzed with XPS. This UV cross-linked film was exposed to 20 mL of DCM for 22 hours, in a beaker. The sample was then dried using N_2 gas and analyzed using XPS. The associated elemental ratios in Table 4.1 are lower than any associated with the non cross-linked polystyrene in the same table. This represents a dramatic improvement in thin film stability. UV cross-linked polystyrene also offers increased stability compared to unmodified polystyrene. Optical evidence for the stability of the DVB cross-linked substrate to 48 hours of toluene exposure was presented earlier. This stability is likely related to extensive cross-linking within the bulk and the surface. The UV cross-linked polystyrene and DVB cross-linked polystyrene feature are the two substrates studied most within this work, due to the strength of their cross-linked networks. Ultimately, the DVB cross-linked polystyrene was chosen for QCM-D application.

4.3.3.3 Effect of Carbene Insertion on Thin Film Stability

The carbene chemistry conducted here involves harsh conditions, namely the exposure to organic solvents and temperatures ranging between 90 - 180^{o}C. Any prepared thin film must be stable to these general conditions. Based on the above evidence, it was thought that a polystyrene thin film modified by a 30 minute exposure to UV-radiation would be stable to both the solvents and temperatures used to facilitate the carbene chemistry. This particular substrate is relatively stable to 22 hours of DCM exposure and should be stable to temperatures less than its melting point (< 240^{o}C).[42] This hypothesis was tested by inserting he chemical linker into the substrate, thus creating *surface* **2** in Figure 4.2. The insertion occurred at a temperature of 120^{o}C and it was stopped when the pink colour of the initial solution had disappeared (5 min.). The resultant surface was analyzed using XPS, by comparing its O1s/C1s and Si2p/C1s ratios to that of UV-PS after exposure to 22 hours of DCM (see Table 4.1). From this comparison, we see that the elemental ratios have increased value after the as-prepared UV-PS is exposed to the carbene chemistry. This may indeed be evidence for the attachment of diaryl species to UV-PS. The attachment of branched chains to polystyrene materials is known to degrade its structure.[16, 43, 44] However, the success of the carbene reaction has not been chemically proven at this point, therefore some other effect could be contributing to the increased O1s / C1s and Si2p / C1s ratios. The UV-modified films were still used for chemical attachment of diazo compounds, but it is likely, based on the earlier evidence in section 4.3.1 that DVB cross-linked polystyrene is withstanding the carbene chemistry to a better extent.

4.3.4 XPS Characterization of As-Prepared Polystyrene Thin Films

By monitoring the surface chemistry of polystyrene thin films by XPS, the chemical changes at the interface caused by carbene and azo-coupling chemistry can be followed. In addition, XPS analysis will confirm the thickness of the as-prepared thin films. XPS analysis was conducted to determine the surface chemistry of various, unmodified polystyrene substrates. Four types of polystyrene films were studied by XPS: XAD-4 polystyrene beads (PS beads), non cross-linked polystyrene, UV-modified polystyrene, and DVB-modified polystyrene. The substrates used to support these layers included carbon tape (for PS beads), microscope glass slides, and gold-coated silicon squares.

4.3.4.1 Wide Scan XPS

The XPS results were typical of polymer layers and the substrates used to support them. A representative wide scan spectra of these layers is shown in Figure 4.5, with the associated elemental ratios and binding energies found in Tables 4.2 and 4.3, respectively. The Au spectrum has characteristic XPS peaks, including the 5p, 4f, 4d, 4p and 4s photoelectron signals.[45] Prominent silicon signal from the Si2p and Si2s core levels of SiO_2 can be seen in the spectra associated with a glass slide, which is consistent with the main constituent of glass – SiO_2.[45] Carbon tape was used to secure a layer of polystyrene beads or polystyrene powder to the XPS sample stub for some samples. The XPS spectrum of carbon tape is typical for that containing a quantity of adventitious and oxidized carbon; there is a negligible amount of nitrogen on this sample, as confirmed by the elemental ratio analysis in Table 4.2. Spin-coating a thin film of non-crosslinked polystyrene onto glass leads to the attenuation of the Si2p and Si2s photoelectron signal. A similar attenuation of the gold photoelectron signal in the case of UV cross-linked polystyrene and DVB cross-linked polystyrene on a gold terminated substrate can be seen. These observations are consistent with the presence of an organic overlayer on top of the supporting substrate.[46]

Preliminary studies aimed to confirm the success of the carbene and azo-coupling chemistry using modified XAD-4 polystyrene beads. However, the strategy that will be

		Elemental Ratios				Charging	
Sample	Underlying Substrate	$Au4f_{7/2}$/C1s	N1s/C1s	O1s/C1s	Si2p/C1s	relative to C1s (285.0 eV)	relative to $Au4f_{7/2}$ (84.0 eV)
Au		1.48		0.12		16.5	16.8
Glass Slide				2	0.88	11.5	
Carbon Tape			neg.	0.21		7.8	
PS Beads	Carbon Tape		0.13	0.21		6.3	
PS (Sigma Aldrich)	Carbon Tape			0.06			
NCL PS	Glass Slide			0.06	0.01	4.9	
UV PS	Au	0.01		0.09		9.3	10
2% DVB PS	Au	0.08		0.38		11.5	13.4

Table 4.2: XPS elemental ratios and charging values of various supporting substrates and polystyrene overlayers.

		Binding Energies						FWHM					
		C1s			O1s		N1s	C1s			O1s		N1s
Sample	Underlying Substrate	C-C/C-H	C-O/C-N	C=O	C-O	C=O	NH_2	C-C/C-H	C-O/C-N	C=O	C-O	C=O	NH_2
Au		285	287.8		532.5	533.9		1.9	2.5		1.6	1.2	
Glass Slide		285	286.6	288.8	531.3	532.1		1.7	1.8	2.3	2.6	2	
Carbon Tape		285	286.6	289	532.6	534		1.7	1.5	1.4	1.8	1.6	
PS Beads	Carbon Tape	285	286.3	288.2	532.9	534.6	401	1.7	1.8	2.2	2.3	2.9	2.2
PS (Sigma Aldrich)	Carbon Tape	285			530.3	532.9		1.9			3.4	3.6	
NCL PS	Glass Slide	285			531.6	534		1.7			4.3	2.8	
UV PS	Au	285	286.1		532.9			2.1	2.5		2.9		
2% DVB PS	Au	285	286.8		532.6	534.5		1.7	2		1.9	1.9	

Table 4.3: XPS binding energies and FWHM for various supporting substrates and PS overlayers.

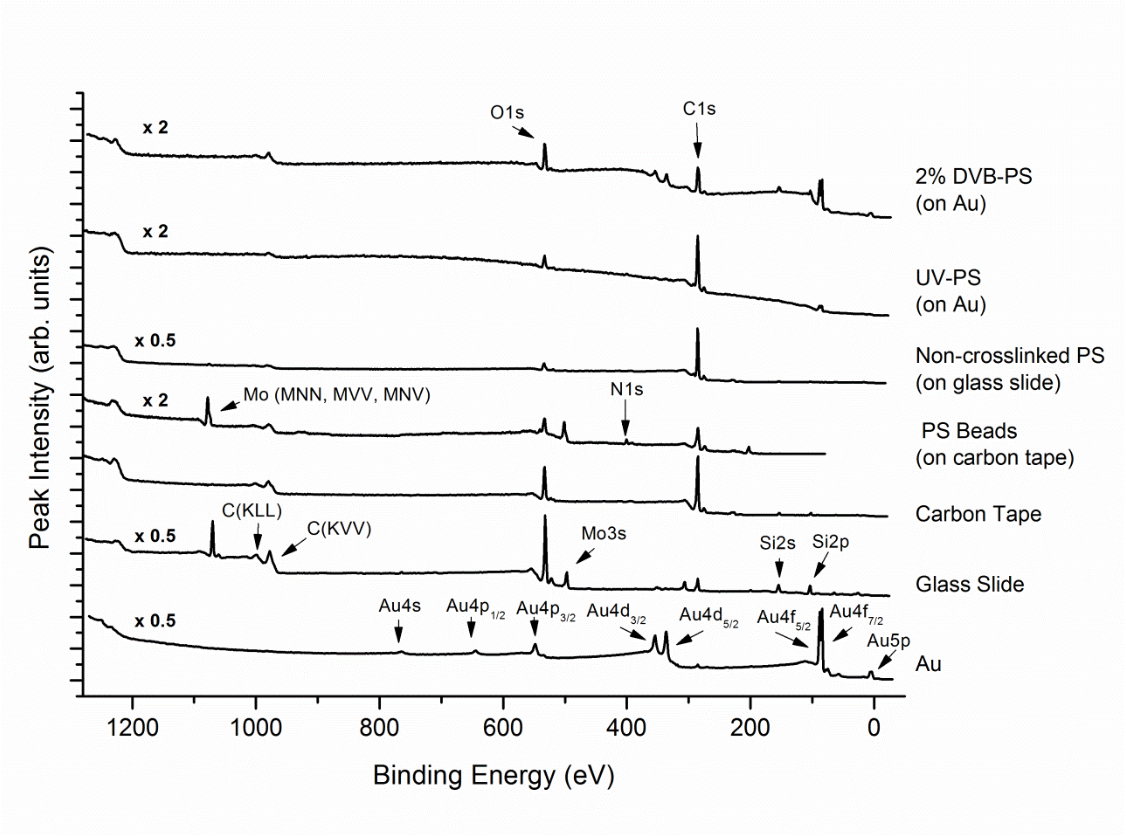

Figure 4.5: XPS wide scan spectra of various supporting substrates and polystyrene overlayers. Important photoelectron and Auger electron peaks are highlighted.

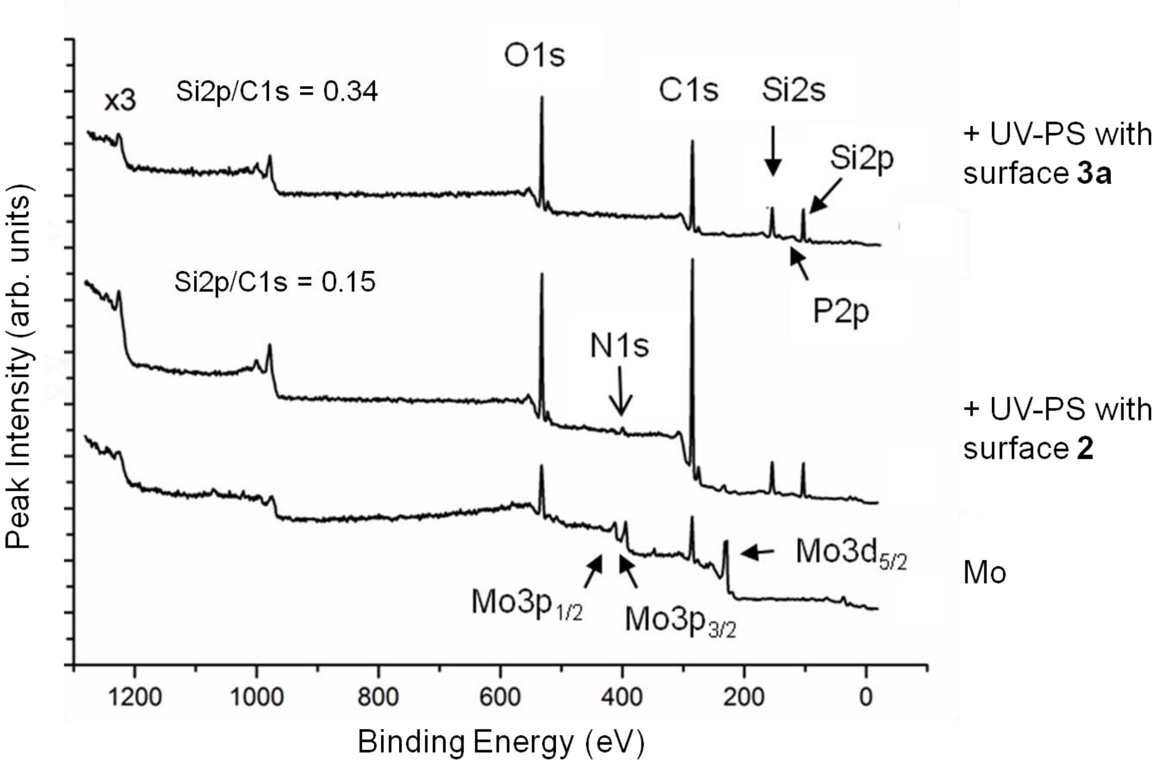

Figure 4.6: Wide Scan XPS of bare Mo; Mo with an overlayer of UV-PS with *surface* **2** (aniline, see Figure 4.2); and Mo with an overlayer of UV-PS with *surface* **3a** (phosphate disaster).

employed to follow chemical change at such surfaces required the use of unambiguous photoelectron signals, preferably those with high photo-emission cross-section and not present in polystyrene; the I, N, and P, core levels are ideal for this purpose.[47] The use of the N1s signal is particularly important, since nitrogen is added to the surfaces during all stages of the modification scheme in Figure 4.2. (i.e. N1s/C1s ratio should be ever increasing). Unfortunately, XAD-4 polystyrene beads are not compatible with this strategy as it has N1s photoelectron signal which does not originate from the underlying carbon tape, in the wide scan spectra in Figure 4.5. The manufacturer's description of these beads indicate that the polystyrene was cross-linked by DVB and an un-named initiator [48], which may contain N [e.g. azobixisobutyronitrile (AIBN)]. Therefore, non-cross linked polystyrene films, UV cross-linked films, or DVB cross-linked films using a nitrogen-free initiator were used to conduct the majority of XPS confirmation of the modification chemistry described in this chapter.

The use of silicon could be a marker of physical or chemical change on those thin films, if they are supported by glass slides. As described in section 4.3.3., an increase in the Si2p/C1s ratio could indicate the dissolution or degradation of a prepared thin film (see Table 4.1). However, the silicon signal is not expected to be a marker of chemical change on thin films not supported by glass slides. Yet, Si2s and Si2p photoelectron signal is seen on all thin films, regardless of supporting substrate, after carbene chemistry or azo-coupling is completed. To explore the origin of this signal, a UV-PS thin film was produced on a clean molybdenum metal sample and modified, as per Figure 4.2. The result of this experiment is shown in Figure 4.6. There is no Si2s or Si2p associated with a clean Mo substrate. Silicon photoelectron signal is introduced after the carbene insertion reaction, and it persists after the azo-coupling reaction. The source of this additional silicon is likely from the glassware which held various reagents, with those containing the diazo compound particularly suspect. The chemical linker could be forming reactive carbenes at room temperature, which react with the silicon-based glassware. It can be concluded that the Si XPS signal cannot be used reliably to determine film thickness etc. for intensity measurements and that this contamination is present on many of the prepared samples.

4.3.4.2 C1s Region

Before comprehensively analyzing the surface chemistry of modified polystyrene thin films, it is useful to consider the C1s region of the unmodified polystyrene thin films and XAD-4 beads. This data is shown in Figure 4.7, with associated elemental ratios and peak parameters in Tables 4.2 and 4.3, respectively. The C1s spectra were deconvoluted into one to three photoelectron peaks, with each peak having contributions from different C1s chemical environment: the first contains photoelectron signal from C-C and C-H (≈ 285.0 eV); the second has contributions from C-N (≈ 285.9) and C-O (≈ 286.5); and the third is associated with C=O (≈ 288.5 eV).[49] There is a small feature towards high binding energy, at ≈ 291.5 eV, which is characteristic of photoelectron interactions with the π-π* transitions of aromatic rings.[31, 49] Polystyrene contains many such rings within its structure, and this feature is characteristic of unmodified polystyrene films and those cross-linked with divinylbenzene.[27, 50]

The C1s spectrum can be used to compare the surface chemistry of the as-received XAD-4 polystyrene beads to those films prepared by spin-coating. Three C1s peaks could be deconvoluted from the spectrum of the unmodified XAD-4 polystyrene beads. As noted earlier, the XAD-4 beads contain nitrogen, and it is likely that much of the signal at ≈ 286 eV relates to the presence of C-N functionality. The signal at ≈ 289 eV is likely due to general oxidation by ageing in atmospheric conditions or chemical residue from the manufacturing process required to make these beads.[48, 51] By contrast, the C1s spectrum of the prepared non cross-linked polystyrene, using a nitrogen-free source of polystyrene, has the C1s character expected for unmodified polystyrene films.[27, 51] This spectrum is characterized by a single C1s signal, with no evidence of the presence of oxidized carbon. Non cross-linked polystyrene does not have signal at higher binding energies, likely because toluene exposure removes impurities. Changes to the C1s character of unmodified polystyrene should be easy to observe after this surface is modified.

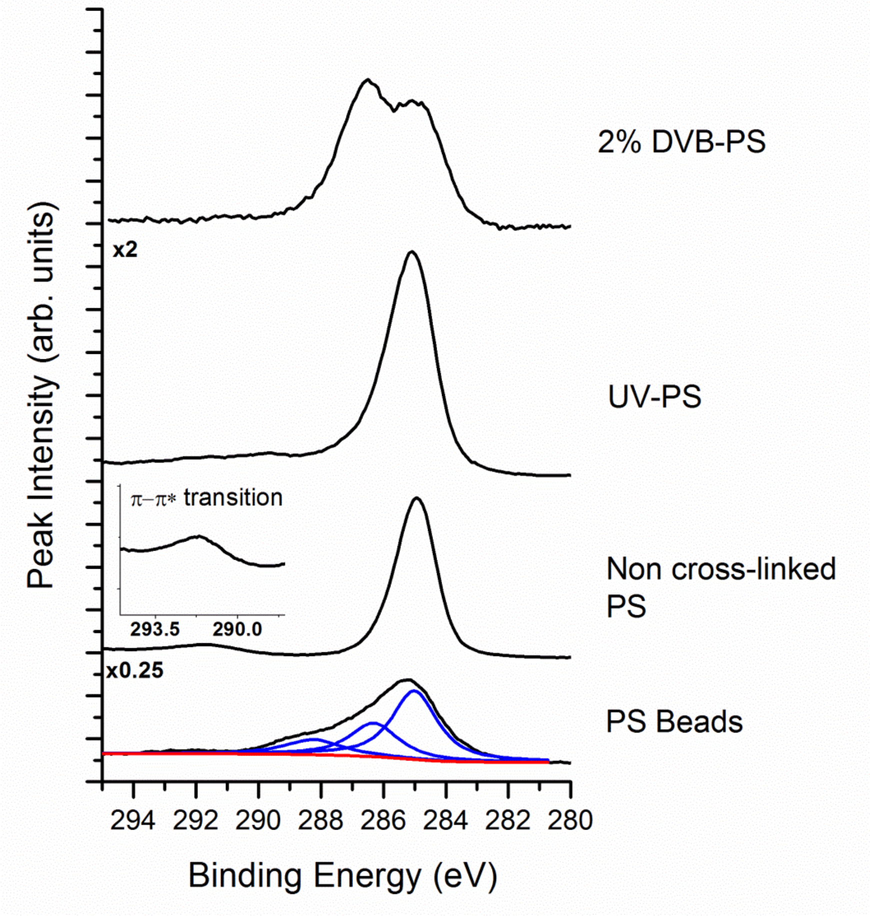

Figure 4.7: XPS of C1s region for the four types of polystyrene substrates prepared in this work. The inset highlights the presence of the π - π* transition peak at ≈ 291.5 eV.

Compared to the unmodified polystyrene thin film, UV modified films lead to a slight change in the peak shape at higher binding energies and a higher O1s/C1s ratio. This is consistent with an increased density of oxygen at its surface, which is characteristic of UV-treated polystyrene.[25] After cross-linking the unmodified polystyrene film using DVB, an intense peak at high binding energy can be seen. This peak is associated with the C-O functionality. Also, DVB cross-linked substrates have the highest O1s/C1s ratio and do not have any nitrogen content. The origin of this signal is likely the residue of benzoyl peroxide used to initiate the cross-linking of polystyrene and DVB, the dibutyl phthalate paste, and various side-products of the cross-linking reaction. Other XPS spectra of DVB cross-linked polystyrene show similar C1s lineshape.[27]

4.3.4.3 I3d region and an Investigation of the Carbene Reaction

The most important use of XPS in this study is for the confirmation of the successful insertion of the chemical linker (compound **2**) into the polystyrene thin films *via* carbene chemistry. This is best done by monitoring the photoelectron signal of an element not present in the underlying polystyrene thin films. As mentioned before, N, P, and I core levels could be used for this purpose. However, I core levels have the highest photo-emission cross section of all the elements studied in this work; this is reflected by its high atomic sensitivity factor, compared to other elements (i.e. I3d$_{5/2}$ 6 ; C1s 0.25 ; N1s 0.45 ; O1s 0.66 ; P2p 0.39). [47] Therefore, of these elements, XPS is most sensitive to added iodine. Here, iodine is introduced to UV-modified, polystyrene surfaces in the form of bis(4-iodophenyl)diazomethane, which can attach to polystyrene *via* the same carbene chemistry as compound **2**. If any iodine is present in XPS spectra after this surface is rinsed with DCM to remove any weakly bound species (i.e. *surface* **2**, Figure 4.2), then the successful, covalent attachment of bis(4-iodophenyl)diazomethane by carbene chemistry can be confirmed. This approach was taken by Wang *et al.*[20], who confirmed the reaction of this compound at diamond surfaces.

Bis(4-iodophenyl)diazomethane was reacted with UV-modified polystyrene at 120^{o}C for 20 minutes, and then washed with DCM. The wide scan XPS spectrum associated with this surface is shown in Figure 4.8. The I3d$_{5/2}$ and I3d$_{3/2}$ photoelectron peaks at ≈ 620.1 eV and ≈ 631 eV can be observed, along with those from other iodine core levels and an Auger signal at ≈ 970 eV.[45] This signal is not seen in spectra associated with unmodified polystyrene thin films (see Figure 4.5, ‘2% DVB-PS’ and ‘UV-PS’). The magnitude of the $I3d_{5/2}$ / C1s ratios seen in Table 4.4 is non-negligible. Collectively, this evidence confirms that bis(4-iodophenyl)diazomethane has been successfully attached to the UV-modified polystyrene. By extension, this conclusion would apply to the reaction of the chemical linker in Figure 4.2. (compound **2**) to any polystyrene substrate, as has been suggested elsewhere.[18]

$\Delta_{\text{step A}}$ (°C)	$I3d_{5/2}$/C1s	Grafting Density (10^{13} cm^{-2})	Time of Reaction (min.)
93	0.005	3.2	40
120	0.011	5.4	20
180	0.018	8.7	4

Table 4.4: Elemental ratios and diphenyl grafting densities associated with adsorbed diphenyl carbene compounds at *surface* **2** in Figure 4.2.

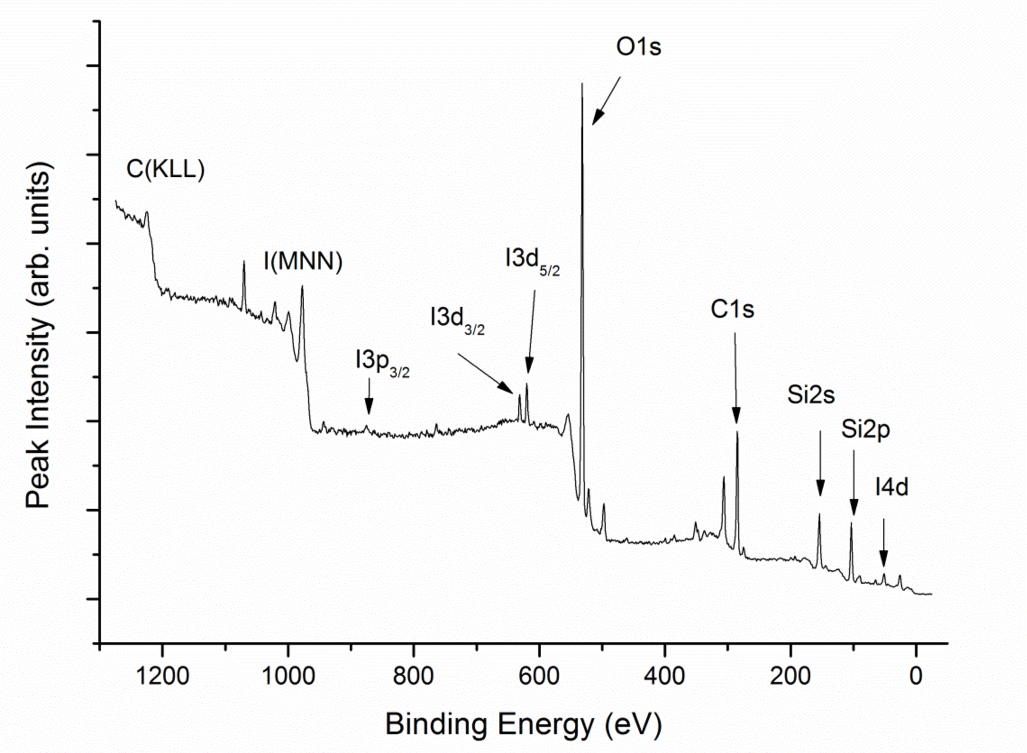

Figure 4.8: Wide scan spectra of UV-PS modified by bis(4-iodophenyl)diazomethane.

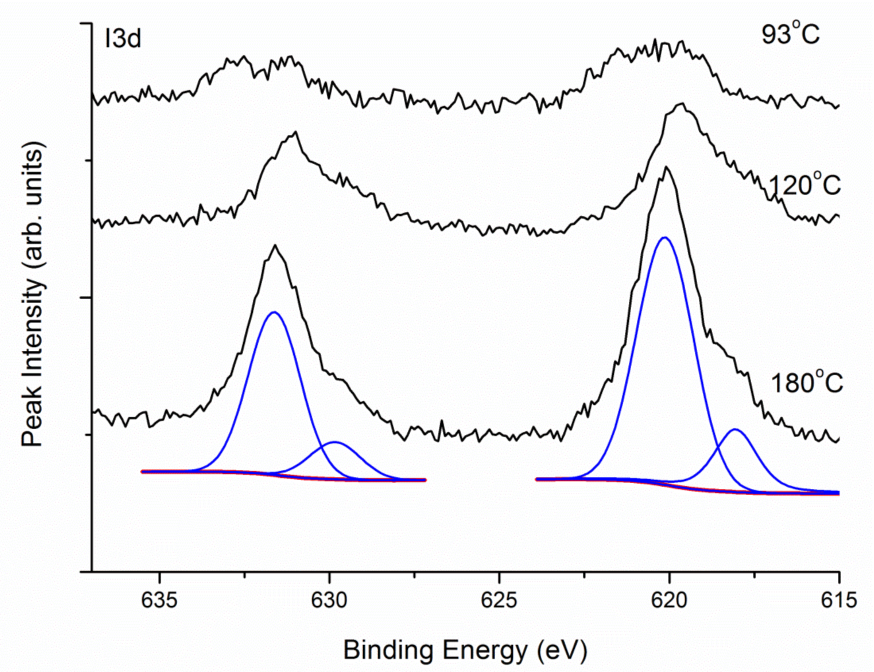

Figure 4.9: Narrow scan spectra of the I3d region after bis(4-iodophenyl)diazomethane has been deposited onto UV-PS using three different temperatures.

The nature of the attached species can be determined from the narrow scan XPS spectra associated with insertion at 120°C, as shown in Figure 4.9. The spectra clearly show the photoelectron signal from the two spin orbit states, I3d$_{5/2}$ and I3d$_{3/2}$ in more detail. Whilst these peaks have the expected binding energy, there is asymmetry to the lineshapes. This suggests that iodo groups are in two different oxidation states at this interface. Using a table of I3d$_{5/2}$ peak positions, one can assign two distinct chemical environments to these spectra.[45] When present in the anionic form (i.e. CuI , KI, NaI) the I3d$_{5/2}$ peak position is located between 618 and 619 eV, but when in molecular form (i.e. CH_3I) the I3d$_{5/2}$ peak position shifts to higher binding energies around 620.8 eV.[20, 45] Smetnowski *et al.*[52] note that when CF_3I is deposited onto diamond, the I3d$_{5/2}$ signal is at ≈ 620 eV, but shifts to lower binding energies when I binds directly to the diamond surface (≈ 619 eV), or when bound as HI (≈ 616.5 eV). Considering the above, the I3d$_{5/2}$ peak at ≈ 620.1 eV can be assigned to chemisorbed bis(4-iodophenyl)diazomethane, whilst the secondary peak at ≈ 618.1 eV is assigned to iodine adsorbed to polystyrene in some other state with more anionic character. Since the former peak is more dominant, it is reasonable to conclude that the dominant result of the carbene insertion reaction is the covalent attachment of the diarylcarbene species used here. In fact, based on the peak heights, one estimates that there is a 4:1 ratio between the chemisorbed and anionic forms of bis(4-iodophenyl)diazomethane at this interface. This conclusion is consistent with the results obtained by Wang *et al.*[20] who inferred that most of the iodine present is in chemisorbed form at a diamond surface even after washing it with DCM.

The extent of the reaction can be quantified by determining the grafting density of bis(4-iodophenyl)diazomethane to these UV-PS samples. This can be determined from the XPS data. If an atomic monolayer of bis(4-iodophenyl)diazomethane (species A) is adsorbed to a uniform and homogeneous polystyrene (species B), then the number density of adsorbed species A (n_A) can be determined from the ratio of the spectral intensities of I3d$_{5/2}$ from the overlayer (I_A) and C1s from the bulk solid (I_B)[20]:

$$\frac{I_A}{I_B} = \frac{n_A S_A}{P_A \int_0^\infty D_B S_B e^{\frac{-x}{\lambda_B}} dx} = \frac{n_A S_A}{P_A D_B S_B \lambda_B} \qquad \text{(Equation 4.1)}$$

The value of x is the depth below the surface, D_B is the carbon atomic density in the bulk, λ_B is the inelastic mean free path (IMFP) of emitted photoelectrons from the bulk solid through the overlayer, P_A is their transmission probability through the adsorbed overlayer, and S_i are the atomic surface sensitivity factors, which are obtained by dividing the bulk factors by appropriate values of IMFP.[20, 53] Here, the value for λ_B is the IMFP for a C1s photoelectron through an organic overlayer. This normally has a value between 3.1 - 3.7 nm, and here a value of 3.1 nm is used.[54-58] The IMFP for I3d$_{5/2}$ photoelectrons (λ_A) needs to be determined in order obtain a value for S_A. The value used was 2.4 nm, which is the same used by Wang *et al.*[20]. Thus, S_A is 2.5 and S_B is 0.08. The polystyrene density is 1.05 g cm^{-3}, and this was used to calculate D_B at 4.8 x 10^{22} atoms cm^{-3}. P_A was assumed to equal 1, since the adsorbed overlayer is assumed to be thinner than the IMFP of C1s photoelectrons. Using the above parameters and the spectral intensity ratio, the number of iodine atoms at the surface (n_A) can be calculated. Since there are two iodine atoms attached to each adsorbed molecule, the resultant figure was divided by two to obtain the grafting density shown in Table 4.4.

The reported grafting densities range from 3.2 – 8.7 x 10^{13} cm^{-2}. This represents about 1/10th of a closed-packed monolayer, which has been previously observed for the reaction of bis(4-iodophenyl)diazomethane with diamond surfaces.[20] If benzene were attached to a surface and oriented in a vertical arrangement, the estimated packing density would be 3.0 x 10^{14} cm^{-2}.[20] The attachment of similar molecules to surfaces - such as mercaptobiphenyl derivatives on gold (tilted arrangement), phenyl rings on diamond (vertical), and trifluororethyl esters of ω-undecenoic acid - have densities ranging from ≈1 – 3 x 10^{14} cm^{-2}.[20, 59-61] The lower grafting densities obtained here are probably related to several causes, including: low density of polystyrene [D_B for diamond (see Equation 4.1) is 4 times greater than polystyrene], diffusion of the diazo species into the bulk regions of a porous polystyrene layer, limited extent of diffusion of the diazo species at the surface, or due to differences in the kinetic, or thermodynamic, control of the insertion reaction.[20]

The optimized temperature for the carbene reaction needed to be determined. This was done by reacting bis(4-iodophenyl)diazomethane to UV-modified polystyrene at three different reaction temperatures: 93°C, 120°C, and 180°C. The I3d spectra associated with these samples are shown in Figure 4.9, and the associated I3d$_{5/2}$ / C1s ratios and grafting densities are shown in Table 4.4. These results show that the I3d peak intensities, I3d$_{5/2}$ / C1s ratios, and grafting densities increase in magnitude at higher temperatures, even when lower reaction times were used. This indicates a significant activation energy for the reaction has to be overcome, thus favoring higher reaction temperatures. Improved rates of diffusion of reactants across the surface may also occur at higher temperatures, thus increasing the probability that a molecule would find a reactive site on the surface.[62, 63]

Collectively, the XPS analysis of the $I3d_{5/2}$ region suggests that bis(4-iodophenyl)diazomethane is covalently attaced to polystyrene. Thus, one is reasonably confident that the attachment of similar molecules to polystyrene, such as the chemical linker in Figure 4.2., can be achieved *vi*a the carbene reaction.

4.3.4.4 Investigation into the Azo-Coupling Reaction

Ideally, confirmation of the azo-coupling reaction between the dialkylaniline of the chemical linker and the substituted diazonium salt (see *surface* **2** → *surface* **3**, Figure 4.2) would be made by attaching an iodine label to the diazonium salt. After attachment, the persistent presence of an $I3d_{5/2}$ photoelectron signal would then signal a successful reaction. Unfortunately, the relevant diazonium salts were not available and alternative methods had to be used to confirm the attachment of surface functionalization *via* diazonium chemistry. As mentioned before, nitrogen and phosphorous can be used as labels, since they are not present in the underlying polystyrene film. However, compared to the I3d photoelectrons, N1s and P2p photoelectrons have lower photo-emission cross-sections and thus it is harder to detect low amounts of added N or P by XPS. Phosphorous photoelectron signal has the advantage of being unique to only the azo-coupling chemistry, as it appears only at *surface* **3a** (see Figure 4.2), and not within any underlying surface. Analysis of the N1s signal is made complicated by the various species of nitrogen within the chemical linker. However, an increase in the N1s photoelectron signal should be seen when *surface* **2** (see Figure 4.2) is subsequently modified by diazonium salts terminated with amino (*surface* **3b**, Figure 4.2) or nitro groups (*surface* **3c**, Figure 4.2). In addition, the lineshapes and peak positions of the N1s spectra of an amino-terminated surface should be different to that of a nitro-terminated surface. By analyzing the N1s and P2p regions for specific reactions, the success of the azo-coupling reaction can be confirmed.

Nitrogen is in theory added when *surface* **2** (see Figure 4.2) undergoes an azo-coupling reaction with diazonium salts terminated with amino or nitro groups. Therefore, an analysis of the N1s photoelectron signal should provide the necessary evidence of successful azo-coupling. The XAD-4 polystyrene beads were the only material studied here which was terminated with amine and nitro groups was the polystyrene beads. Therefore, it is crucial to determine whether N1s analysis can be made on these substrates in light of the high nitrogen content within these beads (see Table 4.2). Unmodified XAD-4 polystyrene beads have a N1s / C1s of 0.13, which is reduced to 0.03, after these beads are terminated with the chemical linker (cf. Table 4.2. and Table 4.5). This suggests that the nitrogen signal from the untreated beads is either well-attenuated or originates from weakly bound species, which are removed during the carbene treatment or the subsequent rinse with DCM. Any remaining nitrogen should only be from covalently attached species. Considering the above, *surface* **2** (see Figure 4.2) becomes a good reference point from which the subsequent attachment of surface functionality can be proven.

Surface Termination	Label	N1s/C1s	O1s/C1s
surface **2**		0.03	0.25
COOH	3f	0.05	0.31
NH_2	3b	0.1	0.27
NO_2	3c	0.09	0.17

Table 4.5: Table of XPS elemental ratios for modified XAD-4 polystyrene beads.

At least two atoms of nitrogen are added to the surface after the azo-coupling step, which should result in an increase in the N1s/C1s ratio at fully functionalized polystyrene surfaces. This is indeed true, as shown in Table 4.5. In the case of an amine or nitro-terminated, one more nitrogen atom is added, which is reflected in the higher N1s/C1s ratio for those two surfaces compared to an carboxyl-terminated surface. The N1s/C1s ratio for the amine and nitro terminated surfaces are also approximately in a 1:1 ratio, which is expected based on the stoichiometry of the attached molecules. As an aside, the O1s/C1s ratios have been included in Table 4.5, but they are less useful for characterizing the polystyrene thin films. However, the carboxyl-terminated surface does have the highest O1s/C1s ratio, as would be expected. These results are consistent with the addition of nitrogen to the functionalized polystyrene surfaces after the azo-coupling reaction.

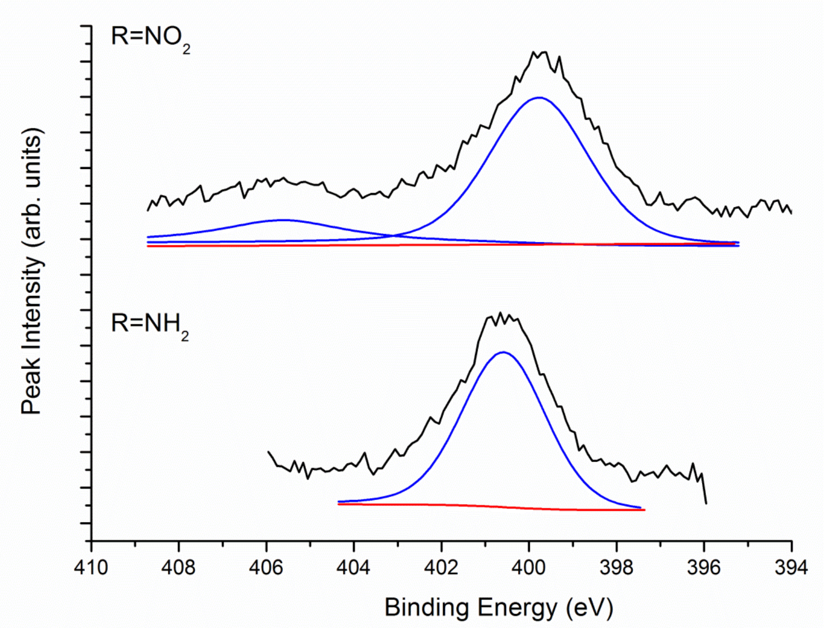

Figure 4.10: N1s region and peak fits for XAD-4 polystyrene beads with nitrogen containing surface terminations: R=NO_2 and R=NH_2.

The success of the azo-coupling reaction can also be confirmed by comparing the N1s photoelectron signal of two surfaces which contain nitrogen in different oxidation states. In the case of NO_2, the N1s peak should be at a higher binding energy and *vice versa* for the case of NH_2.[20] The N1s region for beads terminated with NO_2 and NH_2 is shown in Figure 4.10. The surface terminated with an amine group only has one photoelectron peak at ≈400.5

eV, which is expected.[20, 60] In contrast, a surface terminated with NO_2 groups produces two photoelectron peaks. Only one photoelectron peak at ≈ 405 eV is expected for a nitro-terminated surface.[20, 60] However, it is known that nitro groups, in the presence of secondary electron flux produced during an XPS experiment, can reduce to amine groups.[20, 60] Thus, the larger peak seen at the lower binding energy of ≈ 399.9 eV is probably due to this effect. The presence of a N1s peak at about 405 eV for NO_2-terminate substrates is evidence for the successful attachment of NO_2 by azo-coupling.

An estimate of the final grafting density can be attempted using the total photoelectron N1s for amine and nitro terminated surfaces, and the approach associated with Equation 4.1. The inelastic mean free path can be estimated by using the formula:

$$\lambda = B\sqrt{E_{kin}} \qquad \text{(Equation 4.2)}$$

where B is an material parameter equal to 0.087 for organic layers and E_{kin} is the energy of the photoelectron of interest.[64, 65] For an N1s photoelectron excited with Al Kα radiation through an organic overlayer, λ_A in this case is approximately 2.8 nm. Using this value and the N1s atomic sensitivity factor of 0.45, a value for S_A associated with N1s photoelectrons is equal to 0.16. The above parameters can be substituted into Equation 4.1. The grafting density of NH_2 and NO_2 can be determined by using the intensity of the NH_2 peak at ≈400.5 eV, and the NO_2 peak at ≈405 eV, respectively, for I_A in Equation 4.1. The calculated grafting density of NH_2 and NO_2 layers on polystyrene beads as 10.6×10^{14} cm^{-2} and 1.8×10^{14} cm^{-2}, respectively. These grafting densities are about 10 times higher than those seen in Table 4.4 for bis(4-iodophenyl)diazomethane terminated polystyrene thin films. They are also higher, but still comparable to, a range of molecular densities, from 2×10^{12} to 3×10^{13} cm^{-2}, found for other polystyrene beads modified using similar chemistry.[17, 66, 67] It is probable that the grafting densities calculated here are artificially higher, due to the contribution to the N1s signal by nitrogen in underlying layers. Regardless, it is clear that the azo-coupling is adding a monolayer of NO_2 or NH_2 termination to the polystyrene thin film.

Another element which can be used as an XPS diagnostic tool is the P2p photoelectron signal. The P2p spectrum of a UV cross-linked polystyrene thin film terminated with a phosphate diester is shown in Figure 4.11. A *very* weak signal is seen at 133.5 eV, which is consistent with a phosphate ester chemical environments.[64, 68] The grafting density was calculated for this sample, using the same method described in the previous paragraph, using values for λ_A and S_A - appropriate to P2p photoelectrons - which are 3.2 nm and 0.12, respectively. Using Equation 4.1, the grafting density of phosphate diesters was calculated to be 8.0 x 10^{11} cm^{-2} on UV-treated polystyrene.[20, 64, 65] This density is comparable to the molecular density of phosphate diesters attached to polystyrene beads, which were modified using the same chemistry (1.21 x 10^{12} cm^{-2}).[17] The presence of P2p photoelectron signal after the azo-coupling of a phosphate diester to the chemical linker confirms the success of the azo-coupling reaction.

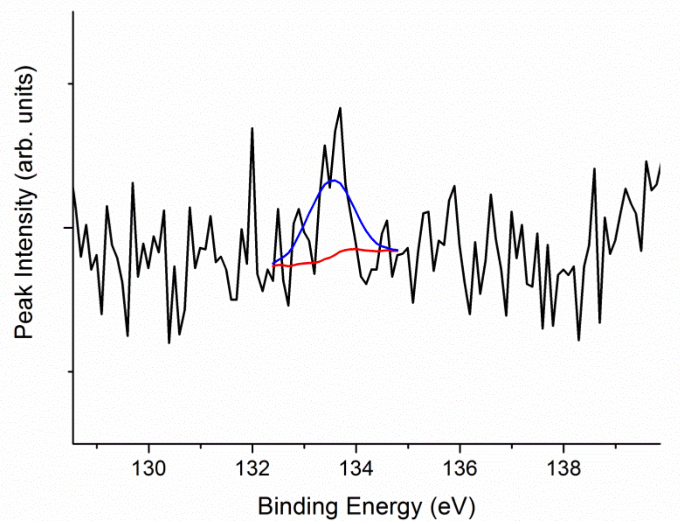

Figure 4.11: The XPS P2p region of UV cross-linked polystyrene with a phosphate diester surface.

4.3.4.5 XPS Analysis of DVB Cross-linked Polystyrene Thin Films

The above XPS studies conducted using UV-modified polystyrene thin films, but the conclusions confirm the success of the carbene and azo-coupling reactions on polystyrene materials. However, preliminary studies using QCM-D determined that these thin films were not stable during QCM-D experiments. Fortunately, an alternative cross-linked polystyrene thin film had been prepared. Earlier, it was shown that by cross-linking polystyrene with DVB made the film most resilient to the chemical conditions and reactions employed here (see section 4.3.2). It was these films which were ultimately used in the QCM-D applications described in Chapter 5. Whilst the two film types of polystyrene should behave similarly, some limited experiments were carried out to investigate the use of the carbene chemistry for the DVB films. This is the topic of this section.

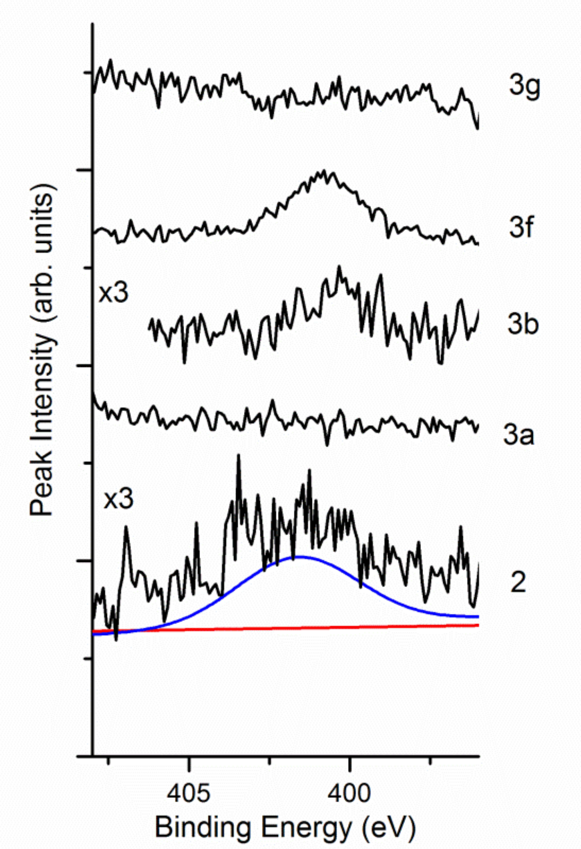

Figure 4.12: The XPS N1s region of 2 % DVB cross-linked polystyrene on top of two underlying substrates: gold (**3a**, **3g**) and glass slides (**2**,**3b**, **3f**).

The polystyrene thin films here were prepared as outlined in section 4.3.1., but with the thin film spin-coated onto Au-coated silicon squares, in order to mimic the presence of this thin film on a QCM-D crystal. Many of the surface terminations noted in Figure 4.2 are studied here, including *surface **2*** and *surfaces* **3a**, **3d**, **3g**. For comparison, two other terminations (*surfaces* **3b** and **3f**, Figure 4.2) were completed on UV- treated polystyrene

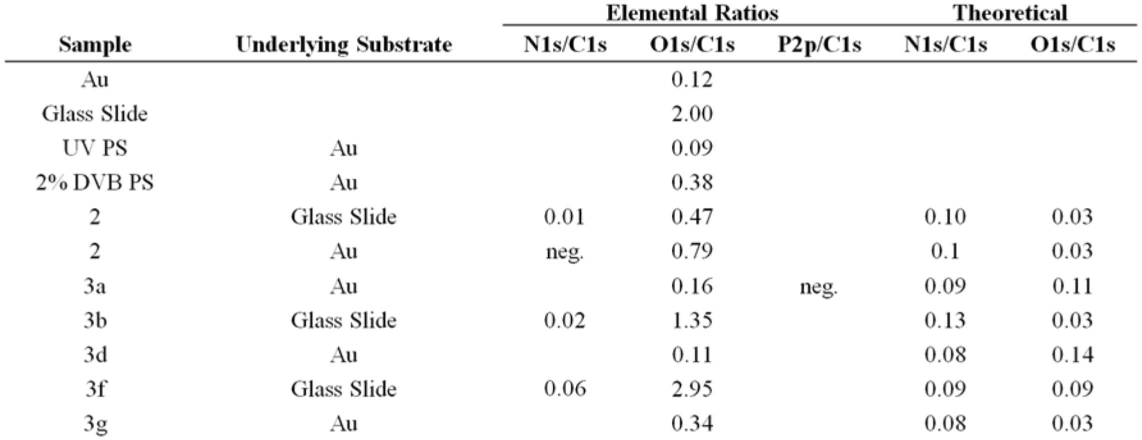

Sample	Underlying Substrate	Elemental Ratios N1s/C1s	O1s/C1s	P2p/C1s	Theoretical N1s/C1s	O1s/C1s
Au			0.12			
Glass Slide			2.00			
UV PS	Au		0.09			
2% DVB PS	Au		0.38			
2	Glass Slide	0.01	0.47		0.10	0.03
2	Au	neg.	0.79		0.1	0.03
3a	Au		0.16	neg.	0.09	0.11
3b	Glass Slide	0.02	1.35		0.13	0.03
3d	Au		0.11		0.08	0.14
3f	Glass Slide	0.06	2.95		0.09	0.09
3g	Au		0.34		0.08	0.03

Table 4.6: Elemental Ratios of differently terminated polystyrene samples, with a focus on 2% DVB cross-linked polystyrene (**2**, **3a**, **4d**, **3g**) and some UV cross-linked polystyrene (**3b**, **3f**).

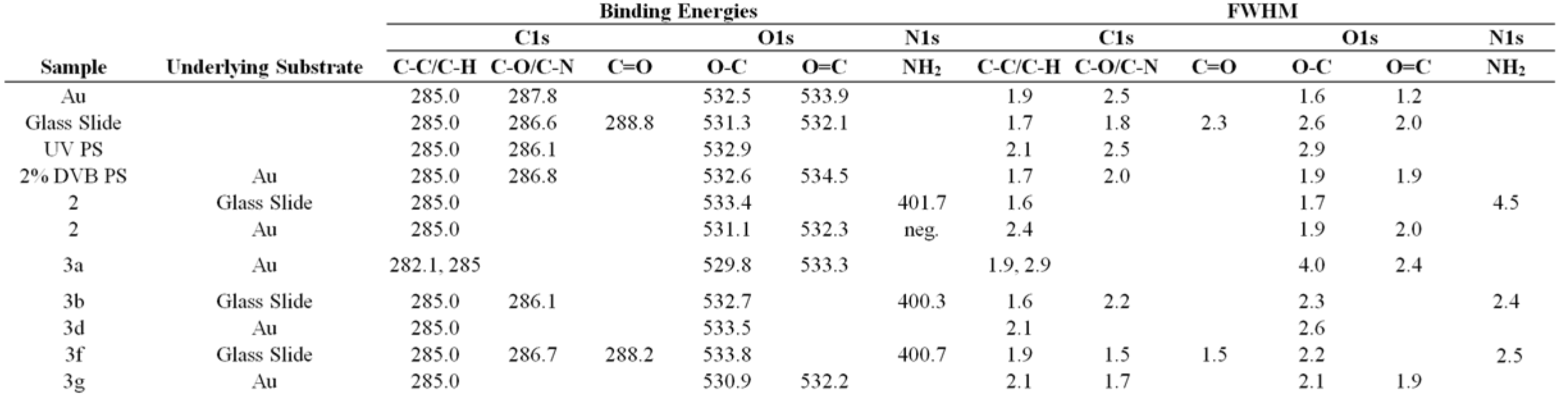

		Binding Energies						FWHM					
		C1s			O1s		N1s	C1s			O1s		N1s
Sample	Underlying Substrate	C-C/C-H	C-O/C-N	C=O	O-C	O=C	NH_2	C-C/C-H	C-O/C-N	C=O	O-C	O=C	NH_2
Au		285.0	287.8		532.5	533.9		1.9	2.5		1.6	1.2	
Glass Slide		285.0	286.6	288.8	531.3	532.1		1.7	1.8	2.3	2.6	2.0	
UV PS		285.0	286.1		532.9			2.1	2.5		2.9		
2% DVB PS	Au	285.0	286.8		532.6	534.5		1.7	2.0		1.9	1.9	
2	Glass Slide	285.0			533.4		401.7	1.6			1.7		4.5
2	Au	285.0			531.1	532.3	neg.	2.4			1.9	2.0	
3a	Au	282.1, 285			529.8	533.3		1.9, 2.9			4.0	2.4	
3b	Glass Slide	285.0	286.1		532.7		400.3	1.6	2.2		2.3		2.4
3d	Au	285.0			533.5			2.1			2.6		
3f	Glass Slide	285.0	286.7	288.2	533.8		400.7	1.9	1.5	1.5	2.2		2.5
3g	Au	285.0			530.9	532.2		2.1	1.7		2.1	1.9	

Table 4.7: Binding Energies and FWHM of peak fitting for XPS spectra of modified polystyrene samples, with a focus on 2% DVB cross-linked polystyrene (**2**, **3a**, **4d**, **3g**) and some UV cross-linked polystyrene (**3b**, **3f**).

supported by a glass microscopy slide. Various XPS analyses will be discussed, including: the N1s region (Figure 4.12), the C1s region (Figure 4.13), and the O1s region (Figure 4.14). All the relevant elemental ratios (i.e. O1s/C1s and N1s/C1s) are shown in Table 4.6, with the parameters of the peak fits shown in Table 4.7.

As described in section 4.3.4.4, the N1s spectrum can be used to confirm the attachment of nitrogen-containing functional groups by azo-coupling, using *surface* **2** (Figure 4.2) as a control. The change of lineshapes in Figure 4.12, and the trends of the N1s/Cs ratios in Table 4.6, show that modification of *surface* **2,** *via* azo-coupling, either increases the N1s signal or decreases the N1s signal, depending on the surface termination. When this process results in a surface terminated with a hexyl or phosphate group, negligible N1s content can be found at these surfaces. By contrast, when this chemistry leads to acid or amine termination, the N1s photoelectron signal increases, as does its N1s/C1s ratio, compared to the control. Attenuation of underlying N1s signal or varying reaction yields of the coupling reaction may explain the above results. Longer chain lengths are known to attenuate photoelectron signal in hydrocarbon substrates[69], thus explaining the reduced N1s signal for the addition of hexyl and phosphate diester, compared to the acid and amine functionalities. Reaction yields may be lowered due to the presence of bulky subtituents or increased by having an electron withdrawing substituent on the diazo compound (n.b. more positive diazo groups act as better electrophiles in the azo-coupling reaction mechanism.[70]) Of course, the two above mentioned phenomena could be occuring simultaneously.

The C1s and the O1s spectra also useful for characterizing the modified DVB cross-linked surfaces, but their utility is less than that of the N1s signal. The C1s and O1s spectra are shown in Figures 4.13 and 4.14, respectively. There is little change to the C1s region between samples, with the exception the DVB cross-linked polystyrene case, which was described in section 4.3.4.2. The lack of obvious changes to the C1s spectra here, render this

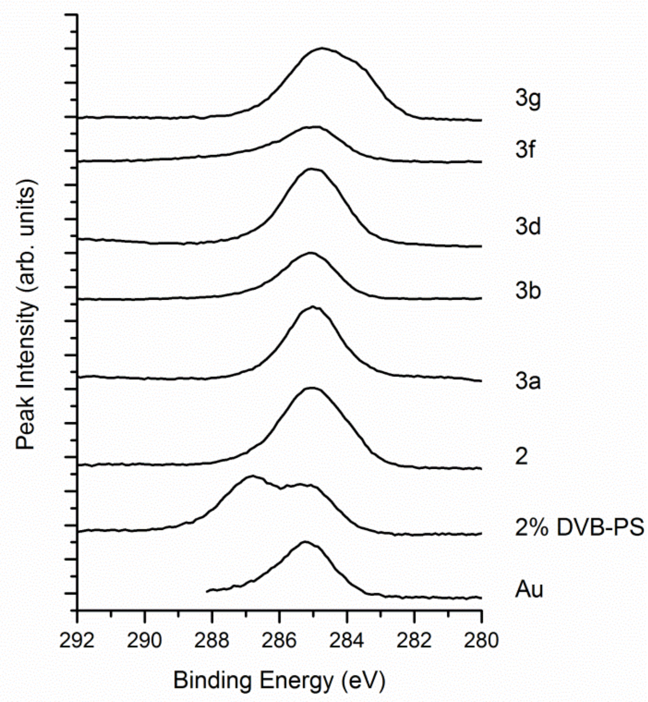

Figure 4.13: The XPS C1s region of 2 % DVB cross-linked polystyrene. Two underlying substrates were used: gold (2 % DVB PS, **2**, **3a**, **3d**, **3g**) and glass slides (**3b**, **3f**).

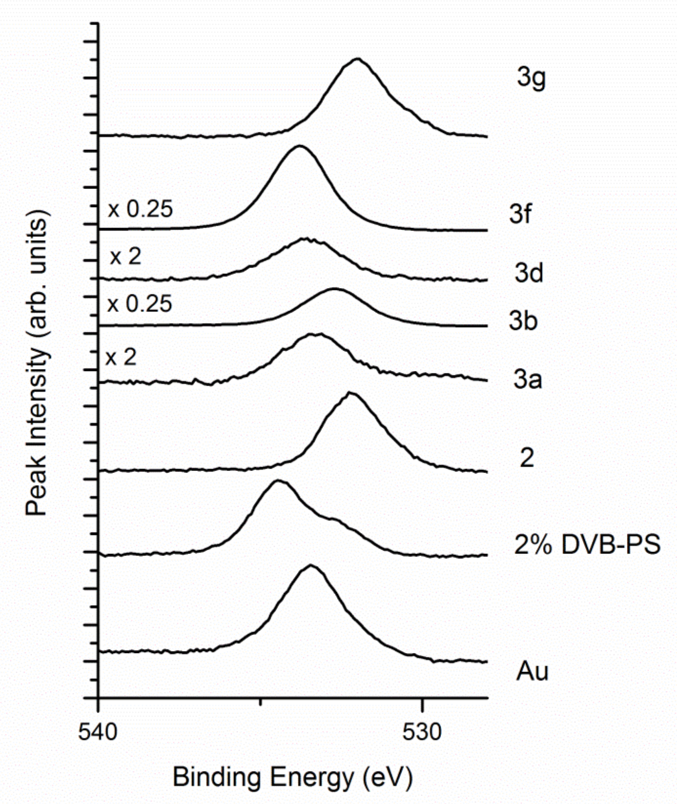

Figure 4.14: The XPS O1s region of 2 % DVB cross-linked polystyrene. Two underlying substrates were used: gold (2 % DVB PS, **2**, **3a**, **3d**, **3g**) and glass slides (**3b**, **3f**)

region unsuitable for the characterization of the thin films studied in this section. On the other hand, there are discernible changes in the O1s spectra, which make this region more useful to this XPS analysis.

The O1s photoelectron peaks seen in Figure 4.14 can be deconvoluted into two chemical environments. O1s peaks at ≈ 532 eV are associated with the C-O chemical environment, whilst peaks at ≈ 534.5 eV originate from carbonyl or carboxyl environments.[25] This distinction is most obvious for the spectrum associated with an unmodified DVB cross-linked polystyrene in Figure 4.14. The increased carbonyl/carboxyl content at this surface is due to the presence of residual benzoyl peroxide and dibuytl phthalate involved in the cross-linking reaction. Most of this residue is removed or underlying O1s signal attenuated, after the insertion of the chemical linker (i.e. *surface* **2**, Figure 4.2). The new lineshape is consistent with the addition of ether functionality, which is part of the chemical linker. Oxygen-rich surface functionality, such as the **3a**, **3d**, and **3f**, are associated with O1s peaks having higher binding energy and higher O1s/C1s ratios in Table 4.6. Shifts to lower binding energy for some functionalities (**3b** and **3g**) are consistent with their lower oxygenated character. However, their high oxygen content (see Table 4.6) is unexpected, and may be related to sample ageing in an atmospheric environment. [25, 51] In general, the above is consistent with successful azo-coupling of the DVB cross-linked films.

4.3.4.6 Film Thickness using XPS and Ellipsometry

To ensure a consistent response from the QCM-D apparatus, films placed on top of the QCM-D quartz crystals should be less than 100 nm thick.[71] Therefore, it is crucial to confirm whether the as-prepared polystyrene films are less than 100 nm thick. This can be accomplished using both XPS and ellipsometry.[46, 72] Using XPS, the thickness of hydrocarbon overlayers on top of gold can be obtained using the following expression[46]:

$$I_s = I_o e^{-\lambda/t} \qquad \text{(Equation 4.3)}$$

where I_s is the Au4$f_{7/2}$ peak intensity of the sample of interest, I_o is the peak intensity of the cleaned gold substrate, λ is the IMFP of Au4$f_{7/2}$ through a hydrocarbon, and *t* is the sample thickness. All peak intensity values were normalized relative to their spectrometer background signal above the Fermi energy level.[46] The value for λ used was 3.3 nm, as estimated by Equation 4.2. This value of λ is higher than the IMFP for a C1s photoelectron (3.1 nm), as expected, but it is lower than other possible literature values (3.7 to 4.2 nm), reflecting the uncertainty concerning the exact values of these parameters.[46] The calculated XPS thickness for unmodified and modified DVB cross-linked, polystyrene thin films ranges from 4 – 9 nm, as shown in Table 4.8. The results exhibit a trend towards increasing thickness after each modification step, as expected. In general, these results are consistent with other spin-coated polymer films.[46] The results here indicate that these as-prepared polystyrene films are in the range of recommended film thickness for QCM-D application, and are further evidence for successful modification of the thin films.

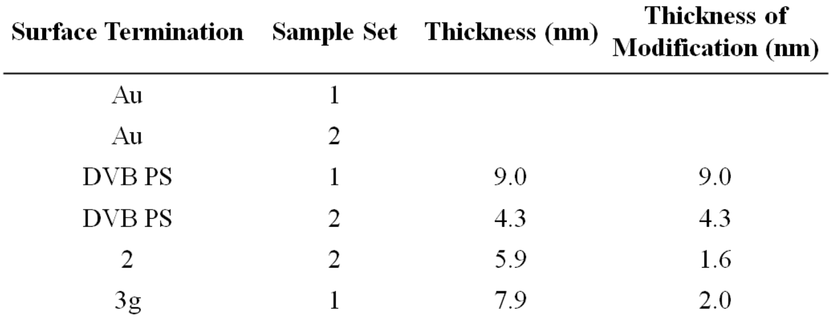

Surface Termination	Sample Set	Thickness (nm)	Thickness of Modification (nm)
Au	1		
Au	2		
DVB PS	1	9.0	9.0
DVB PS	2	4.3	4.3
2	2	5.9	1.6
3g	1	7.9	2.0

Table 4.8: Thickness of various polystyrene thin films obtained using XPS. Errors in the absolute values are approximately ± 0.1 nm. Sample thicknesses are best compared within a sample set. The thickness of the modification is approximated by subtracting the thickness of the previous modification (e.g. t_{3g}–t_2 = thickness of added hexyl chain).

Sample	Thickness (nm)	Thickness of Modification (nm)	S.D. (± nm)
DVB PS	82.4		> 6.9
2	88.9	6.5	1.5
3a	91.7	9.3	2.1
3b	92.9	10.5	6.9
3d	90.2	7.8	3.4
3f	95.2	12.8	<0.01
3g	94.8	12.4	2.2

Table 4.9: Ellipsometric thickness of unmodified and modified, DVB cross-linked, polystyrene films. The thickness of the modification is approximated by subtracting the thickness of the previous modification (i.e. $t_{3g} - t_2$ = thickness of added hexyl chain).

The thicknesses obtained using ellipsometry are found in Table 4.9. All the ellipsometric thicknesses are less than 100 nm, which further confirms the suitability of the as-prepared polystyrene surfaces for QCM-D use. Again, the trend towards increased thickness after the azo-coupling reaction is observed in these results. However, the thickness values obtained here are 8 times higher than those obtained using XPS. Two possible reasons for the large discrepancy exist: first, islands of exposed Au within the interface could artificially increase the $Au4f_{7/2}$ photoelectron signal, which has the consequence of lowering the XPS thickness value; second, the polystyrene-gold interface could have air pockets, or other inhomogeneities which could interfere with the ellipsometric measurements. [73] Also, the XPS and ellipsometry techniques are conducted in two different environments, with the former in UHV conditions and the latter in ambient conditions. This would certainly affect the amount of solvent present within the thin film, as each environment has very different solvent evaporation or sublimation rates. A high solvent content would increase polymer swelling and thus, a larger apparent thickness values would be detected.[26] Therefore, the ellipsometric and XPS thicknesses should be considered as qualitative, not quantitative measures of thin film thickness. At minimum, both techniques confirm that the as-prepared thin films are less than 100 nm thick and are suitable for QCM-D analysis.

4.3.5 Contact Angle Measurements

Surface modifications using the carbene chemistry attempted here are known to change the surface wettability of polystyrene.[17] Contact angle measurements were conducted on modified DVB cross-linked polystyrene and the results are shown in Table 4.10. First, it is apparent that the contact angle values do not have a large range – only 16.6^o. This was not expected, as the chemistry involved is known to impart a wide range of wettability (range from 37^o – 73^o) to polymeric beads, as recently shown by Choong *et al*..[17] However, it is important to note that contact angles were measured differently here than in their study. Choong *et al.*[17] placed a curved bead on the surface of a water droplet and measured the contact angle in side-elevation – the so-called “floating” contact angle measurement.[74] Here, the traditional method was used, in which a water droplet it placed on a thin film, with the contact angle measured in side elevation. Surface roughness is also a factor known to affect contact angle measurements.[75] Despite these issues, we see that a surface terminated by hexyl or an amine group makes a DVB cross-linked polystyrene surface more hydrophobic, whilst the addition of a phosphate diester makes the surface more hydrophilic. Such trends are still consistent with the trends seen for the similarly modified polystyrene beads.[17] Contact angle data supports the broad view that the surfaces have been modified as depicted by Figure 4.2.

Sample	Termination	Contact Angle (degrees)	S.D.$_{\text{Contact Angle}}$ (± degrees)
δ-PS	δ-PS	87.2	3.8
2	chemical linker	83.6	6.3
3a	$CH_2P(O)(OEt)_2$	82.6	4.4
3b	NH_2	99	3.2
3d	$O(CH_2CH_2O)_3CH_3$	92.9	7.9
3e	H	89.8	2.9
3f	CH_2COOH	91.1	4.8
3g	C_6H_{13}	94.3	6.9

Table 4.10: Contact angles of unmodified and modified DVB cross-linked polystyrene.

4.5 Summary and Conclusions

A variety of unmodified, cross-linked, and modified polystyrene surfaces were synthesized and their surfaces were characterized by XPS, optical microscopy, ellipsometry, and contact angle measurements. The above investigation has lead to a series of conclusions:

- Of the polystyrene thin films studied here, a film with 2 % content of divinylbenzene is the most stable to the carbene and azo-coupling chemistry used to modify them.
- The carbene insertion step is quite harsh to the polystyrene films, but the use of solvents with higher dipole moments, and polystyrene with a high cross-linking, ensures successful modification with less damage to the polystyrene thin film.
- By using several techniques, particularly the XPS technique, the surface characterization of polystyrene thin films modified by carbene and azo-coupling was conducted for the first time. Evidence for the successful attachment of a diaryl, diazo chemical linker to the thin films *via* carbene chemistry was determined by

analysis of the I3d photoelectron signal. Also, chemical evidence for the attachment of a variety of diazonium salts to the terminal aniline group on this chemical linker was also found by XPS. This evidence supported the view that successful modification of polystyrene thin films occurred, as depicted in Figure 4.2.

- Spin-coated films of DVB cross-linked polystyrene are within the thickness range recommended for QCM-D application (i.e. < 100 nm).

The surface characterization done here further supports the consensus that this carbene and azo-coupling modification scheme is successfully changing the macro-chemistry of materials. This study also suggests ways in which the modification process can be optimized to prevent degradation of materials to which this industrial process is applied. Finally, the stability and low thickness of the optimized DVB cross-linked polystyrene thin films suggests that they can be used in protein adsorption studies by QCM-D. The imminent real-world application of these coatings on polymers for biomedical use makes such protein adsorption studies both timely and necessary.

References

[1] M.B. Patel, S.A. Patel, A. Ray, *et al.*, J. Appl. Polym. Sci., 89 (2003) 895.

[2] E.S. Park, H.J. Lee, H.Y. Park, *et al.*, J. Appl. Polym. Sci., 80 (2001) 728.

[3] E. Ranucci, P. Ferruti, Polymer, 32 (1991) 2876.

[4] A. Roosjen, W. Norde, H.C.v.d. Mei, *et al.*, Prog. Colloid Polym. Sci., 132 (2006) 138-144.

[5] E.R. Kenawy, S.D. Worley, R. Broughton, Biomacromolecules, 8 (2007) 1359-1384.

[6] A.G. Gristina, Science, 237 (1987) 1588-1595.

[7] B. Zdyrko, V. Klep, X. Li, *et al.*, Materials Science and Engineering: C, 29 (2009) 680-684.

[8] M. Rai, A. Yadav, A. Gade, Biotechnol. Adv., 27 (2009) 76-83.

[9] S. Perni, C. Piccirillo, J. Pratten, *et al.*, Biomaterials, 30 (2009) 89-93.

[10] V. Sambhy, B.R. Peterson, A. Sen, Langmuir, 24 (2008) 7549-7558.

[11] C.M. Grozea, G.C. Walker, Soft Matter, 5 (2009) 4088-4100.

[12] A. Muñoz-Bonilla, M. Fernández-García, Prog. Polym. Sci., 37 (2012) 281-339.

[13] L. Ferreira, A. Zumbuehl, J. Mater. Chem., 19 (2009) 7796-7806.

[14] E. Ostuni, R.G. Chapman, R.E. Holmlin, *et al.*, Langmuir, 17 (2001) 5605-5620.

[15] C.D. Bain, G.M. Whitesides, Angew. Chem. Int. Ed., 28 (1989) 506-512.

[16] K.M. Awenat, P.J. Davis, M.G. Moloney, *et al.*, Chem. Commun., (2005) 990-992.

[17] C. Choong, J. Foord, J.-P. Griffiths, *et al.*, New J. Chem., 36 (2012) 1187-1200.

[18] M.G. Moloney, J. Phys. D: Appl. Phys., 41 (2008) 174006.

[19] E. Parker, Surface Active Polymers as Anti-infective and Antibiofouling Materials, in: D.Phil. Thesis, Organic Chemistry, University of Oxford, U.K. (2012).

[20] H. Wang, J.-P. Griffiths, R.G. Egdell, *et al.*, Langmuir, 24 (2008) 862-868.

[21] M.E. Hyde, T.J. Davies, R.G. Compton, Angew. Chem. Int. Ed., 44 (2005) 6491-6496.

[22] M.M. Browne, G.V. Lubarsky, M.R. Davidson, *et al.*, Surf. Sci., 553 (2004) 155-167.

[23] K. Reimhult, K. Petersson, A. Krozer, Langmuir, 24 (2008) 8695-8700.

[24] G.T. Carroll, M.E. Sojka, X. Lei, *et al.*, Langmuir, 22 (2006) 7748-7754.

[25] D. Zhang, S.M. Dougal, M.S. Yeganeh, Langmuir, 16 (2000) 4528-4532.

[26] R. Zhang, T. Cherdhirankorn, K. Graf, *et al.*, Microelectron. Eng., 85 (2008) 1261-1264.

[27] T. Pongprayoon, N. Yanumet, E.A. O'Rear, *et al.*, J. Colloid Interface Sci., 281 (2005) 307-315.

[28] F. Höök, Development of a Novel QCM Technique for Protein Adsorption Studies, in: Ph.D. Thesis, Chalmers University, Sweden, (1997).

[29] P. Jiang, M.J. McFarland, J. Am. Chem. Soc., 126 (2004) 13778-13786.

[30] F.C. Krebs, Sol. Energy Mater. Sol. Cells, 93 (2009) 394-412.

[31] F. Clément, B. Held, N. Soulem, *et al.*, The European Physical Journal - Applied Physics, 18 (2002) 135-151.

[32] M. Chakraborty, D. Chowdhury, A. Chattopadhyay, J. Chem. Educ., 80 (2003) 806.

[33] M. Antonietti, H. Sillescu, M. Schmidt, *et al.*, Macromolecules, 21 (1988) 736-742.

[34] S. Al Akhrass, R.-V. Ostaci, Y. Grohens, *et al.*, Langmuir, 24 (2008) 1884-1890.

[35] LOT-Europe, Sensor Crystals, in: Belgium, June 6, 2012. <http://www.lot-oriel.com/ru/en/home/qsense/sensorcrystals>

[36] M.I. Smith, J.S. Sharp, Langmuir, 27 (2011) 8009-8017.

[37] "Physical Constants of Organic Compounds", in: R.C. Weast (Ed.) Handbook of Chemistry and Physics, CRC Press, Cleveland, Ohio, (1972) p. C494.

[38] J. Zhao, S. Jiang, Q. Wang, *et al.*, Appl. Surf. Sci., 236 (2004) 131-140.

[39] D. Briggs, "XPS: Basic Principles, Spectral Features, and Qualitative Analysis", in: David Briggs, J.T. Grant (Eds.) Surface Analysis by Auger and X-ray Photoelectron Spectroscopy, IM Publications and Surface Spectra Ltd., Charlton, UK (2003), pp. 31-56.

[40] "Selected Values of Electric Dipole Moments for Molecules in the Gas Phase", in: R.C. Weast (Ed.) Handbook of Chemistry and Physics, CRC Press, Cleveland, Ohio, (1972) pp. E51-E54.

[41] J. Clayden, N. Greeves, S. Warren, *et al.*, "Nucleophilic Substitution at C=O with loss of Carbonyl Oxygen", in: Organic Chemistry, Oxford University Press, Oxford, (2001) pp. 353-429.

[42] J.R. Wunsch, Polystyrene – Synthesis, Production and Applications, Smithers Rapra Publishing (2000).

[43] X. Wang, X. He, G. Huang, *et al.*, Polymer, 53 (2012) 665-672.

[44] M. Erber, A. Khalyavina, K.J. Eichhorn, *et al.*, Polymer, 51 (2010) 129-135.

[45] C.D. Wagner, A.V. Naumkin, A. Kraut-Vass, *et al.*, "NIST X-ray Photoelectron Spectroscopy Database", in: N.I.o.S.a.T. (NIST) (Ed.), U.S. Secretary of Commerce, USA, Washington, USA (2007).

[46] G.W. Nelson, M. Perry, S.-M. He, *et al.*, Colloid Surface B, 78 (2010) 61-68.

[47] C.D. Wagner, "Auger and X-ray Photoelectron Spectroscopy", in: D. Briggs, M.P. Seah (Eds.) Practical Surface Analysis, J.Wiley and Sons (1990).

[48] R.A. Haas, Amberlite XAD-4 Industrial Grade Polymeric Adsorbent, (2001) p. 4. <http://www.dow.com/assets/attachments/business/process_chemicals/amberlite_xad/amberlite_xad4/tds/amberlite_xad4.pdf>

[49] D. Briggs, J.T. Grant, "Polymer C1s Chemical Shifts", in: Surface Analysis by Auger and X-ray Photoelectron Spectroscopy, IM Publications, Charlton, UK (2003), p. 900.

[50] S.B. Idage, S. Badrinarayanan, Langmuir, 14 (1998) 2780-2785.

[51] J. Larrieu, B. Held, H. Martinez, *et al.*, Surf. Coat. Technol., 200 (2005) 2310-2316.

[52] V.S. Smentkowski, J.T. Yates Jr, X. Chen, *et al.*, Surf. Sci., 370 (1997) 209-231.

[53] C.D. Wagner, L.E. Davis, M.V. Zeller, *et al.*, Surf. Interface Anal., 3 (1981) 211.

[54] S. Tanuma, “Electron Attenuation Lengths”, in: D. Briggs, J.T. Grant (Eds.) Surface Analysis by Auger and X-ray Photoelectron Spectroscopy, IM Publications and Surface Spectra Limited, London (2003) p. 900.

[55] C.J. Powell, A. Jablonski, NIST Electron effective-Attenuation-Length Database: Version 1.3, SRD 82, National Institute of Standards and Technology, Gaithersburg, MD (2011).

[56] R.W. Paynter, M. Ménard, H. Benalia, Plasma Processes and Polymers, 1 (2004) 111-122.

[57] J.C. Ashley, M.W. William, Radiat. Res., 81 (1980) 364-373.

[58] C.D. Bain, G.M. Whitesides, J. Phys. Chem., 93 (1989) 1670-1673.

[59] A. Ulman, Acc. Chem. Res., 34 (2001) 855-863.

[60] S.Q. Lud, M. Steenackers, R. Jordan, *et al.*, J. Am. Chem. Soc., 128 (2006) 16884-16891.

[61] T. Strother, T. Knickerbocker, J.N. Russell, *et al.*, Langmuir, 18 (2002) 968-971.

[62] M. Aglietto, R. Alterio, R. Bertani, *et al.*, Polymer, 30 (1989) 1133-1136.

[63] D.A. Olsen, A.J. Osteraas, J. Appl. Polym. Sci., 13 (1969) 1523-1535.

[64] M. Textor, L. Ruiz, R. Hofer, *et al.*, Langmuir, 16 (2000) 3257-3271.

[65] M.P. Seah, W.A. Dench, Surf. Interface Anal., 1 (1979) 2-11.

[66] D. Leonard, M.G. Moloney, C. Thompson, Tetrahedron Lett., 50 (2009) 3499-3502.

[67] J. Bernard, C. Branger, T.L.A. Nguyen, *et al.*, React. Funct. Polym., 68 (2008) 1362-1370.

[68] A.M. Puziy, O.I. Poddubnaya, A.M. Ziatdinov, Appl. Surf. Sci., 252 (2006) 8036-8038.

[69] J.P. Folkers, P.E. Laibinis, G.M. Whitesides, Langmuir, 8 (1992) 1330-1341.

[70] J. March, M.B. Smith, Advanced Organic Chemistry: Reactions, Mechanisms, and Structure, 5 ed., John Wiley and Sons, Inc., New York (2001).

[71] M.C. Dixon, J. Biomol. Tech., 19 (2008) 151.

[72] F. Höök, J. Vörös, M. Rodahl, *et al.*, Colloid Surface B, 24 (2002) 155-170.

[73] S. Guo, E. Hedborg, I. Lundström, *et al.*, Thin Solid Films, 293 (1997) 179-184.

[74] G.V. Lubarsky, M.R. Davidson, R.H. Bradley, Appl. Surf. Sci., 227 (2004) 268-274.

[75] R.J. Good, J. Adhes. Sci. Technol., 6 (1992) 1269-1302.

5. Protein Adsorption on Carbene Modified Polystyrene Thin Films

5.1 Introduction

5.1.1 Background

Coating technologies which are either bio-active or bio-resistant are of importance in such areas as advanced biosensors, medical devices, food packages, and marine surfaces (i.e. pipelines, ship hulls).[1, 2] There are many efforts to optimize these coatings[3-5], and one such effort was described in the previous chapter. There, polystyrene was modified with a chemical linker *via* carbene chemistry, which is subsequently modified to change the surface chemistry of the polymer. The technique is simple, and promises to create a range of robust and commercially viable bio-materials. The development of long-lasting and effective coatings is key to the controlled use of organic materials in biological environments. Since the adsorption of proteins is a known precursor to subsequent cell attachment and growth[1], one means to test the relative bio-activity or bio-resistance of any given coating is to conduct protein adsorption studies on the surface.

Protein studies, particularly for the early stages of adsorption, have the benefit of elucidating the fundamental mechanisms and chemical interactions which govern the adsorption of proteins at the solid-liquid interfaces.[1, 6, 7] Protein adsorption studies have been done on polystyrene[8, 9], as well as other materials, including: self-assembled monolayers[4, 10], synthesized polymers[3, 11, 12], metal oxides (e.g. TiO_2 [13, 14]), and metallic surfaces (e.g. gold[13, 15], stainless steel[16]). Examples of protein adsorption studies include those involving, the serum albumins (human (HSA) and bovine (BSA)[17-21], fibronectin[13], fibrinogen[22], lysozyme[23] and β-lactoglobulin[24], among others. These protein studies have not been limited to a single technique, with optical methods[14], infrared spectroscopy[25], QCM-D[14, 26, 27], ellipsometry[14, 26], and XPS[28, 29] all being used in complementary ways.

From these studies, researchers have begun to elucidate the key processes by which surfaces influence the adsorption or resistance of proteins. At the protein-solid interface, there exists an 'ensemble of events'[30], including: adsorption, desorption, conformational change, adsorption of ions, change in protein and surface hydration, and entropy changes of the entire system.[6, 30] At a macro-level, these events are related to surface area, topography, hydrophilicity, functional groups, and the grafting density of modification.[30-32] At the molecular level, electrostatic and van der Waals interactions, along with steric effects and hydrogen bonding govern the protein-surface interaction.[4] The extent to which these events and interactions occur vary widely, depending on the protein studied and the environmental conditions (i.e. pH, protein concentration, ionic strength), which often makes it difficult to compare experiments.[18] Despite this knowledge, the understanding of protein-surface interactions remains complex and, in particular, much controversy remains on the effect of roughness on protein adsorption.[3, 32]

Some consensus has emerged on a number of protein-surface interactions. The resistance to protein adhesion is enhanced by surfaces which are electrically neutral, are hydrophilic, contain hydrogen bond acceptors, but without having hydrogen bond donors - with a few exceptions, such as mannitol.[3, 4] It is generally accepted that hydrophobic surfaces adsorb more protein than hydrophilic surfaces, but that proteins can attach to both by re-orienting themselves at a surface to maximize adhesion.[1, 6] In the case of certain well-characterized protein systems, such as the adsorption of the serum albumins (BSA and HSA) onto surfaces, the interactions between the protein and the surface have been described for a variety of functional groups, including: oligo/poly(ethylene) glycol (OEG/PEG)[33, 34], tertiary amine oxides[33], phosphate derivatives[4, 35], amines[36, 37], hydroxyl[37], carboxyl[38, 39] and alkyl[31] chains. The well-known characteristics of protein binding to PEG and alkyl chains has transformed those two surfaces into the standard benchmark to which all protein adsorption experiments are compared.[4] Using this knowledge, an ever growing number of materials, with different surface properties, are being created, tested, and employed as biomaterials.

5.1.2 Aims and Overview

Protein adsorption studies to-date lead to meaningful results, but the typical protein adsorption study suffers from several limitations. Most experiments study the adsorption qualities of one or more proteins on fairly simple, well-defined surfaces. The most studied surfaces are metal surfaces or self-assembled monolayers, which have the advantage of controllable surface chemistry and topography. Both surfaces have biological uses, but this is limited, as metals can be toxic if leached into the human body, whilst SAMs are not robust. Thus, there is a need to conduct protein adsorption studies on bio-materials with more practical potential. The as-prepared polystyrene films are examples of materials with imminent industrial relevant as bio-materials.

There are limitations to previous protein adsorption studies which are addressed in this work. First, there is the issue of adsorption time. Protein adsorption studies on polystyrene beads functionalized with the same chemistry described here have been limited by a lack of adsorption data at time frames less than 1 hour [31] – a time scale thought to be of fundamental importance to protein deposition events.[7] As well, this limited time frame applies to many of the best ‘protein-SAM’ studies done to date.[3, 4] Second, systematic QCM-D studies on polymers having a range of surface functionalization in a single study have been limited. Typical studies of this type involve SAMs, in which a rich library of surface functionalizations can be studied at once. Until recently, methods to functionalize polymers in a similarly controlled manner did not exist. Chemistry involving the addition of a chemical linker to a polymer surface promises to address this need. Third, there is a limit to the type of materials that can be studied by QCM-D using present methods. For instance, thin films grown under high temperature conditions which destroy the piezo-electric properties of quartz have not been well-studied. Polymers which are modified by harsh chemical conditions, which tend to degrade polymer thin films are another class of materials that are not well-studied by QCM-D; normally this type of modification leads to an unstable QCM-D response. The protocols developed in this work enable polystyrene thin films modified by carbene chemistry to be studied by QCM-D. Fourth, the standard QCM-D analysis can be improved. This standard method includes the use of accumulation mass, desorbed mass, and dissipation *vs.* frequency plots to obtain the amount of added mass and viscoelastic information about the interface. The data density of QCM-D – up to 200 points per second – has rarely been exploited to provide even more detail about the dynamics at this interface.[14,42] Kinetic analysis in this manner has been done to great effect using other techniques.[7] Here, detailed kinetic data of protein adsorption on the materials of interest is obtained.

With the above in mind, a controlled and detailed study of the effect that surface functionalization of industrially relevant materials has on protein adsorption dynamics, should be of considerable scientific interest. The results may inform users and manufacturers of the next-generation of polymeric materials for bio-medical purposes.

5.2 Experimental Details

(a) *Chemicals*

Most of the chemicals and solutions used here have been outlined in Chapters 3 and 4. The concentration of protein (BSA) added to 0.1M phosphate buffer is 0.08 g L^{-1}. Hellmanex (2% in H_2O v/v, Hellma Analytics) was used to clean substrates at the end of every QCM-D experiment.

(b) *Substrates*

There were two types of substrates used in the described QCM-D experiments: gold-terminated QCM-D crystals (QSense, Sweden), and as-prepared polystyrene thin films spin-coated onto gold-terminated QCM-D crystals. As-received QCM-D crystals were cleaned with piranha solution for 10 minutes, followed by rinsing with copious amounts of water and acetone. Following this, they were exposed to ozone for 30 minutes. These substrates were then used in a QCM-D experiment, or spin-coated with the as-prepared thin films. The method for creating these particular DVB cross-linked, polystyrene thin films and their characterization can be found Chapter 4. Some QCM-D crystals were used repeatedly, if they had a stable QCM-D response (i.e. no visible cracks, ≤ ± 1Hz drift in phosphate buffer after overnight exposure). Such crystals are cleaned between experiments by piranha solution and ozone.

(c) *Carbene modification chemistry*

The DVB cross-linked polystyrene films were terminated with the following: phosphate diester (**3a**), amine (**3b**), glycol (**3d**), phenyl (**3e**), acid (**3f**), hexyl (**3g**), and the chemical linker (**2**, with all labels referring to Figure 4.2), using chemistry described in Chapter 4.

(d) *QCM-D Experimental*

The basic QCM-D experimental method has been described in Chapter 2 with the experimental protocol being similar to that described in Chapter 3. Briefly, once the Δf and ΔD plots had stabilized overnight at 25^{o}C, the QCM-D experiment proceeded in four stages: phosphate buffer was passed over the sample to establish a baseline; a BSA containing phosphate buffer solution was exposed to the sample for at least 20 minutes; a rinse with phosphate buffer occurred for at least 40 minutes; followed by exposure to a 2% Hellmanex solution (>5 min.). Further details regarding the experimental protocol and the methods used to fit data to the 1 or 2-layer Voight model are described in section 2.2.2.

5.3 Results

5.3.1 General Data Features

Typical protein deposition studies using QCM-D involve the initial establishment of a stable crystal response in protein-free buffer, followed by protein deposition; in some cases, a rinse with protein-free buffer is incorporated to test the reversibility of protein adsorption.[9, 15, 26, 40] Figure 5.1 shows that this protocol leads to changes in frequency (Δf) and dissipation (ΔD), as a function of time. As expected, a stable baseline is established for all samples with Δf and ΔD having magnitudes less than or equal to ± 1 Hz and 2.5×10^{-7}, respectively. This demonstrates that the experimental conditions are well controlled in all cases (i.e. stable temperature, flow rate), and that the as-prepared substrates are stable to a flowing, protein-free phosphate buffer. The observed stability in the f and D traces under these conditions confirms the suitability of the as-prepared thin films for QCM-D experiments.

BSA was introduced to the QCM-D cell by switching the source solution to the BSA-containing, phosphate buffer solution. The physical act of switching solutions caused the baseline data to have increased values of f and D for a brief moment, with values returning to the baseline values before showing behaviour consistent with protein deposition. As the protein enters the QCM-D cell, a mass is added to the crystal's surface, resulting in a negative shift in the frequency data and a positive shift in the dissipation data. The general shapes and magnitudes of the f and D data obtained from the adsorption of BSA to gold, and the as-prepared polystyrene surfaces, is comparable to similar studies.[9, 18, 21, 26] The protein adsorption was allowed to continue for at least 20 minutes, at which point equilibrium was reached in both the *f* and D traces.

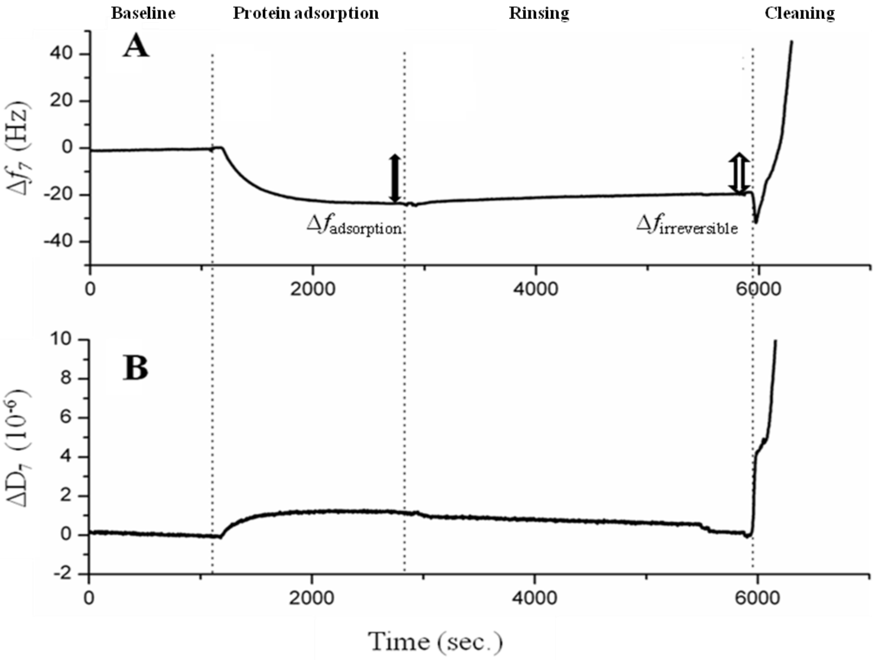

Figure 5.1 : Frequency (A) and dissipation (B) traces for an entire protein adsorption-desorption experiment. The sample used was an unmodified DVB cross-linked polystyrene thin film on a QCM-D crystal. Data from the 7th harmonic is shown. The solutions used at the various points in the experiment are: 0.1M phosphate buffer (baseline and rinsing); 0.08 g L^{-1} BSA in phosphate buffer (protein adsorption); 2 % v/v Hellmanex in aqueous solution (cleaning).

The presence of loose protein layers and/or the reversibility of a protein adsorption process can be tested by flowing protein-free buffer over adsorbed layers.[17, 41] Here, a protein-free buffer solution was flowed over the substrate for at least 20 minutes, as demarked in Figure 5.1. Irreversible adsorption of BSA to unmodified polystyrene is expected[41], and this is shown here as a <10% change in the frequency and dissipation traces after a 50 minute rinse by protein-free buffer. The extent of reversibility is dependent on surface chemistry and this is discussed later.

Finally, at the end of each experimental run, the entire QCM-D cell, including the connected tubing, was cleaned with an aqueous solution of 2% Hellmanex for a few minutes. A dramatic and positive change, in both the frequency and dissipation traces, accompanies this event. Notably, the frequency values rise above the baseline trace. The extent of this change indicates the removal of both BSA *and* the polymer layer, thus partially justifying the repeated usage of crystals for further experiments, with the proviso of additional cleaning by piranha solution and ozone.

5.3.2 QCM-D Modelling

5.3.2.1 Application of the Sauerbrey Equation to Protein Adsorption Data

One of two models needs to be applied to frequency data in order to obtain the mass density of protein films. Normally, a protein layer is considered to be viscoelastically coupled to the bulk fluid, thus requiring that the Voight model be used to obtain mass density (see section 2.2.1). However, many researchers report mass densities calculated from the Sauerbrey equation (Equation 2.10), rather than the Voight model.[13, 26, 41] These researchers assume that the mass adsorbed is thin, rigid, and poorly coupled - in a viscoelastic sense - to the bulk fluid. The results obtained from the Sauerbrey method, whilst approximate, have proved useful for describing protein behaviour at surfaces.

An example of the typical Sauerbrey mass output is shown in Figure 5.2, with BSA deposition onto unmodified polystyrene as an exemplar. The deposition of BSA onto all surfaces is characterized by an initial, sharp increase in mass, followed by a slower increase, until equilibrium is reached. The data associated with ‘rinsing’ is described in section 5.3.2.3. The observed magnitude and changes to the Sauerbrey mass can be directly compared to most of the QCM-D literature and enable a kinetic analysis, which is discussed later. Trends between this data and the mass calculated by the Voight model (see next section) can be compared qualitatively.

For ideal, rigid overlayers, the Sauerbrey mass at all overtones should be the same. This is true during early adsorption, which is consistent with the low dissipation during this time frame (see Figure 5.1B). Here, protein layers formed between 0 and 500 seconds can be approximated as rigid layers. It is this relative rigidity which justifies the use of the Sauerbrey equation as an exclusive measure of mass density in some literature reports.[13-15] However, deviations from this behaviour signal the presence of overlayers, which are likely non-rigid. The observed breakdown of the expected Sauerbrey behaviour in Figure 5.2 indicates the presence of soft overlayers, particularly at saturation mass (and during the rinse phase). Thus, caution should be employed when using $m_{\text{Sauerbrey}}$ as a measure of mass density for protein layers, particularly at adsorption times > 500 seconds. One must note that Sauerbrey mass reported here is properly described as an apparent mass. The observed changes in Sauerbrey mass include the slow conformational changes and rearrangements of proteins which are known to follow protein adsorption at surfaces, as well as real changes of mass because of adsorption or desorption.[40]

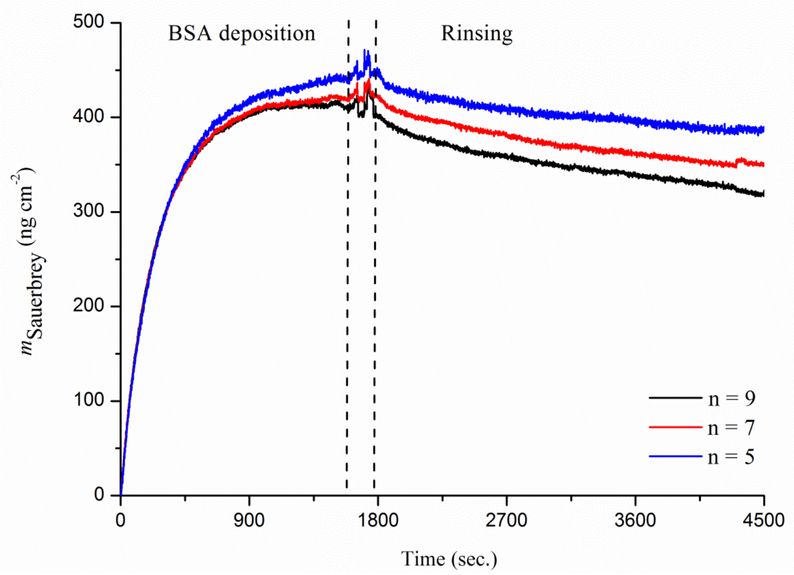

Figure 5.2 : Sauerbrey Mass calculation of the BSA deposition and rinsing stages on an unmodified DVB cross-linked polystyrene film. The start of the BSA deposition was normalized to t = 0 seconds for all cases.

The calculated Sauerbrey mass ($m_{\text{Sauerbrey}}$) associated with protein adsorption on the as-prepared substrates is shown in Table 5.1. This data is also shown graphically in Figure 5.3A to facilitate easy comparison between data sets. The magnitude of $m_{\text{Sauerbrey}}$ for all

	5 min. Deposition[a]		10 min. Deposition[a]		20 min. Deposition[a]		30 min. Deposition[a]		End of Deposition[b]		
Variable	Avg. $m_{\text{Sauerbrey}}$ (ng cm^{-2})	S.D.(±ng cm^{-2})	Avg. $m_{\text{Sauerbrey}}$ (ng cm^{-2})	S.D.(±ng cm^{-2})	Avg. $m_{\text{Sauerbrey}}$ (ng cm^{-2})	S.D.(±ng cm^{-2})	Avg. $m_{\text{Sauerbrey}}$ (ng cm^{-2})	S.D.(±ng cm^{-2})	Avg. $m_{\text{Sauerbrey}}$ (ng cm^{-2})	S.D.(±ng cm^{-2})	Total Time of Deposition (min.)
Au	295.8	13.2	358.8	3.6	390.4	1.4	400.4	1.3	401.6	1.5	38.9
PS	274.1	18.3	370.8	6.3	418.4	1.8			420.0	2.7	24.3
2	181.5	12.1	248.7	4.5	293.8	2.1	310.2	1.9	315.7	2.4	46.5
3a	146.1	7.5	184.0	2.2	192.3	1.1	179.5	1.4	140.8	2.2	57.3
3b	239.6	17.4	328.4	6.2	402.2	3.7	448.6	2.8	491.9	6.5	45.3
3d	207.3	21.4	344.4	10.2	461.5	4.5	508.7	1.9	524.1	5.7	37.7
3e	113.8	6.7	150.8	2.5	174.7	1.1	183.0	0.9	187.8	1.1	44.3
3f	217.0	11.3	278.0	4.4	323.2	2.0	338.9	2.0	363.4	2.7	61.2
3g	294.5	15.3	377.8	6.5	444.8	3.0	474.4	2.3	521.3	2.1	77.4

Table 5.1: Average values of Sauerbrey masses during BSA deposition. Sample labels are as follows, as per Figure 4.2: linker terminated (**2**), phosphate diester (**3a**), amine (**3b**), glycol (**3d**), phenyl (**3e**), carboxylic acid (**3f**), hexyl (**3g**). Notes: [a] Sauerbrey masses for individual overtones were averaged at each time point using either a 50 point adjacent average; [b] an average of the last 300 points in the deposition region. Standard deviations and the total time for BSA deposition are shown.

	5 min. Deposition[a]		10 min. Deposition[a]		20 min. Deposition[a]		30 min. Deposition[a]		End of Deposition[b]		
Variable	m_{Voight} (ng cm^{-2})	S.D.(±ng cm^{-2})	m_{Voight} (ng cm^{-2})	S.D.(±ng cm^{-2})	m_{Voight} (ng cm^{-2})	S.D.(±ng cm^{-2})	m_{Voight} (ng cm^{-2})	S.D.(±ng cm^{-2})	m_{Voight} (ng cm^{-2})	S.D.(±ng cm^{-2})	Total Time of Deposition (min.)
Au	312.7	20.0	365.8	3.6	397.4	1.2	407.7	1.6	409.2	3.6	38.9
PS	282.1	18.3	377.9	6.1	424.0	1.2			425.1	1.7	24.3
2	208.5	13.9	285.4	6.7	337.8	6.2	344.3	8.3	318.0	1.8	46.5
3a	176.7	8.5	216.9	2.5	220.6	1.3	204.4	1.7	151.6	2.9	57.3
3b	247.3	17.7	337.4	6.2	411.8	3.2	457.9	2.4	500.9	6.2	45.3
3d	602.7	338.3	538.3	58.5	650.6	22.5	597.0	23.3	647.0	106.5	37.7
3e	118.7	6.8	156.8	2.6	180.0	0.7	188.0	0.6	192.7	0.8	44.3
3f	231.9	11.3	293.8	4.3	340.2	1.6	357.0	1.6	399.5	4.1	61.2
3g	1836.9	108.3	1848.2	75.8	1818.0	67.4	1803.8	62.3	1777.5	53.4	77.4

Table 5.2: Average values of Voight masses during BSA deposition. Notes: [a] Voight masses for individual overtones were averaged at each time point using either a 50 point adjacent average; [b] an average of the last 300 points in the deposition region. Standard deviations and the total time for BSA deposition are shown.

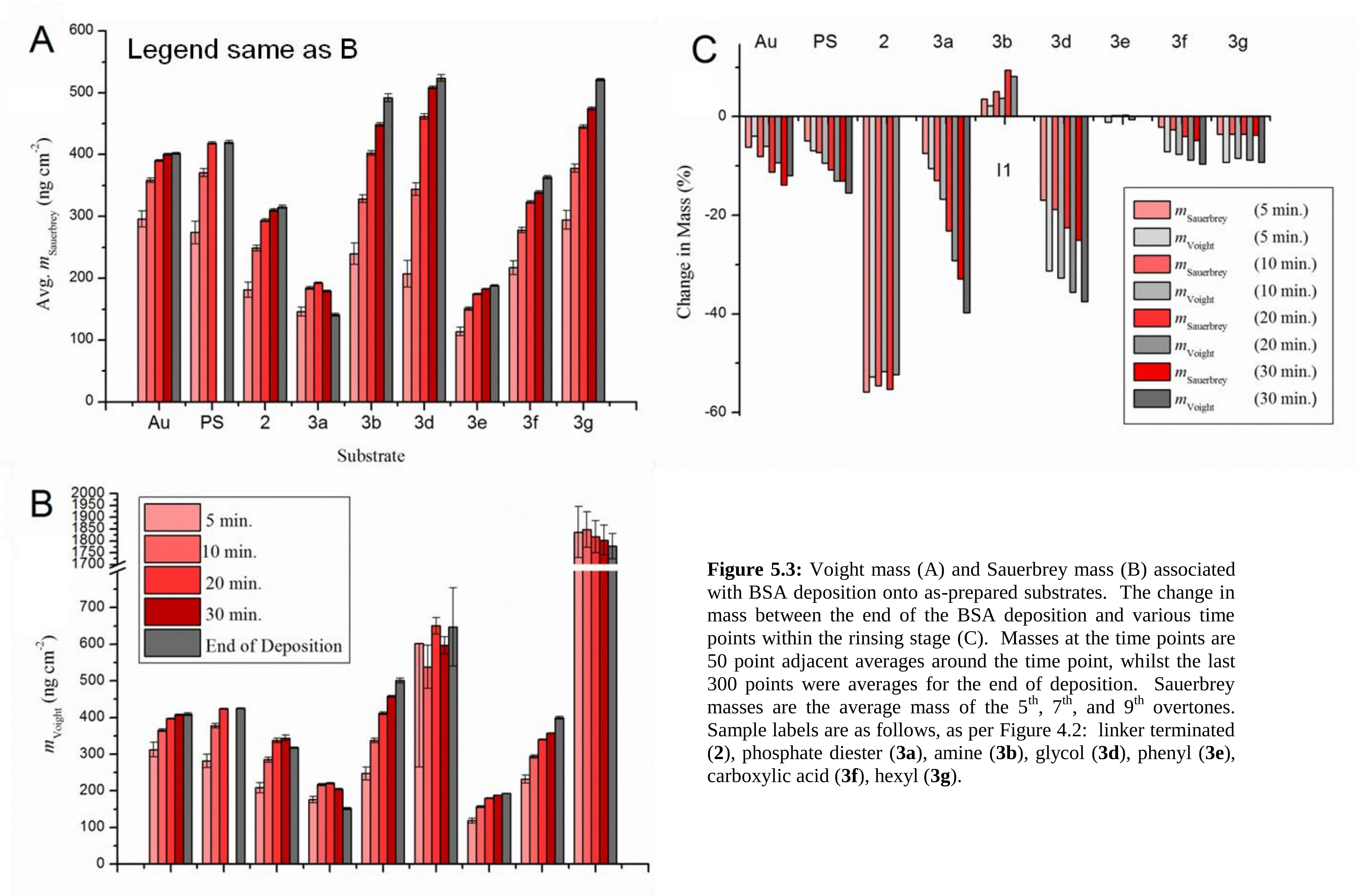

Figure 5.3: Voight mass (A) and Sauerbrey mass (B) associated with BSA deposition onto as-prepared substrates. The change in mass between the end of the BSA deposition and various time points within the rinsing stage (C). Masses at the time points are 50 point adjacent averages around the time point, whilst the last 300 points were averages for the end of deposition. Sauerbrey masses are the average mass of the 5th, 7th, and 9th overtones. Sample labels are as follows, as per Figure 4.2: linker terminated (**2**), phosphate diester (**3a**), amine (**3b**), glycol (**3d**), phenyl (**3e**), carboxylic acid (**3f**), hexyl (**3g**).

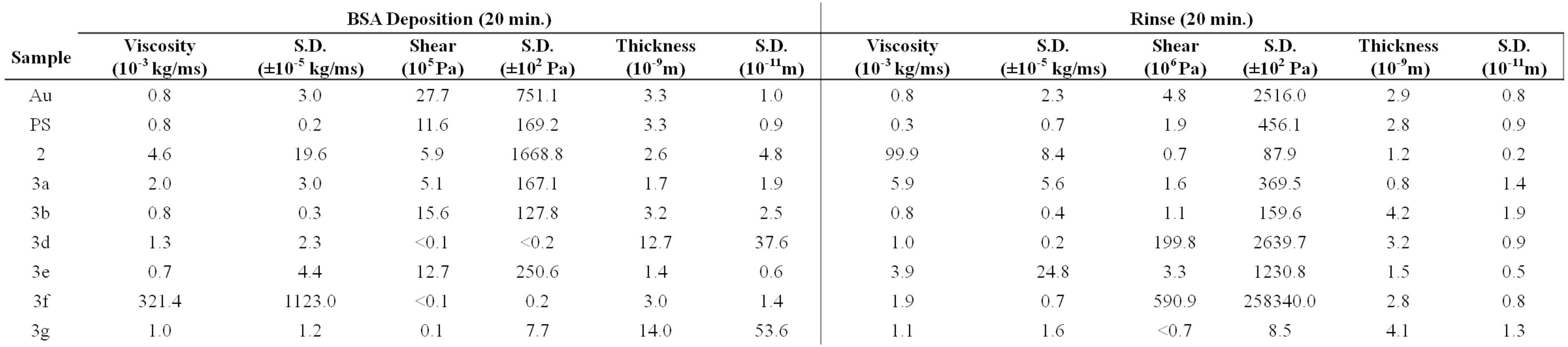

Sample	BSA Deposition (20 min.) Viscosity (10^{-3} kg/ms)	S.D. ($\pm 10^{-5}$ kg/ms)	Shear (10^{5} Pa)	S.D. ($\pm 10^{2}$ Pa)	Thickness (10^{-9}m)	S.D. (10^{-11}m)	Rinse (20 min.) Viscosity (10^{-3} kg/ms)	S.D. ($\pm 10^{-5}$ kg/ms)	Shear (10^{6} Pa)	S.D. ($\pm 10^{2}$ Pa)	Thickness (10^{-9}m)	S.D. (10^{-11}m)
Au	0.8	3.0	27.7	751.1	3.3	1.0	0.8	2.3	4.8	2516.0	2.9	0.8
PS	0.8	0.2	11.6	169.2	3.3	0.9	0.3	0.7	1.9	456.1	2.8	0.9
2	4.6	19.6	5.9	1668.8	2.6	4.8	99.9	8.4	0.7	87.9	1.2	0.2
3a	2.0	3.0	5.1	167.1	1.7	1.9	5.9	5.6	1.6	369.5	0.8	1.4
3b	0.8	0.3	15.6	127.8	3.2	2.5	0.8	0.4	1.1	159.6	4.2	1.9
3d	1.3	2.3	<0.1	<0.2	12.7	37.6	1.0	0.2	199.8	2639.7	3.2	0.9
3e	0.7	4.4	12.7	250.6	1.4	0.6	3.9	24.8	3.3	1230.8	1.5	0.5
3f	321.4	1123.0	<0.1	0.2	3.0	1.4	1.9	0.7	590.9	258340.0	2.8	0.8
3g	1.0	1.2	0.1	7.7	14.0	53.6	1.1	1.6	<0.7	8.5	4.1	1.3

Table 5.3: Output from the Voight modelling, at saturation - considered to be 20 minutes after the start of the deposition or rinse. Sample labels are as follows, as per Figure 4.2: linker terminated (**2**), phosphate diester (**3a**), amine (**3b**), glycol (**3d**), phenyl (**3e**), carboxylic acid (**3f**), hexyl (**3g**). Data represents a 50 point adjacent average around the time point.

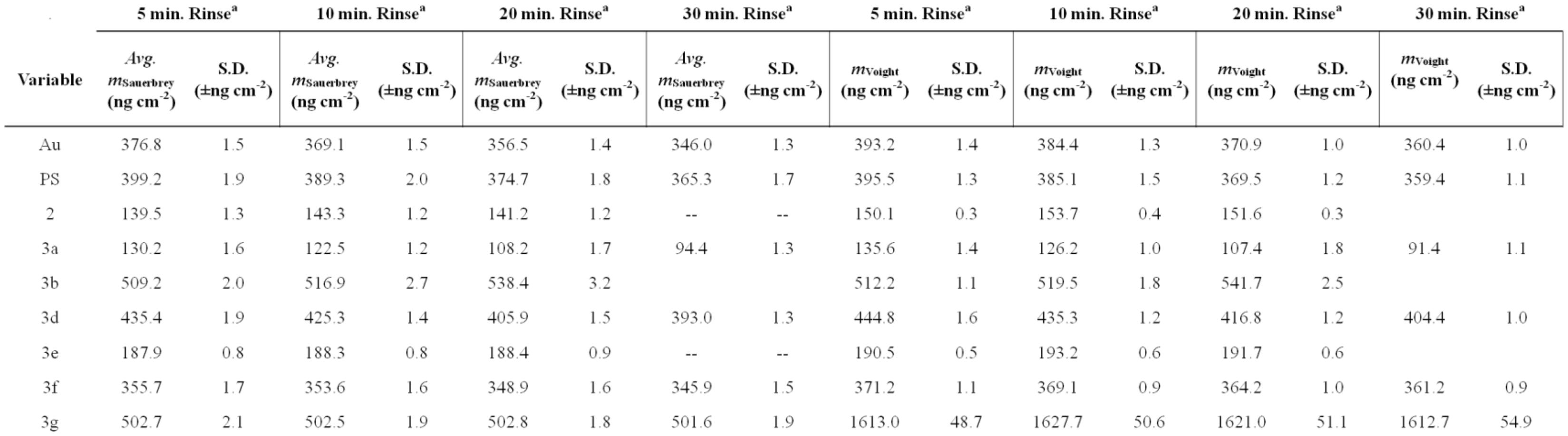

Variable	5 min. Rinse[a] Avg. $m_{\text{Sauerbrey}}$ (ng cm^{-2})	S.D. (±ng cm^{-2})	10 min. Rinse[a] Avg. $m_{\text{Sauerbrey}}$ (ng cm^{-2})	S.D. (±ng cm^{-2})	20 min. Rinse[a] Avg. $m_{\text{Sauerbrey}}$ (ng cm^{-2})	S.D. (±ng cm^{-2})	30 min. Rinse[a] Avg. $m_{\text{Sauerbrey}}$ (ng cm^{-2})	S.D. (±ng cm^{-2})	5 min. Rinse[a] m_{Voight} (ng cm^{-2})	S.D. (±ng cm^{-2})	10 min. Rinse[a] m_{Voight} (ng cm^{-2})	S.D. (±ng cm^{-2})	20 min. Rinse[a] m_{Voight} (ng cm^{-2})	S.D. (±ng cm^{-2})	30 min. Rinse[a] m_{Voight} (ng cm^{-2})	S.D. (±ng cm^{-2})
Au	376.8	1.5	369.1	1.5	356.5	1.4	346.0	1.3	393.2	1.4	384.4	1.3	370.9	1.0	360.4	1.0
PS	399.2	1.9	389.3	2.0	374.7	1.8	365.3	1.7	395.5	1.3	385.1	1.5	369.5	1.2	359.4	1.1
2	139.5	1.3	143.3	1.2	141.2	1.2	--	--	150.1	0.3	153.7	0.4	151.6	0.3		
3a	130.2	1.6	122.5	1.2	108.2	1.7	94.4	1.3	135.6	1.4	126.2	1.0	107.4	1.8	91.4	1.1
3b	509.2	2.0	516.9	2.7	538.4	3.2			512.2	1.1	519.5	1.8	541.7	2.5		
3d	435.4	1.9	425.3	1.4	405.9	1.5	393.0	1.3	444.8	1.6	435.3	1.2	416.8	1.2	404.4	1.0
3e	187.9	0.8	188.3	0.8	188.4	0.9	--	--	190.5	0.5	193.2	0.6	191.7	0.6		
3f	355.7	1.7	353.6	1.6	348.9	1.6	345.9	1.5	371.2	1.1	369.1	0.9	364.2	1.0	361.2	0.9
3g	502.7	2.1	502.5	1.9	502.8	1.8	501.6	1.9	1613.0	48.7	1627.7	50.6	1621.0	51.1	1612.7	54.9

Table 5.4: Average values of Sauerbrey and Voight masses during the rinsing stage of the QCM-D experiment. Sample labels are as follows, as per Figure 4.2: linker terminated (**2**), phosphate diester (**3a**), amine (**3b**), glycol (**3d**), phenyl (**3e**), carboxylic acid (**3f**), hexyl (**3g**). Note: [a] Sauerbrey masses for individual overtones were averaged at each time point using a 50 point adjacent average. Standard deviations are shown.

samples are comparable to theoretical and experimental values for BSA on gold, polystyrene, and other substrates.[14, 18, 31] Hook *et al.*[14] determined that the theoretical mass for a BSA monolayer at maximum surface coverage is 226 or 155 ng cm^{-2} for side on and end on adsorption, respectively; at maximum RSA coverage (see Figure 2.11) it is 129 and 84 ng cm^{-2}, respectively (assuming a heart shaped BSA of 8 nm x 8.7 nm x 6 nm in size). Hydrated BSA monolayers have masses ranging between ≈ 390 - 910 ng cm^{-2}, with multilayers having mass in excess of 901 ng cm^{-2}.[18] It is notable that the range of Sauerbrey masses obtained here is higher than the values of Hook *et al.*[14], but on the lower end of the range of values for hydrated monolayers of BSA. This observation probably relates to the following: the Sauerbrey method underestimates the total mass, proteins are hydrated at the surface, and that deposition does not occur with pure RSA kinetics. Consequently, it is difficult to make any firm assignment of protein layer structure with Sauerbrey masses alone.

The surface modification scheme does affect the amount of protein adsorbed onto the surface, with a range of values in Table 5.1 and Figure 5.3A, with magnitude above and below those of the control substrates, gold, polystyrene and the chemical linker - which is terminated by aniline functionality (see *surface* **2**, Figure 4.2). Compared to polystyrene, the amount of protein is decreased upon the addition of the chemical linker. Surfaces terminated with **3a** (phosphate diester) and **3e** (phenyl) lead to a further reduction in adsorbed mass. Surfaces terminated with **3b** (amine), **3d** (glycol), **3f** (acid), and **3g** (hexyl) increase adsorbed mass. The high mass associated with **3g** is consistent with literature that suggests that alkyl terminated surfaces have ‘maximum’ BSA adsorption.[4] The high mass obtained for surface **3d** was unexpected, as poly(ethylene) chains are known to resist protein adsorption.[4] However, the magnitude of resistance does depend on several factors, including the surface coverage of modification, chain length, orientation, hydration spheres and steric interactions.[4]

5.3.2.2 Application of the Voight Equation to Protein Adsorption Data

As explained earlier, the use of the Sauerbrey equation may not reflect the true mass of soft, flexible and hydrated protein layers.[1, 42] The Voight model is the better of the two models to apply to such viscoelastic systems (see sections 2.2.1 and 2.2.2, and Equations 2.11 and 2.12).[42] The use of the Voight model first requires defining the number of viscoelastic layers within the studied system (see Figure 2.9). On a gold-coated QCM-D crystal, there is only one viscoelastic layer – adsorbed BSA. On polystyrene thin films, there are two viscoelastic layers – the polystyrene and the adsorbed BSA. The 1-layer and 2-layer Voight model was applied to the "protein adsorption" region, as defined in Figure 5.1, for both of the aforementioned systems, in order to obtain protein mass density and other viscoelastic parameters.

The application of the Voight model to this data is well described in sections 2.2.2 and 3.2.3 for the 1-layer Voight model. However, the exact methodology used for the 2-layer Voight model has not been explained previously. This 2-layer model required that certain variables be fixed, including: bulk fluid density (p_3, 1000 kg m^{-3}), bulk fluid viscosity (η_3, 0.001 kg m^{-1} s^{-1}), protein layer density (p_2 , 1200 kg m^{-3}), polystyrene density (p_1 , 0.105 kg m^{-3}), polystyrene viscosity (η_1, 1 x 10^9 kg m^{-1} s^{-1}), and polystyrene shear modulus - for a thin film[43] (μ_1, 1.43 GPa). The variables representing the viscoelastic properties of the protein layers were automatically fit by the QCM-D program (QSoft, QSense) within the following ranges: protein viscosity (η_2: $1x10^{-4}$ – $1x10^{-1}$ kg m^{-1} s^{-1}), protein shear (μ_2, $1x10^3$ – $1x10^{14}$ Pa), with one of either protein thickness (h_2, $1x10^{-10}$ – $1x10^{-7}$ m) or protein mass density (m_{Voight}, 0 – 2000 ng cm^{-2}), as h_2 or m_{Voight} cannot be fit simultaneously These fixed variables and range of values are reasonable, considering both the physical properties of water and proteins, as well as their use by others.[44 - 46] To apply the Voight model to the collected frequency data, the descending fit mode, 50 step initial grid fit, and logarithm fitting mode – as defined in the modelling software - was used, regardless of the number of viscoelastic layers involved. Representative outputs of this fitting protocol are shown in Figure 5.4. For all the studied samples, the mass densities for BSA adsorption calculated by the Voight model are shown in both Table 5.2 and Figure 5.3B. The reported values of m_{Voight} at 5, 20 and 30 minutes are 50 point adjacent averages around the time point, whilst the mass density at the 'end of deposition' is an average of the last 300 points of the protein deposition (i.e. saturation mass). For reference, the values of η_2, μ_2, h_2 after 20 minutes of BSA adsorption are shown in Table 5.3.

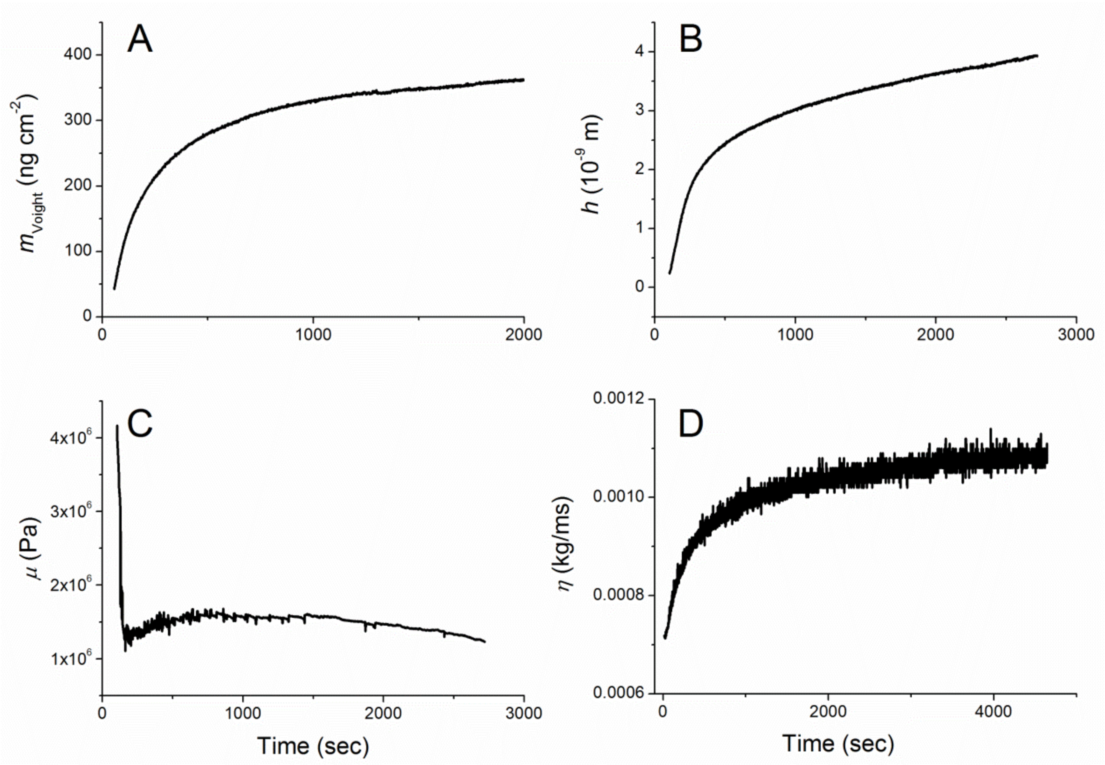

Figure 5.4 : Representative outputs of viscoelastic modelling, with spectra based on BSA deposition on surfaces **3f** (A), **3b** (B, C) , and **3g** (D).

There are several features of these results which must be considered here. In general, the output of the Voight model in this chapter is reasonable and consistent with the literature. Protein layer thickness ranged from < 1 monolayers of BSA to values associated with multilayer adsorption of BSA.[18] Viscosity values compare well to those for hydrated albumin layers on polystyrene.[44] The shear modulus for *most* studied protein layers was around 1.0 x 10^6 Pa - 1.3 x 10^7 Pa , which is consistent with BSA on polystyrene and HSA on hydrophilic surfaces, respectively.[44, 47]

However, there is data scattering of up to 10 - 15% in the output in Figure 5.4, particularly for the shear modulus and the viscosity of BSA layers. More reliable values of μ_2 and η_2 are obtained during early adsorption, rather than at saturation. This scatter may simply be a consequence of protein films becoming viscoelastic over time, when structural change and the formation of integrated protein layers would be more prevalent. This scatter is not detrimental to the analysis of Voight output in this chapter, but it does prevent the use of m_{Voight} for kinetic analysis. Unreasonable smoothing of m_{Voight} (i.e. by adjacent averaging) would be required to make such analysis possible. A more reasonable approach is to use the $m_{\text{Sauerbrey}}$ data, as use of $m_{\text{Sauerbrey}}$ enables protein behaviour to be estimated at short time frames, when protein layers are relatively rigid (see section 5.3.2.1). By contrast, m_{Voight} is a better approximation of protein behaviour at time frames longer than ≈ 500 seconds, when proteins layers are softer and viscoelastic.

A comparison of the $m_{\text{Sauerbrey}}$ and m_{Voight} values in Figures 5.3A and 5.3B is useful. Here, it is clear that the m_{Voight} values follow the same trend as the $m_{\text{Sauerbrey}}$ values, which was described at the end of section 5.3.2.1. For some systems, the magnitude of m_{Voight} is similar to that of $m_{\text{Sauerbrey}}$ (i.e. Au, PS, **2**, etc.), whilst for other systems m_{Voight} is larger than $m_{\text{Sauerbrey}}$ (i.e. **3d**, **3g**, etc.). The Voight mass density includes the mass of both the protein layer and the surrounding solvent, therefore one should expect $m_{\text{Voight}} > m_{\text{Sauerbrey}}$ for a thick, viscoelastic layer of protein. By contrast, the Sauerbrey mass density should underestimate the total protein mass at a soft, viscoelastic interface.[14] Therefore, in the case of systems having similar m_{Voight} and $m_{\text{Sauerbrey}}$, the protein layer has less viscoelastic character (i.e. more rigid). In the case of systems with larger magnitude of m_{Voight}, the protein layers are likely more viscoelastic.

The magnitude of the Voight mass can indicate the type of protein layer which has formed at the surface. Figueira *et al.* [18] has noted that monolayers of hydrated BSA should have mass ranging between 390 - 910 ng cm^{-2}, depending on protein orientation and layer structure (see section 3.3.4.2 and Figure 3.11). A comparison of this note to Figure 5.3B, we might associate m_{Voight} values after 20 minutes of adsorption (i.e. saturation) with the following BSA orientations and structure. Monolayers or less-than-monolayer coverage of flat BSA, in a closed-packed arrangement, is likely present at the following interfaces: Au**, 2, 3a, 3e**, **3f**. Multilayers of BSA are likely forming on **3g**. BSA at interfaces PS, **3b,** or **3d** likely have a mixture of flat and end-on orientation; other results will refine this conclusion.

5.3.2.3 Surface Rinsing

Rinsing the surface of protein layers is commonly used as a test for the reversibility of protein adsorption.[17, 41] The viscoelastic parameters after 20 minutes of rinsing are shown in Table 5.3, whilst m_{Voight} and $m_{\text{Sauerbrey}}$ for the rinsing step can be found in Table 5.4 and Figure 5.3C. All results are broadly consistent with the mass and viscoelastic parameters obtained when these models were applied to the adsorption data. Conclusions from the analysis which follows could be tempered by the history dependency of protein adsorption; longer adsorption times lead to protein layers which are more strongly bound.[48] However, a range of behaviours, which are not dependent on the total time of the adsorption run, are seen in Figure 5.3C. Therefore, any changes in the data should reflect the relative affinity that BSA has for each surface.

Many suggest that if the mass of adsorbed protein changes $\leq \approx 10\%$ after a rinse, then the protein layers are bound, irreversibly.[14, 15, 49] In Figure 5.3C, this applies to BSA layers on Au, PS, **3f**, **3e** and **3g**. The changes associated with these samples are a simple consequence of a flowing solution over the sample, where loosely bound protein is removed by force, but the majority of bound matter is retained due to significant binding forces. In contrast, mass changes ≥ ≈ 10% are due to protein layers which are bound, reversibly.[14, 15, 49] This is the case for BSA on surfaces **2**, **3d**, and **3a**. The functionalities represented by these surfaces are, respectively: aniline, glycol, and phosphate diester. Albumin is known to bind weakly to these three functionalities, with all three considered to have a common feature - surface hydration shells.[4, 31, 38, 39, 50]

There is a time dependency in the mass densities associated with rinsing, which is best reflected by the results shown in Figure 5.3C. In some cases (e.g. **3a**, **3d**), the mass slowly decreases with time due to the gradual removal of loosely bound proteins by the flowing liquid and the reversibility of adsorption. In other cases (e.g. **3e**, **3g**), there is little change in mass density over time. This is consistent with the presence of strongly bound protein layers on the surface, having little reversibility in adsorption. This behaviour may be explained by the strong binding which is expected to occur between alkyl groups and albumin.[4, 31] In the case of **3b,** an amine-terminated surface, mass increases with time. This is a curious result, which could be dismissed as an artefact of the experiment. However, amine groups are known to have high affinity for the polar binding sites of BSA.[31, 36, 38] Also, amine groups are known hydrogen acceptor groups, which are identified as reason for high protein affinity to some surfaces.[4] Thus, this slight increase in mass could be a consequence of weakly bound proteins adopting a new orientation or conformation leading to stronger adsorption.

The case of surface **2** is made complicated by a long time delay between the adsorption run and the start of surface rinsing. In all other cases, the lag time between the end of the adsorption run and the beginning of the rinse was short – only the time required to switch the incoming solution from a BSA-containing buffer to pure phosphate buffer (2-5 minutes) within the QCM-D cell. For surface **2**, the lag time was about 25 minutes. This was the time necessary for the *f* and D traces to stabilize after an unexpected noise in the data after ≈50 minutes of the adsorption run. The cause of this noise could include one or all of the following: temperature variations, bubbles in the QCM-D cell, a broken crystal, degradation of polystyrene thin film, or some artefact of protein adsorption. After 25 minutes, the signals stabilized and the rinse of the protein layers on surface **2** was conducted. This renewed stability suggests a temporary cause for the noise, such as bubbles in solution. Rinsing of protein layers on surface **2** leads to a mass loss of > 50 %. However, the time dependency seen for the other interfaces in Figure 5.3C is not observed. Likely, the act of removing the noise (e.g. gently increasing and then decreasing flow speed) led to some loss of protein mass prior to the collection of the *f* and D traces for the rinse phase. Considering the above, the mass densities associated with a rinsed surface **2** – across all time frames - should be considered equivalent to the expected mass densities after 30 minutes of rinsing.

5.3.3 Dissipation versus Frequency Plots (ΔD vs. Δ*f* plots)

In sections 3.2.3.2 and 3.2.3.3, the use of ΔD vs. Δf plots was described, for the case of BSA deposition onto diamond surfaces. The previous methodology is applied here in the case of *f* and D data from the adsorption and rinsing phases (see Figure 5.1) of the experiments conducted for this chapter. The ΔD vs. Δ*f* plots relating to protein layers on the as-prepared polystyrene thin films is shown in Figure 5.5. The data associated with BSA adsorption is in black, whilst the data associated with rinsing is shown in red. To facilitate discussion, overlays of the ΔD vs. Δ*f* plots of both the adsorption and rinse regions are shown in Figures 5.6 and 5.7, respectively. As assumed in section 3.2.3, gradient changes in the ΔD vs. Δf plots can be associated with changes in protein conformation, orientation, hydration or layer structure.[15,26,40]

Ideally, there would be no gap between the adsorption and rinse data in any of the ΔD vs. Δ*f* plots in Figure 5.5. Protein adsorption and desorption should be a continual process. However, a time lag between the adsorption and rinse phases is unavoidable, since protein-free buffer must be introduced in order to initiate the rinse phase. For most samples, this time

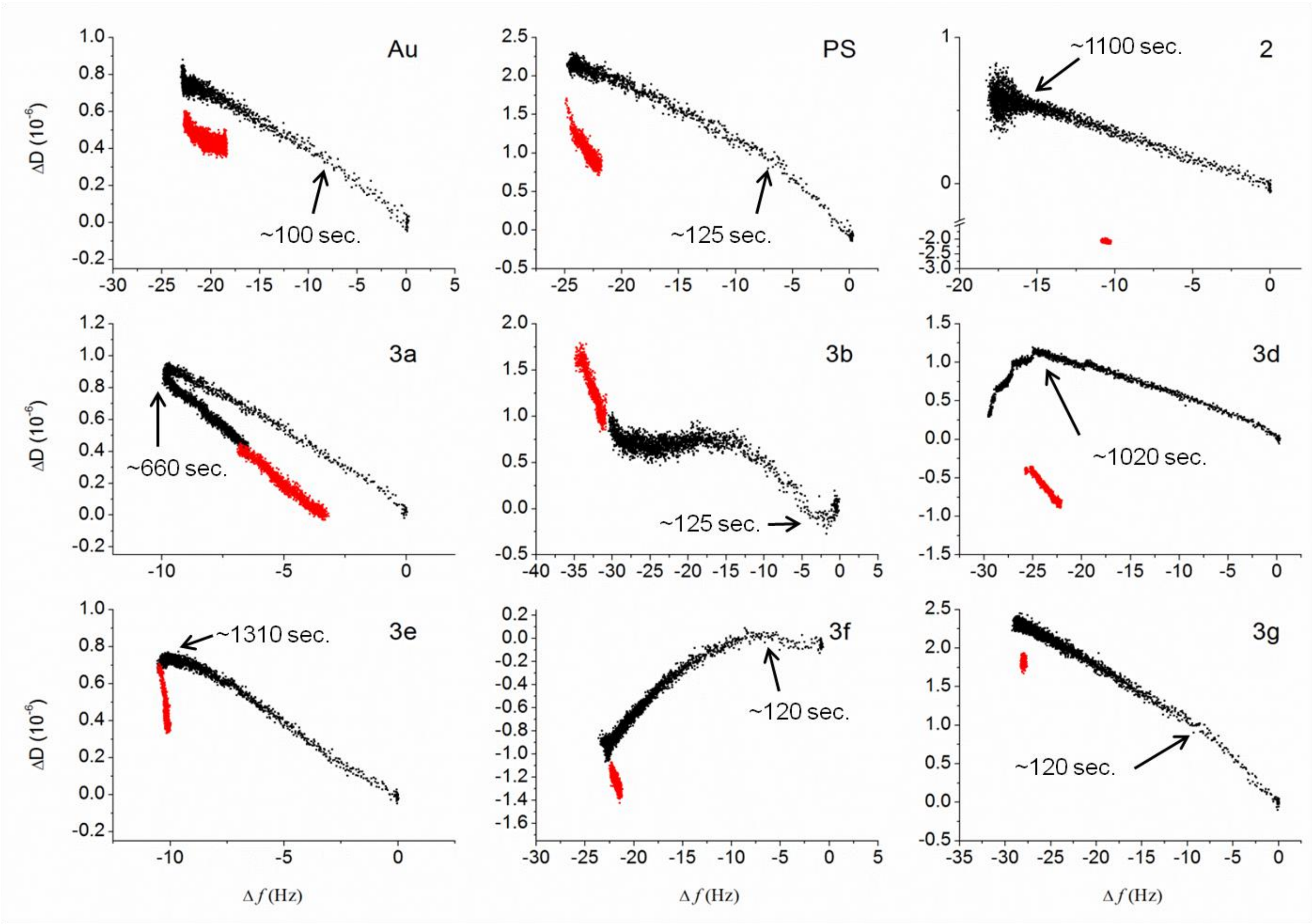

Figure 5.5: Change of dissipation versus change of frequency plots of BSA deposition onto various samples (black), along with the rinse with phosphate buffer (red). Sample labels are as follows, as per Figure 4.2: linker terminated (**2**), phosphate diester (**3a**), amine (**3b**), glycol (**3d**), phenyl (**3e**), carboxylic acid (**3f**), hexyl (**3g**). Each change of gradient is highlighted with an arrow and an approximate time point (± 5 seconds) for the event.

lag is minimal, but the exception is the lag time associated with surface **2.** This manifests itself as a large 'gap' between the adsorption and rinse phase ΔD vs. Δ*f* data (see Figure 5.5, **2**). The reasons for this extended lag time were explained in section 5.3.2.3. Therefore, viscoelastic properties of the rinse region for surface **2** should only be considered to be related to the 'final state' of BSA layers on this surface, after rinsing.

There is a common feature shared by ΔD vs. Δ*f* plots. The spacing between data points in the ΔD vs. Δ*f* plots is either small or large. This is related to the kinetics of adsorption or desorption, in which fast and slow processes are related to the former and latter, respectively.[26, 27] An example of a fast process is initial protein binding, whilst a slow process is the rearrangements of proteins within an established adlayer.[1] Earlier, in sections 3.2.3.2 and 3.2.3.3, the mass at the first gradient change was identified as being a marker for the completion of an initial RSA monolayer in flat or vertical arrangement. By applying the same analysis here, BSA is found to have a flat orientation during initial binding on all surfaces, except BSA on surface **3b**. Notably, the time required to form this initial layer differs between samples. The formation of an initial layer is slow on surfaces **2**, **3a**, **3d**, and **3e**. It may be possible that clustering, aggregation, extensive rearrangements, or surface hydration changes are features of BSA adsorption onto these surfaces, as all of these processes are known to slow protein adsorption kinetics.[6, 51]

The shape and magnitude of the ΔD vs. Δ*f* plots seen in Figure 5.5 is consistent with the literature.[17, 41, 52] For instance, the shape associated with BSA deposited onto unmodified polystyrene has similar shape to that found by Feiler *et al*..[41] The magnitude of *f* and D data seen here is consistent with BSA adsorption on polystyrene, other polymers, and metal surfaces.[17, 52] The variety of shapes seen for the ΔD vs. Δ*f* plots suggest that the surface functionalities affect protein adsorption behaviour.

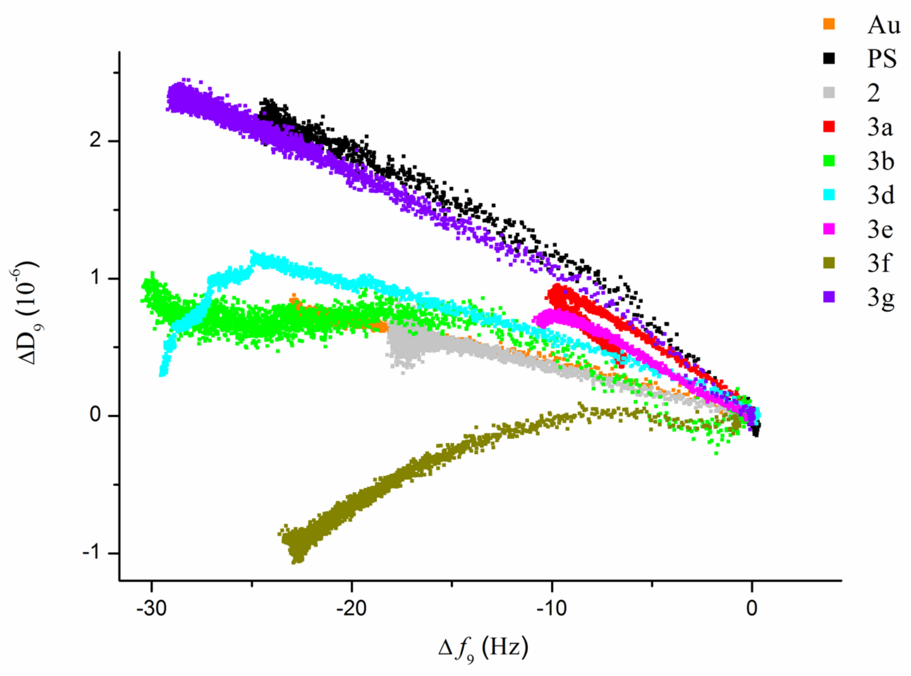

Figure 5.6: Dissipation and frequency plot (9th harmonic) of Au, unmodified and modified polystyrene samples, using data from the BSA deposition region only.

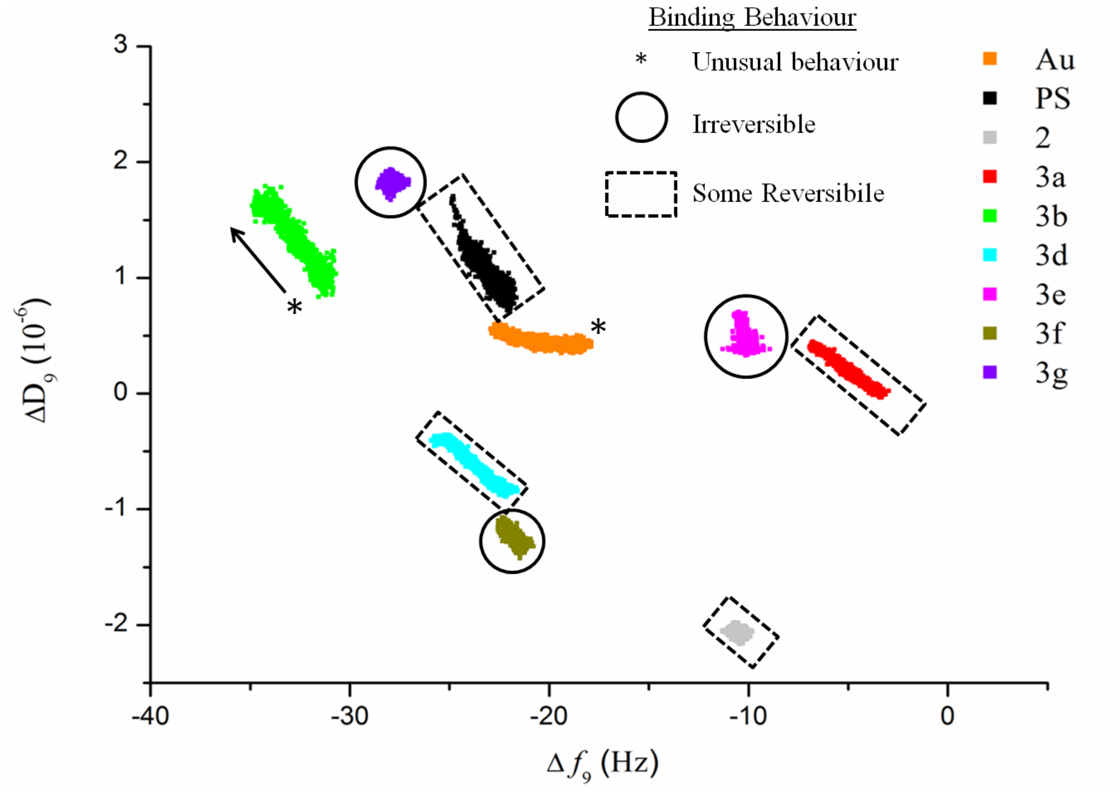

Figure 5.7: Dissipation and frequency plot (9th harmonic) associated with the rinsing of protein layers on various as-prepared substrates. During rinse, *f* and D decrease, except for the data associated with **3b**, in which both *f* and D increase.

The protein adsorption behaviour of the ΔD vs. Δ*f* plots in Figure 5.5 depends on the surface chemistry, and this is best seen in Figure 5.6 where adsorption phase ΔD vs. Δ*f* data for all interfaces has been overlaid. The observed behaviour can be broadly placed within four groups. The first group has linear regions with high dissipation (PS, **3g**). The second group has linear regions with intermediate dissipation (Au, **2**, **3e**,). The third group has linear regions with intermediate dissipation, but whose dissipation decreases during later adsorption processes (**3a**, **3d**). Finally, the fourth group is uniquely associated with BSA deposition on amine and acid (**3b**, **3f**), and share the common feature of having constant dissipation during some, if not most, of the adsorption phase. These groupings are associated with the following behaviours:

- Linear profiles indicate that BSA is adsorbing in a single conformational state at each stage of adsorption[15]
- Higher dissipation suggest the formation of loose layers or multi-layers, whilst lower dissipation indicates the presence of more rigid layers[15, 41]
- Loss of dissipation with added mass at the later stages of adsorption (e.g. **2**, **3a**, **3d**) may relate to the removal of loosely bound proteins, dehydration of the layer, change of protein orientation, and/or a change in the structure of the adsorbed protein layers.[18, 41]
- Curved plots having regions of constant dissipation (e.g. **3b**, **3f**) might indicate strong binding between functional groups and the protein, which result in the formation of rigid protein layers (cf. lysozyme on PAA[52]).

Further insight into the behaviour of BSA on the as-prepared films can be obtained from the ΔD vs. Δ*f* data associated with rinsing. This data for all interfaces is overlaid in Figure 5.7. There is a paucity of literature on the viscoelastic behaviour of proteins during rinsing, but the report of Feiler *et al.* is helpful to interpreting these results.[41] There seem to be three broad groups associated with the data in this figure. The first group is associated with little change in D or *f* during the rinse (e.g. **3f**, **3g**, **3e**). Such behaviour is expected for irreversible binding of protein to a surface. The second group has a gradual decrease in both dissipation and frequency values (e.g. PS, **3a**, **3d**). The behaviour of this group is consistent with some reversible adsorption, where a loss of matter on surface would cause ΔD and Δ*f* to decrease slowly. The behaviour of BSA on surface **2** can also be assumed to belong to this group, since earlier results suggest that binding is reversible at this surface (cf. Figure 5.3C). Finally, there is a third group associated with unusual viscoelastic behaviour upon rinsing. At the Au interface, the decrease in frequency is comparable or larger than that seen for group 2, but the decrease in ΔD is much smaller than group 2 (i.e. $\Delta D < 2 \times 10^{-7}$). This suggests that is consistent with a loss of mass and an increase in the viscoelasticity of the film (i.e. higher D/f ratio). As BSA leaves this film, the protein layer which remains has an ever looser arrangement. At surface **3b**, there is a gradual increase in both dissipation and frequency – behaviour opposite to that of group 2. This is truly unexpected behaviour. However, this behaviour may be unique to BSA at an amine (**3b**) surface due to the strong protein-surface interaction, as noted in the previous paragraph. Rinsing may be re-hydrating these protein layers or there is a change of layer thickness and viscosity due to the integration of weakly bound protein into the protein layer, thereby increasing both *f* and D in the near-surface region.

As Feiler *et al.*[41] note, protein layers having similar ΔD vs. Δ*f* slope (i.e. similar D/*f* ratios) have similar layer or protein structure. By adopting a qualitative approach here, it is clear that the data for the as-prepared films in Figure 5.7 during - and especially at the end of - rinsing can be organized based on this concept. Group 1 includes **3b**, **3d**, **3f**, and **2**. Group 2 includes **3g** and PS. Group 3 includes **3e** and **3a**. The various orientations and layer structure (flat monolayers – **2**, **3f**; vertical monolayers – **3b, 3d**, see section 5.3.2.2) associated with the interfaces in the first group make a *primae facie* assessment difficult.

Similar proteins structure, rather than a similar protein layer arrangement, may be the common element leading to the observed ΔD vs. Δ*f* behaviour upon rinsing. The second group includes two surfaces with known hydrophobicity, thus it is not unreasonable to expect similar protein behaviour on both surfaces (i.e. multilayer formation due to strong hydrophobic interactions.[1]) Whilst the two interfaces in Group 3 do not share the same binding mode, they do share the same orientation and layer structure (< flat monolayer, see section 5.3.2.2), and have a similar ability to limit BSA adsorption. This may explain their similar ΔD vs. Δ*f* behaviour after rinsing.

5.3.4 Adsorption Rate *versus* Mass Density or Time (d*m*/dt *vs*. *m* or d*m*/dt *vs.* time)

The kinetic analysis used here has been explained previously in section 2.2.3 and applied to the case of BSA adsorption on gold and nanodiamond thin films in section 3.2.3.4. Ideally, the m_{Voight} data would be used, but in some cases unreasonable levels of data smoothing were required to facilitate analysis. Instead, the $m_{\mathrm{Sauerbrey}}$ data is used here. This is justified on the basis that BSA is more rigid and less viscoelastic during early adsorption processes, which is the focus of this kinetic analysis (see section 5.3.2.1). Moreover, the $m_{\mathrm{Sauerbrey}}$ data is used throughout the literature to estimate mass density and kinetics of protein adsorption.[26, 27, 53] The advantage of the data density of the QCM-D technique will be exploited to enable this analysis. Several approaches will be synthesized, in order to ensure a comprehensive and systematic kinetic analysis of BSA deposition on the modified polystyrene.[7, 51, 53, 54]

By plotting the rate of mass uptake *versus* adsorption mass or time (i.e. d*m*/dt plots), one can obtain a general sense of the kinetics of protein adsorption. For each of the studied interfaces, d*m*/dt *versus* adsorption mass plots are shown in Figure 5.8. For comparison, an example of a d*m*/dt vs. time plot is shown in Figure 5.9. The ‘transport-limited’, ‘reaction-limited’ and ‘asymptotic’ regions can be clearly seen in each of these d*m*/dt plots (see Figure

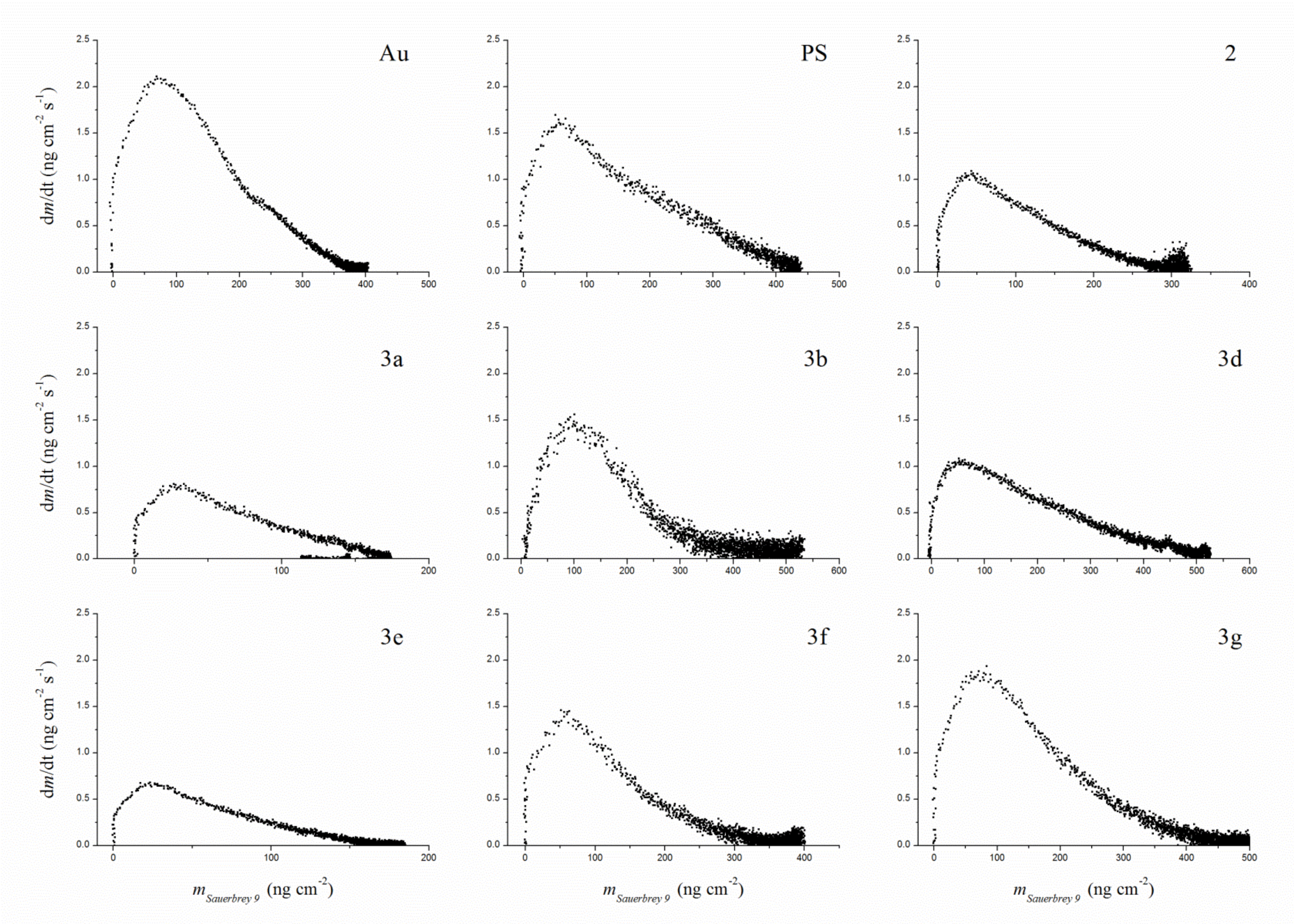

Figure 5.8: d*m*/dt vs. $m_{\mathrm{Sauerbrey}}$ plots for BSA adsorption on variously modified polystyrene substrates.. Sample labels are as follows, as per figure 4.2: chemical linker (i.e. aniline) – terminated; (**2**) phosphate diester; (**3a**) amine; (**3b**) glycol; (**3d**) phenyl; (**3e**) carboxylic acid (**3f**); hexyl (**3g**).

2.13) .[53] Analyses of the d*m*/dt vs. mass plots will enable the rate constant (k_a) and a measure of adsorption size (C_1) to be obtained, as previously mentioned in sections 2.2.3 and 3.2.3.

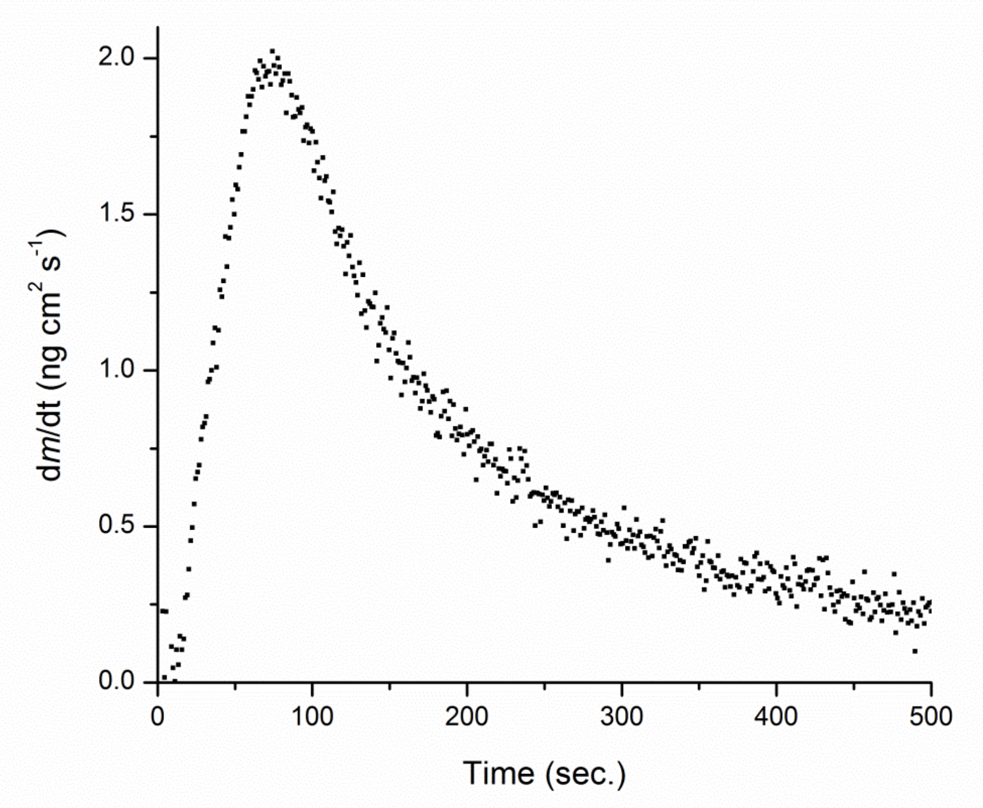

Figure 5.9: Plot of rate of adsorption as a function of time for a hexyl-modified polystyrene surface.

A brief note must be made regarding the transport-limited region seen in Figures 5.8 and 5.9. The transport-limited region is the period in time in which protein deposition is governed by the initial flow of fluid (0.1 mL min^{-1}) into the QCM-D cell having volume of 40 µL. Theoretically, this period should be about 25 seconds long, from the start to the point of maximum rate, where the greatest amount of surface area is available for adsorption. In Figure 5.9, the experimental length of time for this region is about 50 seconds, which is in reasonable agreement with theory. After this transport-limited regime, the reaction-limited regime occurs, where the available surface area drops due to protein deposition which is controlled by features of the protein dynamics (i.e. reaction-limited). The asymptotic regions in Figure 5.8 and 5.9 are those in which mass uptake occurs at a slow rate near equilibrium and this period begins after about 300 to 400 seconds of adsorption time.

Initially, it was thought that the kinetics of BSA adsorption on the as-prepared surfaces could be compared using the overall rate, as needed in studies where the collection of real-time data is impossible. This was calculated by dividing the saturation adsorption mass by the total adsorption time, and the results are shown in Table 5.5. It was thought that the different surface functionalities would affect the long-term kinetics of BSA adsorption, as seen elsewhere.[31] However, there is little correlation between overall rate and protein adsorption. Here, stronger conclusions are obtained by applying a kinetic analysis to obtain the rate constant of adsorption (k_a) and adsorption footprint (C_1), using methods similar to that previously described in this thesis for BSA on nanodiamond (see sections 2.2.3 and 3.2.3) , and elsewhere.[51, 53, 54]

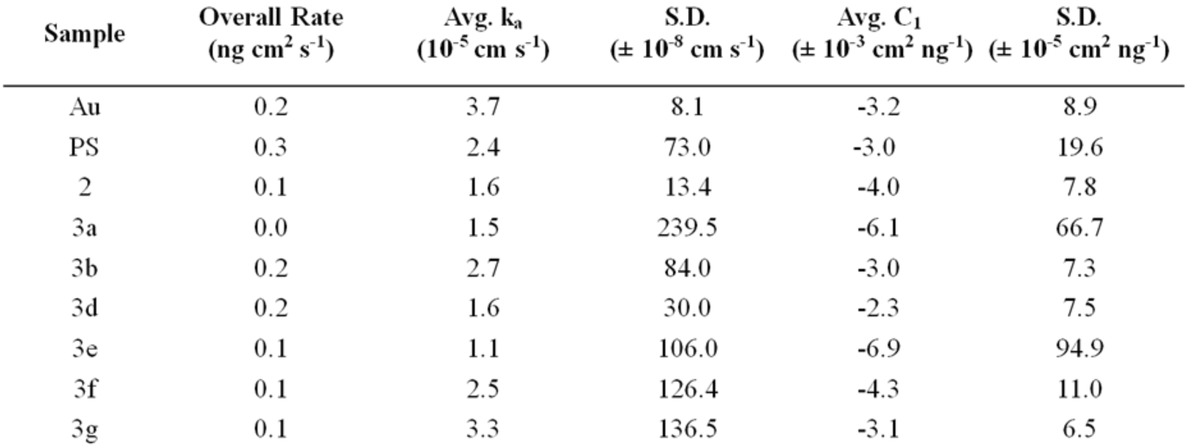

Sample	Overall Rate (ng cm^2 s^{-1})	Avg. k_a (10^{-5} cm s^{-1})	S.D. (± 10^{-8} cm s^{-1})	Avg. C_1 (± 10^{-3} cm^2 ng^{-1})	S.D. (± 10^{-5} cm^2 ng^{-1})
Au	0.2	3.7	8.1	-3.2	8.9
PS	0.3	2.4	73.0	-3.0	19.6
2	0.1	1.6	13.4	-4.0	7.8
3a	0.0	1.5	239.5	-6.1	66.7
3b	0.2	2.7	84.0	-3.0	7.3
3d	0.2	1.6	30.0	-2.3	7.5
3e	0.1	1.1	106.0	-6.9	94.9
3f	0.1	2.5	126.4	-4.3	11.0
3g	0.1	3.3	136.5	-3.1	6.5

Table 5.5: Table of kinetic parameters. All data shown represent averages using the Sauerbrey mass for the following overtones: n = 5, 7, 9. Note: (a) Overall rate relates to the first 20 minutes of BSA adsorption with errors of ± 0.05 ng cm^{-2} s^{-1}.

The core assumption of the subsequent kinetic analysis is that the d*m*/dt plots in Figure 5.9 can be approximated with the RSA model. Use of this model requires that the lineshape of the d*m*/dt plot be concave during the reaction-limited region. Here, those systems with the most distinct, concave profiles (e.g. **3b**, **3f**, **3g**) likely have BSA binding in the most RSA-like manner (i.e. immobile proteins, irreversible adsorption).[51] More linear d*m*/dt plot profiles (e.g. **3a**, **3d**, **3e**) probably indicate the influence of adsorption occurring *via* slower Langmuir processes (i.e. mobile proteins, reversible adsorption, clustering, aggregation).[51] Notwithstanding individual differences, to varying degrees, the plots in Figure 5.8 have concave shape within the reaction-limited region. Thus, for ease of comparison, BSA adsorption onto the as-prepared films will be approximated by the RSA model.[51, 54]

The rate constant (k_a) and the adsorption footprint (C_1) are obtained from a linear regression of the reaction-limited region, as suggested by Equation 2.16 and done by others.[51, 53, 54] The results of this analysis are shown in Table 5.5. The application of this kinetic analysis produces results which are consistent with those obtained by Brusatori *et al.* for the adsorption of HSA onto charged and uncharged surfaces using the OWLS technique.[53] As well, the k_a and C_1 values are close to those obtained using QCM-D for the deposition of other globular proteins onto self-assembled monolayers.[54] This comparison indicates that reasonable conclusions may be inferred from this particular application of the RSA model to BSA adsorption.

Before considering individual results, the physical meaning of k_a and C_1 must be established. As calculated here, k_a should be referred to as a rate constant. However, a correlation between k_a and adsorption mass is seen in Figure 5.10A and this correlation is strongest for short adsorption times. This reflects the fact that k_a is mainly a measure of the interaction of the protein with clean surfaces; at long reaction times, protein-protein interactions need to be taken into account. In the literature k_a is often also called the protein-surface affinity, reflecting a correlation between adsorption kinetics and protein binding energy.[7, 48, 53, 54]

The C_1 values calculated here are kinetic parameters, reflecting how adsorbed protein slows down the subsequent rate of uptake of further protein species. C_1 is considered a measure of 'footprint size' in the literature. [7, 53, 54] One alternative measure of footprint size is A_{ad} (adsorption area), which is calculated directly from adsorption mass:

$$A_{ad} = \frac{M_w}{m\,N_A} \qquad \text{(Equation 5.1)}$$

where M_w is the molecular weight (≈ 66.4 kD for BSA), and N_A is Avogadro's constant, and *m* is the mass density. Values of A_{ad}, as calculated from $m_{\text{Sauerbrey}}$ and m_{Voight} after 20 minutes of adsorption, are shown in Table 5.6. These results are consistent with the range of footprint sizes found in the literature (16-70 nm^2, depending on protein orientation and arrangements).[10, 14] There also some linear correlation between A_{ad} and $-C_1$ ($R^2 = 0.96$ for $A_{ad\ \text{Sauerbrey}}$ or $R^2 = 0.81$ for $A_{ad\ \text{Voight}}$). This supports the use of C_1 as a measure of average footprint size during protein adsorption in this work.

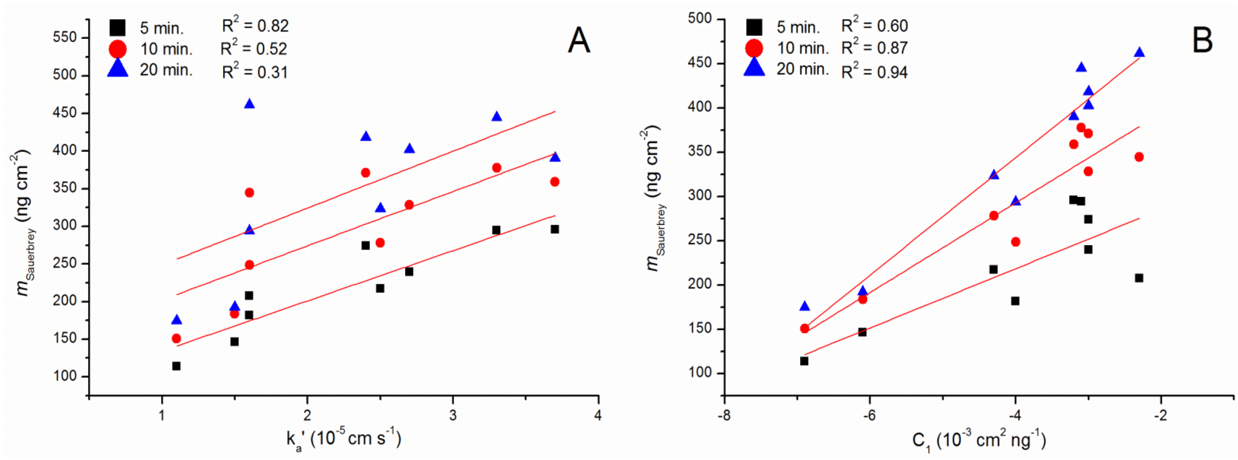

Figure 5.10: Comparisons between adsorption mass at different time points and various surface parameters relating to adsorption kinetics.

There is a positive correlation between C_1 and accumulated mass, as seen in Figure 5.10B; the bigger $|C_1|$, the bigger the footprint and the smaller the mass. In fact, C_1 is a better predictor of *saturation* adsorption mass than k_a (cf. Figures 5.10 A and B). These observations were expected, considering that C_1 is related to the available area function in Equation 2.14 (see also, Equation 2.16). Whilst the rate constant contributes to adsorption mass near time = 0, it is the available area function which governs the area available for adsorption at later time frames Proteins having a larger footprint upon adsorption, by having larger size and/or a larger excluded area, limit the area available to incoming proteins for adsorption. It may also take time for a protein to undergo the conformational changes necessary to adopt an energetically favoured structure at the interface.[10, 55] This explains why C_1 is a better predictor of total mass at saturation, than during initial adsorption.

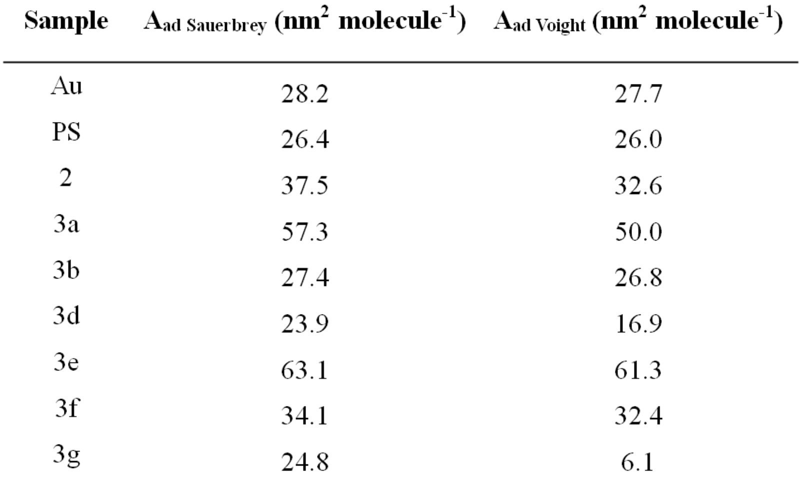

Sample	$A_{ad\ Sauerbrey}$ (nm^2 molecule^{-1})	$A_{ad\ Voight}$ (nm^2 molecule^{-1})
Au	28.2	27.7
PS	26.4	26.0
2	37.5	32.6
3a	57.3	50.0
3b	27.4	26.8
3d	23.9	16.9
3e	63.1	61.3
3f	34.1	32.4
3g	24.8	6.1

Table 5.6: Approximate surface areas of an adsorbed BSA molecule on various substrates

The relationship between surface chemistry and these two parameters can now be described. The surface chemistry affects the magnitude of k_a. This parameter has a higher value on Au, PS, **3g**, **3f**, and **3b** (i.e. BSA has high *initial* affinity for gold, polystyrene, hexyl, acid, and amine functionalities). High *initial* protein-surface affinity is expected in the case of hydrophobic surfaces due to the expected denaturing at such surfaces (e.g. gold, PS, **3g**), surfaces which have hydrogen donors (e.g. **3f**) , and surfaces capable of binding to specific binding sites on albumins (e.g. **3f**, **3b**).[4, 31] Lower k_a values are associated with surfaces **2**, **3a**, **3d**, and **3e** (i.e. BSA has less *initial* affinity for aniline, phenyl, phosphate diester and glycol functionalities). This is consistent with the relative inertness of surfaces known to have some or all of the following characteristics: polar, have no hydrogen donors, neutral electrical charge, and/or large hydration shells.[4] Any structural change on these surfaces would be more likely due to protein-protein interactions. In general, one would expect initial adsorption mass to be higher for those surfaces which promote stronger protein-surface interactions.[6] This is the case, as noted earlier when justifying the use of k_a as a measure of *initial* protein-surface affinity (see Figure 5.10A).

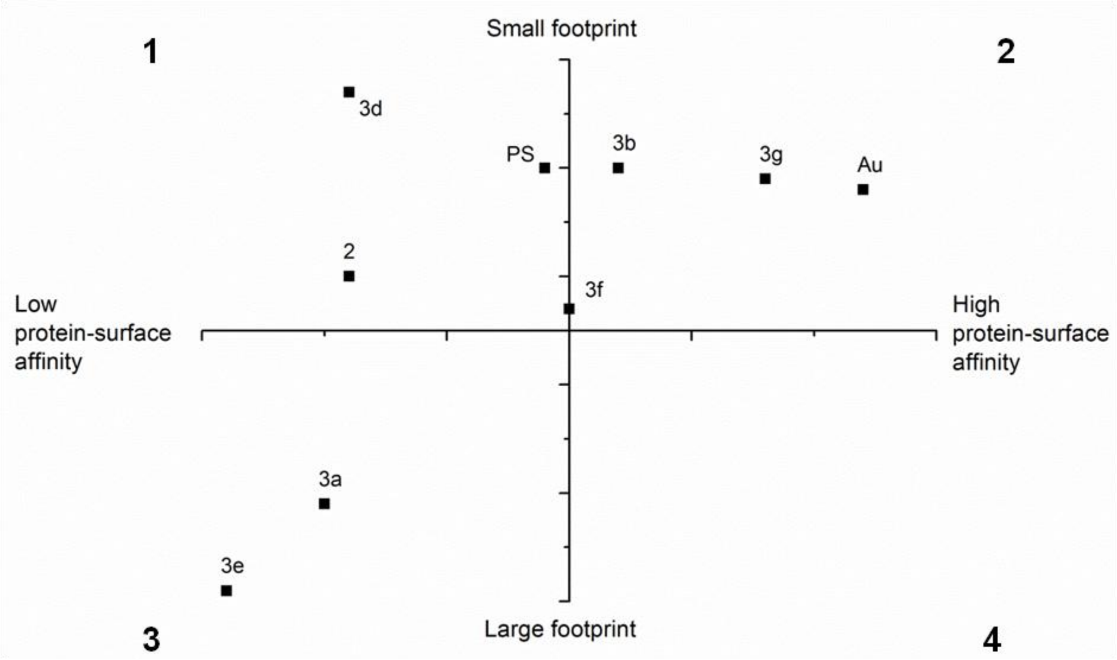

Figure 5.11: Schematic showing relative protein affinity and footprint size, based on the k_a and C_1 data from Table 5.5. The numbers in bold at the corners identify the quadrants referred to in the text.

The surface chemistry affects the footprint size as seen in Tables 5.5 and 5.6. From this data, BSA on these surfaces has three footprint sizes: large, intermediate, and small. Large footprints occur at surfaces **3a** and **3e**. Intermediate footprints are found on surfaces **3f** and **2**. Small footprints are associated with the remaining surfaces, particularly on surface **3d**. Normally, large footprint sizes are associated with a major change in conformation and flat orientations.[7, 14] Smaller footprint sizes are associated with native protein structure, end-on orientations, and/or proteins in a constrained environment (e.g. clustering or aggregation due to high protein-protein interactions).[7, 14, 56] Specific protein-surface interactions could also constrain protein size or orientation. *Primae facie*, it is difficult to deconvolute the contributions to footprint size from all the factors described above, however this may be possible by considering both footprint size and *initial* protein-surface affinity, together.

By plotting C_1 as a function of k_a , as is done in Figure 5.11, the relationship between protein-surface affinity and protein size can be determined. The results are grouped into three quadrants: Quadrant 1 is associated with low protein-surface affinity and small footprint size, and is exemplified by BSA on surfaces **3d** and **2**; Quadrant 2 has protein layers with high protein-surface affinity and small footprint, particularly on surface **3g** and **Au**; Quadrant 3 has protein layers with low protein-surface affinity and large footprint, which is clearly the case for BSA on surfaces **3a** and **3e**. A fourth quadrant is not linked to BSA behaviour on any of the studied surfaces, but layers in this quadrant would have high protein-surface affinity and large footprints. Some systems have more intermediate behaviour (e.g. PS, **3f**), which likely indicates that a mixture of BSA behaviours are occurring at these interfaces.

Interpretation of Figure 5.11 begins by considering the following: strong protein-surface interactions are known to increase protein size (i.e. denaturation)[1], and in the absence of strong protein-surface interactions, a change of size – if any - must occur by other means (i.e. aggregation or clustering, spreading due to strong protein-protein interactions, and/or a change of orientation). The first half of this working hypothesis would be best described by Quadrant 4 behaviour. However, none of the surfaces here are inducing a major conformational change by strong protein-surface affinity. The opposite of Quadrant 4 behaviour is Quadrant 1 behaviour. Protein layers in this quadrant have footprint size consistent with end-on orientation (16 - 48 nm^2, see Table 5.6) and likely have minimal structural change – possibly BSA is in a native state. Aggregation or clustering could be associated with BSA layers on **3d**, as the footprint size of BSA on this surface (16.9 nm^2 or 23.9 nm^2 , see Table 5.6) is smaller than the theoretical footprint size of 24.0 nm^2 (calculated by assuming BSA is a hard sphere with molecular volume of 88.25 nm^2).[57] The kinetics of aggregation or clustering are slow, which is consistent with the kinetics of the ΔD vs. Δ*f* plots for **3d** and **2** described in section 5.3.3. From this one concludes that Quadrant 1 behaviour involves BSA in an end-on orientation, in either a native form or ‘squeezed’ form, depending on the extent of aggregation or clustering.

BSA on surfaces **3b**, **3g**, and Au have obvious Quadrant 2 behaviour in Figure 5.11. There exist strong protein-surface affinity between BSA and these surfaces, but with little of the structural change normally associated with such strong affinity. The formation of BSA multilayers on any of these surfaces, but particularly **3g**, would limit conformational change as protein density increases at the surface. It is interesting to note that surface **3f** has behaviour near that of **3b** and **3g**. BSA is known to have specfic protein-surface binding with these three surfaces – acid, amine, and hexyl functionality, respectively - *via* polar and non-polar binding sites.[31] It may be possible that this specific binding mode imparts a constraint on structural change. Specific binding could also be the major contributor to strong protein-surface affinity, compared to other interactions between a protein and a surface (i.e. hydrogen bonding, hydrophobic forces, etc.). Whether caused by multilayers or specific binding modes, quadrant 2 behaviour constrains BSA to an end-on orientation, with the size of BSA Au, **3b**, and **3g** being between 16 - 48 nm^2 (see Table 5.6).[10,14]

The results in Quadrant 3 (**3a**, **3e**) are associated with low protein-surface affinity, as seen for Quadrant 1, but have larger footprint size. The larger size is unlikely to be due to conformational change by protein-surface interactions, due to the low protein-surface affinity. This increase in size could be due to one of two events: a change to flat orientation from end-on orientation (i.e. ‘flattening’[51], or a change of structure caused by strong protein-protein interactions (i.e. ‘spreading’[58]). On these two surfaces, BSA has a size 170 - 200% larger than its native form (cf. results in Table 5.6 with native footprint of 24.0 nm^2). Whilst this could be caused by spreading, the extent of this change of size is consistent with a change of orientation from end-on to side-on. If end-on and side-on orientation has footprints of 16 - 48

nm^2 and 56 - 70 nm^2, respectively, then one expects a 46 - 250% expansion in the BSA footprint size, upon a change of orientation.[10,14] Moreover, spreading is a process which would lead to quick changes in conformation upon adsorption, which is not the case for BSA on **3a** and **3e**, based on the kinetics of their respective ΔD vs. Δf plots (seen Figure 5.5). Based on the above, one concludes that BSA on surfaces **3a** and **3e** are in a flat orientation with minimal change of protein structure.

5.3.5 Parameters of Surface Terminations

The surface functionalities applied to polystyrene in this work have chemistry of importance to the drug industry.[31] Modern computational methods are used to screen compounds for the specific chemical traits needed to interact with specific biological processes. Compounds are screened using parameters which are known to be important for its chemical function (e.g. pK_a, molecular size, polarizability, etc.[31]). It is also possible to use this same screening method to probe the relationship between surface chemistry and protein interactions at interfaces. This was done recently by Choong *et al.*[31] at polystyrene beads modified using the same carbene chemistry used in this chapter and Chapter 4 (see Figure 4.2). Considerable insight could be gained by replicating their approach, particularly considering that the QCM-D data obtained here enables BSA behaviour at both early and late adsorption to be probed.

Several of these parameters - referred to as ‘surface parameters’ here – have been calculated or experimentally derived for the as-prepared surfaces. They are shown in Table 5.7. The use of pK_a values enables the role of acidity, electrostatic attraction and hydrogen bonding on protein adsorption behaviour to be evaluated; values were estimated from reference tables. The chain lengths of the surface functionalities were calculated using tables of carbon bond lengths, whereby the length of the functionality is calculated from the surface of the polystyrene film to the terminal chemical group. The number of surface-protein interactions, in their various forms (i.e. hydrogen bonding, van der Waals forces, etc.) and the extent of hydration shells could be affected by chain length. The c log P is the octanol/water partition coefficient, calculated using the method of Viswanadham *et al.* for each functionality.[59] The c log P value estimates a surface's lipophilicity, and the values were tabulated using this source.[31] The polar surface area (PSA) is the sum of the surfaces of polar atoms in a compound.[31, 60] The percent polar surface merely reflects PSA as a percentage of the total surface area of the compound, and are taken from here.[31] The PSA value has been shown to correlate well with the transport properties of drugs.[31, 60] The contact angles from Table 4.10 are included here for reference. It was thought that the use of contact angles could provide insight into the role of surface wettability on protein adsorption.[31]

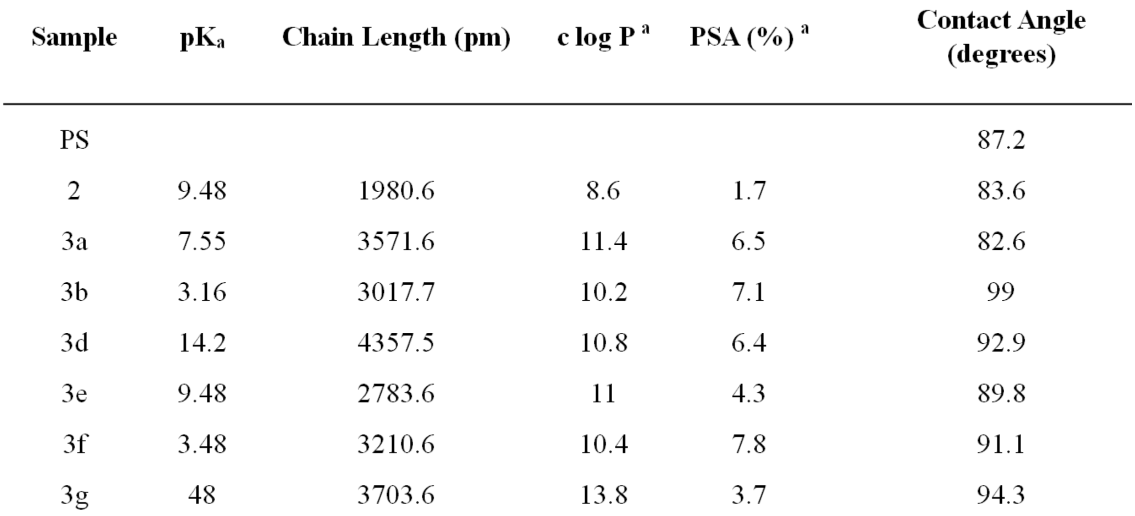

Sample	pK_a	Chain Length (pm)	c log P [a]	PSA (%) [a]	Contact Angle (degrees)
PS					87.2
2	9.48	1980.6	8.6	1.7	83.6
3a	7.55	3571.6	11.4	6.5	82.6
3b	3.16	3017.7	10.2	7.1	99
3d	14.2	4357.5	10.8	6.4	92.9
3e	9.48	2783.6	11	4.3	89.8
3f	3.48	3210.6	10.4	7.8	91.1
3g	48	3703.6	13.8	3.7	94.3

Table 5.7: Data describing the surface terminations of as-prepared polystyrene samples. The pK_a values (in water) were determined using Chemicalize software[31, 61] or from reference tables.[62-64] The pK_a values for **3g** is estimated to be the same as methane and for **3f**, ethylene glycol; **3e** is comparable to **2**. Values for c log P and PSA are from Choong *et al.*.[31] The chain lengths were calculated from bond lengths from chemical drawings using ChemDraw Ultra (v. 12.0), with the length representing the distance from the polystyrene surface to the terminal end-group, assuming a near-vertical orientation.

Here, the mass density of BSA at varying time points (5, 10, and 20 min.) has been plotted against pK_a, chain length, c log P, PSA, and contact angle, in order to link the influence of the various surface chemistries described by these parameters to BSA

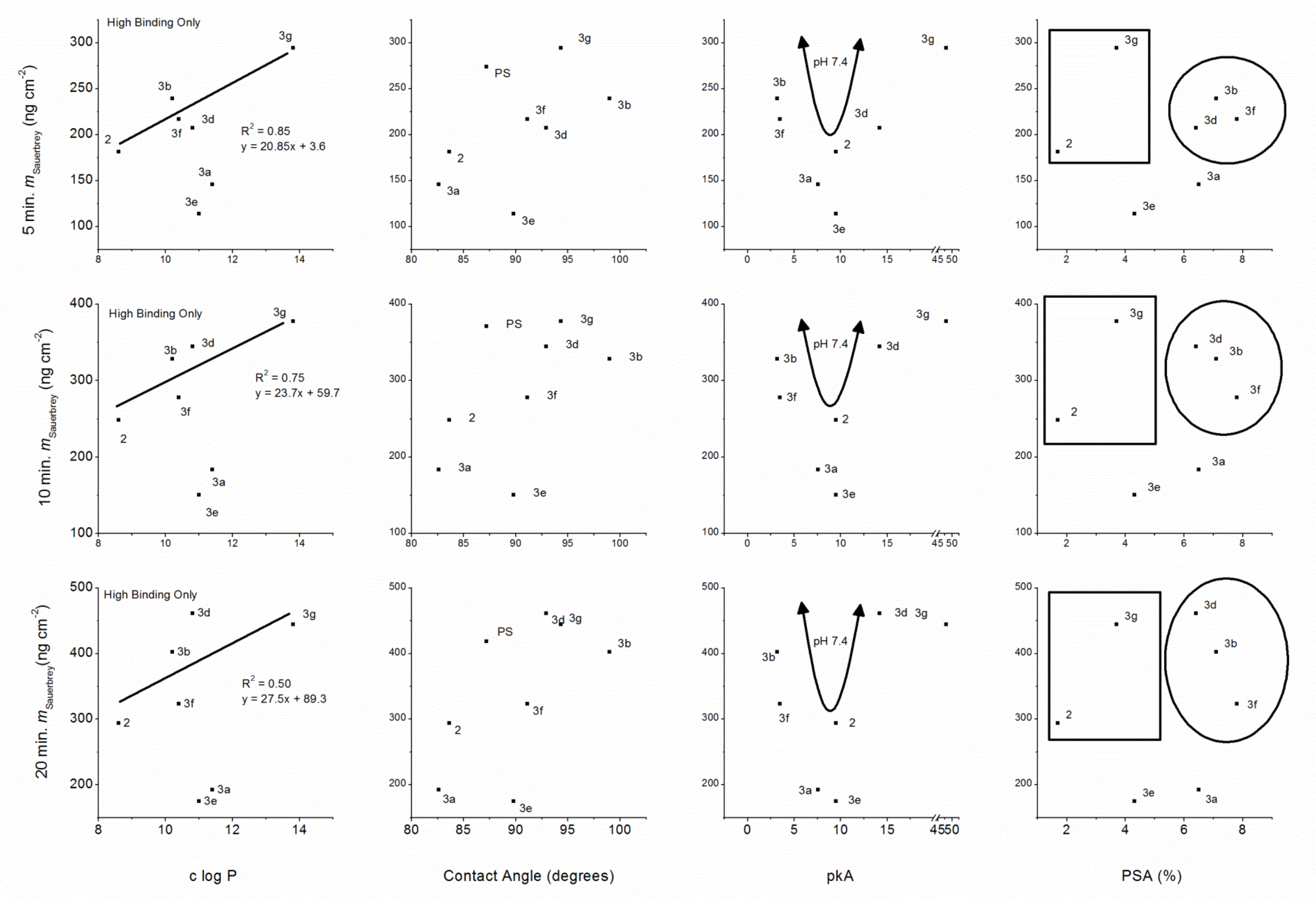

Figure 5.12: Sauerbrey Mass *versus* surface parameters.

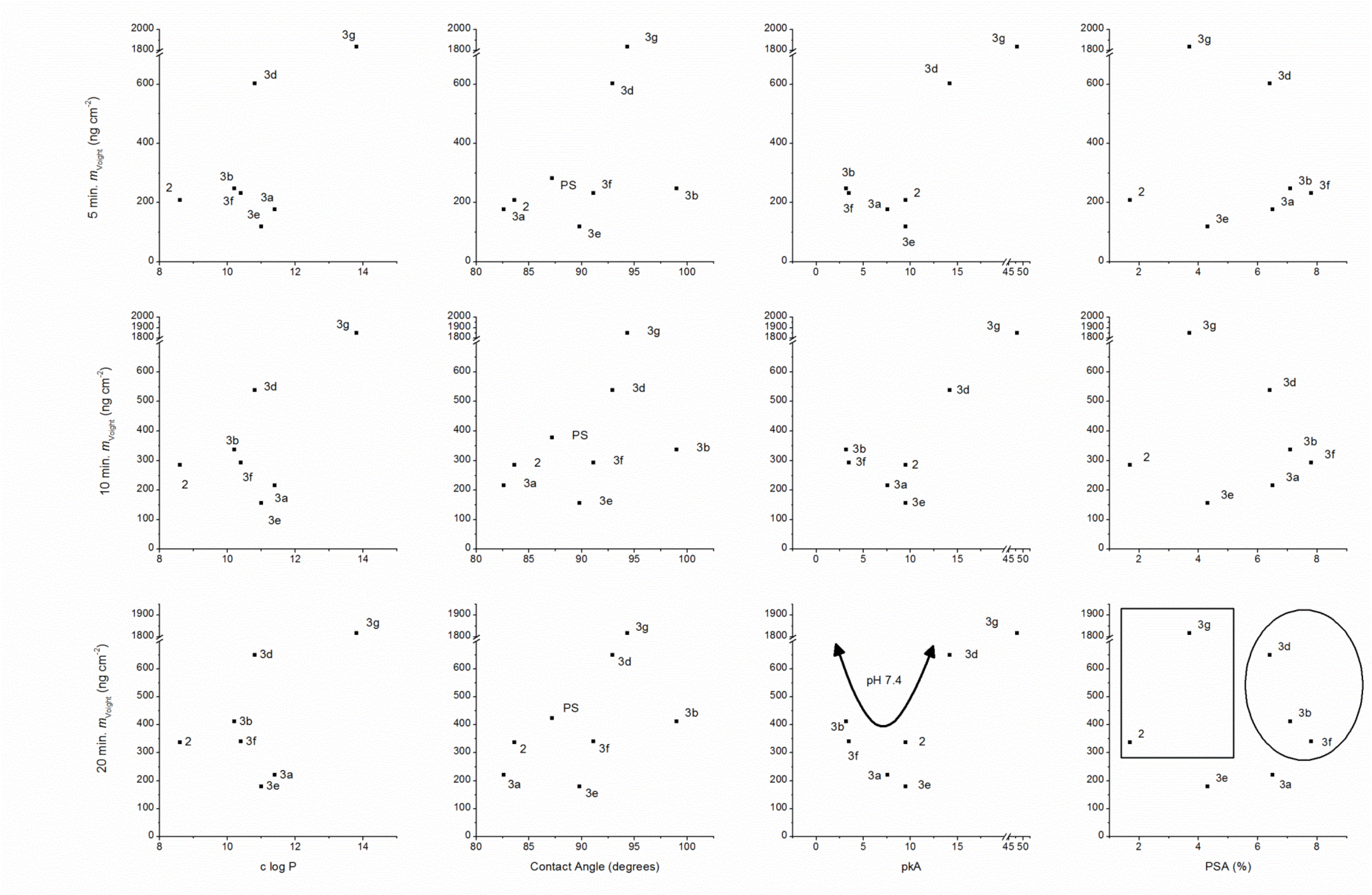

Figure 5.13: Voight Mass *versus* surface parameters.

adsorption. These comparisons are shown in Figures 5.12 and 5.13, using both the Sauerbrey and Voight mass data. The trends in Figures 5.12 and 5.13 that will be discussed are similar when either $m_{\text{Sauerbrey}}$ or m_{Voight} is used. However, these trends are more distinct when $m_{\text{Sauerbrey}}$ is used, over all time frames. Therefore, subsequent description of the results will focus on Figure 5.12.

The role of lipophilicity and surface wettability on BSA adsorption is best evaluated using c log P and contact angles, respectively. Lipophilicity is known to lead to higher adsorption mass.[1, 31] In Figure 5.12 (first column), a correlation between adsorption mass and c log P is seen for surfaces whose mass density > 200 ng cm^{-2} . From this one concludes that BSA binding may depend on lipophilicity. However, the exact relationship is somewhat unclear, considering that surfaces **3a** and **3e** have moderate lipophilicity and low mass density. By contrast, there is no clear, strong trend between adsorption mass and contact angles, as also observed by Choong *et al.*.[31] However, it should be noted that the two most hydrophilic surfaces (**2**, **3a**) have low adsorption mass, whilst **3g**, the sample expected to be most hydrophobic, does have the highest adsorption mass. To a limited extent, this suggests that hydrophilicity could be a feature of protein resistant surfaces.

The pK_a of carboxylic acids is known to affect the binding of such chemical functionality to HSA.[65] Using that study as a template, pKa values were obtained and compared to adsorption mass. The pK_a values relate to either the acid (i.e. carboxyl group) or the conjugate acid (i.e. in the case of the amine functionality). Surfaces with either, very low pK_a (i.e. **3b**, **3f**), or high pK_a (i.e. **3d**, **3g**), have a correlation with higher BSA adsorption. Surfaces with pK_a near that of pH 7 have low BSA adsorption (i.e. **2**, **3a**, **3e**). These observations may relate to the preference, or otherwise, of water at the interface. The presence of strongly bound water layers at an interface is known to prevent protein binding by raising the energy barrier to adsorption.[6] Surfaces with very low pK_a or high pK_a do not have strong polar interactions with water, therefore making protein binding more energetically favourable (i.e. only weakly bound water needs to be displaced prior to adsorption). Surfaces with near-neutral pK_a can easily associate/dissociate hydrogen with water, and form hydrogen bonds between the interface and the bulk fluid. This strong association with water would make adsorption less energetically favourable (i.e. water must be displaced prior to adsorption).

The polar surface area is a parameter which is known to correlate with the transport of drugs through cellular membranes.[31, 60] Since proteins are a constituent of membranes, it is therefore plausible that this parameter may be related to the interactions between proteins and chemical functionality. To test this hypothesis, the adsorption mass at 5, 10 and 20 minutes, was plotted as a function of PSA. As exemplified in Figure 5.12 (last column), BSA adsorption at mass densities greater than 150 - 200 ng cm^{-2} seems to depend on PSA. This relationship is clearer at saturation, and it is particularly prominent at even longer time frames, as Choong *et al.* show, for BSA deposition of < 1 hour.[31] If a surface has PSA less than 4% , or greater than 6%, binding seems to occur. A lack of extreme PSA seems to limit BSA adsorption. Surfaces with the required PSA to promote BSA binding are denoted by the ovals and squares in Figure 5.12. This pattern of binding behaviour is thought to indicate the presence of two types of binding sites on BSA: the polar and non-polar sites.[31, 36] Hydrogen bonding and van der Waals forces are features known to exist at surfaces with high and low PSA, respectively; it is these two interactions which may be driving specific protein binding here.[31]

The relative influence of chain length is thought to be resolved by plotting adsorption mass ($m_{\text{Sauerbrey}}$ and m_{voight}) at three different time points (5, 10 and 20 minutes), as a function of chain length (see Figure 5.14). There is a positive correlation for those functionalities promoting 'high binding' at saturation (i.e. $m_{\text{Sauerbrey}}$ > 250 ng cm^{-2}). In addition, chain lengths > 3500 pm seen to confer an unusually high m_{Voight}. Longer chain length could influence protein adsorption in one of three obvious ways: larger excluded volume (i.e. a steric hindrance to adsorption), increased surface hydration, or increase the number of favourable or unfavourable protein-surface interactions.[4] The first two factors increase the energy requirement for protein adsorption, whilst the third decreases this requirement.[66, 67] It is unlikely that excluded volume is a factor, as a negative correlation would be associated with this affect. Lower excluded volume would correlate to higher adsorption, as the available surface area would be higher, and *vice versa* - this is not the case in Figure 5.14. With the above in mind, the role of protein-surface interactions is clearly suggested by the results for surface **3g**. This hexyl-terminated surface would not have extensive surface hydration, which therefore means that the high adsorption seen on surface **3g** is due to a large number of *favourable* protein-surface interactions. The role of favourable protein-surface interactions is further supported by the fact that the results of Figure 5.14, correlate well with the k_a values seen in Table 5.5. The role of protein-surface interactions is not as clear for surface **3d** , which has time dependent behaviour in Figure 5.14.

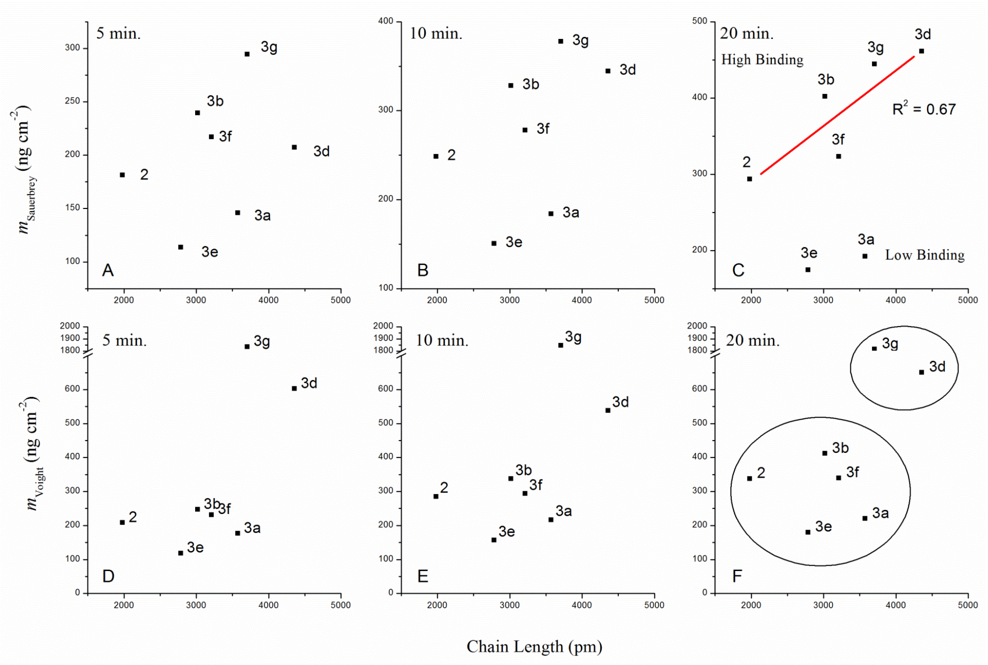

Figure 5.14: Adsorption mass *versus* chain length.

After 5 minutes, the adsorption mass of BSA on surface **3d** is low, but at 20 minutes, the adsorption mass exceeds that of surface **3g**. This behaviour is particularly striking considering the low k_a value associated with surface **3d** (see Table 5.5). This behaviour has been seen before for poly(ethylene glycol) chains (**3d**) over a period of 24 hours.[31] The phenomenon causing this behaviour must both be *initially* resisting BSA adsorption, and then increasing BSA adsorption during later adsorption phases, by increasing the number of *favourable* protein-surface interactions - as inferred from the previous paragraph. Surface hydration would lead to both of these phenomena occurring, and be time dependent. Surface hydration imposes an energy barrier to adsorption, as water molecules bound around surface functionalities must be removed prior to protein adsorption.[6, 31, 68] As hydration is slowly removed, the hydrogen bond network between the surface and water molecules can be replaced by favourable protein-surface interactions (i.e. hydrogen bonding, van der Waals interactions, etc.). This scenario is plausible here as poly(ethylene glycol) chains are known to promote high surface hydration, with water molecules bound in a coiled formation around the ethylene glycol sub-units.[69] The number of water molecules per ethylene glycol unit is about 8 to 25 molecules, for low and high grafting density.[68] The release of an upward of 75 water molecules per ethylene glycol unit would lead to a large entropy gain, and a large increase in favourable protein-surface interactions. There is also a weaker time dependency seen in the data associated with aniline (**2**) and phosphate diester (**3a**) modification. Surface hydration on each of these two surfaces does exist, with 32 water molecules around each aniline unit and 23 to 26 water molecules around each phosphate diester.[70, 71] The reduced protein adsorption at these surfaces is partly explained by the reduced entropy gained, compared to ethylene glycol units, when these water molecules are released to bulk solution upon protein adsorption. It is also possible that the water molecules are more tightly bound at these two interfaces, which would raise the energy barrier to adsorption. This is surmised to be the reason for the low adsorption on phosphate diester and aniline surfaces.[31, 72]

5.4 Discussion

In this chapter, *in situ* protein adsorption studies were conducted on variously modified polystyrene thin films using QCM-D methods. The polystyrene thin films studied here were modified with a carbene-based coating, which has imminent industrial relevance. The application of the coating imparted a different surface chemistry to the polymer, with each having an affect on the dynamics of BSA adsorption, as shown in this chapter. The affects were shown to be similar to that found in the literature for self-assembled monolayers and polystyrene beads, with similar surface chemistry.[4, 31]

The stable QCM-D results obtained in this work show that the as-prepared polystyrene films are suitable for QCM-D analysis. The adsorption of BSA to modified polystyrene films was successful, with data associated with protein mass, viscoelastic properties, and kinetic properties, leading to useful conclusions. The primary conclusion being that the carbene chemistry used to modify these films was capable of inducing a range of different protein-surface behaviours. The relationship between surface chemistry and protein dynamics was determined by closely analyzing the various QCM-D results.

On the as-prepared polystyrene films, protein behaviour can be divided into four classifications. This division is based on an analysis of Table 5.8, which summarizes the results of this chapter. The four classifications of behaviours are: Protein Resistors; Hydration Shells, Specific Binders, and Multilayer Deposition. The 'Protein Resistors' include those surfaces which have low adsorption mass, and includes the phosphate diester (**3a**), phenyl (**3e**), and aniline (**2)** functionalities. The behaviour of BSA on glycol (**3d**) terminated surface is governed by hydration shells, but this surface is also considered a

		Polystyrene (PS)	Aniline (2)	Phosphate diester (3a)	Amine (3b)	PEG (3d)	Phenyl (3e)	Carboxyl (3f)	Hexyl (3g)
Adsorption data	Adsorption Mass	moderate	moderate	low	high	high	low	high	high
	Extent of Hydration	rigid	rigid	rigid	rigid	hydrated	rigid	rigid	hydrated
	Orientation at saturation	end-on or mixed	flat	flat	end-on or mixed	end-on or mixed	flat	flat	multilayers
Rinsing data	Type of Adsorption	irreversible	reversible	reversible	irreversible	reversible	irreversible	irreversible	irreversible
Formation of initial RSA monolayer	Orientation	flat	flat	flat	end-on or mixed	flat	flat	flat	flat
	Kinetics	fast	slow	slow	fast	slow	slow	fast	fast
Other QCM-D data and Surface Parameters	Relationship of protein affinity (k_a) and footprint (C_1)	Quadrant 1	Quadrant 1	Quadrant 3	Quadrant 2	Quadrant 1	Quadrant 3	Quadrant 1 or 2	Quadrant 2
	ΔD vs. Δf behaviour during adsorption	Group 1	Group 2	Group 3	Group 4	Group 3	Group 2	Group 4	Group 1
	ΔD vs. Δf behaviour during rinsing	Group 2	Group 2	Group 2	Group 3	Group 2	Group 1	Group 1	Group 1
	ΔD vs. Δf relationship after rinse	Group 2	Group 1	Group 3	Group 1	Group 1	Group 3	Group 1	Group 2
	Features suggested by surface parameters		high water-surface affinity; binding is weak and non-polar	high water-surface affinity	specific binding; low water-surface affinity	hydration shells; water-surface affinity is time-dependent	high water-surface affinity	specific binding; low water-surface affinity	hydrophobic interactions maximized by long chain length and low water-surface affinity
Conclusions	Dominant processes	hydrophobic	Resistance due to high water-surface affinity, with soluble aggregates of protein at interface. Any protein-surface binding is weak and non-polar.	Resistance due to high water-surface affinity, with soluble aggregates of protein at interface	strong, specific polar binding	slow adsorption due to need to remove hydration shells prior to adsorption	Resistance due to high water-surface affinity, with insoluble aggregates at interface	strong, specific polar binding	strong binding in multilayers by hydrophobic interactions
	Label	Control	Control	Protein Resistor	Specific Binder	Hydration Shells	Protein Resistor	Specific Binder	Multilayers

Table 5.8: Summary of results collected throughout this work. The first column relates conclusions to the various sections in this chapter: Adsorption data (sections 5.3.2.1 and 5.3.2.2); Rinsing data (section 5.3.2.3); Formation of initial RSA monolayer (section 5.3.3); QCM-D data and surface parameters: ΔD vs. Δf behaviour (section 5.3.3); k_a and C_1 (section 5.3.4); surface parameters (section 5.3.5). For convenience, the figures associated with the ΔD vs. Δf data for behaviour during: adsorption (Figure 5.5 and 5.6), rinsing (Figure 5.7), and after rinsing (Figure 5.7). The group labels are described in the text, and are specific to each row.

protein resistor during the early stages of adsorption. Two functionalities facilitate specific binding to BSA, and they are the amine(**3b**) and carboxyl (**3f**) modifications. The last class regards hexyl-terminated (**3g**) functionality, whose strong hydrophobic interactions with BSA leads to multilayer formation at the interface. The justification for the above types of protein-surface behaviours is discussed below.

Protein resistors are those surfaces which promote low mass density of BSA. Four surfaces show this ability throughout adsorption and rinsing stages: phosphate diester (**3a**), phenyl (**3e**), and aniline (**2**), whilst the glycol (**3d**) functionality resists protein adhesion during initial adsorption and rinsing. The protein resistance of the glycol functionality is time dependent, and this was attributed to extensive and weakly bound hydration shells at this interface. This will be discussed later as a special case of protein resistor. As summarized in Table 5.8, the remaining three samples share similar characteristics, all of which have been noted to prevent protein adhesion in studies using self-assembled monolayers and polystyrene beads.[4, 31] Phosphate diester and aniline functionalities are the most hydrophilic studied here, with hydrophilicity known to prevent protein adhesion.[1] In particular, hydrophilic surfaces and surfaces with near-neutral pK_a have a strong association with water at pH 7, thereby raising the energy barrier to protein adsorption, as explained in section 5.3.5. There exists no specific binding between **3a** and **3e** and BSA, with **2** only showing evidence of weak non-polar binding (see Figure 5.12, fourth column). The net effect of the above is that **2**, **3e**, and **3a** have low protein-surface affinity (see section 5.3.4), slow adsorption kinetics (see section 5.3.3 and 5.3.4), with no evidence of major conformational change (see section 5.3.3.). These factors lead to an arrangement of flat BSA in a native state, based on the mass density and adsorption footprint data. Aggregation of BSA is also possible at these interfaces, as mentioned in section 5.3.3. Ultimately, the consequence of such a protein arrangement is to limit the available surface area for further protein deposition and weaken protein-surface interactions to incoming proteins.

Major differences in BSA behaviour exist on this protein resistor which warrants comment. Adsorption is reversible on phosphate diester and aniline-terminated polystyrene, but irreversible on phenyl-terminated polystyrene. This contrasting behaviour is clearly seen in Figure 5.3C, and an explanation is warranted, which is consistent with their protein resistant properties. In the case of the former two surfaces, reversible binding is promoted by the low protein-surface affinity and a lack of conformational change. The mechanism of this reversible binding may be similar to that on the glycol surface, as BSA adsorption on phosphate diesters and aniline moieties, due to their similar viscoelastic and kinetic characteristics (see Table 5.8). BSA adsorption on glycol-terminated surfaces, as argued later, is governed by the formation of soluble aggregates and high surface hydration. [31, 73, 74] Aggregation is possible at phosphate diester and aniline functionality, as BSA adsorption is slow on these two surfaces (see sections 5.3.3 and 5.3.4), with surface hydration being tightly bound. (see section 5.3.5). Surface hydration at phosphate diester and aniline films is likely more extensive than on PEG chains, as evidenced by a glance at the pK_a values and the lack of adsorption data time-dependency, as best seen in Figure 5.14. Thus, one concludes that some protein resistance behaviour on phosphate diester and aniline functionality is governed by surface hydration and the promotion of soluble BSA aggregates.

On the other hand, binding is irreversible at the phenyl interface. Irreversible binding to this interface is surprising. Adsorption of BSA at phenyl interfaces is limited by the weak non-polar binding between BSA and bulky ligands.[31] The structural change expected for irreversible binding *via* non-polar protein-surface interactions is not seen in Figure 5.5. To further complicate matters, the viscoelastic behaviour is approximately the same on phosphate diester – a surface promoting reversible binding – as it is on phenyl-modified polystyrene. Thus, the reason for this irreversible binding is not obvious. A few conjectures can still be made. Aggregate formation, as on the phosphate diester surface, may be occurring, but in an insoluble form, due to subtle structural change induced by protein-protein interactions.[56] Such behaviour has been seen for BSA on polystyrene surfaces before by Norde and Giacomelli[75], and it could be generalized to apply to other hydrophobic surfaces.[56, 75] Another conjecture is that initial protein layers at this interface are rigid and bound by weak protein-surface interactions, but those layers are sufficient to screen-out subsequent protein-surface interactions between phenyl groups and protein in solution.[9, 41] This is called 'protein blocking' and it has been seen before at polystyrene interfaces, as well as gold.[10,19,43]

The glycol-terminated surface is a different class of protein resistors, with resistance highly dependent on the extent of surface hydration. *Primae facie*, it would be convenient to associate the behaviour of BSA on glycol groups (**3d**) with that of BSA on phosphate diesters (**3a**) or aniline (**2**). These interfaces share much in common, as summarized in Table 5.8. For instance, during initial adsorption, BSA at all three interfaces has low mass, flat orientation, and similar viscoelastic properties. After rinsing, BSA adsorption on all three surfaces is highly reversible. Based on this, it is easy to class the glycol functionality as a protein resistor. However, adsorption mass increases at the glycol-based interface at later adsorption to a much greater extent than at the other two surfaces. This is effect is most prominently seen in Figure 5.14. In section 5.3.5, this phenomenon was associated with the slow displacement of weakly bound surface hydration around poly(ethylene glycol) chains. As water is displaced, there is both an entropy and enthalpy gain, respectively, as water molecules are released to the bulk and proteins interact with the ethylene glycol units by non-covalent bonding.[31] This effect is made more dramatic by the long chain length of the glycol functionality, which increases the number of possible polar interactions between BSA and ethylene glycol units (see Figures 5.12 and 5.14).

Specific protein-surface binding is a feature of amine (**3b**) and carboxyl (**3f**) functionality. These two surfaces are linked by their common effects on BSA behaviour, as indicated in Table 5.8. The possibility of specific binding being the dominant behaviour at these surfaces is suggested by the unique viscoelastic behaviour of BSA at their interfaces (see Figure 5.5). Previously, these 'curved' ΔD vs. Δ*f* plots have been associated with electrostatic binding between another globular protein, lysozyme (pI = 11.4[76]), and the carboxyl groups of poly(acrylic acid).[52] Strong protein-surface binding in this manner results in a rigid protein layer of high packing density, due to a lack of protein unfolding.[52] The behaviour of BSA at amine and carboxyl-terminated surfaces is consistent with those observations, as they were found to be rigid (i.e. less negative ΔD/Δ*f* ratio), have strong protein-surface affinity, and have small protein footprint (see Table 5.5). Other evidence for specific binding include: irreversible binding and a clear preference for polar binding with BSA (see Figure 5.12, last column). Strong covalent interactions are possible between albumins and certain functionalities, such as amines[36, 37] and carboxyl[38, 39] groups through, hydrogen bonding, aminolysis (i.e. covalent bonding), and/or electrostatic interactions (n.b. dependent on electrolyte concentration or pH[65]).

As an aside, it must be mentioned that specific binding is different at the amine and carboxyl-modified polystyrene. First, the binding forces are likely stronger at the amine-terminated interface, than the carboxyl-terminated surface. This is evidenced by higher mass uptake, greater irreversibility of binding, and higher protein-surface affinity on the former than the latter. Second, the orientation of BSA is different at each surface: end-on and flat orientation is associated with amine and carboxyl-modified polystyrene, respectively, based on the mass density data (summarized by Table 5.8). Third, the adsorption footprint is smaller on the amine functionality, than the carboxyl functionality (see Table 5.6). This indicates that the structure of BSA on carboxyl-terminated polystyrene is in a slightly less native state. Fourth, whilst similar, the ΔD vs. Δ*f* behaviour during adsorption and rinsing is still quite different, as noted in section 5.3.3. Collectively, this evidence could indicate that each binds to a different binding site on BSA. Each of these sites would have a preferred orientation and protein layer structure to maximize protein-surface interaction. This is not an unreasonable conclusion, considering that BSA has multiple binding sites of a hydrophilic and hydrophobic nature, with binding highly dependent on the chemistry of the bound moiety.[77, 78] It may be possible to target certain binding sites on BSA by using appropriate surface modification, in order to induce a distinct effect (i.e. tailor orientation or protein layer structure). In this manner, coating technology can better address the needs of the bio-materials community. Such coatings promise to find utility in applications were protein-surface interactions need to be highly specific in order to induce cellular growth or act as a bio-sensor.

Extensive hydrophobic protein-surface interactions govern the behaviour of BSA on hexyl-terminated polystyrene films. These interactions lead to multi-layer arrangements of BSA on the surface. In section 5.3.2, the mass density was associated with the presence of at least 4 – 5, or 2 – 3 monolayers of hydrated BSA in a flat or vertical arrangement, respectively. Multilayer formation is likely driven by hydrophobic interactions between BSA and the long alkyl chain lengths.[31] The high correlation between lipophilicity and chain length, with high adsorption mass is the strongest evidence for these hydrophobic interactions (see Figure 5.12 and Figure 5.14). In addition, there may be some specific interaction between non-polar binding sites on BSA and this surface[31], as suggested by the correlation between high adsorption mass and polar surface area in Figure 5.12. The viscoelastic and kinetic behaviour of BSA on hexyl-terminated polystyrene surface most resembles that of

BSA adsorption onto unmodified polystyrene here, to which BSA is known to bind *via* hydrophobic interactions (see Figures 5.6 and Figure 5.11).[1]

5.4.1 Comparison to BSA on Polystyrene Beads

Cleo Choong and co-workers have studied the adsorption of BSA onto polystyrene beads, using the same chemical synthesis and surface terminations described in this work. Their work and the results here are consistent, despite some differences in methodology (i.e. beads vs. thin films, mass determined by QCM-D vs. XPS). Two major similarities exist between the two studies. First, the same classification of protein-surface behaviour (i.e. protein resistors, specific binders, etc.) seen here does broadly apply to their work. Second, their strategy of using pharmaceutical related parameters (%PSA and c log P) to probe protein-surface interactions was successfully applied to the case of polystyrene thin films.

However, the investigation done here has considerable advantages over previous work done in this area. The work described in this chapter is an *in situ* study, not an *ex situ* study, as is the case when XPS is involved. The QCM-D technique enables precise measurement of *hydrated* mass, viscoelastic properties, and adsorption kinetics to be extract from each experiment, which is not possible using XPS. Moreover, for the first time, BSA adsorption on the described carbene-modified polystyrene was analyzed for protein deposition times of ≤ 1 hour here. The QCM-D technique collected precise data during this time frame, which made possible the prediction of BSA behaviour at later adsorption, particularly the total accumulated mass. Furthermore, the precise QCM-D data enabled parameters commonly used to screen drugs based on their chemical functionality (i.e. %PSA, c log P, k_a, etc.) to be used to predict and probe protein dynamics in as little as 5 minutes, rather than over longer time frames. This investigation suggests that short QCM-D experiments, of about 5 minutes, long may become a useful and high throughput method for analyzing and predicting the performance of coatings at polymer surfaces.

5.5 Summary and Conclusions

In this chapter, the relationship between protein adsorption and surface chemistry was studied *in situ* on materials with imminent industrial application in the bio-medical field. This work employed QCM-D in an innovative manner, by synthesizing several approaches to analyzing the mass, kinetic and viscoelastic data provided by this *in situ* technique. Using the protocols described here, the extent of protein adsorption and its dynamics can be evaluated, in detailed, within a short amount of time. The following emerged as key results:

- The carbene chemistry described in the previous chapter has lead to surfaces capable of stable protein adsorption studies using QCM-D.
- This carbene chemistry leads to surfaces having different surface chemistry, with regard to their interaction with BSA.
- Protein behaviour can be divided into four classifications:
    - ‘Protein Resistors’
    - ‘Specific Binders’
    - Surfaces with Hydration Shells
    - Surfaces promoting multi-layer formation
- Protein resistance, of importance to anti-microbial coatings was found to be promoted – to various extents – by phosphate diester (**3a**), phenyl (**3e**) and aniline (**2**) functionality, due to a number of factors including:
    - Hydrophilicity
    - Surface hydration
    - Non-specific protein binding
    - Short chain lengths
    - Large protein footprints
    - Initial layers which ‘block’ further protein adsorption

- Protein adsorption was found to be enhanced by surfaces which promoted specific protein-surface binding *via* the polar binding site [e.g. carboxyl (**3f)**, amine (**3b**)], or non-polar binding site [e.g. hexyl (**3g**)], of BSA.
- Predictions of BSA behaviour, particularly in terms of total accumulated mass, could be determined from QCM-D data collected during early adsorption (i.e. < 5 minutes), which represents an advantage over other methods which are not capable of the same precision, involve long accumulation times, and/or are *ex situ* studies of protein adsorption.

References

[1] W. Norde, Colloid Surface B, 61 (2008) 1-9.

[2] B.D. Ratner, Journal of Biomedical Materials Research, 27 (1993) 837-850.

[3] R.G. Chapman, E. Ostuni, M.N. Liang, *et al.*, Langmuir, 17 (2001) 1225-1233.

[4] E. Ostuni, R.G. Chapman, R.E. Holmlin, *et al.*, Langmuir, 17 (2001) 5605-5620.

[5] E.R. Kenawy, S.D. Worley, R. Broughton, Biomacromolecules, 8 (2007) 1359-1384.

[6] W. Norde, "Driving Forces for Protein Adsorption", in: M. Malmsten (Ed.) Biopolymers at Interfaces, Marcel Dekker Inc., New York (2003) pp. 21-43.

[7] C. Calonder, P.R. Van Tassel, Langmuir, 17 (2001) 4392-4395.

[8] M.M. Browne, G.V. Lubarsky, M.R. Davidson, *et al.*, Surf. Sci., 553 (2004) 155-167.

[9] K. Reimhult, K. Petersson, A. Krozer, Langmuir, 24 (2008) 8695-8700.

[10] C.F. Wertz, M.M. Santore, Langmuir, 18 (2001) 706-715.

[11] G. Belfort, A.L. Zydney, "Interaction of Proteins with Polymeric Synthetic Membranes", in: M. Malmsten (Ed.) Biopolymers at Interfaces, Marcel Dekker Inc., New York (2003).

[12] S. Krishnan, C.J. Weinman, C.K. Ober, J. Mater. Chem., 18 (2008) 3405-3413.

[13] A.G. Hemmersam, K. Rechendorff, M. Foss, *et al.*, J. Colloid Interface Sci., 320 (2008) 110-116.

[14] F. Höök, J. Vörös, M. Rodahl, *et al.*, Colloid Surface B, 24 (2002) 155-170.

[15] F. Höök, M. Rodahl, B. Kasemo, *et al.*, Proc. Natl. Acad. Sci. USA, 95 (1998) 12271-12276.

[16] S. Omanovic, S.G. Roscoe, Langmuir, 15 (1999) 8315-8321.

[17] C. Galli Marxer, M. Collaud Coen, L. Schlapbach, J. Colloid Interface Sci., 261 (2003) 291-298.

[18] V.B.C. Figueira, J.P. Jones, J. Colloid Interface Sci., 325 (2008) 107-113.

[19] S.H. Brewer, W.R. Glomm, M.C. Johnson, *et al.*, Langmuir, 21 (2005) 9303-9307.

[20] R. Kurrat, J.E. Prenosil, J.J. Ramsden, J. Colloid Interface Sci., 185 (1997) 1-8.

[21] A. Dolatshahi-Pirouz, K. Rechendorff, M.B. Hovgaard, *et al.*, Colloid Surface B, 66 (2008) 53-59.

[22] P. Roach, D. Farrar, C.C. Perry, J. Am. Chem. Soc., 127 (2005) 8168-8173.

[23] D. Shen, M. Huang, L.-M. Chow, *et al.*, Sensors and Actuators B: Chemical, 77 (2001) 664-670.

[24] J.T. Kim, N. Weber, G.H. Shin, *et al.*, J. Food Sci., 72 (2007) E214-E221.

[25] R.J. Hamers, C. Stavis, A. Pokhrel, *et al.*, Diamond Relat. Mater., 20 (2011) 733-742.

[26] F. Höök, B. Kasemo, T. Nylander, *et al.*, Anal. Chem., 73 (2001) 5796-5804.

[27] D.E. Otzen, M. Oliveberg, F. Höök, Colloid Surface B, 29 (2003) 67-73.

[28] H.J. Griesser, S.L. McArthur, M.S. Wagner, *et al.*, "XPS, ToF-SIMS, and MALDI-MS for Characterizing Adsorbed Protein Films", in: M. Malmsten (Ed.) Biopolymer at Interfaces, CRC Press (2003) p. 645.

[29] A. Ithurbide, I. Frateur, A. Galtayries, *et al.*, Electrochim. Acta, 53 (2007) 1336-1345.

[30] S. Chakraborty, P. Joshi, V. Shanker, *et al.*, Langmuir, 27 (2011) 7722-7731.

[31] C. Choong, J. Foord, J.-P. Griffiths, *et al.*, New J. Chem., 36 (2012) 1187-1200.

[32] P. Roach, D. Farrar, C.C. Perry, J. Am. Chem. Soc., 128 (2006) 3939-3945.

[33] S.J. Dilly, M.P. Beecham, S.P. Brown, *et al.*, Langmuir, 22 (2006) 8144-8150.

[34] B. Zdyrko, V. Klep, X. Li, *et al.*, Materials Science and Engineering: C, 29 (2009) 680-684.

[35] Y. Inoue, K. Ishihara, Colloid Surface B, 81 (2010) 350-357.

[36] G.L. Trainor, Expert Opin. Drug Discov., 2 (2007) 51-64.

[37] Y. Arima, H. Iwata, J. Mater. Chem., 17 (2007) 4079-4087.

[38] M.P. Gleeson, J. Med. Chem., 50 (2006) 101-112.

[39] J. Ghuman, P.A. Zunszain, I. Petitpas, *et al.*, J. Mol. Biol., 353 (2005) 38-52.

[40] F. Höök, Development of a Novel QCM Technique for Protein Adsorption Studies, in: Ph.D. Thesis, Chalmers University, Sweden (1997).

[41] A.A. Feiler, A. Sahlholm, T. Sandberg, *et al.*, J. Colloid Interface Sci., 315 (2007) 475-481.

[42] M.V. Voinova, M. Rodahl, M. Jonson, *et al.*, Phys. Scr., 59 (1999) 391-396.

[43] O. Wolff, D. Johannsmann, J. Appl. Phys., 87 (2000) 4182-4188.

[44] A. Welle, A. Chiumiento, R. Barbucci, Biomol. Eng, 24 (2007) 87-91.

[45] K. Laos, R. Parker, J. Moffat, *et al.*, Carbohydr. Polym., 65 (2006) 235-242.

[46] J. Benesch, J.F. Mano, R.L. Reis, Acta Biomaterialia, 6 (2010) 3499-3505.

[47] G.V. Lubarsky, M.R. Davidson, R.H. Bradley, Biosens. Bioelectron., 22 (2007) 1275-1281.

[48] C. Calonder, Y. Tie, P.R. Van Tassel, Proceedings of the National Academy of Sciences, 98 (2001) 10664-10669.

[49] W. Norde, J.P. Favier, Colloids and Surfaces, 64 (1992) 87-93.

[50] Philip J. Hajduk, Renaldo Mendoza, Andrew M. Petros, *et al.*, J. Comput. Aided Mol. Des., 17 (2003) 93-102.

[51] J. Ramsden, “Protein Adsorption Kinetics”, in: M. Malmsten (Ed.) Biopolymers at Interfaces, Marcel Dekker, New York (2003) p. 199.

[52] S. Belegrinou, I. Mannelli, P. Lisboa, *et al.*, Langmuir, 24 (2008) 7251-7261.

[53] M.A. Brusatori, Y. Tie, P.R. Van Tassel, Langmuir, 19 (2003) 5089-5097.

[54] G. Anand, S. Sharma, A.K. Dutta, *et al.*, Langmuir, 26 (2010) 10803-10811.

[55] C.F. Wertz, M.M. Santore, Langmuir, 17 (2001) 3006-3016.

[56] A.M. Moulin, S.J. O'Shea, R.A. Badley, *et al.*, Langmuir, 15 (1999) 8776-8779.

[57] D.-H. Tsai, F.W. DelRio, A.M. Keene, *et al.*, Langmuir, 27 (2011) 2464-2477.

[58] F. Caruso, D.N. Furlong, P. Kingshott, J. Colloid Interface Sci., 186 (1997) 129-140.

[59] V.N. Viswanadhan, A.K. Ghose, G.R. Revankar, *et al.*, Journal of Chemical Information and Computer Sciences, 29 (1989) 163-172.

[60] P. Ertl, B. Rohde, P. Selzer, J. Med. Chem., 43 (2000) 3714-3717.

[61] E. Parker, Surface Active Polymers as Anti-infective and Antibiofouling Materials, in: D.Phil. Thesis, Organic Chemistry, University of Oxford, U.K. (2012).

[62] R. Williams, pKa Data, June 21, 2012 <http://research.chem.psu.edu/brpgroup/pKa_compilation.pdf>

[63] J. Clayden, N. Greeves, S. Warren, *et al.*, “Acidity, Basicity, and pKa”, in: Organic Chemistry, Oxford University Press, Oxford (2001).

[64] Dissociation Constants for Acids and Bases, Zirchrom Separations Inc, June 16, 2012. <www.zirchrom.com/organic.htm>

[65] C.M. Stiff, M. Zhong, R.W. Sarver, *et al.*, Bioorganic & Medicinal Chemistry Letters, 17 (2007) 5479-5482.

[66] H. Noh, E.A. Vogler, Biomaterials, 28 (2007) 405-422.

[67] H. Noh, E.A. Vogler, Biomaterials, 27 (2006) 5801-5812.

[68] L. Feuz, M. Textor, European Cells and Materials, 10 (2005) BS9.

[69] Y. Aray, M. Marquez, J. Rodríguez, *et al.*, J. Phys. Chem. B, 108 (2004) 2418-2424.

[70] A. Plugatyr, I.M. Svishchev, The Journal of Chemical Physics, 130 (2009) 114509.

[71] B. Jayaram, M. Mezei, D.L. Beveridge, J. Comput. Chem., 8 (1987) 917-942.

[72] D.M. Spori, N.V. Venkataraman, S.G.P. Tosatti, *et al.*, Langmuir, 23 (2007) 8053-8060.

[73] R.S. Rajan, T. Li, M. Aras, *et al.*, Protein Sci., 15 (2006) 1063-1075.

[74] P. Kingshott, H. Thissen, H.J. Griesser, Biomaterials, 23 (2002) 2043-2056.

[75] W. Norde, C.E. Giacomelli, J. Biotechnol., 79 (2000) 259-268.

[76] L.R. Wetter, et al., J. Biol. Chem., 192 (1951) 237-242.

[77] J.-Q. Tong, F.-F. Tian, Q. Li, *et al.*, Photochemical & Photobiological Sciences, (2012) Advance Article.

[78] D. Agudelo, P. Bourassa, J. Bruneau, *et al.*, PLoS ONE, 7 (2012) e43814.

6. Neurotransmitter Detection with Diamond Electrodes

6.1 Introduction

Living cell-solid state device interfacing is anticipated to be one of the key bio-electronic synergies of the 21st century, especially in the fields of smart sensing, bio-technology, communications and medicine.[1, 2] One of the most fascinating topics in this area is *neuron interfacing* – the coupling of electronic devices to neurons.[3-6] It offers the possibility for future non-invasive long-term neural signal recording from multiple neurons within artificial or natural neural networks. This will enable better understanding of neuronal functions and of associated diseases.[7, 8]

Thin film diamond is ideally positioned to overcome the problems inherent to neuronal interfacing. Silicon is the current material of choice[9, 10], but can react with biological medium and has high noise when interfaced with electronics. In the search for alternative materials, diamond has emerged as an attractive choice. It is biocompatible, robust, conductive when doped, and is capable of electrochemical detection of low quantities of organic compounds, due to its high signal to noise ratio.[9] The properties of diamond should enable highly sensitive diamond FET-based devices to be coupled to electrochemical devices on a single chip.[5, 9]

Neurotransmitter chemistry in neuronal environments is of great interest to clinicians. In particular, catecholamine neurotransmitters have crucial roles in the nervous systems of mammals, where they reinforce stimuli, act as neuronal messengers, and contribute to positive or negative psychiatric conditions.[11-13] The quantities of these neurotransmitters are important for diagnosis, and this can be determined using analytical electrochemical methods. However, this is made difficult as such neurotransmitters oxidize at overpotentials similar to those of other common organic molecules found in neuronal environments. For example, dopamine (DA) and ascorbic acid (AA) oxidize at similar potentials, with the former having micromolar concentration and the latter millimolar concentration.[14] This interference is exacerbated by catalytic reactions between neurotransmitters and interferents, which make quantitative detection difficult.

The reliable, quantitative, electrochemical detection of neuron transmitters under physiological conditions is a crucial hurdle to be crossed, if diamond “chips” are to be fully realized in this field. To achieve this, various surface modifications have been used in the past decade to modify the surface of diamond, including polymer films[15-17], self-assembled monolayers[18, 19], metal catalysts[20], electrochemical treatment[21, 22], oxygen plasma[23], hydrogen plasma[24, 25], carbene chemistry[26], and many other wet chemical methods.[27] Several of these methods have been able to detect neurotransmitters in the presence of interferents, with anodized diamond and polymeric films being amongst the most successful modifications to accomplish this task.[15, 21]

6.1.1 Aims and Approaches

The aim here is to improve the electrochemical detection of dopamine in the presence of ascorbic acid at diamond electrodes. Different surface pre-treatments are applied to diamond in attempts to achieve this aim. This is challenging, as the detection of dopamine (DA) and ascorbic acid (AA) is affected by two factors[28]: first, both species oxidize at similar overpotentials, causing an overlapping voltametric response; second, AA catalyzes the regeneration of DA from an oxidation product (dopamine quinone) *via* an EC’ mechanism in solution. As a result, even if the DA and AA signals can be separated, the magnitude of the DA signals depends on how much AA is present, causing ambiguity in the analysis. This problem arises since AA oxidizes at potentials more positive than DA oxidation. In the present work, electrode treatments are developed that enable the separation of the DA and AA signals, with AA oxidation occurring at lower potentials than DA oxidation.

Several approaches will be used to improve the efficiency of AA oxidation, including: the use of cathodic potential treatment (small and large, i.e. - 2V to - 35V), carbon nanotubes, electro-polymers (acid chrome blue K and Evans Blue), and hydrogen plasma. Of these modifiers, the use of cathodic potentials and hydrogen plasma demonstrate the most promise towards improving the efficiency of ascorbic acid oxidation. All three modifiers increase the sensitivity and selectivity for dopamine in the presence of ascorbic acid. The modifiers which lead to hydrogen-termination of diamond show the most promise as a basis for a diamond-based neuro-electrochemical device in physiological conditions.

6.2 Experimental

6.2.1 Chemicals

The phosphate buffer used here has been prepared in the same manner as described earlier. Nitric acid, acetone, *L*- ascorbic acid, dopamine, dimethylformamide (DMF: N,N), Evans Blue (EB) were used as-received from Sigma Aldrich. Poly(acid chrome blue K) was purchased from the Hanhong Group (China). Multi-walled carbon-nanotubes (MWCNT, O.D. x L: 110-170 nm x 5 μm) were purchased from Sigma Aldrich. For reference, the chemical structures of ACBK, Evans Blue, dopamine and ascorbic acid are shown in Figure 6.1. Contamination was removed from electrodes by *Aqua Regia*, which was prepared by mixing nitric and hydrochloric acid in a 1:3 ratio.

6.2.2 Electrodes

Boron-doped diamond electrodes (BDE; Element Six) and glassy carbon electrodes (CH instruments) were used here. The concentration of boron in the polycrystalline diamond electrodes was approximately 10^{20} cm^{-3}. These were mounted in a PTFE holder, and the exposed electrodes have diameter of 3 mm and area of 0.071 cm^2. Glassy carbon electrodes were not mounted in the holder, but were used as received, having a Teflon sheath with the same exposed electrode area. Prior to use, the diamond and glassy carbon electrodes were polished with alumina powder (particle size: 1 μm, followed by 0.3 μm), or diamond slurry (particle size: 1 μm), respectively. Electrodes were cleaned by ultrasonication in water and acetone. Unless otherwise indicated, boron-doped diamond electrodes were further cleaned by scanning between - 1.7 and 2.5 V in 0.1M HNO_3 for at least 15 scans at a scan rate of 0.1 V s^{-1}. The glassy carbon electrodes were activated by scanning in pH 9 phosphate buffer from -0.2 V to 1.8 V (0.1 V s^{-1}, 40 scans) before use.[29]

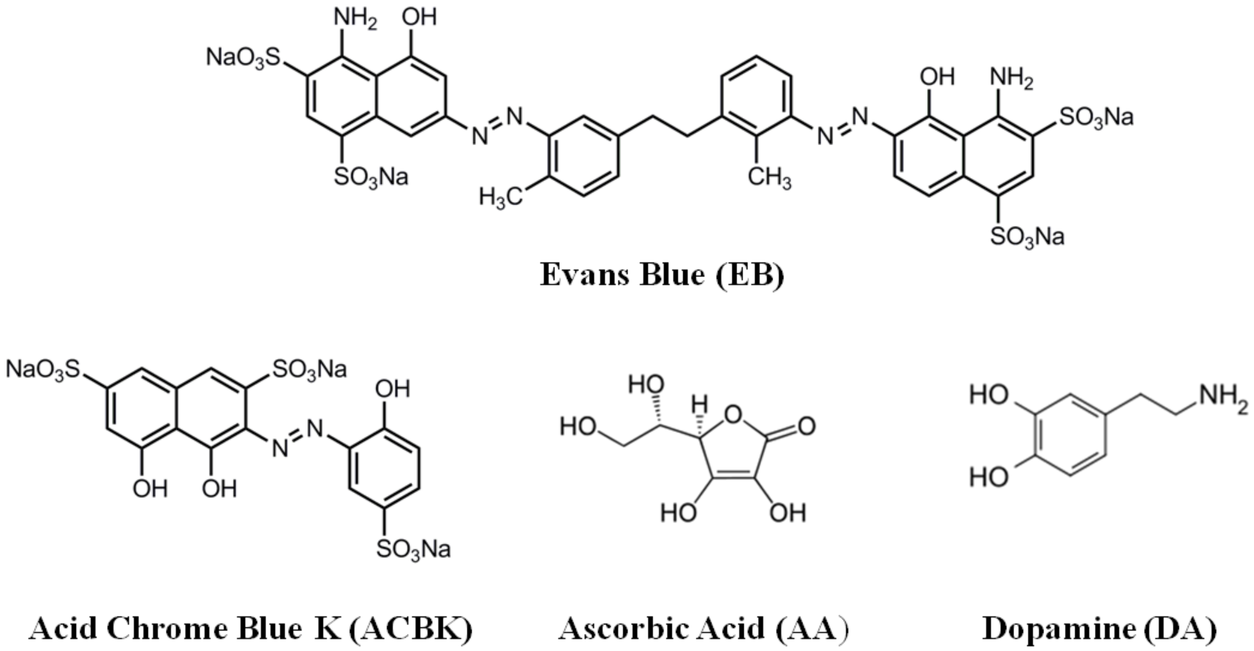

Figure 6.1: Chemical structures of molecules used in this chapter.

6.2.3 Electrochemical Modification of Boron-doped Diamond

Anodic (+ 2 V) or cathodic (- 2 V, - 5 V, and – 10 V) pre-treatments of BDE took place in 0.1 M HNO_3 or H_2SO_4 (0.1 M or 0.5 M), respectively. The length of the treatment was 3 minutes, unless otherwise stipulated. These particular pre-treatments were done by using the apparatus shown in Figure 2.18. Methods used for the pre-treatment of diamond at higher cathodic potentials are described in the text.

6.3 Results

6.3.1 Unmodified Diamond

The electrochemistry of DA and AA at unmodified diamond electrodes was studied first, prior to studying modified diamond electrodes. The expected oxidation and reduction reactions associated with DA and AA is shown in Figure 6.2. Representative cyclic voltammograms for the oxidation of AA and DA at these electrodes at pH 4 and pH 7 are shown in Figure 6.3, with related data shown in Table 6.1.

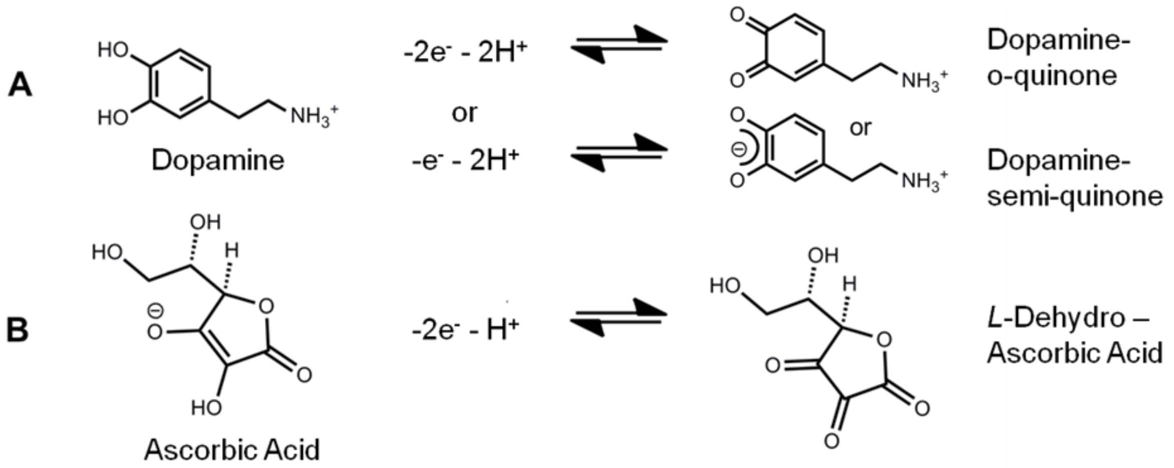

Figure 6.2: (A) Oxidation of dopamine (DA) to dopamine-o-quinone (DA-o-quinone) or dopamine semi-quinone (DAsemi-quinone); (B) Oxidation of *L*-ascorbic acid (AA) to *L*-dehydroascorbic acid (DHA).

Electrode	pH	Species	[Species] (mM)	Peak Position (V)	Current (A)	Current Response (A cm^{-2})
BDE	4	DA	1.0	0.81	2.89×10^{-5}	4.07×10^{-4}
BDE	4	AA	1.0	1.05	4.49×10^{-6}	6.32×10^{-5}
BDE	7	DA	0.1	0.59	2.05×10^{-6}	2.89×10^{-5}
BDE	7	AA	0.1	1.1	6.90×10^{-7}	9.72×10^{-6}

Table 6.1: Peak position and current response data for the first oxidation peaks of AA and DA in pH 4 or pH 7 phosphate buffers.

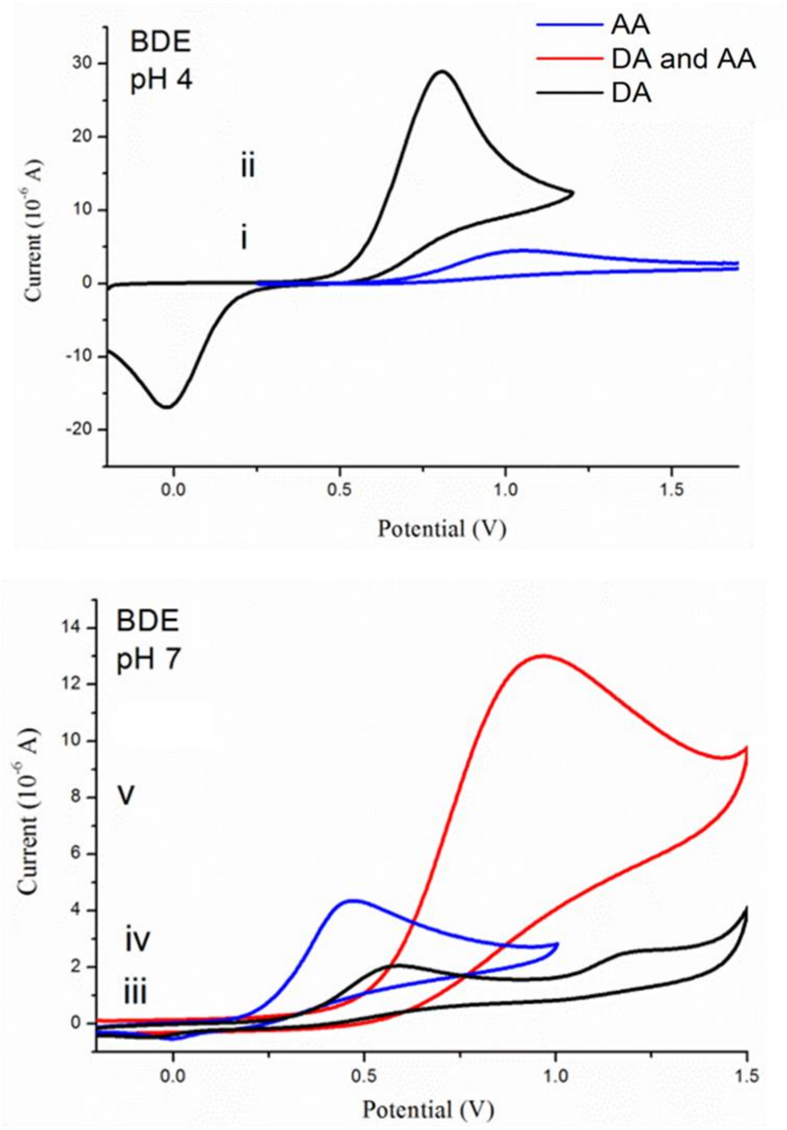

Figure 6.3: Representative cyclic voltammetry of AA and DA oxidation at unmodified boron-doped diamond electrodes (BDE) in pH 4 and pH 7 phosphate buffer solutions, with the [AA] and/or [DA] as follows: (i) 1 mM AA; (ii) 1 mM DA; (iii) 0.1 mM AA; (iv) 0.1 mM DA; (v) 0.4 mM DA and 1mM AA.

In acidic conditions, DA and AA oxidize at peak potentials ($E_{pa,AA}$ or $E_{pa,DA}$) of 0.8 and 1.1 V, respectively. In neutral conditions, $E_{pa,DA}$ is 0.6 V, with no change in the $E_{pa,AA}$ compared to acidic conditions. As expected, at all pH values, AA and DA have irreversible and reversible oxidation, respectively, as only DA shows redox behaviour. There is a second oxidation peak for DA at 1.2 V at both pH values (only pH 7 is shown here). At both pH values, unmodified diamond has a higher current response to DA oxidation than AA oxidation.

These results are consistent with the known oxidation processes of DA and AA (see Figure 6.2) at unmodified diamond electrodes. [21, 22, 30] The second oxidation peak of DA mentioned above, is likely a further oxidation of dopamine-o-quinone (DA-o-quinone), dopamine semi-quinone (DAsemi-quinone), or some other oxidation product of DA. This peak will not be discussed at length, as only the first oxidation peak is the most useful from an analytical point of view.

Primae facie, the oxidation peak positions and current response (i.e. current normalized by electrode area) of AA and DA can be explained by electrostatic interactions. At pH 4, DA and AA have positive and neutral charge, respectively. At pH 7, DA and AA have positive and negative charge, respectively. Diamond electrodes which are exposed to ambient environments and electrochemically cleaned in nitric acid are expected to be oxygen-rich and negatively charged in the range of pH 4 - 7. Therefore, one would expect DA to have a greater electrostatic attraction, hence improved electron transfer and increased mass transfer to the unmodified diamond electrode under the conditions studied here.

In physiological conditions AA and DA exist together in the same solution, and so these conditions were studied here. A cyclic voltammogram of both species detected at pH 7 on diamond electrodes is shown in Figure 6.3(v). The DA and AA oxidation peaks are not resolvable, as expected at unmodified diamond electrodes. These two species have similar oxidation overpotentials, and oxidation products of DA can be reduced back to DA *via* an EC' mechanism with AA (see Figure 6.4).[28] These two factors cause the two species to be detected as a single peak, having a current ($i_{AA/DA}$) larger than that for the AA oxidation (i_{AA}) or DA oxidation (i_{DA}), alone. This process is known to occur when $E_{pa, DA} < E_{pa, AA}$.[28]

Thus, unmodified diamond cannot be used to detect DA and AA in the same aqueous solution.

Although unmodified diamond cannot be used to separately detect DA and AA, the response of this electrode to increasing [AA] in solutions where [DA] is fixed will be of interest later in this chapter. The response of unmodified diamond electrode to these changing conditions is shown in Figure 6.5. As [AA] increases, the anodic peak located from 0.4 V to 0.7 V the current ($i_{pa,\ DA/AA}$) increases by 15.6 μA mM^{-1} ($R^2 = 0.98$). This increase is probably due to one or both effects known to be caused by increasing [AA] in solutions containing DA: an increase in the AA oxidation signal and/or the regeneration of DA from its oxidation products by an EC' mechanism with unoxidized AA.

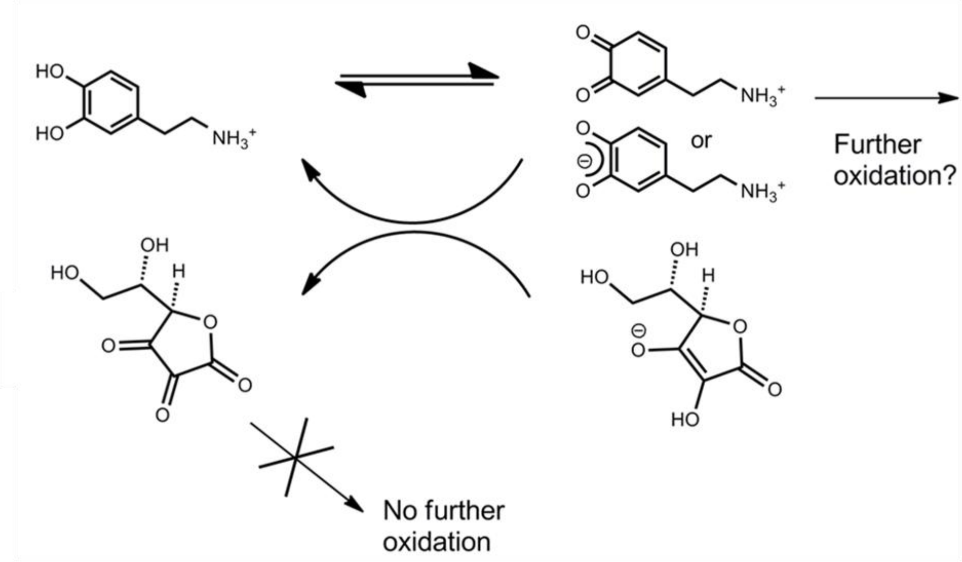

Figure 6.4: EC' mechanism for DA oxidation in the presence of AA at diamond electrodes. Clockwise, from upper left: dopamine (DA); dopamine-o-quinone (DA-o-quinone); dopamine semi-quinone (DAsemi-quinone); *L*-ascorbic acid (AA); *L*-dehydro-ascorbic acid (DHA). (n.b. reduction of DA-o-quinone and DAsemi-quinone require 1 and ½ moles of ascorbic acid, respectively) Adapted from Kondo *et al.*.[28]

In order to detect both species at diamond surfaces, a modification to the diamond surface must be introduced. The best modifications result in one or more of the following events: the separation of the oxidation signal of both species; the elimination of the catalytic cycle by ensuring $E_{pa,\ AA} < E_{pa,\ DA}$; improved efficiency of the EC' reaction, if $E_{pa,\ DA} < E_{pa,\ AA}$, or if $E_{pa,\ DA} \approx E_{pa,\ AA}$.[28] In subsequent sections, the effects of various treatments will be tested with the goal of achieving at least one of the above improvements to diamond electrodes for the purpose of DA detection in the presence of AA.

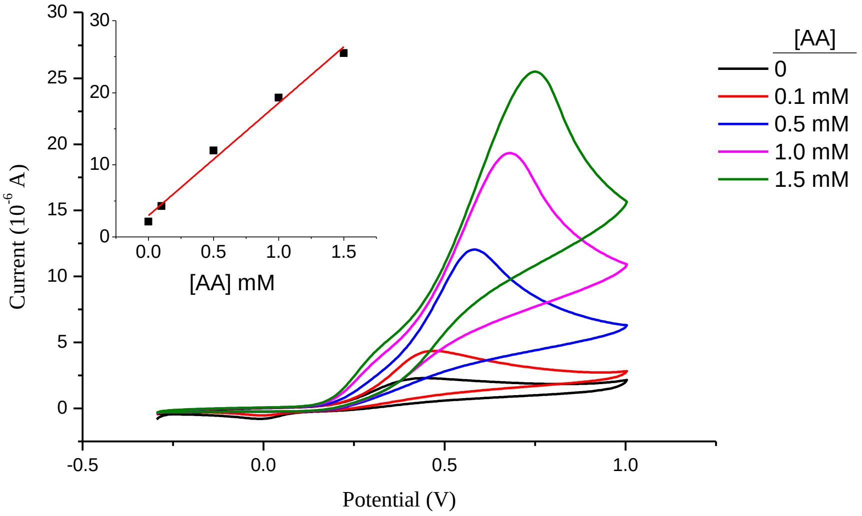

Figure 6.5: Cyclic voltammetry of AA and DA oxidation at unmodified boron-doped diamond electrode to changing [AA] (0 mM, 0.1 mM, 0.5 mM, 1.0 mM, 1.5 mM) in solutions containing a fixed [DA] (0.1 mM). *Inset*: Response of peak current to changing [AA]; linear regression is 15.6 μA mM^{-1} ($R^2 = 0.98$).

6.3.2 Diamond Modified by Small Anodic and Cathodic potentials

(a) Cyclic Voltammetry

Diamond can be electrochemically treated at anodic and cathodic potentials. There are several reports indicating that electrochemical treatment with small, anodic potentials can separate the oxidation signals of DA and AA.[15, 21, 22, 31] None of these reports suggest that the catalytic effect between these two species is eliminated at anodic diamond electrodes. The use of cathodic treated diamond for this purpose is rarer, but some reports suggest that this treatment may achieve the required separation.[31, 32] In this section, electrochemical modification of diamond is evaluated towards the separation of AA and DA oxidation peaks.

Diamond electrodes were modified by applying anodic or cathodic potentials for 3 minutes, in nitric or sulphuric acid, respectively. These electrodes were exposed to solutions containing either AA or DA, as shown in Figure 6.6, with the peak positions and current responses recorded in Table 6.2. For most samples, the voltammetric lineshapes are consistent with AA and DA oxidation at unmodified diamond, with one and two oxidation waves seen for AA and DA oxidation, respectively. Cathodic electrochemical pre-treatments lower $E_{pa,\ AA}$ and $E_{pa,\ DA}$, which is indicative of faster electron transfer for AA and DA at these particular electrodes. The magnitude of this shift to lower E_{pa} is as large as – 800 mV or - 250 mV, respectively. At cathodic diamond, $E_{pa,AA}$ clearly overlaps the position of $E_{pa,DA.}$ However, the onset of AA oxidation peak for the CV at - 10 V treated diamond is at an E_{pa} consistent with its oxidation at metal catalysts.[20, 33] Thus, one must determine whether the observed results are due to characteristics intrinsic to cathodic diamond, or due to metal contamination (e.g. from Pt).

Platinum from the counter electrode is a possible source of metallic contamination here, as the counter electrode and the working electrode are in the same solution. Platinum is known to deposit at potentials lower than - 3.68 V.[34] Therefore, one must confirm that platinum is not depositing during these modifications.

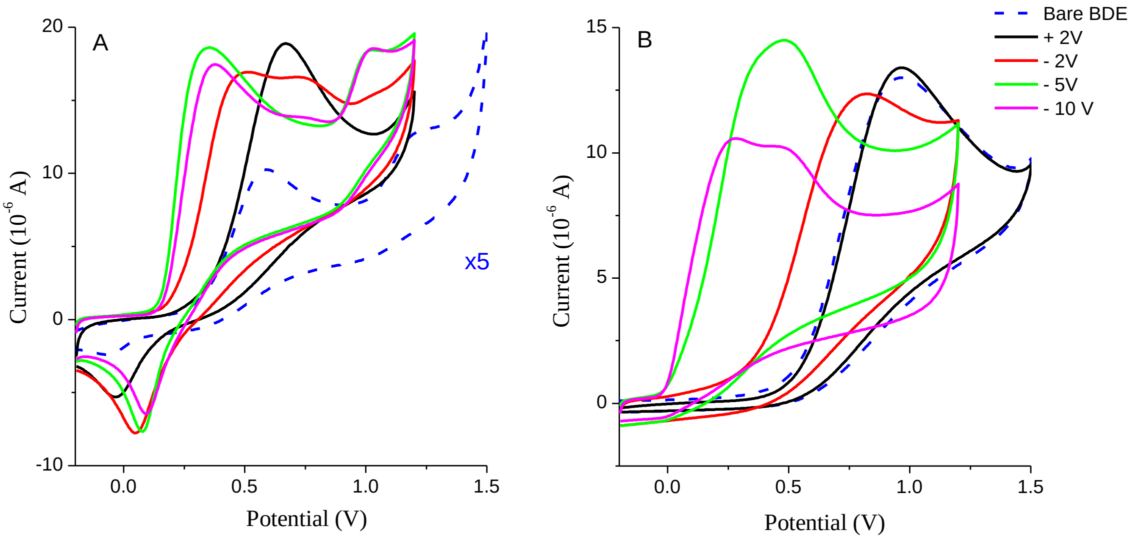

Figure 6.6: Response of electrochemically pre-treated diamond electrodes to DA and AA, separately, in pH 7, 0.1 M phosphate buffer solutions. (A) Electrodes in 1 mM DA, except bare BDE which is in 0.1 mM DA and also has been scaled for better resolution. (B) Electrodes in 1 mM AA. All spectra were taken with a scan rate of 0.1 V s^{-1}. Anodic and cathodic treatments occurred in 0.1 M HNO_3 and 0.5 M H_2SO_4, respectively, for 3 minutes.

Electrode	pH	Species	[Species] (mM)	Pre-treatment (V)	Peak Position (V)	Current (A)	Current Response (A cm^{-2})
BDE	7	DA	1	2	0.66	1.89×10^{-5}	2.66×10^{-4}
BDE	7	DA	1	-2	0.52	1.69×10^{-5}	2.38×10^{-4}
BDE	7	DA	1	-2	0.69	1.66×10^{-5}	2.34×10^{-4}
BDE	7	DA	1	-5	0.34	1.86×10^{-5}	2.62×10^{-4}
BDE	7	DA	1	-10	0.38	1.74×10^{-5}	2.45×10^{-4}
BDE	7	AA	1	2	0.96	1.34×10^{-5}	1.89×10^{-4}
BDE	7	AA	1	-2	0.80	1.23×10^{-5}	1.73×10^{-4}
BDE	7	AA	1	-5	0.46	1.45×10^{-5}	2.04×10^{-4}
BDE	7	AA	1	-10	0.27	1.05×10^{-5}	1.48×10^{-4}
BDE	7	AA	1	-10	0.45	1.03×10^{-5}	1.45×10^{-4}

Table 6.2: Peak position and current response data for the first oxidation peaks of AA and DA in 0.1M phosphate buffers at pH 7. All data relates to the CV spectra in Figure 6.6. In cases where two peaks are resolved at the potential expected for the first oxidation, both peak positions and sensitivities are recorded.

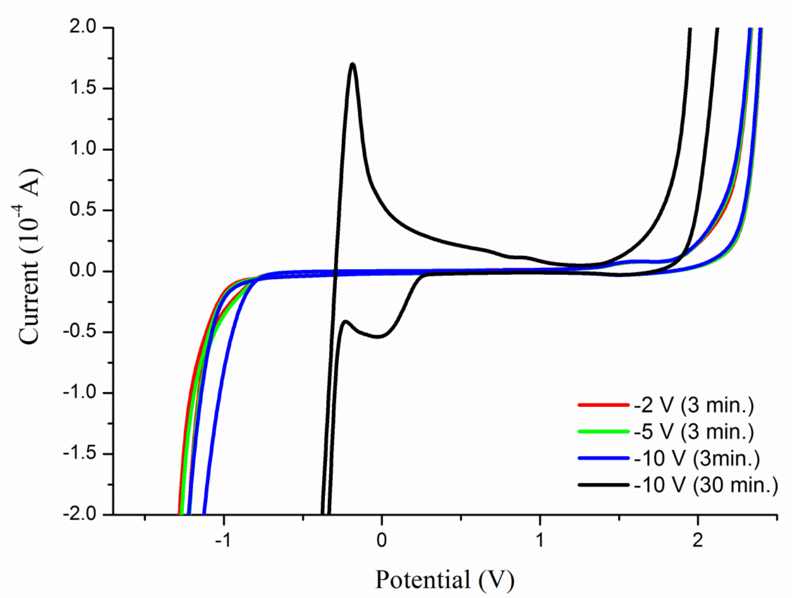

Figure 6.7: Potential windows of cathodic treated diamond electrodes after 15 scans in 0.1M HNO_3.

The lack of platinum present during cathodic pre-treatments at time scales of 3 minutes can be judged from the data in Figure 6.7. The presence of the hydrogen evolution peak at -0.2 V, due to the stripping of hydrogen adsorbed on Pt confirms that Pt is present after long cathodic treatments.[35] However, in this same figure, it is clear that platinum does not deposit on the diamond electrodes at short durations of cathodic pre-treatment. These results are consistent with the observations of Hoffmann *et al.* who indicate that *excessive* platinum deposition requires long exposure to potentials equal to or lower than - 3.68 V.[34] As a consequence, the basic electrochemical cell used here should only be used to modify diamond using cathodic potentials of up to – 10 V, for no more than 3 minutes. In this work, future cathodic pre-treatment, using the apparatus used here, will be limited to potentials greater than or equal to - 5V, for no more than 3 minutes.

(b) Square-wave voltammetry

Modified diamond electrodes in solutions containing AA and DA were probed using square-wave voltammetry. This method is known to have higher peak resolution and a lower limit of detection, since it minimizes the response to background signal. Square-wave voltammograms were recorded for – 5 V diamond electrodes in phosphate buffers containing DA and AA at pH 7. The data is shown in Figure 6.8. The $E_{pa,\,AA}$ and $E_{pa,\,DA}$ occurs at 0.39 V and 0.23 V, respectively. The second oxidation of DA occurs at 0.95 V. When AA and DA are in solution together, with each having the same concentration (1 mM), three peaks are seen at 0.05 V, 0.23 V and 0.9 5V. The peak at 0.95 V can be assigned to a second oxidation of DA, with confidence. However, the other two oxidation peaks do not occur at the expected overpotential for AA oxidation at diamond. Therefore, additional study is required before peak assignment.

Exposing this electrode to changing concentrations of AA or DA enables proper peak assignment. The effect of varying the concentration of one species, whilst fixing the concentration of the other is shown in Figures 6.9 (fixed [DA]) and 6.10 (fixed [AA]); data related to Figure 6.9 is shown in Table 6.3. An increase in the concentration of any electro-active species should increase the currents of any associated redox peaks.[36] When [AA] is increased in the presence of fixed [DA], the current and peak positions of the oxidation peaks change. As [AA] is increased, the current associated with oxidation at 0.07 V and 0.24 V increases, whilst it decreases at 0.94 V. As shown in the inset, changes in current are either proportional to [AA] (at 0.07 V and 0.24V), or inversely proportional to [AA] (at 0.94V). The current-concentration relationships associated with the oxidation peaks at 0.07 V, 0.24 V, and 0.94 V are, respectively, 0.76 µA mM^{-1} (R^2=0.99), 0.50 µA mM^{-1} (R^2=0.98), and -0.08 µA mM^{-1} (R^2=0.99). These values are much lower than the 15.6 µA mM^{-1} response seen at unmodified diamond electrodes (see Figure 6.5). Also, as [AA] is increased, the positions of all three oxidation peaks shift to higher overpotentials, whilst maintaining constant peak-to-peak separation.

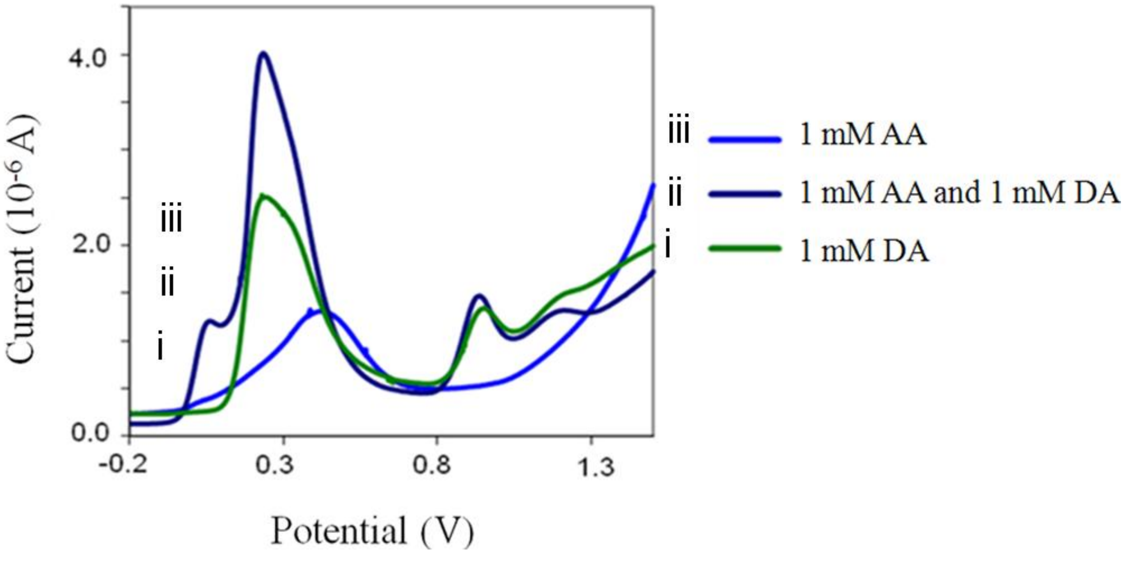

Figure 6.8: Square-wave voltammetry of various BDE, modified by cathodic pre-treatment (-5V, for 3 min in 0.5M H_2SO_4), exposed to solutions of varying AA and DA composition. Electrolyte was 0.1 M phosphate buffer with a pH of 7.

[AA] (mM)	Peak Position (V)	Current (A)	Current Response (A cm^{-2})
1	0.05	1.19×10^{-6}	1.68×10^{-5}
5	0.11	4.56×10^{-6}	6.42×10^{-5}
10	0.26	8.07×10^{-6}	1.14×10^{-4}
1	0.23	3.94×10^{-6}	5.55×10^{-5}
5	0.31	6.39×10^{-6}	9.00×10^{-5}
10	0.41	8.47×10^{-6}	1.19×10^{-4}

Table 6.3: Peak position, current and sensitivity factors of data in Figure 6.9, where BDE was treated with – 5 V for 3 minutes in 0.5 M H_2SO_4, in 0.1 M phosphate buffers at pH 7. The [AA] varied, whilst [DA] remained fixed at 1 mM.

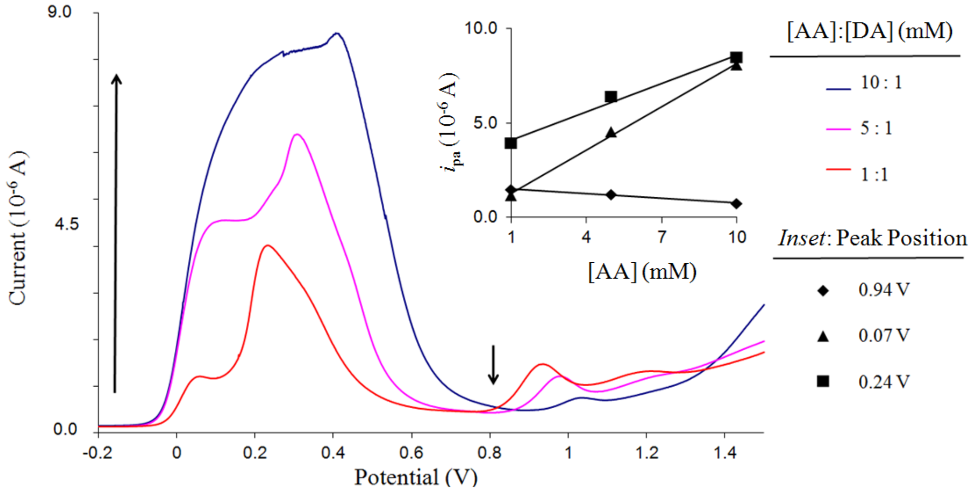

Figure 6.9: Square-wave voltammetry of cathodic pre-treatment (- 5 V, 3 min in 0.5 M H_2SO_4) of BDE in 0.1 M phosphate buffers at pH 7, with varying concentrations of AA (1 mM, 5 mM, 10 mM), whilst [DA] remains fixed at 1 mM. *Inset:* The current-concentration relationships of each oxidation peak.

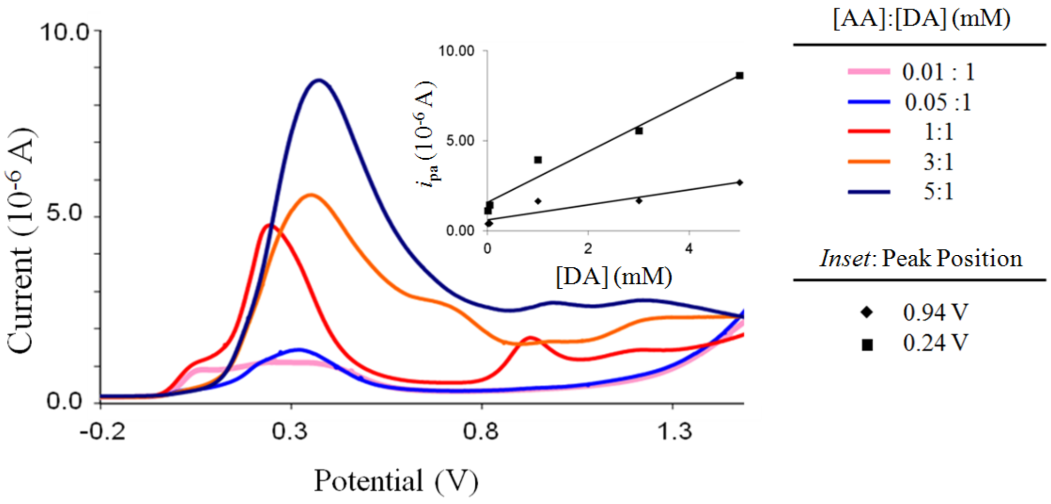

Figure 6.10: Square-wave voltammetry of cathodic pre-treatment (-5V, 3 min in 0.5M H_2SO_4) of BDE in 0.1 M phosphate buffers at pH 7, with varying concentrations of DA (0.1 mM, 0.05 mM, 1 mM, 3 mM, 5 mM), whilst [AA] remains fixed at 1 mM. *Inset:* The current-concentration relationships of each oxidation peak.

When [DA] is increased, in the presence of fixed [AA], the magnitude of currents changes, whilst peak position remains fairly constant (see Figure 6.10). The peaks at about 0.3V and 0.95 V have current proportional to [DA], with responses of 1.41 μA mM^{-1} (R^2=0.97) and 0.42 μA mM^{-1} (R^2=0.86), respectively (see Figure 6.10, *inset*). Clearly, the former oxidation wave is more affected by increasing [DA]. The peak at 0.05 V disappears at high [DA], but at lower concentrations the current of this peak remains constant.

The oxidation waves at this cathodic diamond electrode can now be assigned to particular oxidation processes. Since the peak with E_{pa} of about 0.05 V, has i_{pa} strongly proportional to increasing [AA], but not proportional to increasing [DA], one can assign it to AA oxidation in a solution in which DA is present. Peaks having E_{pa} of 0.25 V are strongly affected by increasing [DA], thus they can be assigned to DA oxidation. The peak at ≈ 0.95 V is assigned to a second oxidation product of dopamine, such as dopamine-o-chrome, or some other oxidation product of dopamine.[15, 37]

The behaviour of all three peaks is quite complex. $E_{pa, AA}$ is less positive than $E_{pa, DA}$, which should help to eliminate the catalytic EC' mechanism. However, it is still occurring, since the peaks associated with the first and second oxidation products of DA are affected by the [AA]. As [AA] increases, the rate of DA regeneration *via* the EC' mechanism increases, thereby enhancing the current of the DA oxidation peak. The decreasing i_{pa} for the second DA oxidation as [AA] increases, is consistent with an EC' mechanism which lowers the amount of first DA oxidation products available to be further oxidized. The peak separation between the AA and DA oxidation peaks is about 180 mV (see Figure 6.9). This is probably insufficient to completely eliminate the catalytic cycle.[38] It is clear that some AA is not oxidized before DA oxidation occurs. Therefore there is some remaining AA available to participate in the EC' reaction with the oxidation products of DA. Cathodic BDE does not eliminate the EC' mechanism associated with the presence of dopamine and ascorbic acid in the same solution.

To improve DA detection in the presence of AA, one needs to ensure that either the interfering effect of AA is eliminated by stopping the EC' reaction, or enable the determination of the [DA] from the catalytic enhancement of $i_{pa,\ DA}$ by quantifying the efficiency of the EC' reaction. Accomplishing the former would be most ideal. The trends seen within this section, and the previous section, suggest that $E_{pa,AA}$ trends towards ever lower overpotentials after diamond has been pre-treated with more negative potentials (see Figures 6.6, 6.9 and Table 6.2). Also, the response of $i_{pa,DA}$ to increasing [AA] is slower at cathodic diamond than at unmodified diamond (0.5 µA mM^{-1} vs. 15.6 µA mM^{-1}, cf. Figures 6.5 and 6.9). Collectively, these observations suggest that pre-treatments at highly negative potentials may further separate the AA and DA oxidation peaks, and realize the elimination of the EC' reaction at diamond electrodes. Such highly cathodic pre-treatments cannot be done with the apparatus used in these experiments, due to the risk of Pt deposition onto BDE. Later, a different electrochemical apparatus will be used to modify diamond at higher cathodic potentials.

6.3.3 Diamond Modified by Electropolymers

Complete separation of DA and AA oxidation peaks has been achieved on sp^2 carbon electrodes by electro-polymerization. Evans Blue (EB) and acid chrome blue K (ACBK) enable glassy carbon to achieve this level of separation.[29, 36, 39] Therefore, both polymers are candidates for improving DA detection in the presence of AA at diamond electrodes. Electro-polymers have been used on diamond in the past[15], thus this strategy is promising.

Boron-doped diamond and glassy carbon electrodes were electro-polymerized with ACBK and EB. Electro-polymerization of ACBK on both types of electrodes was done using the protocol of Zou *et al.*.[39] The electrodes were first activated towards electro-polymerization by scanning from - 0.2 V to 1.8 V in 0.5 mM ACBK in a phosphate buffer at pH 9 (0.1 V s^{-1}, 40 scans). Poly-ACBK was deposited from 0.5 mM solutions of ACBK in phosphate buffer at pH 7.4 by cyclic scanning from -0.4 V to 1.5 V for 5, 20, 25, and 40 times. Evans Blue was deposited from 1mM solutions in phosphate buffer at pH 9 by cyclic scanning from - 0.2 V to 1.8 V for 40 times.[28, 31] The methods to electro-polymerize poly(Evans Blue) and ACBK onto glassy carbon were adopted for as-received diamond electrodes with no pre-treatments aside from cleaning in nitric acid.

The process of electro-deposition leads to characteristic cyclic voltammograms, which are shown in Figure 6.11. Redox peaks are expected to appear during the electro-polymerization of both polymers, if they are grafted in a polymerized, molecular form on the surface.[29, 36, 39] For ACBK deposition onto BDE, the expected weak redox behaviour is seen; however, the current of the observed redox peaks are 50 times less than that seen on ACBK-modified glassy carbon. Redox peaks are not seen during the polymerization of EB, after first deposition scan. From this one concludes that ACBK, but not EB, may be electro-polymerizing onto diamond.

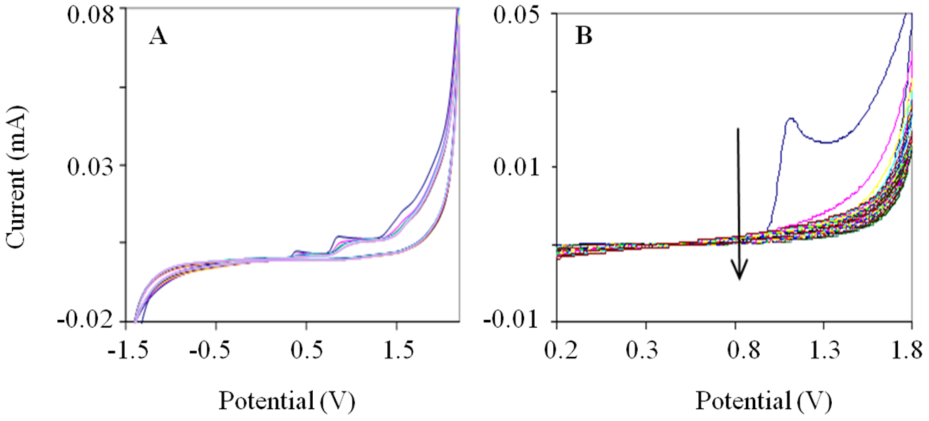

Figure 6.11: Cyclic voltammograms of the electro-polymerization of ACBK (A) and EB (B) onto BDE.

Each modified electrode was exposed to solutions containing AA to quickly ascertain its ability to affect $E_{pa,\ AA}$. In the last section, it was determined that lower values of $E_{pa,\ AA}$

would improve DA detection in the presence of AA. Initially, these electrodes were exposed to AA solutions in a 0.1 M phosphate buffer of pH 4 – a common test of the AA oxidation kinetics at electrodes. For comparison, AA oxidation at unmodified and modified glassy carbon electrode (GCE) was also conducted, under the same conditions. The results are shown in Figure 6.12 and detailed in Table 6.4.

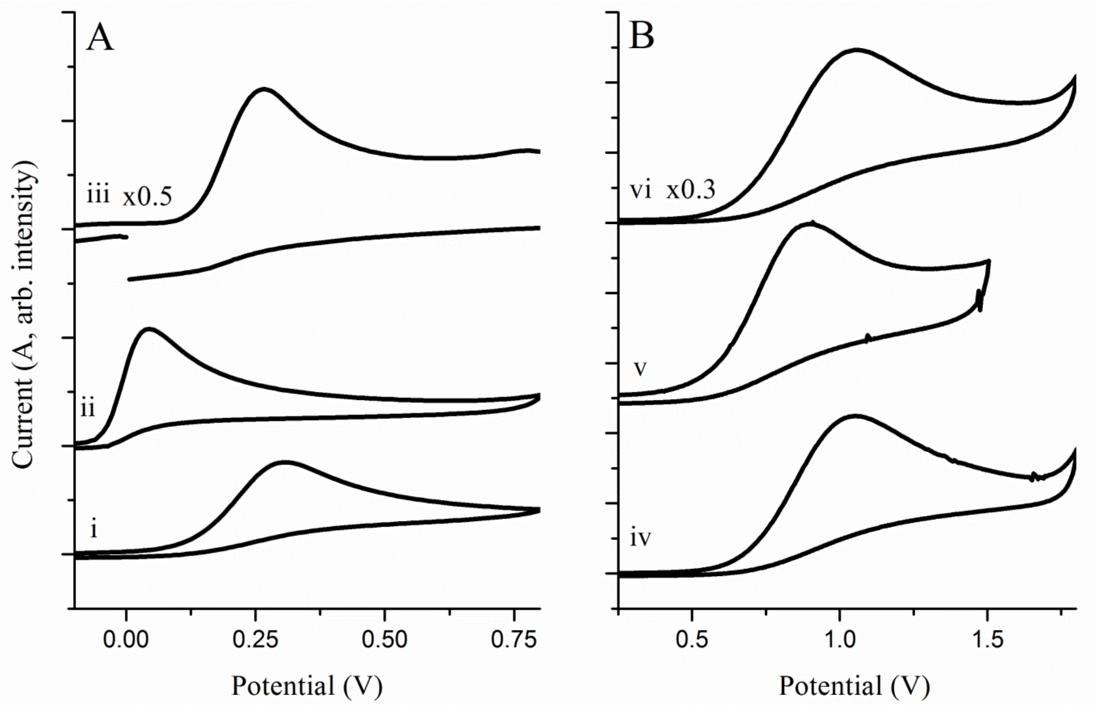

Figure 6.12: Detection of AA in pH 4 solutions of phosphate buffer at: (A) GCE; (B) BDE. (i) unmodified GCE; (ii) GCE with 20 scans of ACBK; (iii) GCE with 40 scans of Evans Blue; (iv) unmodified BDE; (v) BDE with 20 scans of ACBK; (vi) BDE with 40 scans of EB; The [AA] varied: 0.5 mM (i, ii); 1mM (iii, iv, vi); 0.3 mM (v). Current is of arbitrary intensity and is scaled for convenience, in some cases. For ease of interpretation, the oxidation peak currents for unmodified GC and BDE are 8.5μA and 4.5 μA. All voltammograms were conducted at a scan rate of 0.1 V/s.

The electro-polymerization of ACBK and EB onto BDE does not lower $E_{pa,\ AA}$ significantly. Neither electro-polymerization shifts $E_{pa,\ AA}$ to a position comparable to its position on cathodic diamond or at equivalently modified GCE. Of the two polymer modifications, ACBK shifts $E_{pa,\ AA}$ the most, by about -220 mV and -260 mV at BDE and GCE, respectively. It is clear that ACBK electro-polymerizes in a more functional manner on GCE, than BDE. The fact that an EB-modification to BDE does not shift $E_{pa,\ AA}$ to lower potential compared to GCE, is surprising. Reports indicate that EB should shift $E_{pa,\ AA}$ on

GCE by at least -150 mV.[36] Anodic and cathodic modification of BDE and GCE by small potentials, prior to electro-deposition, did not dramatically improve the kinetics of AA oxidation either (see Table 6.4). Viewed together, the results indicate that ACBK is electro-polymerizing onto diamond in a state that improves the oxidation kinetics of AA, but not to the same extent as seen on glassy carbon. Electro-polymerized Evans Blue produces no useful effects. Neither polymer modification seems suitable for detecting dopamine in the presence of ascorbic acid, as neither shifts $E_{pa,\ AA}$ sufficiently.

Electrode	**[AA] (mM)**	**Peak Position (V)**	**Current (A)**	**Current Response (A cm^{-2})**
i	0.5	0.30	8.52×10^{-6}	1.20×10^{-4}
ii	0.5	0.04	1.10×10^{-5}	1.55×10^{-4}
iii	1	0.27	2.63×10^{-5}	3.70×10^{-4}
iv	1	1.10	4.26×10^{-6}	6.08×10^{-5}
v	0.3	0.88	4.90×10^{-6}	6.90×10^{-5}
vi	1	1.05	1.63×10^{-5}	2.30×10^{-4}
vii	1	1.16	1.07×10^{-5}	1.50×10^{-4}
viii	1	0.99	4.97×10^{-6}	7.00×10^{-5}

Table 6.4: AA oxidation peak positions, current, and current response for electrodes described in Figure 6.12. Also, results from two additional electrodes are shown: (vii) BDE modified with + 2 V prior to EB deposition; (viii) BDE modified with – 2 V prior to EB deposition. The [AA] exposed to vii and viii was 1mM. All voltammograms were conducted at a scan rate of 0.1 V s^{-1}.

6.3.4 Diamond Modified by Carbon Nanotubes

Electro-polymerization of ACBK seemed to be more successful on GCE, than BDE. This suggests that sp^2 carbon may have a role in mediating electro-polymerization. Thus, it is hypothesized that this process could be improved by increasing the sp^2 content of BDE. Also, the addition of carbon nanotubes to carbon-based electrodes increases the electro-active area, which is usually of benefit for detecting trace amounts of analytical species.[33]

Diamond electrodes were modified using multi-walled carbon nanotubes (MWCNT). The as-received MWCNTs (Sigma Aldrich) required further purification and a consistent, oxidized, surface termination. This was accomplished by using the methods of Yang *et al.*[40], in which oxidized MWCNTs are prepared by heat treatment (400°C, 1 hr, in air), exposure to 5M Nitric acid (80°C, 3 hours, reflux), and rinsed in water until solution pH is neutral. Suspensions of 1 mg/mL of MWCNT in DMF were made and sonicated for 1 hour. A 5μL drop was placed on the electrode and dried in an oven at 150°C for 1 hour. The deposition of randomly-oriented MWCNTs[33, 40] onto GCE and BDE was visually confirmed, as shown in Figure 6.13.

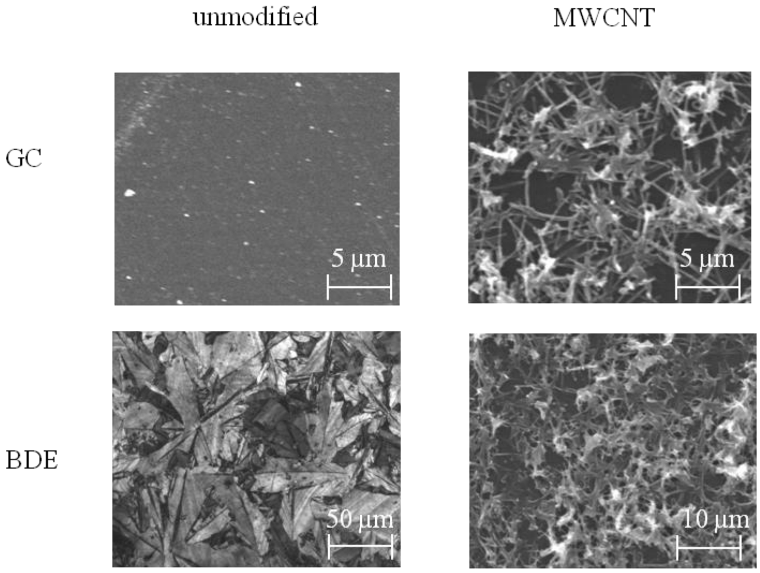

Figure 6.13: Scanning electron microscopy of glassy carbon (GC) and boron-doped diamond films with and without modification by deposition of multi-walled carbon nanotubes.

As done previously, the modified electrodes were tested by oxidizing AA in phosphate buffers at pH 4, with results shown in Figure 6.14. No change in peak position is observed for the GCE-MWCNT composite electrode. The addition of MWCNT to diamond electrodes shifts $E_{pa,\ AA}$ by - 470 mV. No change in peak position is observed for the GCE-MWCNT composite electrode. Thus one concludes that the MWCNTs are imparting - as expected - some sp^2 character onto the diamond electrodes.

The ability of BDE-MWCNT, with or without electrochemical modification, to separate the oxidation peaks of AA and DA in physiological conditions was evaluated. The related results are shown in Figure 6.15, along with those results associated with BDE. The peak positions of AA and DA are well-separated at anodic and cathodic treated BDE-MWCNT. However, $E_{pa,AA}$ remains higher than $E_{pa,DA}$ in all experiments. The ideal electrode for the detection of DA, in physiological conditions, would eliminate the EC' reaction, by ensuring that $E_{pa,AA} < E_{pa,DA}$.

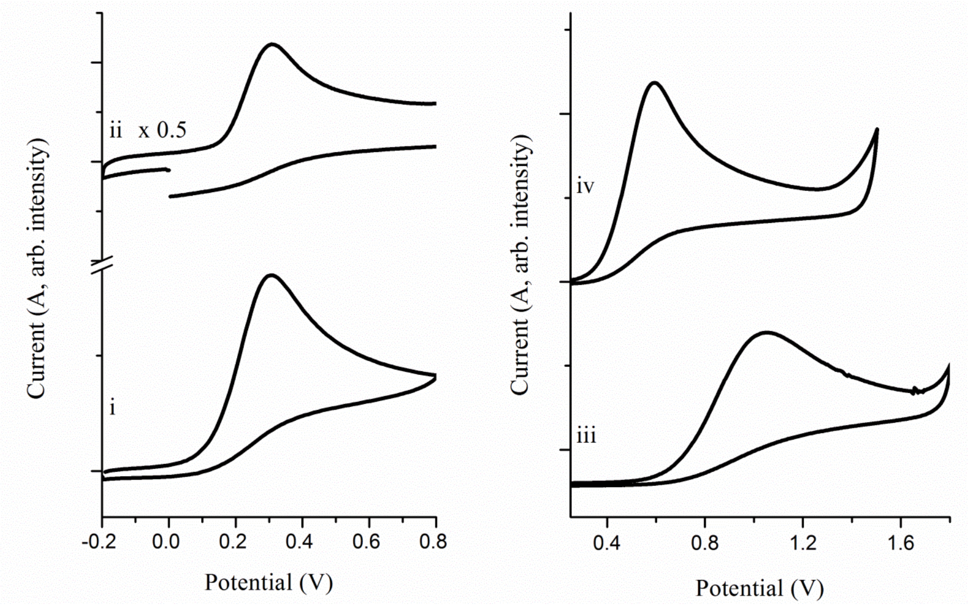

Figure 6.14: Detection of AA at unmodified and MWCNT modified GCE and BDE electrodes. Electrodes studied are: (i) GCE; (ii) GCE-MWCNT; (iii) BDE; (iv) BDE-MWCNT. The [AA] for (i) was 0.5 mM, and (ii – iv) was 1 mM. Conditions were as follows: 0.1 M phosphate buffer at pH 4. Current is displayed as arbitrary intensity and is scaled for convenience in some cases. For ease of interpretation, the oxidation peak currents for unmodified BDE-MWCNT and GCE-MWCNT are approximately 8.5×10^{-6} A and 4.5×10^{-6} A.

Several reports in the literature suggest that ACBK and Evans Blue can deposit onto sp^2 carbon-based electrodes.[29, 36, 39] Depositing MWCNT onto BDE does impart some sp^2 characteristics to the diamond surface. Therefore, the electro-polymerization of ACBK and EB may be possible on the as-prepared BDE-MWCNT electrodes. The use of this composite electrode may be a useful means to separate the oxidation peaks of AA and DA at diamond electrodes.

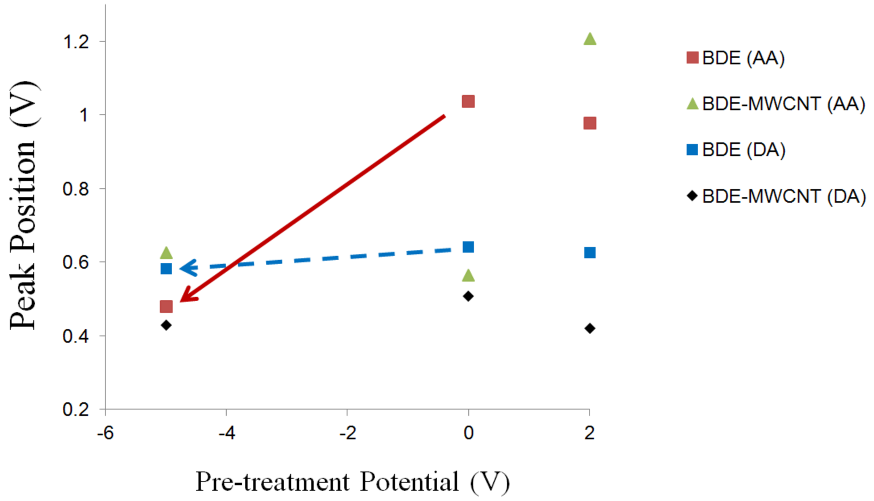

Figure 6.15: Peak position of the AA and DA oxidation peaks as a function of the electrochemical pre-treatment used to modify BDE or BDE-MWCNT electrodes. Electrodes were modified using anodic potential (in 0.1 M HNO_3) or cathodic potential (in 0.5 H_2SO_4). Solutions contained AA or DA at concentrations of 1mM in 0.1 M phosphate buffer at pH 7. Pre-treatment time was 3 minutes.

6.3.5 Diamond Modified by Carbon Nanotubes and Electro-polymers

Cyclic voltammograms of ACBK and EB deposition onto MWCNT-modified electrodes is shown in Figure 6.16. For comparison, glassy carbon electrodes with MWCNT deposited on their surfaces (GCE-MWCNT) were also modified with ACBK and EB. Redox peaks, characteristic of ACBK deposition, can be seen on GCE-MWCNT and BDE-MWCNT electrodes, which are consistent with ACBK deposition onto carbon nanotubes.[40] No characteristic redox peaks can been seen in the case of EB deposition on either of these two types of electrodes. From this one concludes that ACBK, but not EB, can be electro-polymerized on diamond electrodes modified with MWCNT.

Again, the performance of these electrodes was tested in phosphate buffer solutions containing AA at pH 4. The results are shown in Figure 6.17, along with those associated with GCE-MWCNT. MWCNT-modified BDE raises $E_{pa,\ AA}$ by at least 170 mV. In contrast, on GCE-MWCNT, ACBK lowers $E_{pa,\ AA}$ by 140 mV. EB-modification does not induce any shift in $E_{pa,\ AA}$ on either GCE-MWCNT or BDE-MWCNT. This is consistent with its continued lack of electro-activity towards AA, in this work. However, EB should lower $E_{pa,}$

AA on GCE-MWCNT, as it has done so in the past; the results presented here suggest that previous experiments may be unreliable.[36] None of these results show an improvement in the AA oxidation kinetics compared to cathodic-treated diamond. In conclusion, the strategy proposed in this section would not accomplish the aims of this work.

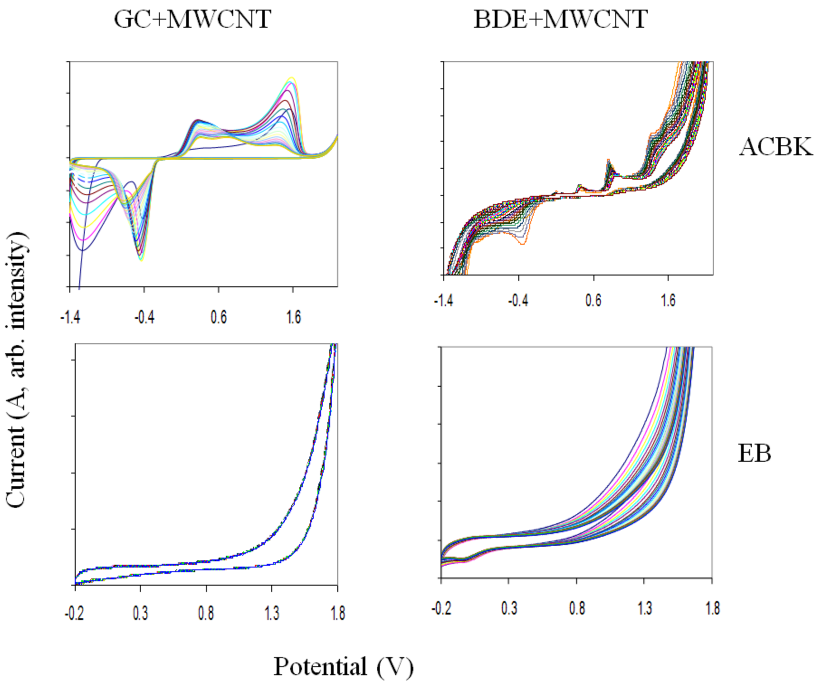

Figure 6.16: Cyclic voltammograms of glassy carbon and boron-doped diamond, modified with multi-walled carbon nanotubes and electro-polymers. These spectra were taken during the electro-polymerization, *in situ*.

Thus far in this work, small cathodic treatments have been seen to show a superior capability of lowering the position of the AA oxidation peak. Earlier, full exploitation of this ability was not possible due to excess Pt deposition at high cathodic potentials. However, in 2010, Hoffmann *et al.*[34] reported that cathodic pre-treatment of BDE could be done at highly cathodic potentials, without Pt deposition. Their method will be evaluated here for its effect on AA and DA oxidation.

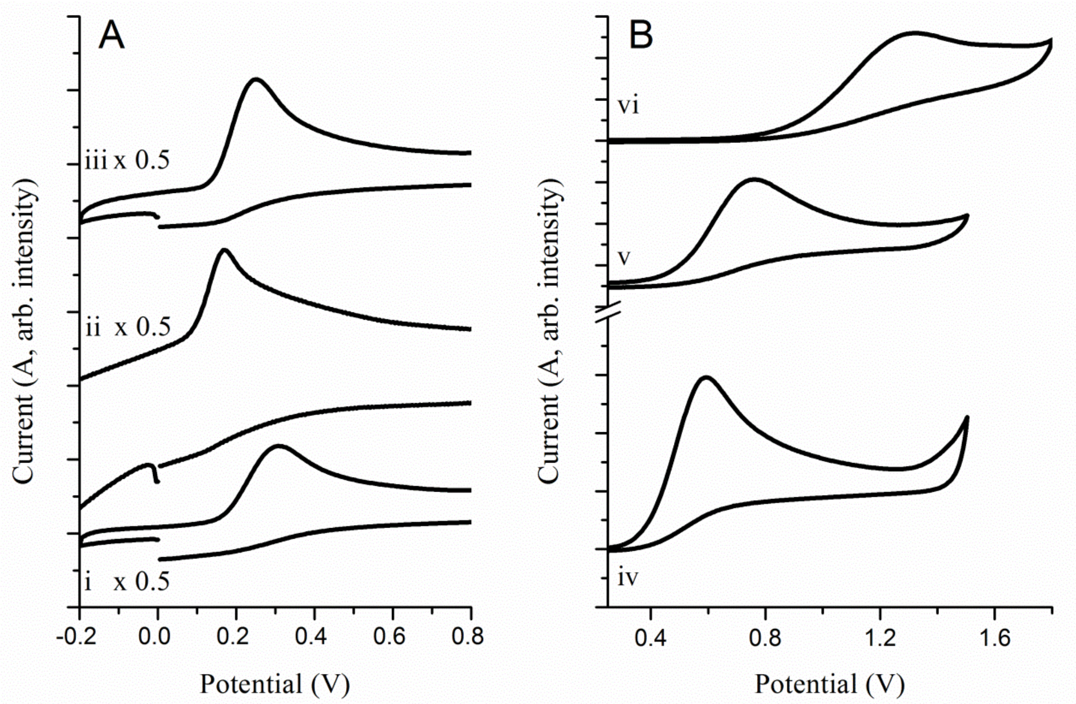

Figure 6.17: Detection of AA at various MWCNT electrodes in 0.1M phosphate buffer (pH 4): (i) GCE-MWCNT; (ii) GCE-MWCNT with 20 scans of ACBK; (iii) GCE-MWCNT with 40 scans of EB; (iv) BDE-MWCNT; (v) BDE-MWCNT with 20 scans of ACBK; (vi) BDE-MWCNT with 40 scans of EB. The [AA] was 1mM for all experiments. Conditions were 0.1 M phosphate buffer at pH 4. For reference, $i_{\mathrm{pa,\,AA}}$ for (i) and (iv) are 2.0 x 10^{-5} A and 6.0 x 10^{-6} A, respectively.

6.3.6 Diamond Modified by High Cathodic Potentials

The method of Hoffmann *et al.*[34] is reproduced here, using the optimized applied potential of -35 V. A bespoke electrochemical cell was made to accomplish this task, and it is shown in Figure 6.18. Pt deposition is prevented by use of a Vycor porous glass membrane (BAS, Inc) to separate the counter-electrode and the working electrode. (n.b. This glass tube is closed off at one end by Araldite glue.) The counter-electrode and working electrode were placed in 2M H_2SO_4 and 2M HCl, respectively. High cathodic potential was applied using two power supplies in series. Hydrogen gas produced at the surface of the working electrode was swept away by a stream of nitrogen gas.

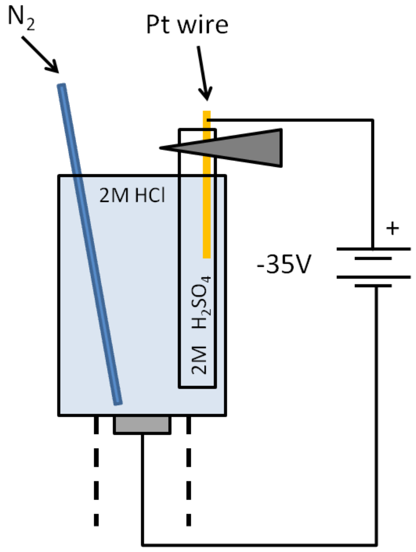

Figure 6.18: Optimized experimental set-up using PTFE electrochemical holder in which the diamond electrode is at the bottom of the electrochemical cell. A porous glass tube separates two electrolyte solutions and is held in place by self-closing tweezers to reduce cracking, which is caused by thermal expansion. A low flow of N_2 gas is introduced *via* a glass pipette.

Initial experiments confirmed that platinum was not depositing onto diamond surfaces during high cathodic treatment. The results are shown in Figure 6.19. No redox behaviour due to the hydrogen adsorption on Pt is seen in the potential window of diamond cleaned with both *Aqua Regia* and nitric acid (see A, Figure 6.19). After - 35 V treatment for 3 minutes, a cyclic voltammogram of the treated electrode was taken in 0.1 M nitric acid. A small oxidation peak is seen at about - 0.1 V, along with an anodic peak at 1.5 V. The former could be assigned to hydrogen evolution at platinum, but this is not the case. It is shown in Figure 6.19D (*inset*) that this peak disappears after the first scan in nitric acid, whilst if it was due to hydrogen at any Pt deposits, a stable response would be expected.[35] Quinone formation at the electrode surface is the likely source of this oxidation peak.[41, 42] From the above, one concludes that the no platinum is depositing onto diamond at high cathodic treatments, using the apparatus described here.

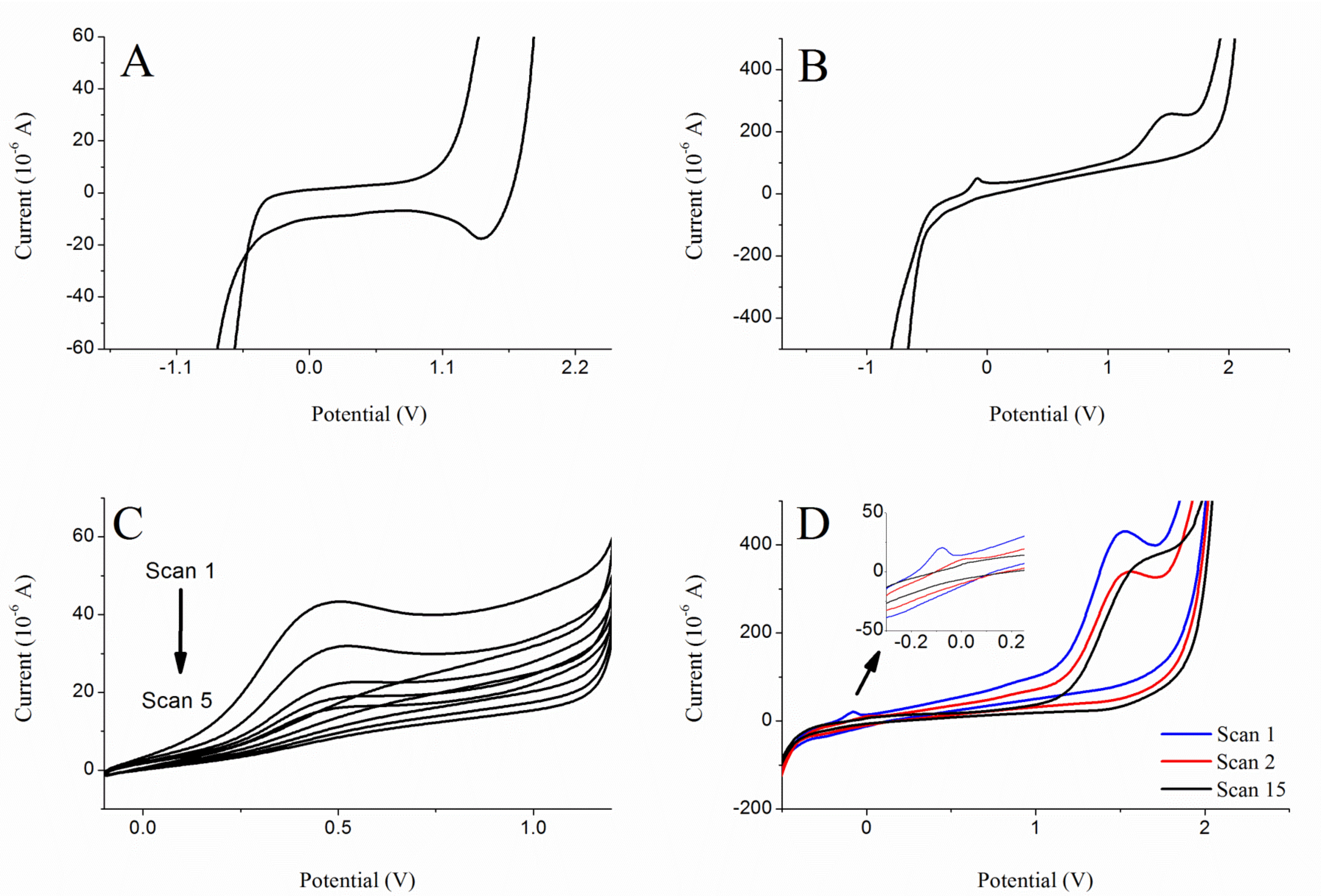

Figure 6.19: A series of cyclic voltammagrams showing the effect of various conditions on the surface of a single BDE electrode: (A) electrode given Aqua Regia treatment followed by 15 scans in 0.1M HNO_3 (scan 15 shown); (B) electrode after -35V treatment for 3 minutes, followed by 1 scan in 0.1M HNO_3; (C) electrode after exposure to 1mM AA in 0.1 mM phosphate buffer pH 7; (D) followed by exposure to 0.1M HNO_3 for 15 scans (n.b. only scans 1, 2, and 15 are shown).

High cathodic treatment of diamond is known to convert hydrophilic diamond surfaces to hydrophobic surfaces.[34] This simple test was conducted to confirm the success of the - 35 V electrochemical treatment. Contact angle data is shown in Table 6.5 and images of water droplets at the surface are shown in Figure 6.20. Anodic-treated diamond, a well-oxidized diamond surface, was made more hydrophobic by a 3 minute application of - 35 V (see 1 and 2, Table 6.5; A and B, Figure 6.20). Treatment at this applied potential for an additional 17 minutes did not change the contact angle to a great extent (see 2 and 3, Table 6.5). This change in hydrophobicity is reversible. *Aqua Regia* converts an as-treated diamond surface from a hydrophobic state to a hydrophilic state (see 3 and 4, Table 6.5). The – 35 V treatment is then able to make this surface hydrophobic again (see 4 and 5, Table 6.5; C and D in Figure 6.20). These results are reasonably consistent with Hoffman *et al.*[34], despite their reporting contact angles of > 90 degrees, which indicates that their methods lead to diamond electrodes with higher hydrophobicity. The extent of hydrophobicity may be reduced here by slight differences in apparatus, cleaning methods, or electrode properties (i.e. doping levels, roughness, etc.), which combine to effect a reduction in the quality of the cathodic treatment here. Notwithstanding this, it is clear that a -35V treatment produces hydrophobic diamond surfaces.

Electrode	**Pre-treatment Potential (V)**	**Time (min.)**	**Avg. Contact Angle (degrees)**	**S.D. (± degrees)**
1[a]	+2	3	32.7	5.8
2[b]	-35	3	53.5	11.8
3[c]	-35	20	58.8	4.4
4[d]	0	0	< 5.0	n/a
5[e]	-35	9	63.8	3.0

Table 6.5: Contact Angle data for a variety of BDE with various pre-treatments. Notes: (a) polished, cleaned in 0.1M HNO_3 (30 scans) prior to pre-treatment; (b) took Electrode 1, pre-treated as indicated; (c) took Electrode 2, pre-treated for additional 17 minutes; (d) took Electrode 3, cleaned with A*qua Regia* solution (at 90°C, 3 hours); (d) took Electrode 4, pre-treated as indicated. All samples were cleaned for 30 seconds in acetone, and then dried with N_2, prior to measurement. Values are an average of six measurements on the surface, with standard deviations reported.

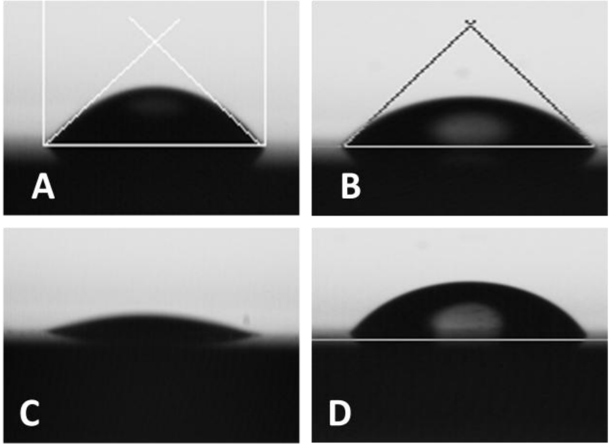

Figure 6.20: Representative images of water droplets on diamond electrodes mentioned in Table 1. (A) 2V pre-treated BDE (Electrode 1) (B) after – 35 V pre-treatment for 20 minutes. (Electrode 3) (C) after *Aqua Regia* cleaning (Electrode 4) (D) after – 35 V pre-treatment for 9 minutes (Electrode 5).

Since the high negative potential treatment of diamond is well-characterized, a systematic study of its ability to oxidize DA and AA can proceed. Cyclic voltammograms show that in neutral conditions, high cathodic BDE has an $E_{pa,\ AA}$ is 0.45 V (see Figure 6.19C), whilst $E_{pa,\ DA}$ is 0.25 V (not shown); these overpotentials are similar to those at BDE treated with small cathodic potentials (see Figures 6.6, 6.8 and 6.9). Also, square-wave voltammetry was conducted, in which [AA] is varied whilst [DA] remained fixed. The results are shown in Figure 6.21 and Table 6.6. Two oxidation peaks are seen in all voltammograms. When [AA] is increased, the E_{pa} and i_{pa} for both peaks shift to higher values. The response of the peak at low and high E_{pa} to increasing [AA], is 1.30 µA mM^{-1} and 0.62 µA mM^{-1}, respectively. These effects are also similar to that seen at BDE treated with small cathodic potentials (see Figure 6.9), therefore similar conclusions can be drawn here. First, the oxidation waves in Figure 6.21 can be assigned to AA oxidation, in the case of the peak at low E_{pa}, and DA oxidation, for the peak at high E_{pa}. Second, the EC’ reaction between AA and DA is not eliminated at a diamond electrode pre-treated with high cathodic potentials.

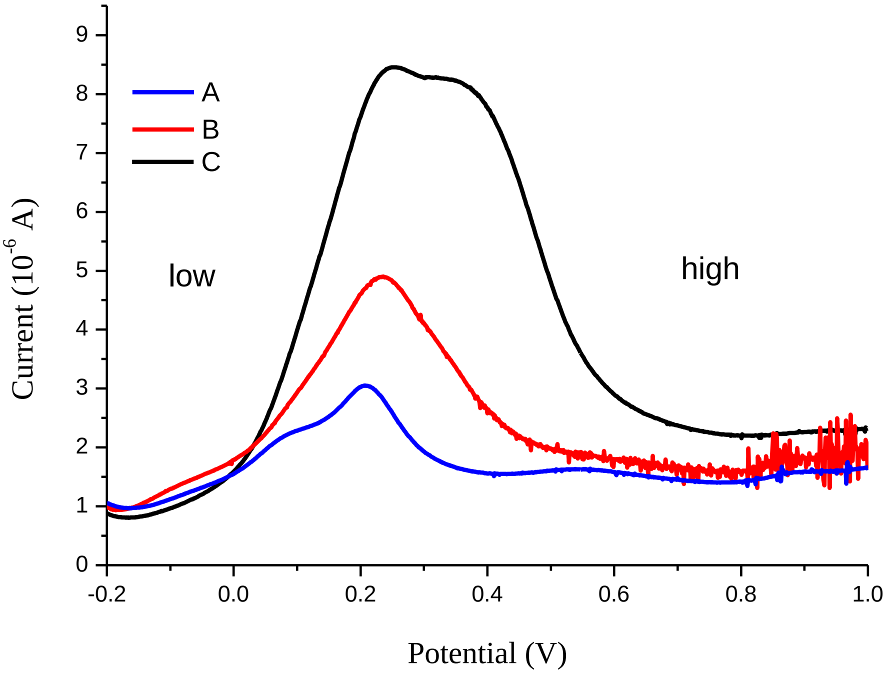

Figure 6.21: Square-wave voltammetry of BDE modified by a 3 minute exposure to – 35 V in 0.1M phosphate buffer solutions at pH 7 containing 0.1 mM DA and: (A) 0.1 mM AA; (B) 1 mM AA; (**C**) 5 mM AA.

Peak Label	**[AA] (mM)**	**Peak Position (V)**	**Current (A)**	**Current Response (A cm^{-2})**
low	0.1	0.08	4.00 x 10^{-6}	5.63 x 10^{-5}
low	1	0.11	3.92 x 10^{-6}	5.52 x 10^{-5}
low	5	0.25	7.59 x 10^{-6}	1.07 x 10^{-4}
high	0.1	0.21	3.96 x 10^{-6}	5.58 x 10^{-5}
high	1	0.24	5.82 x 10^{-6}	8.20 x 10^{-5}
high	5	0.34	7.44 x 10^{-6}	1.05 x 10^{-4}

Table 6.6: Electrochemical data associated with Figure 6.21 for electrodes which have been treated with – 35 V for 3 minutes.

6.3.7 Diamond Modified by Hydrogen Plasma

There is a growing consensus that cathodic pre-treatment of diamond, hydrogen-terminates the diamond surface and increases the amount of sub-surface hydrogen within diamond.[34, 43-45] In addition, such a surface is defect free, clean, and hydrophobic. The combined effect is thought to be the reason for the improved electrochemical detection of negatively charged organic molecules in physiological conditions.[46] Hydrogen-plasma (HP) modification of diamond is known to have many of the above characteristics. [34, 47, 48] Therefore, this strategy was used to attempt the improved detection of DA in the presence of AA in physiological conditions.

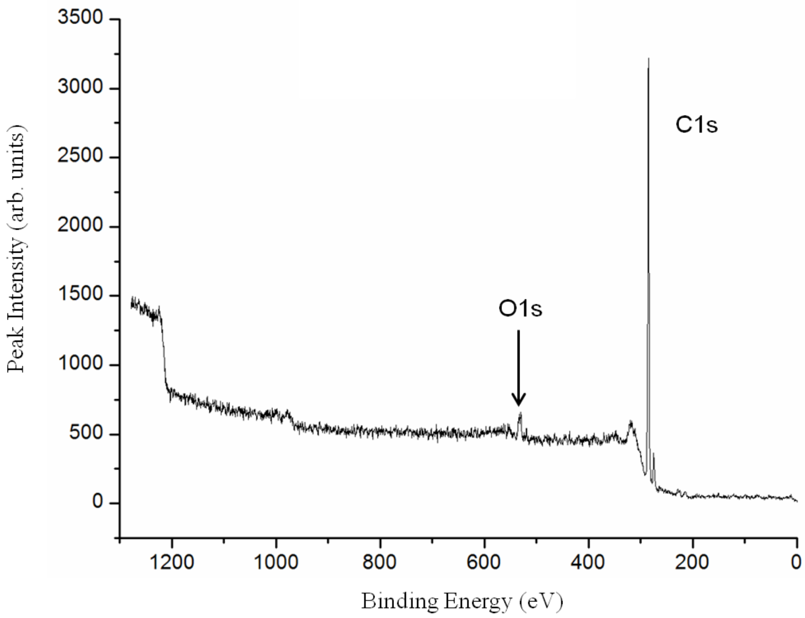

Figure 6.22: Wide scan XPS spectrum of hydrogen plasma treated diamond electrode

Diamond electrodes were modified by high temperature, hydrogen plasma (H_2 gas, 45 Torr, 600^{o}C, 1100 W), for 10 minutes, with electrodes cleaned prior to HP-treatment by cyclic voltammetry in 0.1 M HNO_3, and after treatment by a 30 second ultrasonic rinse in methanol. Electrodes were used once, and re-modified before subsequent usage. Basic surface characterization of HP-BDE shows that such substrates are free of metal contaminants, are well hydrogenated, and highly hydrophobic. A wide scan XPS of HP-BDE is shown in Figure 6.22. There is no Pt $4f_{7/2}$ photoelectron signal at 70.9 eV. The oxygen content is low, having O1s/C1s ratio less than 0.04. Contact angles for this surface are greater than 90 degrees (not shown). The methanol rinse is thought to remove the thin films of sp^2 carbon known to deposit onto diamond after HP-modification.[48] Thus, these results indicate that the surface is free of metal contamination, and has surface chemistry consistent with a uniform, hydrogen-terminated, diamond surface.

Cyclic voltammetry of AA, DA, and mixed solutions of both species is shown in Figure 6.23. For the first cyclic voltammetric scan, in all tested solutions, the peak positions, currents and general electrode response at HP-modified diamond is similar to the equivalent response at small and high cathodic treated BDE. Fouling of the surface occurs, but this is not unexpected when oxidizing AA and DA on diamond, and was seen throughout this work. The cyclic voltammetric results suggest that the electrochemical separation of AA and DA may be occurring at this electrode (see Figure 6.23C), but further evidence is required.

A better understanding of the electrochemical events at the surface was obtained using square-wave voltammetry where HP-BDE was exposed to mixed solutions of DA and AA in phosphate buffer at pH 7. These results are shown in Figures 6.24 and Table 6.7. In the absence of the other species, $E_{pa,\ AA}$ and $E_{pa,\ DA}$ occurs at 0.004 V and 0.160 V, respectively. In mixed solutions, no shifts to higher overpotentials are observed. The current response of the peaks around 0.01 V to increasing [AA] is 1.62 µA mM^{-1} ($R^2 = 0.96$), whereas the current the peak at higher E_{pa} changes by 0.10 µA mM^{-1} ($R^2 = 0.17$). Thus, with confidence, AA and DA oxidation occurs at about 0.01 V and 0.16 V, respectively, at HP-BDE when the two species are present in the same solution. Collectively, these results are normally only seen when the EC’ mechanism is eliminated. [28, 29, 31, 33] Therefore, complete oxidation of AA is occurring before DA is oxidized at this electrode, during time-scale of the experiment.

Whilst negatively charged molecules in solution are known to have low overpotentials on HP-BDE[46], a literature survey did not reveal evidence of AA oxidation occurring at a lower potential than DA oxidation at HP-BDE. However, in one case the $E_{pa,AA}$ and $E_{pa,\ DA}$ were very close to each other at HP-BDE.[28] In the present work, results were obtained without the aid of metal catalysts, and occurred reproducibly on two similarly treated

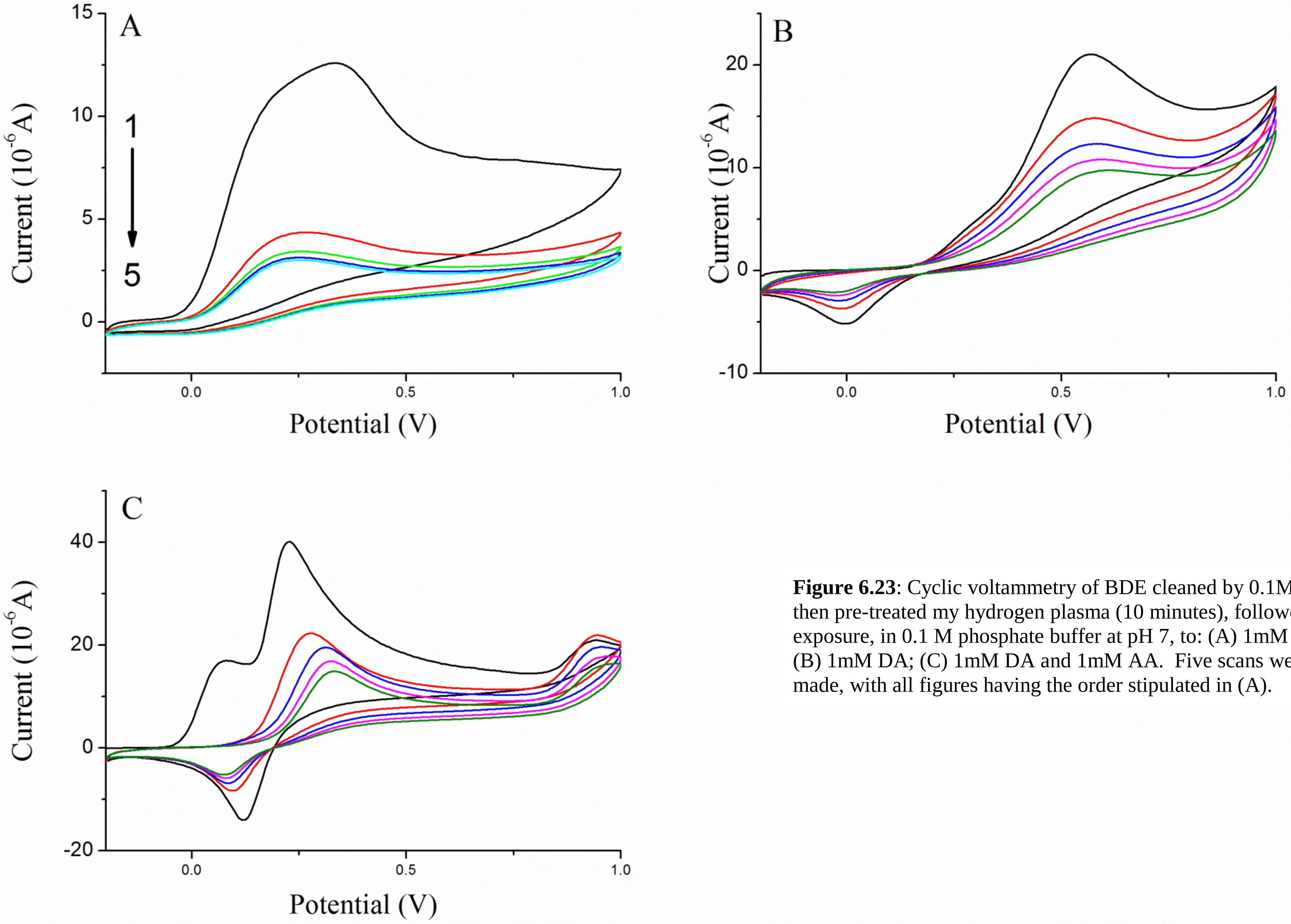

Figure 6.23: Cyclic voltammetry of BDE cleaned by 0.1M HNO_3 then pre-treated my hydrogen plasma (10 minutes), followed by exposure, in 0.1 M phosphate buffer at pH 7, to: (A) 1mM AA; (B) 1mM DA; (C) 1mM DA and 1mM AA. Five scans were made, with all figures having the order stipulated in (A).

diamond electrodes. Thus, one argues that DA can be detected in the presence of AA at HP-BDE, with minimal AA interference and minimal catalytic effects by AA participation in the EC' mechanism mentioned in this work.

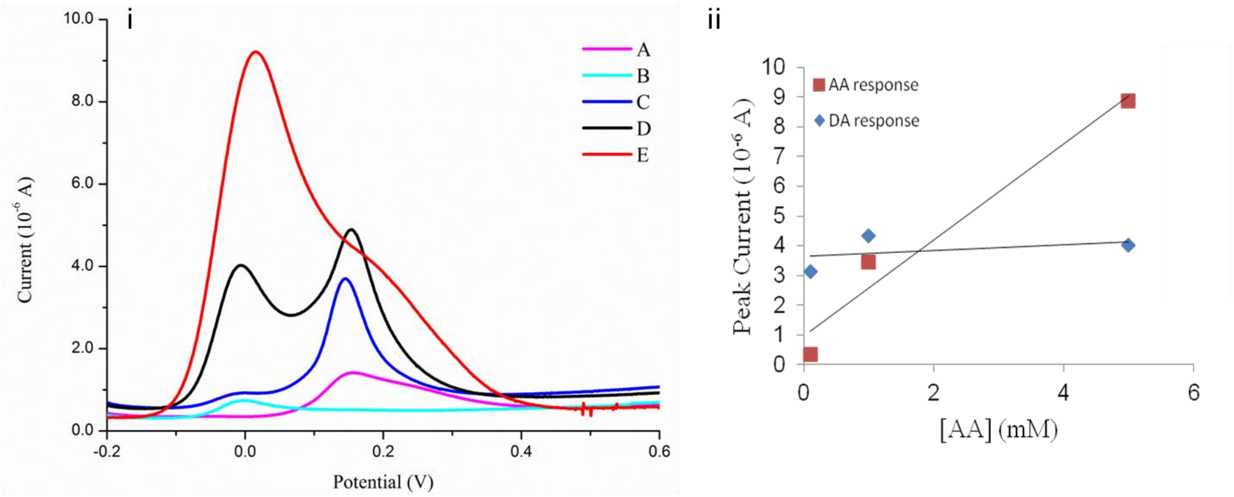

Figure 6.24: (i) Square-wave voltammetry of hydrogen plasma modified BDE in various 0.1 M phosphate buffer solutions at pH 7: (A) 0.1 mM DA (B) 0.1 mM AA (C) 0.1 mM DA and 0.1 mM AA (D) 1mM AA and 0.1 mM DA (E) 5 mM AA and 0.1 mM DA.; (ii) Peak current as a function of [AA] for the data in C, D and E in (i), where AA oxidation occurs at ≈0.01 V and DA oxidation occurs at ≈ 0.15 V.

Peak Label	[AA] (mM)	[DA] (mM)	Peak Position (V)	Current (A)	Current Response (A cm^{-2})
AA	0.1	0	0.004	4.30×10^{-7}	6.06×10^{-6}
DA	0	0.1	0.160	1.06×10^{-6}	1.49×10^{-5}
AA	0.1	0.1	0.004	3.60×10^{-7}	5.07×10^{-6}
DA	0.1	0.1	0.145	3.14×10^{-6}	4.42×10^{-5}
AA	1	0.1	0.007	3.48×10^{-6}	4.90×10^{-5}
DA	1	0.1	0.155	4.35×10^{-6}	6.13×10^{-5}
AA	5	0.1	0.010	8.88×10^{-6}	1.25×10^{-4}
DA	5	0.1	0.170	4.02×10^{-6}	5.66×10^{-5}

Table 6.7: Peak current, position and current response for the assigned AA and DA peaks in Figure 6.24.

6.4 Discussion

In this work, the improvement of dopamine detection in the presence of ascorbic acid on diamond electrodes is accomplished by improving the AA oxidation kinetics, and by minimizing, or even eliminating, the EC' reaction between the two species in solution. Both effects were fully realized after modifying diamond by hydrogen plasma treatment, and partially so, after modifying diamond with electrochemical pre-treatment at small and large negative potentials. Summaries of these primary conclusions are found in Figures 6.25 and 6.26.

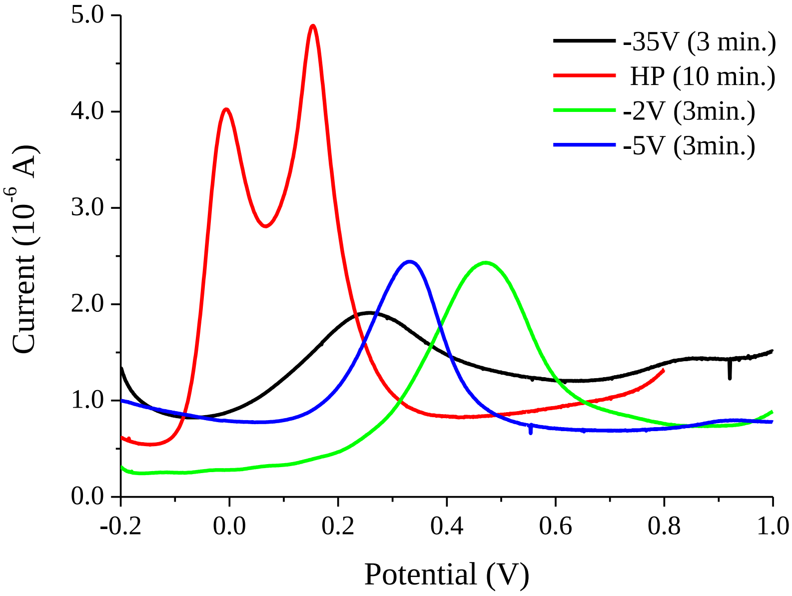

Figure 6.25: (A) Square-wave voltammetry of variously modified diamond electrodes in 0.1mM DA and 1mM AA in 0.1M phosphate buffer at pH 7.

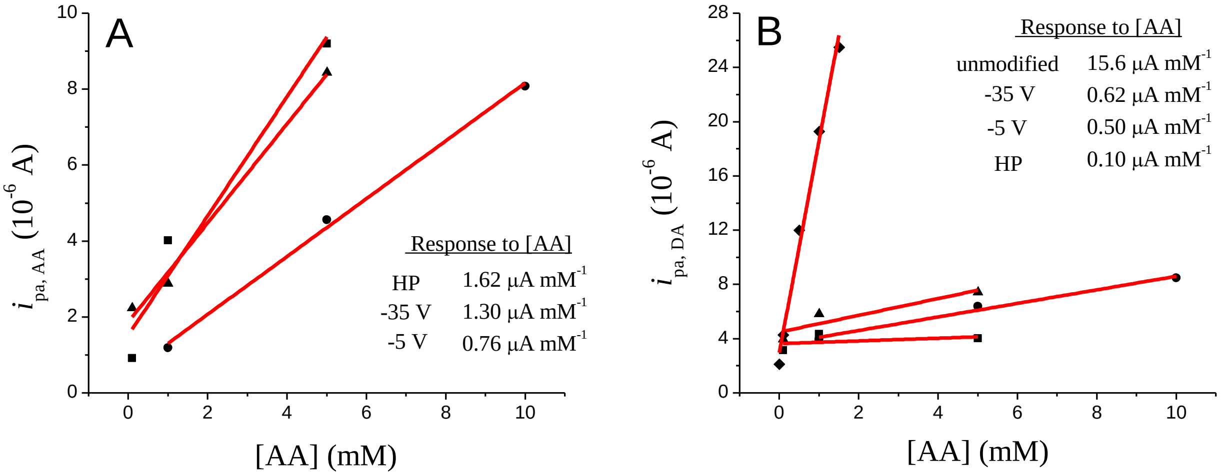

Figure 6.26: (A) Response of $i_{pa, AA}$ to changing [AA]; (B) Response of $i_{pa, DA}$ to changing [AA]. In all cases, the [DA] was 0.1 mM, and the solution was a 0.1 M phosphate buffer at pH 7.

Figure 6.25 summarizes the effects of various pre-treatments on the observed peak positions which result from mixed solutions of AA and DA. Cathodic and hydrogen plasma modifications to diamond surfaces shift the AA oxidation peak such that $E_{pa,AA}$ is less than $E_{pa,DA}$. Partial and full separation of these two signals is possible at cathodic diamond (see Figures 6.9 and 6.21), and hydrogen plasma modified diamond, respectively. Figure 6.26 shows the effects of changing [AA] on $i_{pa,AA}$ and $i_{pa,DA}$, in solutions where [DA] is fixed at 0.1 mM. The response of $i_{pa,AA}$ to [AA] is improved by highly cathodic treatment and hydrogen plasma treatment (see Figure 6.26A). The response of $i_{pa,DA}$ to [AA] is minimized by both cathodic treatment and eliminated at diamond electrodes treated by hydrogen plasma. The above results show that AA oxidation kinetics are improved at cathodic and hydrogen plasma modified diamond electrodes, and that the EC' reaction between AA and DA in solution can be minimized or even eliminated. The electrode which achieves both of these effects to the greatest degree is HP-BDE.

The main conclusions of this study suggest that hydrogen-termination of diamond surfaces may be key to the superior detection of DA in the presence of AA. Modifying diamond with hydrogen plasma leads to hydrogen-termination; doing so cleans diamond surfaces, replenishes the sub-surface concentration of hydrogen, decreases negative charged species at its surface (at physiological conditions), and increases diamond's hydrophobicity.[34, 48] All of these features are known to improve electron transfer of small, negatively charged molecules at a surface.[25, 33, 48] The extent of hydrogen termination due to cathodic treatments seems dependent on the potential used, with higher cathodic potentials leading to a more hydrogen terminated surface[34]; this is best shown here by the results of Figure 6.26A. Highly hydrogenated diamond surfaces likely improve the kinetics of AA oxidation by increasing hydrophobic interactions and reducing electrostatic repulsion between AA and diamond electrodes.[31] As a consequence, the minimization or elimination of the EC' reaction between AA and DA is made possible at hydrogenated diamond electrodes, if the oxidation kinetics of the former are faster than the latter.

The complete electrochemical separation of dopamine and ascorbic acid was seen at hydrogen plasma modified diamond electrodes. This is the first time that this has been accomplished without adding non-diamond materials to the diamond electrode surface. Whilst, the best results were achieved using hydrogen plasma modified diamond, the results achieved by modifying diamond by large, cathodic potentials were promising. Thus, this study is also proof-of-principle that the use of diamond electrodes modified with large cathodic potentials is of electro-analytical use.

6.5 Summary and Conclusions

In this chapter, various modifications to diamond surfaces lead to improved detection of dopamine in the presence of ascorbic acid. The main conclusions are as follows:

- The following did not sufficiently improve the detection of dopamine, in the presence of ascorbic acid, at diamond electrodes within physiological conditions:
    - Electro-polymerization by Evans Blue or ACBK
    - Deposition of multi-walled carbon nanotubes
    - Creation of polymer-nanotube modifications using the above mentioned materials.
- The following sufficiently improved the detection of dopamine, in the presence of ascorbic acid, at diamond electrodes within physiological conditions:
    - Small and large cathodic electrochemical pre-treatments
    - Hydrogen plasma modification

- Small cathodic, large cathodic, and hydrogen plasma treatments all lowered the overpotential required to oxidize ascorbic acid to a potential lower than that required to oxidize dopamine.
- Small cathodic and large cathodic treatments minimized the effects of the EC' mechanism that occurs in solutions containing both AA and DA.
- Hydrogen plasma modification of diamond *eliminated* the EC' mechanism which normally occurs in solutions containing both AA and DA.
- The extent of hydrogen termination of diamond surfaces is likely the root cause of the improved detection of dopamine in the presence of ascorbic acid at these electrodes.
- Proof-of-principle that highly cathodic, electrochemical treatments can be of benefit to analytical electrochemistry is made in this study.
- At hydrogen plasma treated diamond electrodes, the complete electrochemical separation of dopamine and ascorbic acid was possible. This is the first time this has been accomplished without adding non-diamond material to the diamond electrode surface.

References

[1] B.P. Helmke, A.R. Minerick, Proceedings of the National Academy of Sciences, 103 (2006) 6419-6424.

[2] M. Merz, P. Fromherz, Adv. Funct. Mater., 15 (2005) 739-744.

[3] J. Pine, Journal of Neuroscience Methods, 2 (1980) 19-31.

[4] P. Bergveld, J. Wiersma, H. Meertens, Biomedical Engineering, IEEE Transactions on, BME-23 (1976) 136-144.

[5] G.W. Gross, W.Y. Wen, J.W. Lin, Journal of Neuroscience Methods, 15 (1985) 243-252.

[6] P. Fromherz, A. Offenhausser, T. Vetter, *et al.*, Science, 252 (1991) 1290-1293.

[7] P.G. Patil, D.A. Turner, Neurotherapeutics, 5 (2008) 137-146.

[8] T.W. Berger, M. Baudry, R.D. Brinton, *et al.*, Proceedings of the IEEE, 89 (2001) 993-1012.

[9] C.E. Nebel, B. Rezek, D. Shin, *et al.*, J. Phys. D: Appl. Phys., 40 (2007) 6443.

[10] P.J. Rousche, R.A. Normann, Journal of Neuroscience Methods, 82 (1998) 1-15.

[11] S. Alwarappan, G. Liu, C.-Z. Li, Nanomedicine: Nanotechnology, Biology and Medicine, 6 (2010) 52-57.

[12] R.A. Wise, Nat Rev Neurosci, 5 (2004) 483-494.

[13] M.A. Ungless, Trends in Neurosciences, 27 (2004) 702-706.

[14] N.F. Atta, M.F. El-Kady, A. Galal, Anal. Biochem., 400 (2010) 78-88.

[15] P.R. Roy, M.S. Saha, T. Okajima, *et al.*, Electroanalysis, 16 (2004) 1777-1784.

[16] X.Y. Zhao, J.B. Zang, Y.H. Wang, *et al.*, Electrochem. Commun., 11 (2009) 1297-1300.

[17] P. Fei Huang, L. Wang, J. Yue Bai, *et al.*, Microchimica Acta, 157 (2007) 41-47.

[18] M.J. Giz, B. Duong, N.J. Tao, J. Electroanal. Chem., 465 (1999) 72-79.

[19] C.R. Raj, K. Tokuda, T. Ohsaka, Bioelectrochemistry, 53 (2001) 183-191.

[20] M. Wei, L.-G. Sun, Z.-Y. Xie, *et al.*, Adv. Funct. Mater., 18 (2008) 1414-1421.

[21] E. Popa, H. Notsu, T. Miwa, *et al.*, Electrochem. Solid-State Lett., 2 (1998) 49-51.

[22] Z. Guo-hua, L. Ming-fang, L. Ming-li, Central European Journal of Chemistry, 5 (2007) 1114-1123.

[23] H. Notsu, I. Yagi, T. Tatsuma, *et al.*, Electrochem. Solid-State Lett., 2 (1999) 522-524.

[24] O.A. Williams, M. Nesladek, M. Daenen, *et al.*, Diamond Relat. Mater., 17 (2008) 1080-1088.

[25] M.C. Granger, M. Witek, J. Xu, *et al.*, Anal. Chem., 72 (2000) 3793-3804.

[26] H. Wang, J.-P. Griffiths, R.G. Egdell, *et al.*, Langmuir, 24 (2008) 862-868.

[27] A. Krueger, D. Lang, Adv. Funct. Mater., 22 (2012) 890-906.

[28] T. Kondo, Y. Niwano, A. Tamura, *et al.*, Electrochim. Acta, 54 (2009) 2312-2319.

[29] R. Zhang, G.-D. Jin, D. Chen, *et al.*, Sensors and Actuators B: Chemical, 138 (2009) 174-181.

[30] A. Dalmia, C.C. Liu, R.F. Savinell, J. Electroanal. Chem., 430 (1997) 205-214.

[31] D.A. Tryk, H. Tachibana, H. Inoue, *et al.*, Diamond Relat. Mater., 16 (2007) 881-887.

[32] W. Smirnov, N. Yang, R. Hoffmann, *et al.*, Anal. Chem., 83 (2011) 7438-7443.

[33] W.C. Poh, K.P. Loh, W.D. Zhang, *et al.*, Langmuir, 20 (2004) 5484-5492.

[34] R. Hoffmann, A. Kriele, H. Obloh, *et al.*, Appl. Phys. Lett., 97 (2010) 052103.

[35] J. Hu, X. Lu, J.S. Foord, *et al.*, physica status solidi (a), 206 (2009) 2057-2062.

[36] L. Lin, J. Chen, H. Yao, *et al.*, Bioelectrochemistry, 73 (2008) 11-17.

[37] C.L.L. Pham, S.L. Leong, F.E. Ali, *et al.*, J. Mol. Biol., 387 (2009) 771-785.

[38] D. Zhang, Y. Peng, H. Qi, *et al.*, Sensors and Actuators B: Chemical, 136 (2009) 113-121.

[39] X.P. Zou, J.h. YU, N.j. Yang, *et al.*, Hubei Chemical, 4 (2001).

[40] P. Yang, W. Wei, L. Yang, Microchimica Acta, 157 (2007) 229-235.

[41] R. Ramesham, M. Rose, J. Mater. Sci. Lett., 16 (1997) 1693-1699.

[42] G.Pastor-Moreno, D.J. Riley, Electrochem. Commun., 4 (2002) 218-221.

[43] N. Simon, H. Girard, M. Manesse, *et al.*, Diamond Relat. Mater., 17 (2008) 1371-1375.

[44] G.R. Salazar-Banda, L.S. Andrade, P.A.P. Nascente, *et al.*, Electrochim. Acta, 51 (2006) 4612-4619.

[45] H.B. Suffredini, V.A. Pedrosa, L. Codognoto, *et al.*, Electrochim. Acta, 49 (2004) 4021-4026.

[46] Yuan Yu, Yanli Zhou, Liangzhuan Wu, *et al.*, International Journal of Electrochemistry, (2012).

[47] C.H. Goeting, F. Marken, A. Gutiérrez-Sosa, *et al.*, Diamond Relat. Mater., 9 (2000) 390-396.

[48] B. Rezek, C.E. Nebel, Diamond Relat. Mater., 15 (2006) 1374-1377.

7. Summary and Outlook

The surface functionalization of carbon-based materials for biological applications was the focus of this thesis. Three materials were of primary interest: nanodiamond, carbene-modified polystyrene, and boron-doped diamond thin films. Nanodiamond is a candidate as a non-inflammatory platform for drug delivery. Carbene-modified polymers with the appropriate surface chemistry will be used in advanced anti-microbial materials. Boron-doped CVD diamond thin films have conductive and bio-compatible properties which make them ideal candidates for integration into advanced bio-sensors and bio-electronic devices. Each material was studied in this thesis in an environment or scenario which is likely to be crucial to its future use and performance. The study of their surface chemistry was conducted using standard surface science techniques, with their functionality in the chosen scenario evaluated either by QCM-D or electrochemistry.

This thesis contains several accomplishments. For the first time, protein adsorption of a common blood protein (BSA) onto nanodiamond particles was studied using QCM-D. The surface chemistry affected the nature and extent of BSA adsorption, with surface roughness affecting the *initial* stages of BSA adsorption. Results suggest that nanoparticle forms of inorganic materials can be studied using QCM-D and the methodology can be extended to other protein systems or experimental conditions for more advanced protein adsorption studies. Also, for the first time *chemical* evidence of successful functionalization of polystyrene using a novel reaction scheme (carbene insertion, followed by azo-coupling of a chemical functionality) was confirmed using X-ray photoelectron spectroscopy. Thin films made from this functionalized material were found to be suitable for protein adsorption studies using QCM-D. It was determined that surface chemistry was strongly linked to protein behaviour and that predictions of that behaviour could be made in short time frames using QCM-D data. Diamond thin films are considered an ideal material for neurotransmitter detection in neuronal environments, provided that they can be modified to detect those molecules in the presence of interferents. The best approaches used thus far to accomplish this task have required the placement of non-diamond materials at a diamond electrode surface. In this thesis, the hydrogenation of diamond surfaces was found to minimize the effects of ascorbic acid on the oxidation peak of dopamine at physiological conditions. In fact, near-complete electrochemical separation of the dopamine and ascorbic acid was made at a hydrogen plasma-modified diamond electrode – this is an important result, as it has never been seen on diamond without some non-intrinsic modification to its surface. Collectively, these results make important contributions to our existing knowledge and use of nanodiamond, carbene-modified polymers, and boron-doped diamond thin films in biological environments.

Whilst the results here are informative and promising, there is extensive scope to expand upon them. Protein adsorption studies involved the simple case of the adsorption of a common, globular protein within a fixed, physiological environment (i.e. pH 7, 20^{o}C, fixed buffer concentrations, etc.). The QCM-D methodology developed in this thesis can be used to analyze the character and kinetics of protein adsorption onto surfaces. The successful study of protein deposition onto two different materials – inorganic nanoparticles and polymers – having different surface chemistry and surface roughness, suggests that the described approach has wider application. With this in mind, the following could become variables for future experiments: substrate type, temperature, pH, buffer concentration, protein type, finer variations in surface roughness. The results of such experiments would have even wider implications for the control of protein adsorption on various surfaces. This methodology and the results would be of interest to biochemists, and bio-material and medical scientists. The end goal would be to better control the behaviour of proteins at surfaces under a variety of conditions, in order to achieve any intended functionality.

Chapter 7 Summary and Outlook

The results of Chapter 6 suggest that the hydrogenation of diamond electrodes leads to improved detection of dopamine in the presence of ascorbic acid by limiting the catalytic interaction between the two species at the electrode interface. Whilst experiments were conclusive, they do not represent an in-depth study - only a proof-of-principle confirmation of this effect. Several questions remain, including: Can any improvement to the cathodic electrochemical pre-treatment achieve the same result as a hydrogen-modified diamond electrode? What is the extent of hydrogenation on cathodic and hydrogen-plasma modified diamond? What is the key influence over the separation of the two species – hydrophobic, electrostatic, or some other physical effect? Can these hydrogenated electrodes be used to directly probe the electrochemistry of neuronal cells? The results of this thesis suggest that hydrogenation is a useful surface modification for diamond in conditions that mimic neuronal environments, yet a considerable amount of work remains in order to realize a real neuronal bio-sensor which exploits its properties and potential.

This thesis has advanced our understanding of the relationship between surface modification and functionality at the solid-liquid interface of three carbon-based materials. Nanodiamond, carbene-modified polymers, and boron-doped diamond thin films, with the right surface chemistry, have been shown to induce desirable biological behaviours relating to their intended use. Using the methodologies employed here, further experiments relating to their surface modification and interactions with biological systems will be possible using XPS, QCM-D and electrochemistry.